



저작자표시-비영리-변경금지 2.0 대한민국

이용자는 아래의 조건을 따르는 경우에 한하여 자유롭게

- 이 저작물을 복제, 배포, 전송, 전시, 공연 및 방송할 수 있습니다.

다음과 같은 조건을 따라야 합니다:



저작자표시. 귀하는 원저작자를 표시하여야 합니다.



비영리. 귀하는 이 저작물을 영리 목적으로 이용할 수 없습니다.



변경금지. 귀하는 이 저작물을 개작, 변형 또는 가공할 수 없습니다.

- 귀하는, 이 저작물의 재이용이나 배포의 경우, 이 저작물에 적용된 이용허락조건을 명확하게 나타내어야 합니다.
- 저작권자로부터 별도의 허가를 받으면 이러한 조건들은 적용되지 않습니다.

저작권법에 따른 이용자의 권리는 위의 내용에 의하여 영향을 받지 않습니다.

이것은 [이용허락규약\(Legal Code\)](#)을 이해하기 쉽게 요약한 것입니다.

[Disclaimer](#)

공학박사 학위논문

**Experimental and Numerical Investigations of Design
Tractive Force in the Compound Open Channel**

복단면 하도에서 설계 소류력에 대한 실험적·수치적 연구

2016년 12월

서울대학교 대학원

건설환경공학부

이 두 한

ABSTRACT OF DISSERTATION

Experimental and Numerical Investigations of Design Tractive Force in the Compound Open Channel

by Du Han Lee

Doctor of Philosophy in Civil and Environmental Engineering

Seoul National University

Professor Il Won Seo, Advisor

Tractive forces in the compound open channels are distributed differently according to section shapes. In river design works, design tractive forces are evaluated usually using cross sectional averaged values or results by two-dimensional numerical models, and applied to revetment design as external forces. However, cross sectional distributions of tractive forces in compound open channels are directly affected by sectional shapes and show three dimensional characteristics. Design tractive forces evaluated by cross sectional averaged values are underestimated or overestimated, and it causes bank erosion and an excess design. Although there are many experimental and numerical studies of compound open channels, results of the studies are not applied to river design works. As most previous studies have focused mainly on the narrow width channel or some selected shapes, results of the studies could not be applied to river design works. The objective of this study is to develop the design factors for tractive force evaluation in compound open channel through the investigation of the relationship

between averaged tractive forces and local tractive forces along the cross sectional shapes. In this study tractive forces in representative compound open channels are measured by experiments, and three dimensional CFD model is calibrated by the experimental results. Using the calibrated numerical model, characteristics of tractive force distribution with floodplain width and height are analyzed. Characteristics of tractive force distribution compared with average tractive forces are investigated on bank, floodplain and levee. In the experiment tractive force distributions are measured using Preston tube. In the numerical simulation, OpenFoam model is applied. OpenFoam model is verified by the experimental results for LES. Numerical simulation are conducted for various width ratio and depth ratio on the compound open channel. The nomograph for determining tractive force is suggested by the numerical experiments. The nomograph developed in this study can be applied for the given geometric ratio and help to calculate the design tractive forces in the simple procedure.

keywords: compound open channel, design tractive force, wall shear stress, Preston tube , OpenFoam, Large eddy simulation, nomograph for design tractive force

Student Number: 2007-30846

TABLE OF CONTENTS

ABSTRACT OF DISSERTATION	i
LIST OF FIGURES	vi
LIST OF TABLES	xviii
CHAPTER 1. INTRODUCTION	1
1.1 Background	1
1.2 Objectives and Methodology	2
CHAPTER 2. THEORETICAL BACKGROUNDS	5
2.1 Evaluation of Design Tractive Forces	5
2.1.1 Domestic Status of Design Standards	5
2.1.2 Velocity and Boundary Shear Stress Distribution	5
2.1.3 Shiono and Kinght Method (SKM)	17
2.2 Experimental Research on Wall Shear Stress	40
2.2.1 Overview of Techniques of Wall Shear Stress Measurements	40
2.2.2 Preston Tube Method	49
2.3 Numerical Research	69
2.3.1 Turbulence Modelling	69
2.3.2 Brief Review of OpenFOAM	89
2.3.3 Literature Review of Simple Section Channel Flows	90
2.3.4 Literature Review of Compound Open Channel Flows	103
CHAPTER 3. LABORATORY EXPERIMENTS ON WALL SHEAR STRESS	117
3.1 Experimental Setup	117
3.2 Calibration of the Preston Tube	122

3.3 Experimental Results in the Compound Open Channel	128
3.3.1 Experimental Conditions	128
3.3.2 Experimental Results	132
CHAPTER 4. NUMERICAL SIMULATION OF COMPOUND OPEN CHANNEL	143
4.1 Verification of OpenFOAM Model	143
4.1.1 Numerical Setup	143
4.1.2 Results and Analysis	148
4.2 Rectangular Compound Open Channels	163
4.2.1 Simulation Cases	163
4.2.2 Results and Analysis	169
4.3 Trapezoidal Compound Open Channels	185
4.3.1 Simulation Cases	185
4.3.2 Results and Analysis	188
CHAPTER 5. METHODS FOR DETERMINING DESIGN TRACTIVE FORCE	200
5.1 Strategy for the Evaluation Methods	200
5.2 Design Factors for Cross Sectional Averaged Shear Stress	200
5.2.1 Rectangular Compound Channels	200
5.2.2 Trapezoidal Compound Channels	206
5.3 Design Friction Factors for Depth Averaged Velocity	215
5.3.1 Depth Averaged Velocity and Friction Factors	215
5.3.2 Design Friction Factors	238
5.4 Application of the Nomograph	249
5.4.1 Application of the Design Factor for Design Tractive Forces	249
5.4.2 Application of the Design Friction Factor	257
5.4.3 Applicability and Limitation	263

CHAPTER 6. CONCLUSIONS	265
REFERNECES	268
ABSTRACT IN KOREAN	287

LIST OF FIGURES

Figure 1.1 Methodology Outline.	4
Figure 2.1 Velocity distribution in various open channel sections (Chow 1959).	9
Figure 2.2 External flow past a flat plate (Massey 1998).	10
Figure 2.3 Law of wall () with DNS data.	10
Figure 2.4 Boundary shear stress on an inclined element (Shiono and Kinght 1988).	18
Figure 2.5 Panel structure (Sharifi 2009).	21
Figure 2.6 Constant and side domains (Sharifi 2009).	21
Figure 2.7 Distribution of vertical velocity, shear stress mixing length and eddy viscosity (Sharifi 2009).	31
Figure 2.8 Vertical distribution of eddy viscosity (Nezu and Nakagawa 1993).	31
Figure 2.9 Visualization of the averaged secondary flow term (Chlebek and Knight 2006).	35
Figure 2.10 Secondary currents in a rectangular channel (Nezu and Rodi 1985).	37
Figure 2.11 Secondary currents in smooth rectangular channels (Tominaga et al. 1989).	39
Figure 2.12 Secondary currents in a smooth trapezoidal channels (Tominaga et al. 1989).	40
Figure 2.13 Number of panels and sign of secondary current term for simple trapezoidal channels (Kinght et al. 2007).	40
Figure 2.14 Floating element techniques.	43
Figure 2.15 Oil-film interferometry technique.	44
Figure 2.16 Preston tube technique.	45
Figure 2.17 Surface fence technique.	46
Figure 2.18 Wall pulsed wire technique.	47
Figure 2.19 Hot wire technique.	49
Figure 2.20 Water surface profile.	50
Figure 2.21 Forces acting on a typical open channel flow control volume.	53

Figure 2.22 Flow approaching the pitot-static tube (Rouse 1978).	56
Figure 2.23 Schematic of pitot-static tube (Thornton et al. 2008)	57
Figure 2.24 Measured velocity profiles (Ludwig and Tillmann 1950).	58
Figure 2.25 Schematic of Preston tube experiment (Preston 1954).	60
Figure 2.26 Results from Preston (1954).	61
Figure 2.27 Velocity distribution of Ippen and Drinker (1960)	63
Figure 2.28 Preston tube configuration (Thornton et al. 2008).	67
Figure 2.29 Dimension of the Preston tube (Thornton et al. 2008).	67
Figure 2.30 Picture of the Preston tube (Thornton et al. 2008).	68
Figure 2.31 Representation of an arbitrary filter function (Villiers 2006).	83
Figure 2.32 Shape of filter functions (Piomelli 1999).	85
Figure 2.33 Measured secondary-current velocity vectors at a section (Nezu 2005). ...	93
Figure 2.34 Isovels of streamwise velocity and secondary currents in rectangular open-channel for aspect ratio 2 (Tominaga et al. 1989).	94
Figure 2.35 Calculated secondary current streamlines in open-channels under various aspect ratios (after Naot and Rodi 1982).	95
Figure 2.36 Predicted (RSM) and measured secondary flow in rectangular open-channel: Aspect ratios (a) 2; (b) 3.94; (c) 8 (Cokljat and Younis 1995).	96
Figure 2.37 Contours of primary velocity in rectangular open-channel: Aspect ratios (a) 2; (b) 3.94; (c) 8 (Cokljat and Younis 1995).	97
Figure 2.38 Predicted (RSM) and measured turbulence anisotropy for open rectangular channel with aspect ratio = 2 (Cokljat and Younis 1995).	97
Figure 2.39 Secondary current vectors: (a) RSM by Kang and Choi (2006a); (b) experiment Nezu and Rodi (1985); (c) RSM by Cokljat (1993); and (d) LES by Shi et al. (1999) (Kang and Choi 2006a).	99
Figure 2.40 Secondary current vectors in smooth trapezoidal channels (Tominaga et al. 1989).	100
Figure 2.41 Secondary flow cells pattern in smooth trapezoidal channels with different aspect ratio: (a) $2b/H \leq 2.2$; (b) $2b/H \geq 4$ (Knight et al. 2007).	101
Figure 2.42 Velocity contours and secondary velocity vectors in smooth trapezoidal	

channels: (a) ; (b) SSG; (c) SMC- (Knight et al. 2005).	102
Figure 2.43 Schematic representation of compound channel (Shiono and Knight 1991).	103
Figure 2.44 Hydraulic parameters associated with overbank flow in a trapezoidal compound channel (Shiono and Knight 1991).	105
Figure 2.45 Schematic representation of flow field in: (a) a shallow depth flow; (b) deep depth flow (Nezu et al. 1999).	107
Figure 2.46 Experimental and computed contours of the streamwise velocity (Filonivichi 2015).	108
Figure 2.47 Vector plots of the secondary currents and contours of the primary velocity in asymmetric compound channels for $\alpha = 0.5$ (Cokljat and Younis 1995).	110
Figure 2.48 Contours of the streamwise velocity in asymmetric compound channels for $h_r = 0.5$ (adapted from Thomas and Williams 1995a, Cater and Williams 2008, Kara et al. 2012).	112
Figure 2.49 Boundary shear stress in symmetric compound channel with trapezoidal cross-section (Knight et al. 2005).	115
Figure 3.1 Preston tube configuration.	117
Figure 3.2 The pressure gauge (LD300).	118
Figure 3.3 The data logger (GL220).	119
Figure 3.4 Schematic of the experimental channel.	119
Figure 3.5 Setup of the pressure gauges.	120
Figure 3.6 Measurement of water depth.	120
Figure 3.7 Measurement of wall shear stresses.	121
Figure 3.8 Picture of the Preston tube measuring wall shear.	121
Figure 3.9 Procedure of the calibration test.	123
Figure 3.10 Measurement of the pressure difference (case01).	124
Figure 3.11 Measurement of the pressure difference (case02).	124
Figure 3.12 Measurement of the pressure difference (case03).	125

Figure 3.13 Measurement of the pressure difference (case04).	125
Figure 3.14 Results of the calibration test.	127
Figure 3.15 Schematic description of floodplain open channel flow.	128
Figure 3.16 Geometry and water elevation of the case CR01Ex.	129
Figure 3.17 Geometry and water elevation of the case CR02Ex.	129
Figure 3.18 Geometry and water elevation of the case CR03Ex.	130
Figure 3.19 Geometry and water elevation of the case CR11Ex.	130
Figure 3.20 Geometry and water elevation of the case CR12Ex.	130
Figure 3.21 Experiment in the compound open channel (CR01Ex).	131
Figure 3.22 Experiment in the compound open channel (CR11Ex).	131
Figure 3.23 Results in the compound open channel (CR01Ex).	139
Figure 3.24 Results in the compound open channel (CR02Ex).	139
Figure 3.25 Results in the compound open channel (CR03Ex).	140
Figure 3.26 Results in the compound open channel (CR11Ex).	140
Figure 3.27 Results in the compound open channel (CR12Ex).	141
Figure 3.28 Comparison with Tominaga and Nezu ($h/H = 0.75$).	141
Figure 3.29 Comparison with Tominaga and Nezu ($h/H = 0.5$).	142
Figure 3.30 Comparison with Tominaga and Nezu ($h/H = 0.25$).	142
Figure 4.1 Schematic of compound open channels.	144
Figure 4.2 Computational setup and boundary conditions for LES.	144
Figure 4.3 Geometry of compound channels in verification tests.	145
Figure 4.4 Disretization of the computation domain (S2 case).	146
Figure 4.5 Composition of cross sectional grid points (S2 case).	146
Figure 4.6 Composition of cross sectional grid points (S1 case).	146
Figure 4.7 Composition of cross sectional grid points (S3 case).	147
Figure 4.8 Streamwise mean velocity for S1 case.	149
Figure 4.9 Streamwise mean velocity for S2 case.	150
Figure 4.10 Streamwise mean velocity for S3 case.	150
Figure 4.11 Secondary currents in S1.	153

Figure 4.12	Secondary currents in S2.	153
Figure 4.13	Secondary currents in S3.	154
Figure 4.14	Streamwise turbulence intensity of S2.	156
Figure 4.15	Vertical turbulence intensity of S2.	156
Figure 4.16	Lateral turbulence intensity of S2.	157
Figure 4.17	Anisotropy of turbulence of S2.	157
Figure 4.18	Reynolds stress distribution of in S2 case.	159
Figure 4.19	Reynolds stress distribution of in S2 case.	159
Figure 4.20	Wall shear stress distribution of S1.	161
Figure 4.21	Wall shear stress distribution of S2.	162
Figure 4.22	Wall shear stress distribution of S3.	162
Figure 4.23	Wall shear stress distribution of the present LES (S1, S2 and S3).	163
Figure 4.24	Geometry of the simulation cases (CR01, CR02, CR03 and CR04).	165
Figure 4.25	Geometry of the simulation cases (CR11, CR12, CR13 and CR14).	166
Figure 4.26	Geometry of the simulation cases (CR21, CR22, CR23 and CR24).	167
Figure 4.27	Geometry and mesh of case CR02.	168
Figure 4.28	Geometry and mesh of case CR03.	168
Figure 4.29	Geometry and mesh of case CR04.	168
Figure 4.30	Geometry and mesh of case CR12.	168
Figure 4.31	Geometry and mesh of case CR13.	168
Figure 4.32	Geometry and mesh of case CR14.	169
Figure 4.33	Geometry and mesh of case CR22.	169
Figure 4.34	Geometry and mesh of case CR23.	169
Figure 4.35	Geometry and mesh of case CR24.	169
Figure 4.36	Streamwise mean velocity in case CR01.	170
Figure 4.37	Streamwise mean velocity in case CR02.	170
Figure 4.38	Streamwise mean velocity in case CR03.	171
Figure 4.39	Streamwise mean velocity in case CR04.	171
Figure 4.40	Streamwise mean velocity in case CR11.	171
Figure 4.41	Streamwise mean velocity in case CR12.	171

Figure 4.42	Streamwise mean velocity in case CR13.	172
Figure 4.43	Streamwise mean velocity in case CR14.	172
Figure 4.44	Streamwise mean velocity in case CR21.	172
Figure 4.45	Streamwise mean velocity in case CR22.	172
Figure 4.46	Streamwise mean velocity in case CR23.	173
Figure 4.47	Streamwise mean velocity in case CR24.	173
Figure 4.48	Secondary flows in case CR01.	174
Figure 4.49	Secondary flows in case CR02.	174
Figure 4.50	Secondary flows in case CR03.	175
Figure 4.51	Secondary flows in case CR04.	175
Figure 4.52	Secondary flows in case CR11.	175
Figure 4.53	Secondary flows in case CR12.	175
Figure 4.54	Secondary flows in case CR13.	176
Figure 4.55	Secondary flows in case CR14.	176
Figure 4.56	Secondary flows in case CR21.	176
Figure 4.57	Secondary flows in case CR22.	176
Figure 4.58	Secondary flows in case CR23.	177
Figure 4.59	Secondary flows in case CR24.	177
Figure 4.60	Wall shear distribution in case CR01.	178
Figure 4.61	Wall shear distribution in case CR02.	178
Figure 4.62	Wall shear distribution in case CR03.	179
Figure 4.63	Wall shear distribution in case CR04.	179
Figure 4.64	Wall shear distribution in case CR11.	181
Figure 4.65	Wall shear distribution in case CR12.	181
Figure 4.66	Wall shear distribution in case CR13.	182
Figure 4.67	Wall shear distribution in case CR14.	182
Figure 4.68	Wall shear distribution in case CR21.	183
Figure 4.69	Wall shear distribution in case CR22.	184
Figure 4.70	Wall shear distribution in case CR23.	184
Figure 4.71	Wall shear distribution in case CR24.	185

Figure 4.72	Geometry and mesh of case CT01.	186
Figure 4.73	Geometry and mesh of case CT02.	186
Figure 4.74	Geometry and mesh of case CT03.	187
Figure 4.75	Geometry and mesh of case CT11.	187
Figure 4.76	Geometry and mesh of case CT12.	187
Figure 4.77	Geometry and mesh of case CT13.	187
Figure 4.78	Geometry and mesh of case CT21.	187
Figure 4.79	Geometry and mesh of case CT22.	188
Figure 4.80	Geometry and mesh of case CT23.	188
Figure 4.81	Streamwise mean velocity in case CT01.	189
Figure 4.82	Streamwise mean velocity in case CT02.	189
Figure 4.83	Streamwise mean velocity in case CT03.	190
Figure 4.84	Streamwise mean velocity in case CT11.	190
Figure 4.85	Streamwise mean velocity in case CT12.	190
Figure 4.86	Streamwise mean velocity in case CT13.	190
Figure 4.87	Streamwise mean velocity in case CT21.	191
Figure 4.88	Streamwise mean velocity in case CT22.	191
Figure 4.89	Streamwise mean velocity in case CT23.	191
Figure 4.90	Secondary flows in case CT01.	192
Figure 4.91	Secondary flows in case CT02.	192
Figure 4.92	Secondary flows in case CT03.	193
Figure 4.93	Secondary flows in case CT11.	193
Figure 4.94	Secondary flows in case CT12.	193
Figure 4.95	Secondary flows in case CT13.	193
Figure 4.96	Secondary flows in case CT21.	194
Figure 4.97	Secondary flows in case CT22.	194
Figure 4.98	Secondary flows in case CT23.	194
Figure 4.99	Wall shear distribution in case CT01.	195
Figure 4.100	Wall shear distribution in case CT02.	196
Figure 4.101	Wall shear distribution in case CT03.	196

Figure 4.102	Wall shear distribution in case CT11.	197
Figure 4.103	Wall shear distribution in case CT12.	197
Figure 4.104	Wall shear distribution in case CT13.	198
Figure 4.105	Wall shear distribution in case CT21.	198
Figure 4.106	Wall shear distribution in case CT22.	199
Figure 4.107	Wall shear distribution in case CT23.	199
Figure 5.1	The design factors for rectangular compound channels with b/B (main channel).	202
Figure 5.2	The design factors for rectangular compound channels with h/H (main channel).	203
Figure 5.3	The design factors for rectangular compound channels with b/B (floodplain).	203
Figure 5.4	The design factors for rectangular compound channels with h/H (floodplain).	204
Figure 5.5	The design factors for rectangular compound channels with b/B and h/H (main channel).	205
Figure 5.6	The design factors for rectangular compound channels with b/B and h/H (floodplain).	206
Figure 5.7	The design factors for trapezoidal compound channels with b/B (main channel).	207
Figure 5.8	The design factors for trapezoidal compound channels with h/H (main channel).	208
Figure 5.9	The design factors for trapezoidal compound channels with b/B (bank). ...	208
Figure 5.10	The design factors for trapezoidal compound channels with h/H (bank). ·	209
Figure 5.11	The design factors for trapezoidal compound channels with b/B (floodplain).	209
Figure 5.12	The design factors for trapezoidal compound channels with h/H (floodplain).	210
Figure 5.13	The design factors for trapezoidal compound channels with b/B (levee). ·	210

Figure 5.14	The design factors for trapezoidal compound channels with h/H (levee).	211
Figure 5.15	The design factors for trapezoidal compound channels with b/B and h/H (main channel).	212
Figure 5.16	The design factors for trapezoidal compound channels with b/B and h/H (bank).	213
Figure 5.17	The design factors for trapezoidal compound channels with b/B and h/H (floodplain).	214
Figure 5.18	The design factors for trapezoidal compound channels with b/B and h/H (levee).	215
Figure 5.19	Depth averaged velocity in case CR01.	217
Figure 5.20	Friction factor from depth averaged velocity in case CR01.	217
Figure 5.21	Depth averaged velocity in case CR02.	218
Figure 5.22	Friction factor from depth averaged velocity in case CR02.	218
Figure 5.23	Depth averaged velocity in case CR03.	219
Figure 5.24	Friction factor from depth averaged velocity in case CR03.	219
Figure 5.25	Depth averaged velocity in case CR04.	220
Figure 5.26	Friction factor from depth averaged velocity in case CR04.	220
Figure 5.27	Depth averaged velocity in case CR11.	221
Figure 5.28	Friction factor from depth averaged velocity in case CR11.	221
Figure 5.29	Depth averaged velocity in case CR12.	222
Figure 5.30	Friction factor from depth averaged velocity in case CR12.	222
Figure 5.31	Depth averaged velocity in case CR13.	223
Figure 5.32	Friction factor from depth averaged velocity in case CR13.	223
Figure 5.33	Depth averaged velocity in case CR14.	224
Figure 5.34	Friction factor from depth averaged velocity in case CR14.	224
Figure 5.35	Depth averaged velocity in case CR21.	225
Figure 5.36	Friction factor from depth averaged velocity in case CR21.	225
Figure 5.37	Depth averaged velocity in case CR22.	226
Figure 5.38	Friction factor from depth averaged velocity in case CR22.	226
Figure 5.39	Depth averaged velocity in case CR23.	227

Figure 5.40	Friction factor from depth averaged velocity in case CR23.	227
Figure 5.41	Depth averaged velocity in case CR24.	228
Figure 5.42	Friction factor from depth averaged velocity in case CR24.	228
Figure 5.43	Depth averaged velocity in case CT01.	229
Figure 5.44	Friction factor from depth averaged velocity in case CT01.	229
Figure 5.45	Depth averaged velocity in case CT02.	230
Figure 5.46	Friction factor from depth averaged velocity in case CT02.	230
Figure 5.47	Depth averaged velocity in case CT03.	231
Figure 5.48	Friction factor from depth averaged velocity in case CT03.	231
Figure 5.49	Depth averaged velocity in case CT11.	232
Figure 5.50	Friction factor from depth averaged velocity in case CT11.	232
Figure 5.51	Depth averaged velocity in case CT12.	233
Figure 5.52	Friction factor from depth averaged velocity in case CT12.	233
Figure 5.53	Depth averaged velocity in case CT13.	234
Figure 5.54	Friction factor from depth averaged velocity in case CT13.	234
Figure 5.55	Depth averaged velocity in case CT21.	235
Figure 5.56	Friction factor from depth averaged velocity in case CT21.	235
Figure 5.57	Depth averaged velocity in case CT22.	236
Figure 5.58	Friction factor from depth averaged velocity in case CT22.	236
Figure 5.59	Depth averaged velocity in case CT23.	237
Figure 5.60	Friction factor from depth averaged velocity in case CT23.	237
Figure 5.61	The design friction factors for trapezoidal compound channels with b/B (main channel).	241
Figure 5.62	The design friction factors for trapezoidal compound channels with h/H (main channel).	241
Figure 5.63	The design friction factors for trapezoidal compound channels with b/B (bank).	242
Figure 5.64	The design friction factors for trapezoidal compound channels with h/H (bank).	242
Figure 5.65	The design friction factors for trapezoidal compound channels with b/B	

(floodplain).	243
Figure 5.66 The design friction factors for trapezoidal compound channels with h/H (floodplain).	243
Figure 5.67 The design friction factors for trapezoidal compound channels with b/B (levee).	244
Figure 5.68 The design friction factors for trapezoidal compound channels with h/H (levee).	244
Figure 5.69 The design friction factors for trapezoidal compound channels with b/B and h/H (main channel).	245
Figure 5.70 The design friction factors for trapezoidal compound channels with b/B and h/H (bank).	246
Figure 5.71 The design friction factors for trapezoidal compound channels with b/B and h/H (floodplain).	247
Figure 5.72 The design friction factors for trapezoidal compound channels with b/B and h/H (levee).	248
Figure 5.73 Test section 1 for a rectangular compound channel.	249
Figure 5.74 Design factor from the nomograph (main channel in rectangular open channels).	250
Figure 5.75 Design factor from the nomograph (floodplain in rectangular open channels).	251
Figure 5.76 Resultant design tractive forces for test section 1.	251
Figure 5.77 Test section 2 for a trapezoidal compound channel.	252
Figure 5.78 Design factor from the nomograph (main channel in trapezoidal open channels).	253
Figure 5.79 Design factor from the nomograph (bank in trapezoidal open channels). ·	254
Figure 5.80 Design factor from the nomograph (floodplain in trapezoidal open channels).	255
Figure 5.81 Design factor from the nomograph (levee in trapezoidal open channels).	256
Figure 5.82 Resultant design tractive forces for test section 2.	256
Figure 5.83 Design friction factor from the nomograph (main channel in trapezoidal	

open channels).	258
Figure 5.84 Design friction factor from the nomograph (bank in trapezoidal open channels).	259
Figure 5.85 Design friction factor from the nomograph (floodplain in trapezoidal open channels).	260
Figure 5.86 Design friction factor from the nomograph (Levee in trapezoidal open channels).	261
Figure 5.87 Determined friction factors from the nomograph.	262
Figure 5.88 Calculated design tractive forces by nomograph and depth averaged velocity.	262
Figure 5.89 Comparison of geometric ratio.	264

LIST OF TABLES

Table 2.1 Domestic status of river design criteria.	6
Table 2.2 Techniques for wall shear stress measurement.	41
Table 2.3 Diameters of pitot tubes in Preston (1954) experiment.	60
Table 2.4 Calibrated equations for tested pitot tubes (Preston 1954).	62
Table 2.5 Values of the constants in the model for open-channel flows (Nezu and Nakagawa 1993).	77
Table 2.6 Values of the constants in the model (Wilcox 1988).	78
Table 2.7 Values of the coefficients in the BSL model (Menter 1994).	80
Table 3.1 Results of the calibration test.	126
Table 3.2 Experimental conditions	129
Table 3.3 Experimental result of wall shear stress (CR01Ex).	134
Table 3.4 Experimental result of wall shear stress (CR02Ex).	135
Table 3.5 Experimental result of wall shear stress (CR03Ex).	136
Table 3.6 Experimental result of wall shear stress (CR11Ex).	137
Table 3.7 Experimental result of wall shear stress (CR12Ex).	138
Table 4.1 Verification cases and flow conditions (Tominaga and Nezu 1991)	144
Table 4.2 Domain discretization in verification tests.	147
Table 4.3 Wall distances in verification tests.	147
Table 4.4 Simulation cases of rectangular compound channels.	164
Table 4.5 Simulation cases of trapezoidal compound channels.	186
Table 5.1 The design factors in rectangular compound channels (main channel).	201
Table 5.2 The design factors in rectangular compound channels (floodplain).	202
Table 5.3 The design friction factors in trapezoidal compound channels (main channel).	239
Table 5.4 The design friction factors in trapezoidal compound channels (bank).	239

Table 5.5 The design friction factors in trapezoidal compound channels (floodplain). · 239

Table 5.6 The design friction factors in trapezoidal compound channels (levee). ······ 240

CHAPTER 1

INTRODUCTION

1.1 Background

Evaluation of external force induced by flow is much important in hydraulic and river engineering because it governs sediment transport and river protection failure. In the channel design, channel boundary materials such as channel revetments and linings should be designed to be safe from flood damage in the design flood condition. Tractive forces (or bed shear stress, wall shear stress) on channel boundary are usually considered as design external forces in channel design works.

River revetments supply levee and bank protection from erosion and scour and they are installed in the part with high velocity or high tractive force. Thus the revetments should supply the protection in the design tractive force. If the tractive force is evaluated incorrectly, serious problems can be happened. Underestimation of the tractive force can cause the bank and levee failures and overestimation of the force can cause serious economic losses by the unnecessary installation of the revetments. It is much important to evaluate the design tractive force correctly to prevent the flood damages and economic losses.

In the river design criteria (MOCT 2009) of Korea, design criteria of levee and revetments are suggested that levee and revetments should be designed to be stable from the tractive force induced by the flow in the design flood. However, standard method or detailed procedure to determine the design tractive forces is not suggested. In the practice of the river design, design tractive forces are usually used as cross-sectional averaged values that are calculated by one dimensional non-uniform flow analysis.

Tractive forces in the channel are distributed non-uniformly according to channel shapes even in the case of the simple rectangular channel. Especially in the compound

channel distribution of the tractive forces is much complicated and distribution range is much higher than the case of simple section. Thus use of the averaged tractive force as design external force causes inevitably local under-design or over-design. This can result in serious flood damages or economic losses. Especially in the river with wide floodplains correct estimation of design tractive force is much more important. In Korea, most rivers have wide floodplains excluding some small creeks.

A compound open channel is characterized by a main channel that conveys low flows and floodplains that pass major flows during floods. Tractive force distribution in compound channel is directly related to the flow and turbulence properties. In compound channel flow, momentum transfer occurs at the interface between deep main channel and shallow floodplains due to the streamwise velocity gradient and the resultant secondary velocities and shear layer. This momentum transfer produces additional energy losses and alters streamwise and secondary velocities, bed shear stresses and turbulence characteristics (Tominaga and Nezu 1991). A considerable amount of theoretical, experimental, and numerical research on the compound open channel is available to study the velocity distribution and boundary shear stress (Kinght and Demetriou 1983, Tominaga and Nezu 1991, van Prooijen *et al.*, 2005, Cater and Williams 2008, Kara *et al.* 2012).

Correct evaluation of tractive forces in compound channel needs calculation of fully 3D flow structures and turbulence properties. However, in the river design practice it is almost impossible. To consider the these flow characteristics in the design practice design factors related to compound channel shapes should be suggested.

1.2 Objectives and Methodology

The main objective of this study is to suggest simple design factors of tractive force evaluation in compound open channel for various channel shapes to prevent the over-design and under-design in river design practice. To achieve the main objective 3D

numerical simulations and laboratory experiments are performed to analyze the flow structures and wall shear stress distribution for various compound channel shapes. The objectives of the present study are:

- 1) to provide design factors of determining design tractive forces for various shapes of compound open channels.
- 2) to provide wall shear stress distribution in the case of wide-shallow flow for rectangular and trapezoidal compound channel.
- 3) to contribute to the understanding of the relation between wall shear stress distribution and flow structures in compound open channel.

In this study tractive forces in representative compound open channels are measured by experiments, and three dimensional CFD model is calibrated by the experimental results. Using the calibrated numerical model, characteristics of tractive force distribution with floodplain width and height are analyzed. Characteristics of tractive force distribution compared with average tractive forcings are investigated in the parts of main channel, bank, floodplain and levee.

In the experiment tractive force distributions are measured using the Preston tubes. The Preston tubes are calibrated by verification tests in uniform flow conditions.

In the numerical simulation, OpenFoam model is applied. OpenFoam is verified by the present experimental results and Tominaga and Nezu (1991)'s experiments for LES in the compound section. Then, numerical simulations are conducted for various width ratio and depth ratio on the compound open channel for rectangular and trapezoidal cases. LES results for compound channels are analyzed in the properties of velocity distribution, secondary flow structures, and wall shear stress distribution according to channel shapes.

Finally, design factors are suggested as multiplying factors of channel parts (main

channel, bank, floodplain, and levee) to cross sectional averaged shear stress considering the compound open channel shapes as the depth ratio and width ratio. Also, design factors are suggested as the friction factors of the channel parts to the depth averaged velocity considering the compound open channel shapes as the depth ratio and width ratio.

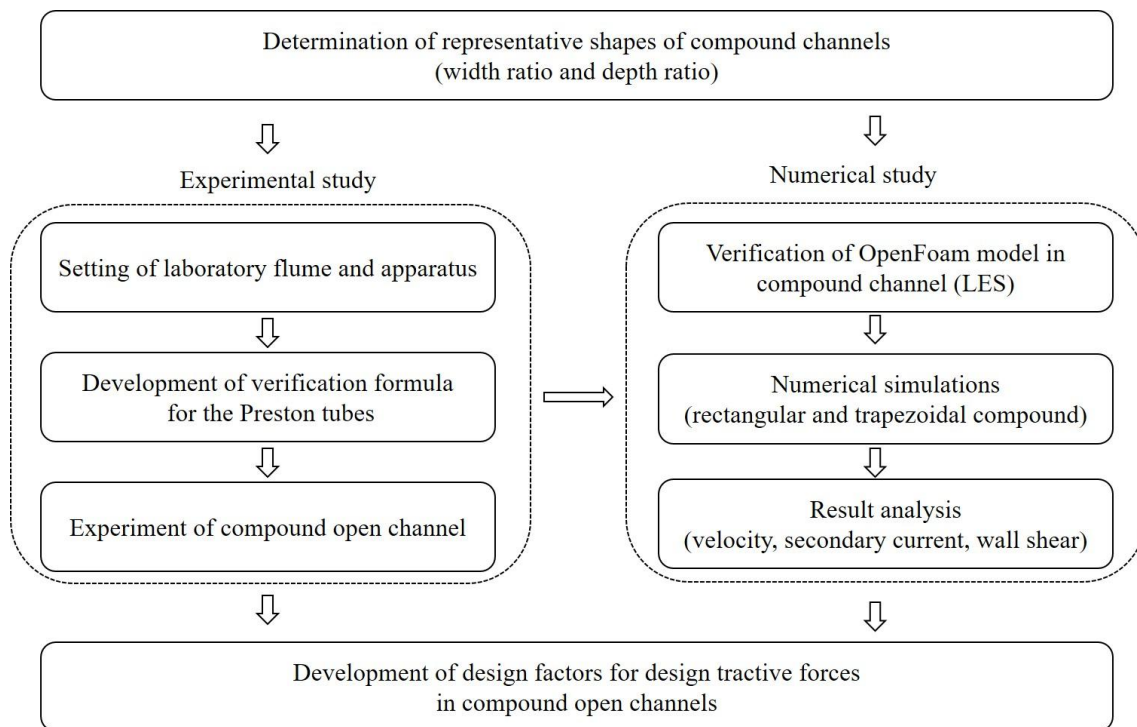


Figure 1.1 Methodology Outline.

CHAPTER 2

THEORETICAL BACKGROUNDS

2.1 Evaluation of Design Tractive Forces

2.1.1 Domestic Status of Design Standards

Korean design criteria of river design can be synthesized as Table 2.1 including the river design criteria of Korea (MOCT 2009). The river design criteria of Korea regulates general design criteria required to river managements and river projects, and it consists of criteria and commentary. The criteria that regulates essential considerations of river design carries legal binding force, and the commentary that consists of specification, supplementary explanation, references, and design examples to give help and references in application of the criteria does no legal binding force. The river design criteria proposes in the field of survey, planning and design. Construction criteria of river projects is regulated in the standard specification of river construction (KWRA 2007). The standard specification of river construction is river construction standard generally used in establishing the construction standard between ordering organization and the contractor. Planning guideline for integrated flood management plan in river basin and river master plan (MOCT 2008) proposes design considerations required in Korean river law. Design practice of river works (MOCT 2009) proposes general design criteria and practice required in establishment for action plans and working design of river improvement plan and related river works by river law and construction management law.

In the river design criteria, revetments (bank or levee protections) are defined as structures constructed in front of levee or bank slope to protect levee and bank from the failure and erosion caused by flow. Revetments consists of head protection, slope protection, slope end, foundation, and foot protection.

Table 2.1 Domestic status of river design criteria.

Criteria	Legislation date	Revision date	Department	Association
River design criteria	2005.6	2009.8	MOCT	KICT/ KWRA
Standard specification of river construction	-	2007.7	MOCT	KWRA
Planning guideline for integrated flood management plan in river basin and river master plan	-	2008.12	MOCT	-
Design practice of river works	2007.	2009.12	MOCT	-

In the river design criteria, it is proposed that revetment design by theoretical calculation is difficult at present technology level and empirical information should be considered in the design process. However, detailed methodology for theoretical and empirical design to secure the stability from the flow has not been suggested. Location and length of revetment installation are recommended to be determined considering hydraulic phenomena, scour and deposition variations. In high gradient or semi high gradient rivers revetment installation is recommended for entire reach and in low gradient rivers revetment installation is recommended at impingement part. Upstream and downstream of the structures such as bridge, weir, and drop structures revetment installation is also recommended. In the urban stream revetment installation is recommended when the bank or levee slope over 1:2.

Revetment types are selected by tractive force or velocity, however, evaluation procedure of tractive force or velocity is not suggested in the design criteria or practice. In practical design, one dimensional non-uniform calculation such as HEC-RAS model is generally applied to evaluate the design velocities or design tractive forces, and proper revetment types are selected by the results and designer's experience.

In river design it is important that flood protection is planned to secure the stability of river in the design flood condition. Unlike the general civil engineering structures, stability of the river is based on the dynamic equilibrium of natural erosion and deposition, thus, it is impossible that artificial structures constructed in the river maintain their stability perfectly. In addition, it is nearly impossible to secure entire river stability considering the local scour due to the complicated flow structures and geometrical irregularity. However, evaluation method for tractive forces should be suggested reflecting present technology level, and it is possible in some degree. In the domestic design criteria detailed evaluation method for design tractive forces is insufficient.

Objective of revetment design is to secure the bank and levee protection from the failure and erosion in the design flood. This means that revetment and other channel components should be protected from the external forces due to the design flood. External forces can be expressed as velocity or tractive force (boundary shear stress) and average values of these are easily calculated by one dimension non-uniform analysis.

Generally velocities and tractive forces are distributed along the lateral direction of sections with cross section shapes. Especially in the compound channel the local values show much difference with the average values. Thus use of the averaged tractive force as design external force causes inevitably local under-design or over-design. This can result in serious flood damages or economic losses. Especially in the river with wide floodplains correct estimation of design tractive force is much more important.

2.1.2 Velocity and Boundary Shear Stress Distribution

(1) Overview of Turbulence

Fluid flow can be classified as laminar or turbulent, or in transition between these two regimes. A flow is laminar if the viscous forces due to molecular cohesion are strong enough to overcome the fluid's inertial forces. Flows that are both steady and laminar

exhibit absolutely no variation in time except for the random motion of fluid molecules. In this regime, the fluid appears to consist of thin layers that flow past one another in smooth pathways and the flow can be accurately described by the Navier-Stokes equations (Bradshaw 1971, Nezu and Nakagawa 1993, Drazin and Riley 2006).

As the inertial forces are increased, a critical point is reached when the viscous forces are no longer able to maintain the laminar structure of the flow. Lumps of fluid migrate between the adjacent fluid layers in a seemingly random manner with velocity component transverse to the main direction of flow. This new regime of fluctuating motion, characterized by chaotic and stochastic property changes is referred to as turbulence (Reynolds 1974, Nezu and Nakagawa 1993). In this chaotic state of motion, the velocity and pressure change continuously with time, within substantial regions of flow and therefore the fluid particles continuously interchange energy and momentum (Schlichting 1979). In open channel flow, turbulence is born near the boundaries where the primary perturbations and eddies form due to high velocity gradients. These eddies rapidly drift into the main flow field and increase in size by entraining particles of the surrounding fluid (Goncharov 1964, Schlichting 1979).

The major difference between laminar and turbulent flow is the appearance of perturbations and formation of a broad spectrum of eddies due to the high velocity gradients. Observing this spectrum led Kolmogorov (1941) to introduce the concept of the “energy cascade”. Based on this idea, the largest eddies, which are created by instabilities, interact with the flow domain and rapidly break and pass their energy onto smaller eddies. Smaller eddies are themselves unstable and they, in turn, pass their energy onto even smaller structures and so on. This cascade process of energy transition continues until the viscous forces become dissipate the energy in the smallest eddies.

(2) Velocity distribution in open channels

In an open channel cross-section, the main difference between the velocity distribution

in laminar and turbulent conditions is that in laminar flow, the maximum velocity occurs at the water surface while for most turbulent flow situations, it occurs somewhat below the water surface which is known as dip phenomena. This is mostly due to the presence of secondary flow cells. Laboratory and field data from many researchers show that the maximum streamwise velocity is found at about 5 to 25% of the water depth below the water surface (Chow 1959). Typical streamwise velocity contour lines for flow in various cross sections are shown in Figure 2.1. Other factors that are important in the distribution of velocity are the shape of the section and roughness.

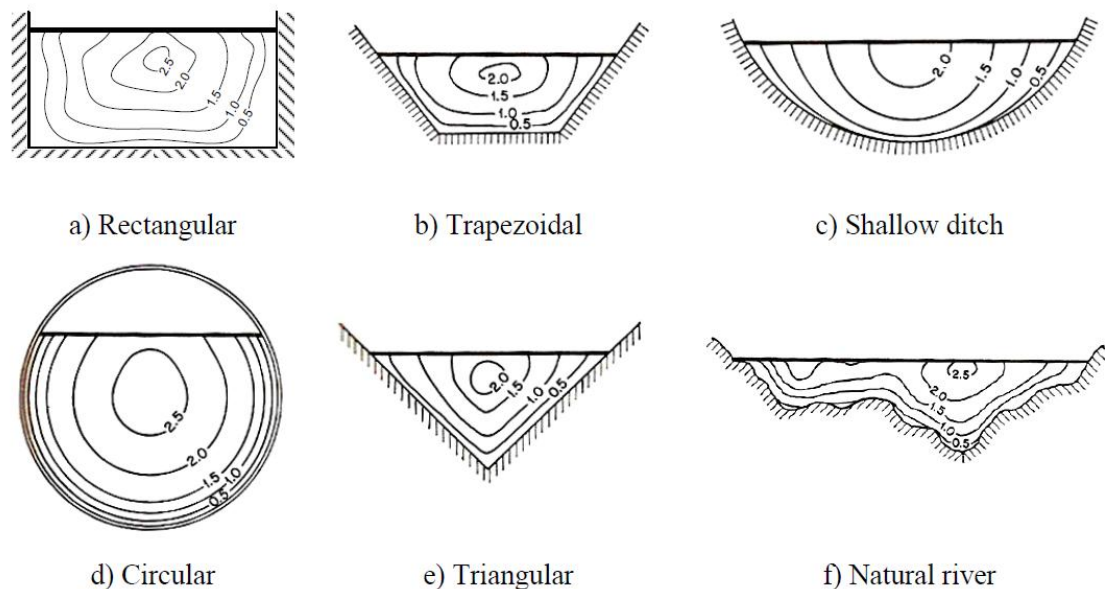


Figure 2.1 Velocity distribution in various open channel sections (Chow 1959).

Generally the velocity profile near the wall in turbulent open channel is expressed as “logarithmic law”. The classical logarithmic law formulation is based on Prandtl’s (1926) description of the “law of the wall” and the “boundary layer” concept. Figure 2.2 shows the motion of a fluid past a flat plate and the formed boundary layer. The boundary layer is a thin region of fluid near a solid surface (bed or wall) where the boundary resistance and the viscous interactions affect the fluid motion and

subsequently, the velocity distribution. In the fully developed turbulent region, this layer includes two main sub-layers. Near the solid boundary, a viscous sub-layer (laminar layer) forms where the viscous force is predominant. In contrast, further away from the boundary, the turbulent shear stresses play a major role in the defect layer (turbulent layer).

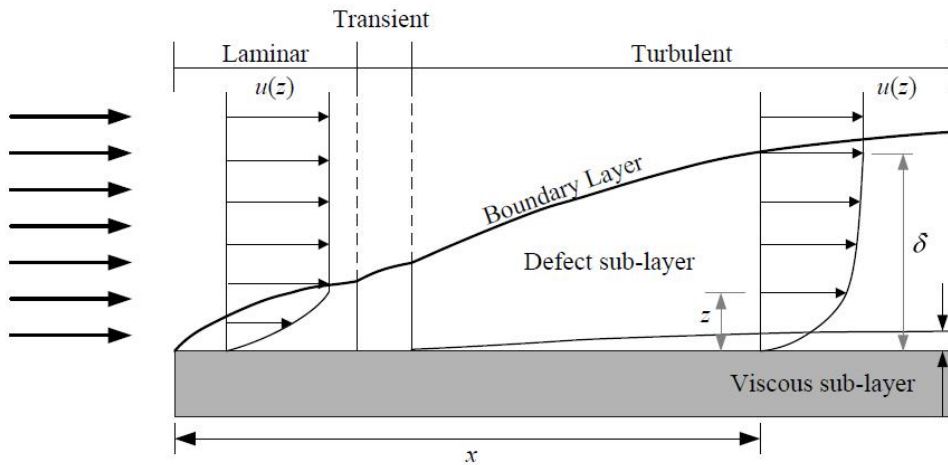


Figure 2.2 External flow past a flat plate (Massey 1998).

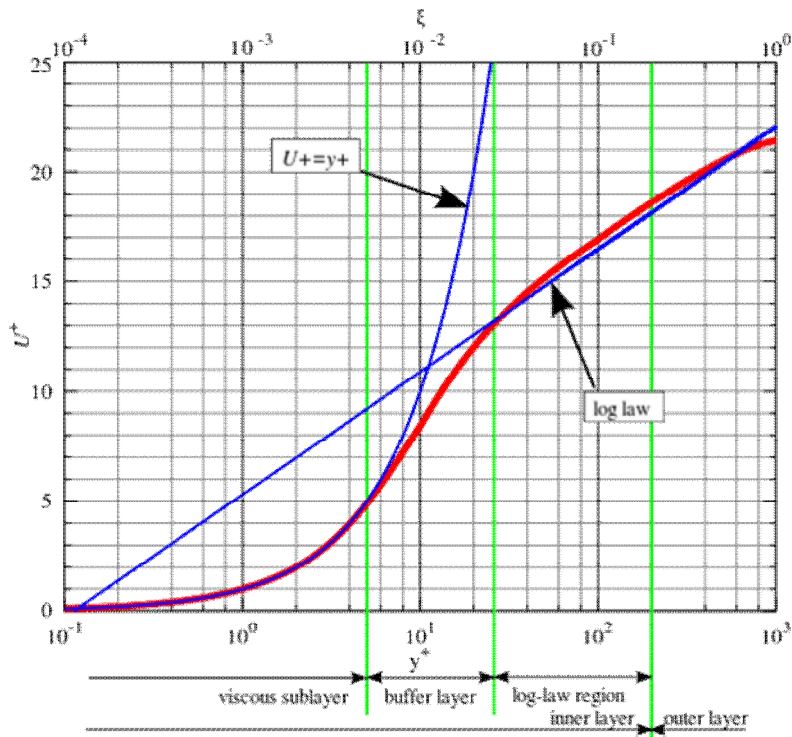


Figure 2.3 Law of wall ($y^+ = z^+$) with DNS data.

The “law of the wall” states that in the streamwise direction, the average fluid velocity in the boundary layer varies logarithmically with distance from the wall surface. This law is used to derive an empirical equation for the vertical distribution of the streamwise velocity in the sub-layers as Equation 2.1.

$$u^+ = f(z^+) \quad (2.1)$$

where the dimensionless velocity, u^+ , the shear velocity (or friction velocity), u_* , and the dimensionless normal distance from the wall, z^+ , are defined as Equation 2.2.

$$u^+ = \frac{u(z)}{u_*}; \quad u_* = \sqrt{\frac{\tau_w}{\rho}}; \quad z^+ = \frac{u_* z}{\nu} \quad (2.2)$$

where τ_w is the wall shear stress and ν is the kinematic viscosity.

In the viscous sub-layer, which has the range of $z^+ < 5$, the shear stress equals the wall shear stress, which is constant for steady flow. Thus, the dimensionless velocity is directly proportional to the dimensionless distance from the wall as Equation 2.3.

$$u^+ = z^+ = \frac{u_* z}{\nu} \quad (2.3)$$

In the defect sub-layer ($5 > z^+$), the effects of turbulent is more important than viscosity. In this region, the law of the wall can be written as Equation 2.4.

$$u^+ = \frac{1}{\kappa} \ln z^+ + C_1 \quad (2.4)$$

where κ is the von Karman’s constant, and C_1 is a dimensionless integration constant related to the thickness of the viscous sub-layer generally, in the range of 4.9 to 7.0.

Based on Nikuradse's (1933) data, the integration constant can be approximated as $\nu/9u_*$ and $\kappa/30$ for smooth and rough surfaces, respectively. This results in the universal laws for smooth and rough turbulent flow as Equation 2.5 and 2.6 (Chow 1959, Rouse 1959, Schlichting 1979).

$$u^+ = 5.75 \log\left(\frac{9u_*z}{\nu}\right) \quad (2.5)$$

$$u^+ = 5.75 \log\left(\frac{30z}{\kappa}\right) \quad (2.6)$$

In the buffer layer, between 5 wall units and 30 wall units, neither law holds with the largest variation from either law occurring approximately where the two equations intercept, at $z^+=11$. That is, before 11 wall units the linear approximation is more accurate and after 11 wall units the logarithmic approximation should be used, though neither are relatively accurate at 11 wall units (Figure 2.3).

(3) Boundary shear stress distribution in open channels

Flow structure in a channel is directly related to the boundary shear stress. Computation of flow resistance, side-wall correction, sediment discharge, channel erosion or deposition, cavitation problems, and designs of channels are among the problems which can be solved by the boundary shear stress distribution (Yang and Lim, 1997; Guo and Julien, 2005).

The boundary shear stress distribution is non-uniform over the wetted perimeter of a channel cross-section. This is widely proven, even for steady flows in straight prismatic channels with a simple cross-sectional geometry. The non-uniformity is mainly due to the anisotropy of the turbulence which produces transverse gradients of Reynolds stresses and secondary circulations (Gessner, 1973). Tominaga *et al.* (1989) and Knight and Demetriou (1983) show that the boundary shear stress increases where the

secondary currents flow towards the wall and decreases when they flow away from the wall.

Several direct and indirect measurement techniques for boundary shear stress are reported in the literature (Al-Hamid 1991). The most practical indirect measurement technique is Preston's (1954) method which has been employed for the boundary shear stress measurements used in this research. A description of this technique is provided in the section 2.2.3. Due to the shortcomings and limitations of these measuring techniques, determining the actual shear stress distribution along the wetted perimeter is extremely difficult (Patel 1965) and hence, various empirical, analytical and computational methods have been developed to predict the boundary shear stress.

These methods can be classified as geometrical methods, empirical methods, analytical methods, and computational methods.

Geometrical methods

Geometrical methods rely on splitting the channel cross-section into sub-regions. The shear force along each segment of the boundary is found by balancing the forces against the weight of fluid in the corresponding sub-region. Leighly's (1932) method, Einstein's (1942) method, Vertical depth Method (VDM), Vertical Area Method (VAM), Normal Area Method (NAM), Merged Perpendicular Method (MPM) (Khodashenas and Paquier, 1999) and Normal Depth Method (NDM) (Lundgren and Johnsson, 1964) are among the stated geometrical methods in literature.

Empirical methods

Empirical methods are basically simple regression models developed from fitting curves to measured experimental data. Knight's (1981) model was the first model of this kind. His model was further developed by him and his colleagues (Knight *et al.*, 1984a & b and 1994), and other researchers (Flintham and Carling 1988). Pizzuto (1991) and

Olivero *et al.* (1999) also proposed similar simple models for the boundary shear stress.

Analytical methods

Analytical methods are based on the mechanism of energy transportation, continuity and momentum equations. Some of these methods lead to a geometric solution for computing the shear stress in open channels. Some of the analytical methods include the work of Yang and Lim (1997, 2005), Zheng and Jin (1998), Guo and Julien (2005) and Bilgil (2005).

Computational methods

A possibly more accurate way of finding the boundary shear stress distribution is using a turbulence closure model to solve the governing equations of motion. For example, Christensen and Fredsoe (1998) used the Reynolds stress turbulence model (RSM) and De Cacqueray *et al.* (2009) used the SSG Reynolds stress turbulence model to solve the equations of motion in a computational fluid dynamics (CFD) software to predict the boundary shear stress in open channels. Details of computational method are provided in the Chapter 4.

The average shear stress ($\bar{\tau}$) for an open channel cross-section can be represented as Equation 2.7.

$$\bar{\tau} = \rho g R S_f \quad (2.7)$$

where R is the hydraulic radius and S_f is the energy gradient which can be approximated from a head loss equation such as Darcy-Weisbach (Equation 2.8).

$$S_f = \frac{h_f}{L} = \frac{f}{4R} \frac{U_m}{2g} \quad (2.8)$$

where h_f is the head loss, L the channel length, f the Darcy-Weisbach friction factor and U_m is the mean velocity. Substituting Equation 2.8 in Equation 2.7 the shear stress can be expressed related to the friction as Equation 2.9.

$$\bar{\tau} = \rho \frac{f}{8} U_m^2 \quad (2.9)$$

In depth-averaged RANS, Equation 2.9 is extended to define the local boundary stress at a specific point in simple cross-section (Knight and Shiono 1996) as Equation 2.10.

$$\tau_i = \rho \frac{f}{8} U_d^2 \quad (2.10)$$

where τ_i is the local boundary stress, f is the local friction factor and U_d is the streamwise depth-averaged velocity. It is shown that the lateral distribution of the local boundary stress is sensitive to changes in f and water depth, and a sudden change in either of these variables will result in a corresponding change in the magnitude and distribution of τ_i (Chlebek and Knight 2006).

Knight (1981) proposed a simple method for separating the mean bed and wall shear stress for rectangular channels. He defined the shear force acting on the walls and bed as Equation 2.11 and 2.12.

$$SF_w = 2h\bar{\tau}_w \quad (2.11)$$

$$SF_b = 2b\bar{\tau}_b \quad (2.12)$$

where τ is the mean shear stress, b is the channel bed width, h is the flow depth, and the subscripts w and b denote walls and bed respectively. The shear force carried by the walls and the bed can be expressed as a percentage of the total shear force (SF_T) as Equation 2.13 and 2.14.

$$\%SF_w = \frac{SF_w}{SF_T} 100 \quad (2.13)$$

$$\%SF_b = \frac{SF_b}{SF_T} 100 \quad (2.14)$$

where $SF_T = \bar{\tau}P = \rho g R S_f P$ and P is the wetted perimeter.

Knight (1981) suggested that the percentage shear force carried by the walls has an exponential relation with the aspect ratio, $2b/h$ in the form of as Equation 2.15.

$$\%SF_w = e^\alpha \quad (2.15)$$

where α is a function of the aspect ratio. Fitting Equation 2.15 to the experimental results in rectangular open channel and rectangular closed conduit channels, Knight *et al.* (1984a) suggested Equation 2.16.

$$\alpha = -3.230 \log\left(\frac{2b}{h} + 3\right) + 6.146 \quad (2.16)$$

Flintham and Carling (1988) suggested a more general equation for calculating $\%SF_w$ in rectangular and trapezoidal channels with homogeneous boundary roughness. Knight *et al.* (1994) suggested more accurate formula for $\%SF_w$ by implementing a shape factor.

2.1.3 Shiono and Knight Method (SKM)

(1) Governing equation and solution

The Shiono and Knight Method (1988, 1990, 1991) (SKM) is a lateral distribution method based on the depth averaged RANS equations. This quasi 2-D model includes some of the 3D flow structures that occur in compound channels and is able to predict the transverse variation of depth-averaged velocity and boundary shear stress distributions of any cross section shape. SKM provides a tool for water level prediction, for distributing flows within a cross section, and for predicting the lateral distributions of boundary shear stress. SKM is adopted by the UK's Environment Agency for use in its 'Conveyance and Afflux Estimation System' software (www.river-conveyance.net).

In this method, the streamwise depth-averaged momentum equation is solved for steady uniform turbulent flow in a prismatic cross-section. The equation for the longitudinal streamwise component of momentum may be combined with the continuity equation to give Equation 2.17.

$$\rho \left[\frac{\partial \overline{UV}}{\partial y} + \frac{\partial \overline{UW}}{\partial z} \right] = \rho g S_0 + \frac{\partial}{\partial y} (-\rho \overline{uv}) + \frac{\partial}{\partial z} (-\rho \overline{uw}) \quad (2.17)$$

(i) (ii) (iii) (iv)

where x , y , z are streamwise, lateral and normal directions respectively, \overline{U} , \overline{V} , \overline{W} are temporal mean velocity components corresponding to x , y , z , u , v , w are turbulent perturbations of velocity with respect to the mean, S_0 is the bed slope gradient. In this equation, term (i) which includes the lateral and vertical components of velocity is called the secondary flow term and term (ii) is the weight component term. The terms (iii) and (iv) account for the Reynolds stresses acting on the vertical and horizontal planes respectively.

The depth-mean-averaged momentum equation can be obtained by integrating equation

2.17 over the water depth, h . Shiono and Knight (1988) show that Equation 2.17 becomes Equation 2.18.

$$\frac{\partial h(\rho \overline{UV})_d}{\partial y} = \rho g h S_0 + \frac{\partial h \overline{\tau_{yx}}}{\partial y} - \tau_b \left(1 + \frac{1}{s^2}\right)^{1/2} \quad (2.18)$$

where τ_b is the bed shear stress, s is the side slope (1:s, vertical: horizontal), the subscript, d denotes the depth average terms. Boundary shear stress terms on an inclined element are provided as Figure 2.4.

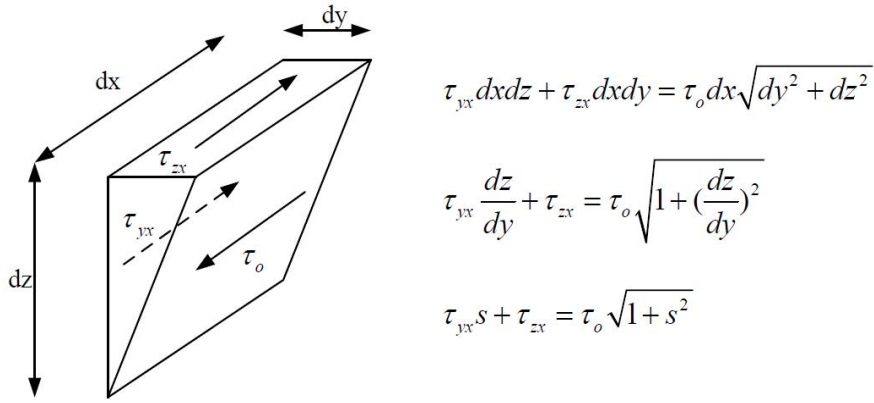


Figure 2.4 Boundary shear stress on an inclined element (Shiono and Kinght 1988).

SKM uses the Boussinesq eddy viscosity model as the closure model to relate the Reynolds shear stress, τ_{yx} , to the mean flow rate as Equation 2.19.

$$\overline{\tau_{yx}} = \rho \overline{\epsilon_{yx}} \frac{\partial U_d}{\partial y} \quad (2.19)$$

where U_d is the depth averaged streamwise velocity and $\overline{\epsilon_{yx}}$ is the depth-averaged eddy viscosity. Based on the Cunge *et al.* (1980) assumption, this parameter is assumed to be

proportional to the water depth, h , and to the shear velocity u_* as Equation 2.20.

$$\overline{\epsilon_{yx}} = \lambda u_* h \quad (2.20)$$

where λ is the dimensionless eddy viscosity. Incorporating Equation 2.10, the shear velocity can be reformulated as Equation 2.21.

$$u_* = \sqrt{\frac{\tau_0}{\rho}} = \left(\frac{1}{8}f\right)^{1/2} U_d \quad (2.21)$$

Substituting Equation 2.19, 2.20 and 2.21 into Equation 2.18 yields Equation 2.22.

$$\rho g h S_0 - \frac{1}{8} \rho f U_d^2 \left(1 + \frac{1}{s^2}\right)^{1/2} + \frac{\partial}{\partial y} \left[\rho \lambda h^2 \left(\frac{f}{8}\right)^{1/2} U_d \frac{\partial U_d}{\partial y} \right] = \frac{\partial}{\partial y} [h(\overline{\rho u v})_d] \quad (2.22)$$

Based on experimental data, Shiono and Knight (1991) suggest that the lateral gradient of the depth averaged secondary flow term, $(\overline{\rho u v})_d$, in prismatic channels can be approximated by constant values for a given element of the cross section called as a panel. Using this concept, the lateral gradient of this term per unit length of the channel may then be written as Equation 2.23.

$$\frac{\partial}{\partial y} [h(\overline{\rho u v})_d] = \Gamma \quad (2.23)$$

where Γ is a dimensionless secondary flow parameter. Finally Equation 2.28 can be expressed in a simpler form as Equation 2.24.

$$\rho g h S_0 - \frac{1}{8} \rho f U_d^2 \left(1 + \frac{1}{s^2}\right)^{1/2} + \frac{\partial}{\partial y} \left[\rho \lambda h^2 \left(\frac{f}{8}\right)^{1/2} U_d \frac{\partial U_d}{\partial y} \right] = \Gamma \quad (2.24)$$

Equation 2.24 is a second order linear differential equation that can be solved analytically (Shiono and Knight 1988; 1991) or numerically. In the analytic procedure, which is used in this research, the cross section is divided into sub-areas (panels) with constant depth domains, or sloping side slope domains (Figure 2.5). The analytical solution to Equation 2.24 is expressed for a constant depth, h , domain as Equation 2.25 (Shiono and Knight 1991).

$$U_d = [A_1 e^{\gamma y} + A_2 e^{-\gamma y} + k]^{1/2} \quad (2.25)$$

where

$$k = \frac{8gS_0 h}{f} (1 - \beta) \quad (2.26)$$

$$\gamma = \sqrt{\frac{2}{\lambda}} \left(\frac{f}{8}\right)^{1/4} \frac{1}{h} \quad (2.27)$$

$$\beta = \frac{\Gamma}{\rho g S_0 h} \quad (2.28)$$

and for a linear side slope domain as Equation 2.29.

$$U_d = [A_3 \xi^\alpha + A_4 e \xi^{-\alpha-1} + \omega \xi + \eta]^{1/2} \quad (2.29)$$

where

$$\alpha = -\frac{1}{2} + \frac{1}{2} \sqrt{1 + \frac{s(1+s)^{1/2}}{\lambda} (8f)^{1/2}} \quad (2.30)$$

$$\eta = -\frac{\Gamma}{\frac{(1+s^2)^{1/2}}{s} \rho \left(\frac{f}{8}\right)} \quad (2.31)$$

$$\omega = \frac{gS_0}{\frac{(1+s^2)^{1/2}}{s} \left(\frac{f}{8}\right) - \frac{\lambda}{s^2} \left(\frac{f}{8}\right)^{1/2}} \quad (2.32)$$

$$\xi = h \pm \frac{y-b}{s} \quad (2.33)$$

In above equations, ξ is the depth function on the side-slope domain (Figure 2.6), b is the semi width of main channel bed and A_1 to A_4 are constants which are defined through applying the boundary conditions. To obtain the full solution to Equation 2.25 and 2.29, the friction factor, f , dimensionless eddy viscosity, λ , and secondary flow term, Γ need to be specified.

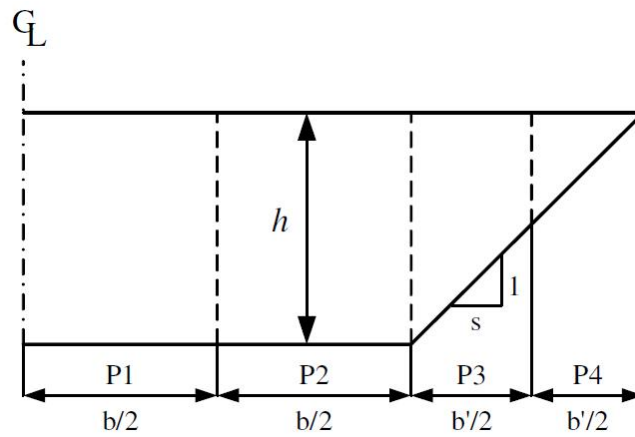


Figure 2.5 Panel structure (Sharifi 2009).

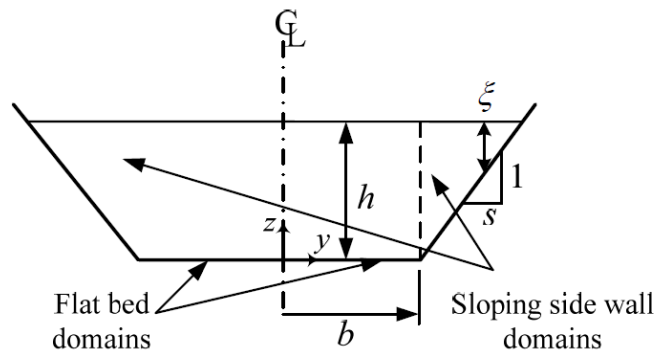


Figure 2.6 Constant and side domains (Sharifi 2009).

Since its introduction by Shiono and Knight (1988), a number of studies have been

carried out to develop the SKM and to show its accuracy in predicting the depth-averaged velocity profile, the boundary shear stress distribution and conveyance in different channels and rivers.

Shiono and Knight (1988; 1990, 1991) and Knight and Shiono (1990) showed the efficiency of this method for compound channels and overbank flow. Knight and Shiono (1996) also compared three different calibration methods for a given dataset. In the first method, all parameters were found through calibration. Then the same data were also calibrated with constant λ ($\lambda=0.13$) and variable Γ . In the final attempt, λ was again held constant at 0.13, but different f were used, with Γ set to zero. It was demonstrated that all three methods result in a reasonable mean velocity distribution but in order to obtain accurate boundary shear stress results, Γ should be taken into account in the model.

Revisiting the boundary conditions, Knight and Abril (1996) and Abril and Knight (2004) calibrated the SKM based on compound channel data and provided the following guidelines for determining the secondary flow term:

$$\Gamma = 0.05h_{fc}\rho g S_0 \quad \text{for inbank flow} \quad (2.34)$$

$$\Gamma = 0.15h_{mc}\rho g S_0 \quad \text{for the main channel during overbank flow} \quad (2.35)$$

$$\Gamma = -0.25h_{fc}\rho g S_0 \quad \text{for the floodplain during overbank flow} \quad (2.36)$$

where subscripts mc and fc denote the main channel and floodplain, respectively. They also found that the model is not sensitive to the value of λ and adopting a constant value of $\lambda=0.13$ for the “whole channel” (i. e. main channel and floodplains) with a uniform roughness distribution gives good results. Although giving satisfactory results for channels with overbank flow, this calibration philosophy cannot be extended to inbank flow. In the original work, the main channel and the floodplains were each considered as one panel and hence no information was derived regarding the lateral variation of

the calibration parameters. Furthermore, knowing that λ is a function of channel geometry and friction (Knight and Abril 1996), assuming a constant value for this parameter for the whole channel is not rational.

Omran (2005) applied the SKM to a number of channels and rivers, with both inbank and overbank flows. In his work, the boundary conditions of the model, particularly for simple trapezoidal channels were re-examined and a two-layer version of the model was developed for modelling flows in compound channels.

Based on the number and position of secondary flow cells in trapezoidal channels, Knight *et al.* (2007) proposed a philosophy for defining the appropriate panel structure. It was demonstrated that by using the methodology, back calculating the friction values from measured data, keeping λ constant as 0.07 and calibrating Γ , the depth-averaged velocity and boundary shear stress could be accurately computed for simple trapezoidal channels.

McGahey (2006) and McGahey *et al.* (2006) developed a semi 2-D model based on the main principles of SKM which they called the Conveyance Estimation System (CES). The CES was thoroughly tested against twenty-four data sets ranging from small scale laboratory experiments to measurements from large natural rivers. The results showed promising improvements when compared to existing one-dimensional hydrodynamic models (McGahey *et al.*, 2008). The sensitivity of the method to its parameters was also investigated in this research. The model was later incorporated in UK's Environment Agency 'Conveyance and Afflux Estimation System' software (www.river-conveyance.net).

Chlebek and Knight (2006) showed that a simple one panel structure for half of a symmetric rectangular channel is sufficient for accurately predicting the percentage of shear force acting on the wall and the total discharge. It was concluded that for the distributions of mean velocity and boundary shear, additional panels should be considered.

Chlebek (2009) illustrated the capability of SKM for modelling simple homogeneous and heterogeneous channels with inbank flows. Simple calibration rules were also derived for selecting the values of f , λ , T . In addition, SKM was used to model the flow in compound channels with skewed floodplains. As a result, expressions for shear force and apparent shear stress acting on certain boundary elements were proposed.

(2) Boundary conditions

To determine the unknown A_i constants different boundary conditions are required at the interface between two adjacent panels. Three different boundary conditions can be considered (Shiono and Knight, 1988).

Continuity of depth-averaged velocity:

$$(U_d)_i = (U_d)_{i+1} \quad (2.37)$$

Continuity of the lateral gradient of the depth-averaged velocity

$$\left(\frac{\partial U_d}{\partial y}\right)_i = \left(\frac{\partial U_d}{\partial y}\right)_{i+1} \quad (2.38)$$

Continuity of the unit force

$$(h\overline{\tau_{yx}})_i = (h\overline{\tau_{yx}})_{i+1} \quad (2.39)$$

Omran (2005) suggested a modification to Eq. (2.74) to get realistic mean velocity distributions by smoothing the spikes caused by the abrupt changes in the local friction and dimensionless eddy viscosity as Equation 2.40.

$$\left(\mu \frac{\partial U_d}{\partial y}\right)_i = \left(\mu \frac{\partial U_d}{\partial y}\right)_{i+1} \quad (2.40)$$

where

$$\mu = \lambda \sqrt{\frac{f}{8}} \quad (2.41)$$

At a rigid side wall, where the no-slip condition holds, the velocity should be equal to zero and hence the boundary condition can be written as Equation 2.42.

$$(U_d)_i = 0 \quad (2.42)$$

Assuming symmetry flow conditions, an additional boundary condition may also be applied at the centreline of a symmetric channel as Equation 2.43.

$$\left(\frac{\partial U_d}{\partial y}\right)_i = 0 \quad (2.43)$$

Once a cross-section is divided into different panels, and the appropriate boundary conditions are applied, a set of linear equations can be obtained in which the A_i coefficients are the unknowns. This set of equations can be solved either by a matrix approach or by a direct approach (Rezaei, 2006), where an elimination procedure is followed to obtain analytical expressions for the A_i coefficients. Once the A_i coefficients are specified, the lateral variation of depth-mean velocity across the channel can be obtained from Equation 2.25 and 2.29. Furthermore it is then possible to calculate the boundary shear stress distribution and the channel conveyance.

(3) Friction factor

The SKM uses the simple Darcy-Weisbach approximation for the boundary shear stress. This assumption is used in both defining the shear velocity and consequently the depth-averaged eddy viscosity and also obtaining the boundary shear stress distribution from the velocity distribution.

As a result, the friction factor, f , is one the important parameters that should be understood and quantified. It is to be stressed that the Darcy-Weisbach friction factor is a resistance coefficient and not a roughness factor. In fact, f is a measure reflecting the dynamic behaviour of the boundary in resisting the fluid flow (Yang and Lim, 1997). This dimensionless coefficient is the representative of surface (skin) friction, drag resistance, wave resistance (from free surface distortion) and resistance associated with local acceleration or flow unsteadiness (Rouse, 1965). Darcy (1857) and Weisbach (1845) developed an equation for calculating the head loss in pipe flow as Equation 2.44.

$$h_f = f \frac{L}{D} \frac{U_m^2}{2g} \quad (2.44)$$

where f is a dimensionless friction factor, L is the pipe length and D is the pipe diameter. As recommended by the Task Force on Friction Factors in Open Channels (TFFF) (1963), this equation can be used for steady, uniform and fully developed open channel flow. Assuming a uniform distribution for the boundary shear stress, D can be substituted by $4R$ (Chow, 1959) and hence f can be calculated by Equation 2.45.

$$f = \frac{8gRS_f}{U_m^2} \quad (2.45)$$

f can be simply related to Chezy's, C , and Manning's, n resistance coefficients as Equation 2.46 and 2.47, respectively.

$$C = \sqrt{\frac{8g}{f}} \quad (2.46)$$

$$n = R^{1/6} \sqrt{\frac{f}{8g}} \quad (2.47)$$

The friction factor, f , in pipes is known to be dependent on the Reynolds number, and a relative roughness factor, i.e. the ratio of a roughness factor that represents the unevenness of the boundary (e.g. the average sediment diameter or Nikuradse's (1933) equivalent sand roughness, k_s) to a shape factor (e.g. pipe diameter, hydraulic radius). Extensive experiments in pipe flow revealed that for smooth surfaces the relative roughness effect vanishes and the friction factor depends only on the Reynolds number (Prandtl 1932). In contrast, for rough surfaces, the Reynolds number is less effective and the friction factor becomes wholly dependent on the relative roughness at high Reynolds numbers (Nikuradse 1933).

Based on the boundary layer theory and the semi-empirical velocity laws, Prandtl (1933) derived an equation for friction factor in smooth pipes by integrating the logarithmic velocity equations over the pipe diameter and assuming no viscous sub-layer for the flow as Equation 2.48.

$$\frac{1}{\sqrt{f}} = C_2 \log(\text{Re} \sqrt{f}) + C_3 \quad (2.48)$$

He also derived a similar Equation for rough pipes as Equation 2.49.

$$\frac{1}{\sqrt{f}} = C_4 \log\left(\frac{2R}{k_s}\right) + C_5 \quad (2.49)$$

where constants are depend on the velocity distribution constants (C_1 and κ in Equation 2.4). Based on experiments on uniform sand grains, Nikuradse (1933) found that values of 2.0, 8.0, 2.0 and 1.74 were appropriate for the constants C_2 , C_3 , C_4 , and C_5 , respectively. These equations do not stand for rough boundaries at relatively low Reynolds numbers, as f varies both with Reynolds number and relative roughness. Conducting similar experiments in pipes with non-uniform roughness, Colebrook and White (1937) proposed an alternative equation in the form of Equation 2.50.

$$\frac{1}{\sqrt{f}} = -C_8 \log \left(\frac{k_s}{C_6 R} + \frac{C_7}{\text{Re} \sqrt{f}} \right) \quad (2.50)$$

where constants are integration constants which depend on the shape of the conduit or channel. Many researchers have tested this Equation on the data of various cross sections with different roughness conditions and have proposed different integration coefficients for it. Incorporating von Karman's universal constant as 0.41 in the velocity distribution, the coefficient C_8 is found to be approximately 2.00 for flows in open channels. A drawback in application of the Colebrook-White equation is that it is implicit in f . To overcome this problem, Moody (1947) developed a diagram by relating the friction factor f , the relative roughness $k_s/4R$ and the Reynolds Number for laminar, transitional and fully turbulent flow through a family of curves. In addition, other researchers have tried to derive alternative explicit equations for the friction factor. One such equation is Barr's (1979) equation (Equation 2.51) for pipe flow, which has been provisionally adapted for wide open channels with $\text{Re} > 30,000$ and $R/k_s R/k_s > 20$, (Yen 1991).

$$f = \frac{1}{4} \left[-\log \left(\frac{k_s}{12R} + \frac{1.95}{\text{Re}^{0.9}} \right) \right]^{-2} \quad (2.51)$$

Henderson (1966) realized that in open channels, in addition to the Reynolds number and the relative roughness, the free surface, secondary currents and the non uniformity of boundary shear stress distribution along the wetted perimeter may also influence the friction factor. Hence he concluded that evaluating the friction factors by substituting the pipe diameter to $4R$ in the pipe equations is not necessarily correct, since the hydraulic radius is an arbitrary linear parameter and an unlimited number of cross sections may be characterized by the same value.

Conducting experiments in smooth rectangular channels, Tracy and Lester (1961) confirmed that the friction factor is a function of the Reynolds number. Myers (1982) also realized that f varies in a complex way with the aspect ratio ($2b/h$). He found that for the same Reynolds number, the friction factor in an open channel is around 8% higher than the equivalent pipe flow. Studying the effect of non uniform distribution of boundary shear stress on resistance, Engelund (1964) suggested replacing the hydraulic radius, R , by another shape factor which he called the resistance hydraulic radius, \bar{R} as Equation 2.52.

$$\bar{R} = R \left(1 + \frac{3}{4} \left(\frac{e}{\bar{h}} - 0.5 \right) \right)^2 \quad (2.52)$$

where \bar{h} is the mean flow depth and e is the distance between the water surface and the centre of area of the cross-section. Using dimensional analysis in conjunction with physical experiments, Kazemipour and Apelt (1980) established a simple correlation between open channel and pipe flow and developed a shape factor for dealing with the shape effect in open channel flow. This method has been found to be appropriate for smooth, rough and transitional turbulent flows in rectangular channels, enabling the calculation of friction factors and mean velocities by the universal resistance formulae for pipe flow.

(4) Dimensionless eddy viscosity

The SKM employs the Boussinesq's hypothesis and the Cunge *et al.* (1980) approximation for the Reynolds stresses. Therefore the value of the dimensionless eddy viscosity (λ) should be known to ensure accurate results.

In many flows, including those in open channels, it is realistic to assume a linear shear stress distribution with a maximum at the bed and zero at the water surface together with a logarithmic velocity law and a parabolic mixing length function as Equation 2.53, 2.54 and 2.55 (also see Figure 2.7).

$$\tau = \tau_b \left(1 - \frac{z}{\delta}\right) \quad (2.53)$$

$$\frac{u}{u_*} = \frac{1}{\kappa} \ln\left(\frac{z}{z_0}\right) \quad (2.54)$$

$$l = \kappa z \sqrt{1 - \frac{z}{\delta}} \quad (2.55)$$

where δ is the boundary layer thickness. In an infinitely wide uniform open channel, δ can be replaced with the flow depth, h , to give Equation 2.56.

$$l = \kappa z \sqrt{1 - \frac{z}{h}} \quad (2.56)$$

Substituting this function in Prandtl mixing length theory, the vertical distribution of the eddy viscosity will be a parabolic function in the form of Equation 2.57.

$$\epsilon_{xz} = \kappa u_* z \left(1 - \frac{z}{h}\right) \quad (2.57)$$

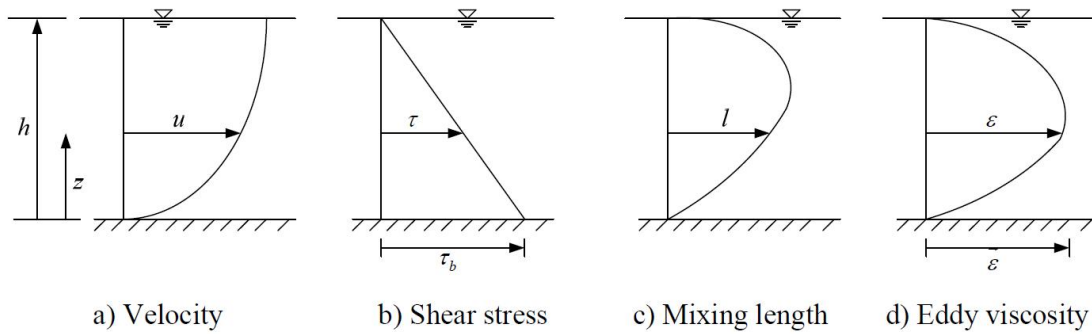


Figure 2.7 Distribution of vertical velocity, shear stress mixing length and eddy viscosity (Sharifi 2009).

This distribution has been proved by many experiments (Figure 2.8).

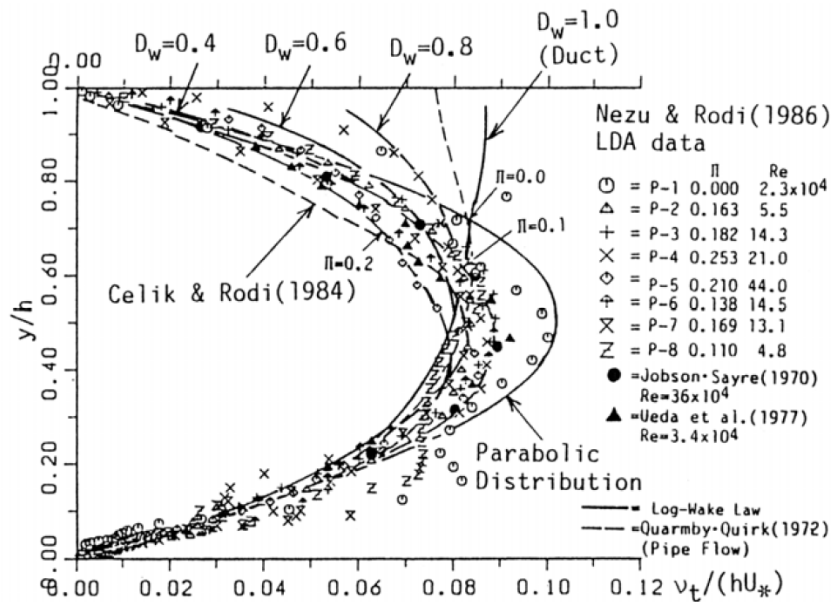


Figure 2.8 Vertical distribution of eddy viscosity ($\nu_t = \epsilon_{xz}$) (Nezu and Nakagawa 1993).

The depth averaged vertical eddy viscosity, $\overline{\epsilon_{xz}}$, can be obtained by integrating Equation 2.57 over the entire depth as Equation 2.58 (Ikeda, 1981).

$$\overline{\epsilon_{xz}} = \frac{1}{h} \int_0^h \epsilon_t dz = \frac{1}{h} \int_0^h \kappa u_* z \left(1 - \frac{z}{h}\right) dz = \frac{\kappa u_* h}{6} \quad (2.58)$$

Based on the strong correlation between the vertical and transverse turbulent velocity fluctuations, Ikeda (1981) have considered the same formulation for the average lateral eddy viscosity. He have suggested a standard value in the order of 0.07 for the dimensionless eddy viscosity, λ . This value is debatable on a number of grounds, most noticeably that relating to the assumed distribution of transverse shear stress. In fact, in the lateral direction, the transverse shear stress cannot be approximated by a simple equation as in the vertical direction (Equation 2.53) and hence no theoretical relation can be derived for $\overline{\epsilon_{xy}}$ and λ (Sharifi 2009). Further works (Elder 1959, Glover 1964, Shiono and Knight 1991) have been conducted to evaluate the dimensionless eddy viscosity. These have led to finding λ in the range of 0.25 to 0.72 for various flow conditions.

A practical method of evaluating the eddy viscosity coefficient is related to the principles of dispersion in flumes and rivers. Elder (1959) used dye in a wide laboratory flume with 10 mm depth of flow and found λ as 0.23. Using polyethylene in a sand bed flume, Sayre and Chamberlain (1964) found $\lambda=0.24$. The same value was found by Fischer and Calif (1967) from their study on a channel approximately 60cm deep and 18.0m wide. Conducting laboratory experiments on rectangular channels, Holley and Abraham (1973) found λ as 0.16. Glover (1964) also reported a value of $\lambda =0.36$ for rectangular channels with bar roughness on the bottom. Rhodes and Knight (1995) measured λ value as 0.13 in rectangular ducts.

Shiono and Knight (1991) have shown theoretically, that λ is influenced by the physical effects of bed generated turbulence, lateral shear and secondary flows. Based on the measurements performed in the Flood Channel Facility (FCF) compound trapezoidal channel, they quantified the influence of both Reynolds stresses and secondary flows on eddy viscosity. It was discovered that the λ value based on turbulence alone is around the standard value of 0.07, but its value based on both secondary flows and turbulence is much higher (e.g. 0.5 for the main channel and 3.0

for the floodplains).

In natural channels, the values of λ are generally larger as the rougher banks and longitudinal irregularities result in more boundary generated turbulence and strong lateral shearing. For example, Yotsukura *et al.* (1970) reported values as high as 0.7 from their experiments on the Missouri River and Glover (1964) measured $\lambda=0.72$ for the Columbia River in Washington.

Assuming that the correlation of transverse eddy viscosity with shear velocity and flow depth is not accurate enough, some researchers (e.g. Lau and Krishnappan 1977, Nokes and Wood 1988, Webel and Schatzmann 1984) investigated the dependence of the transverse eddy viscosity coefficient on other factors like the friction factor and the aspect ratio. Lau and Krishnappan (1977) conducted experiments in rectangular flumes with smooth and rough beds. They analyzed their results together with the results from many previous studies to investigate the dependence of the transverse eddy viscosity coefficient on the friction factor and the aspect ratio. They realized that non-dimensionalizing the values of λ by the channel width gives a better picture on how this parameter changes with the change of friction and aspect ratio.

Furthermore, they concluded that the transverse mixing mechanism in straight open channels is attributable to the secondary flows. Nokes and Wood (1988) showed that λ is constant and that the flow depth is the important length scale rather than the channel width. In their experiments in straight rectangular open channels with both smooth and rough beds, Weble and Schatzmann (1984) found that λ is approximately equal to 0.13 for friction factors greater than 0.09, but below this λ increases to 0.177 for smooth bed flows with friction factors about 0.03.

(5) Depth averaged secondary flow term

The three dimensional fully developed turbulent flow in open channels is characterized by the three fluctuating components of velocity and three dimensional distributions of

Reynolds shear stresses. The streamwise velocity is relatively easy to measure in most cases, while the transverse components are difficult to measure accurately as they are only a few percent of the primary component values (Nezu and Nakagawa, 1993). These transverse velocity components combine together to form secondary (or transverse) currents which are superimposed on the primary flow. Examining the distributions of the primary velocity, Nikuradse (1926) was the first to discover the presence of the secondary flows. However, it was Prandtl (1926) who suggested that turbulent velocity fluctuations cause secondary flow structures (Gessner 1973, Tominaga *et al.* 1989).

Prandtl (1925) distinguished between the secondary flows driven by the centrifugal forces in curved or meandering channels, which he called the first kind, and the secondary flows of the second kind which are caused by the inhomogeneity of anisotropic turbulence. The secondary flows of the first type are driven by the channel geometry, which may affect non-uniform flow in the streamwise direction and hence the generation of streamwise vorticity through vortex stretching. In curved or meandering channels, the centrifugal driving force results in secondary currents in both laminar and turbulent flows with magnitudes typically 20-30% of the mainstream velocity (Nezu and Nakagawa 1993).

Flows of the second type are generally smaller in magnitude and arise in straight channels due to the transverse gradients of the Reynolds stresses, (e.g. \overline{vw} , $\overline{v'^2}$, $\overline{w'^2}$), and anisotropy between the fluctuating velocity components v' and w' (Gessner 1973, Perkins 1970). This anisotropy is caused by the boundary roughness conditions, the free surface and the channel geometry (Nezu and Nakagawa 1993, Tominaga *et al.* 1989). The presence of secondary currents of the second kind influences the spanwise distributions of streamwise velocity and boundary shear stress, resulting in the maximum shear stress and velocity no longer occurring at the channel centre line and free surface respectively (Knight *et al.* 1994). Tominaga *et al.* (1989) and Knight and Demetriou (1983) also stated that boundary shear stress increases where the secondary currents

flow towards the wall and decrease when they flow away from the wall.

The SKM incorporates the average effects of Prandtl's second kind of secondary flows through an advection term Γ . Figure 2.9 shows typical streamwise and transverse velocity profiles, with a secondary flow cell rotating in a counter clockwise direction. Assuming a logarithmic profile for the streamwise velocity, u is always positive, with larger values near the free surface. The lateral velocity, v , is only a small fraction of u and its vertical distribution satisfies three constraints (Wormleaton 1996): i) zero velocity at the bed, ii) zero shear stress at the water surface ($\partial v/\partial z=0$) and iii) continuity for steady flow. Since the lateral velocity at the side edge of the secondary current cell is zero, $(\overline{uv})_d$ would be zero at this position. Thus, it is not unreasonable to assume that $(\overline{uv})_d$ varies from zero at the edge of the secondary cell to a maximum at the centerline of the cell and then back to zero at the other edge of the cell. Based on the assumed coordinates, \bar{v} and consequently $(\overline{uv})_d$ will be positive when the rotation is counter clockwise and negative when the rotation is clockwise.

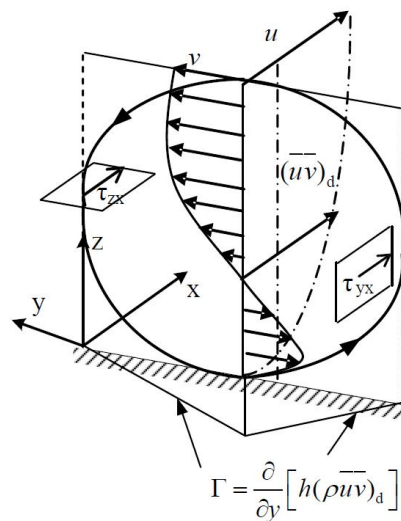


Figure 2.9 Visualization of the averaged secondary flow term (Chlebek and Knight 2006).

The secondary current term, Γ , is equal to the lateral derivative of $h\rho(\overline{uv})_d$, which, based on experimental evidence of Shiono and Knight, (1991) may be regarded as constant in certain regions. Hence, depending on the number, position, and strength of secondary flow cells, Γ can have either negative or positive values throughout the channel. It should be further noted that Γ was initially included in the SKM system of equations as a sink term to count for the planform vorticity in compound channels. Furthermore, it was also concluded that including this term for reflecting the effect of streamwise vorticities in inbank flow, would result in more satisfactory model outcomes. This assumption is debatable since the lateral variation of the apparent shear stress due to the secondary flow term ($\rho(\overline{uv})_d$) seems to be linear only in certain regions (mostly flood plains) of the overbank flow and there is not enough evidence to confidently extend this to inbank flow (Sharifi 2009).

(6) Secondary flow in rectangular channels and trapezoidal channels

The secondary currents in closed rectangular conduits have been measured by Brundrett and Bains (1963), Gessner (1973) and Perkins (1970) using a Hot Wire Anemometer (HWA) and also by Melling and Whitelaw (1965) using a Laser Doppler Anemometer (LDA). They all observed that the two symmetric contra-rotating secondary cells flow along the bisector toward the corner and then from the corner toward the centre of the channel near the bed, finally rising toward the core of channel to complete the cycle.

Using a low power LDA, Muller and Studerus (1979) were the first to measure the secondary currents of the second kind in a rectangular flume. Based on their measurements, Odgaard (1984) observed that the secondary currents in rectangular open channels are similar to those in air conduits, with the difference that in ducts, due to the absence of the free surface, the intensity of the secondary flow is somewhat depressed near the symmetry plane.

The most remarkable secondary flow measurement in rectangular channels has been carried out by Nezu and Rodi (1985). In their work, they accurately measured the streamwise and vertical velocities using a two colour LDA system. They then calculated the transverse velocity from the equation of continuity on the condition of fully developed flow. Plotting the velocity vectors of the secondary currents (Figure 2.10), they observed two main cells of secondary currents separated by the horizontal plane near the sidewalls. Near the surface, a strong vortex called the “free-surface vortex” is generated which transports momentum and energy from the side wall toward the channel centre near the surface. At the channel bed, a smaller “bottom vortex” is formed which rotates in the opposite direction to the upper vortex.

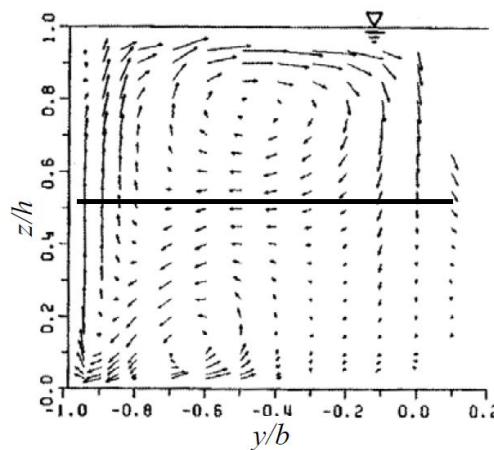


Figure 2.10 Secondary currents in a rectangular channel (Nezu and Rodi 1985).

Nezu and Rodi (1985) also related the cause of the velocity dip at the channel center to the transportation of momentum from the free surface to the mid-depth by the free-surface vortex. Furthermore, they realized that the pattern of the secondary currents depends on the ratio between water depth and channel width ($2b/h$) and hence classified rectangular channels to narrow ($2b/h < 6$) and wide ($2b/h > 6$) channels. In narrow channels, the velocity dip at the channel center is caused by the free surface effect, which dampens the vertical velocity fluctuations. In wide channels, the side-wall

effects are neglected in the channel center, and a series of secondary circulations occurs across the channel width.

Evaluating the boundary shear stress distributions in smooth rectangular open channels and closed rectangular ducts, Knight and Patel (1985) and Knight *et al.* (1983) observed a strong link between the perturbations in the boundary shear stress distribution and the location of secondary cells. They concluded that the number and position of the contra rotating secondary flow cells depends on the channel aspect ratio.

Using a Hot Film Anemometer, Tominaga *et al.* (1989) have studied the effects of geometry and wall roughness on the pattern of secondary currents and compared the results with measurements in closed conduits (Figure 2.11). They found that pattern of vortices in channels are different from closed conduits and the free surface affects the pattern of the secondary currents as it causes the secondary currents to flow toward the side wall along a horizontal plane at around 0.6 of the flow depth. It was also observed that while the spanwise scale of bottom vortex is confined to less than about the flow depth, at larger aspect ratios, the free surface vortex stretches and reaches about two times the depth. They also realized that lateral variation of boundary roughness does not change the basic structure of the secondary currents. However, the scale of the transverse vortex was found to increase as the wall becomes rougher than the bed.

Tominaga *et al.* (1989) also studied the 3D turbulent structure of flow in smooth trapezoidal channels with different side wall inclinations (Figure 2.12). They observed that, the pattern of secondary flow cells in trapezoidal channels is quite different from that of rectangular channel flows as an additional “longitudinal” vortex is generated between the side wall and the “free surface” vortex. It was concluded that as the side slope angle reduces, the free surface vortex gets weaker and the bottom surface expands. It was also realized that maximum value of the secondary current is of the same magnitude as

that in rectangular channels.

Examining the peaks and troughs in the lateral shear stress and mean velocity profiles of several trapezoidal data sets, Knight *et al.* (2007) observed that when the aspect ratio is larger than 2.2, an additional cell appears in the flat bed. They also found that the sign of the secondary current term, Γ , could be determined from the location and rotation of the secondary current cells. Based on the sign of Γ and the number of secondary current cells, they defined a panel structure for modelling the flow with the SKM (Figure 2.13).

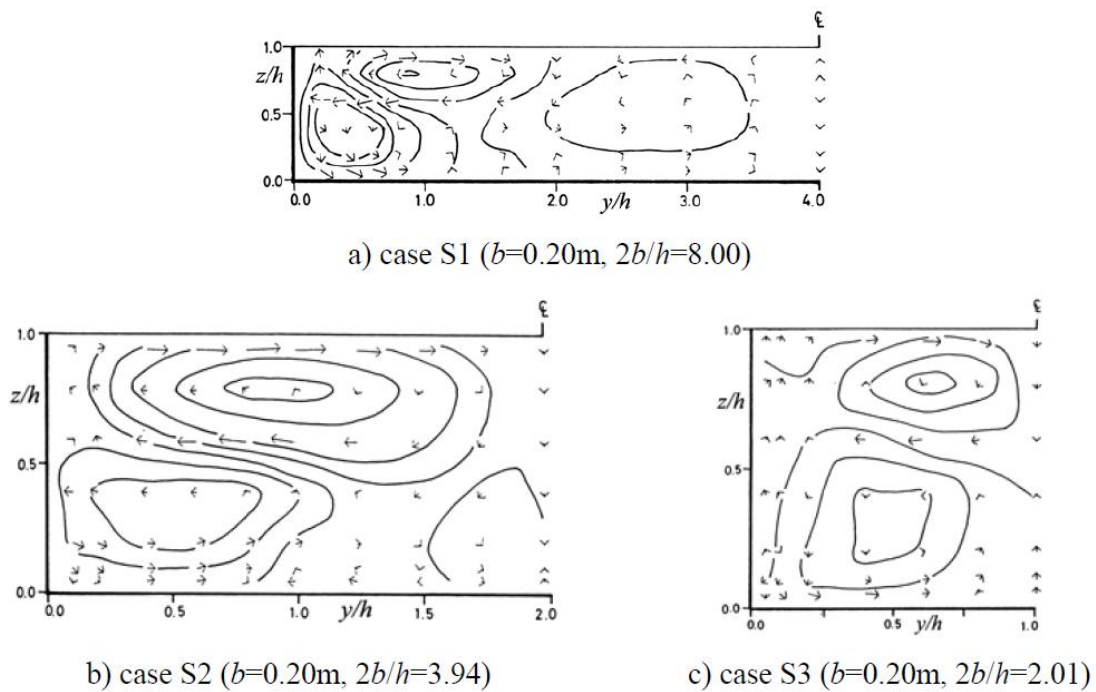


Figure 2.11 Secondary currents in smooth rectangular channels (Tominaga *et al.* 1989).

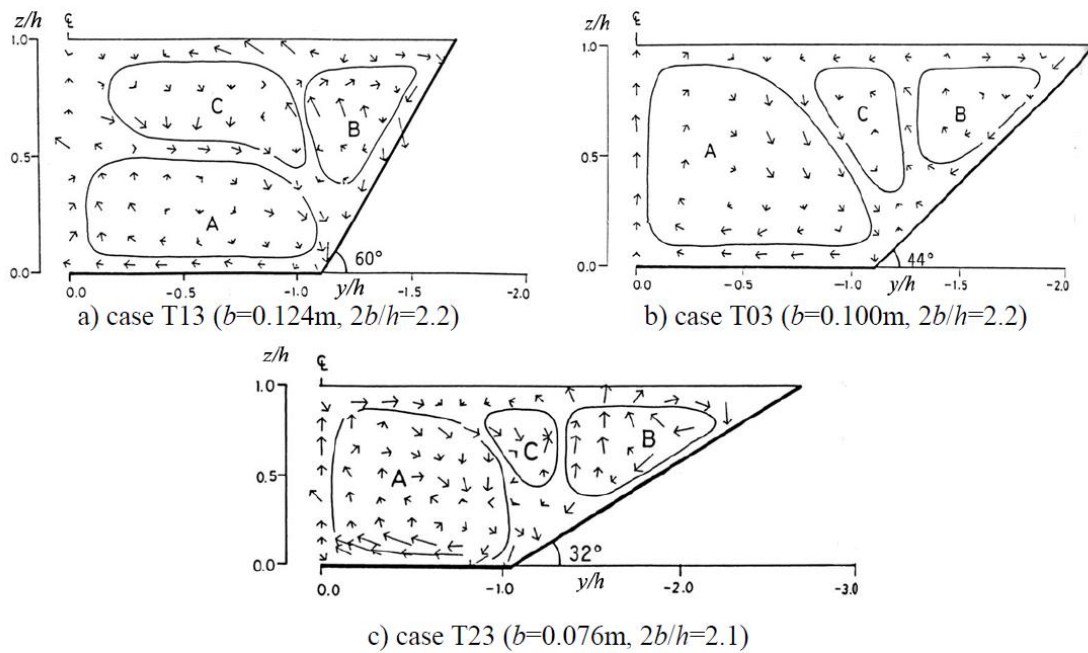


Figure 2.12 Secondary currents in a smooth trapezoidal channels (Tominaga *et al.* 1989).

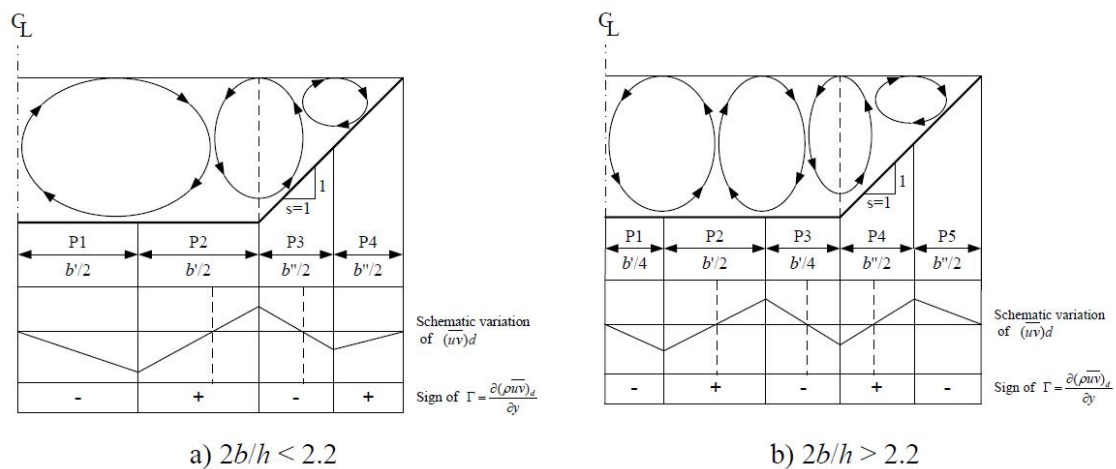


Figure 2.13 Number of panels and sign of secondary current term for simple trapezoidal channels (Kinght *et al.* 2007).

2.2 Experimental Research on Wall Shear Stress

2.2.1 Overview of Techniques of Wall Shear Stress Measurements

Erosion control countermeasures in riverine environments are typically designed to

maintain or stabilize some geometric aspect of the channel cross section. Countermeasures must be able to withstand forces exerted on them by the flow of water during some design event. For a successful design, engineers must have some information regarding the maximum force a specific countermeasure can withstand. Prediction of these forces requires either historical data or information collected from a physical model. Shear stress near the bed acting in the direction of flow is commonly used as a design parameter for selecting and sizing countermeasures.

Several techniques for measuring wall shear stress have been developed and they are used for exploring the boundary layer and wall shear stress. The required spatial and temporal resolutions are specific for each application. For laminar flows, the sensors must be capable to evaluate the time-averaged shear stress, while in turbulent flows, both the mean and its fluctuating components are required.

Haritonidis (1989) classified the techniques for wall shear stress measurements, depending on whether the wall shear stress is measured directly or is evaluated from other measured properties (Table 2.2). The direct methods are floating element method and oil film interferometry and indirect methods are Preston tube, surface fence, wall pulsed wire, hot wire and wall hot-film. The indirect methods need some kinds of calibrations.

Table 2.2 Techniques for wall shear stress measurement.

Group	Techniques
Direct Methods	Floating element balance
	Oil-film interferometry
Indirect Methods	Preston tube
	Surface fence
	Wall pulsed wire
	Hot-wire

A comparison between 4 wall shear-stress measuring techniques, namely wall hot-wire,

wall pulsed-wire, oil-film interferometry and surface fence in turbulent wall-bounded shear flows was presented, see Fernholz *et al.* [1996]. They showed that oil-film interferometry and wall hot-wires may safely be applied in attached boundary layers and wall bounded shear layers with variable pressure gradients, while for wall hot-wires no reversal flow is required. Moreover, in highly accelerated boundary layers the surface-fence can not be used and in flows where direction reverses Preston tubes must not be used. They concluded also that the wall-pulsed wire, the oil-film and the surface-fence techniques may be used in such flows with small deviations occurring for the surface-fence measurements close to separation and re-attachment due to probe small asymmetries.

The direct techniques are based on the mechanical evaluation of the force applied on an element with a floating wall. Meanwhile, the indirect techniques are based on the analogy between the wall shear-stress and other physical parameters.

Direct techniques for the wall shear-stress measurements rely on detection of the total amount of viscous drag experienced by a surface-mounted force balance. The force needed to maintain the floating element in equilibrium is a measure of the wall shear stress. This technology implies a large area and a very sensitive technique to determine small forces. It allows a very accurate measurement of the steady wall shear-stress values, about $\pm 2\%$. The system frequency response is limited by the floating element size.

(1) Floating element balance

The floating element balance, illustrated in Figure 2.14, is one of the old device for wall shear-stress measurements implying a large area. It's a very sensitive technique for small forces determination.

Kempf (1929) used such a floating element balance for subsonic flow and, as the area of the balance could be reduced due to the high wall shear-stress, this technique

could be applied in compressible boundary layers. An detailed survey on the design and applications of these balances was provided by Winter (1977), while a list of test cases in compressible boundary layers is presented by Fernholz and Finley (1977), Fernholz and Finley (1981).

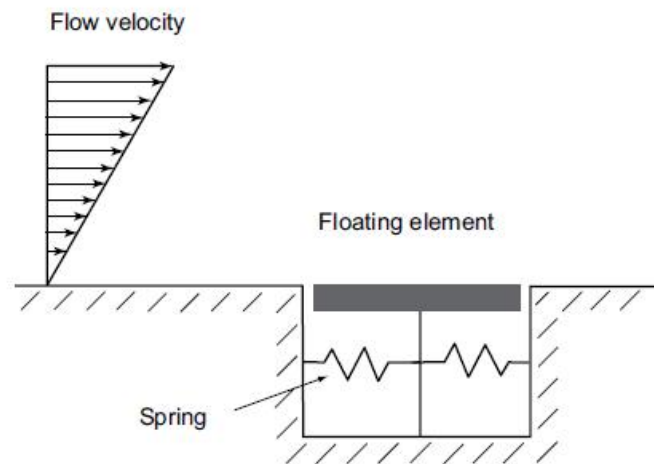


Figure 2.14 Floating element techniques.

The main disadvantage of the floating-element sensors is that they have poor spatial and temporal resolution for low-magnitude shear stress measurement, offers a shear-stress value, integrated over a larger or a smaller area and fails in providing exact pointwise measurements. To obtain a measurable output signal in a low-shear environment, a large sensing element is required, leading to a loss of spatial resolution. Hence it is not possible to simultaneously achieve a high sensitivity and high bandwidth.

(2) Oil-film interferometry

This technique is based on the measurement of a oil drop's deformation, which is deposited on the test facility flow (Figure 2.15). The oil film is developed by drop's spreading due to the shearing. The thinning ratio of the oil film measured by interferometry is determined by interference fringes produced by a monochromatic light source.

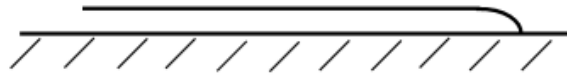


Figure 2.15 Oil-film interferometry technique.

A first attempt of wall shear stress evaluation from the movement of interference fringes of a thin oil film was realized by Tanner and Blows (1986). A complete theory of the application of this technique have been described by Janke (1993). As no calibration and no complex instrumentation for implementing it to the wall are needed - requiring only an optic access to the measurement zone, this technique is attractive. Moreover, it does not require any assumptions concerning the flow field. An accurate measurement of the mean wall shear-stress is acquired using this technique, being capable to measure reverse flow. The accuracy of the oil film method can be better, than within $\pm 4\%$. Meanwhile, it is easy to apply and needs little instrumentation. Thus, a precise knowledge of the oil's viscosity is required.

The main disadvantage of this method is measuring time is relatively high, between 10 minutes and 3 hours are required, depending on the oil viscosity and wall shear-stress magnitude. Another disadvantage are that oil's film speed should not be too high and that a minimum wait time, 1-2 minutes, is necessary to obtain a steady state.

(3) Preston tube

For turbulent boundary layers, one of the most commonly used instrument for wall shear-stress measurements is the Preston tube (Figure 2.16). The validity of this measuring technique depends on the validity of the logarithmic law of the wall.

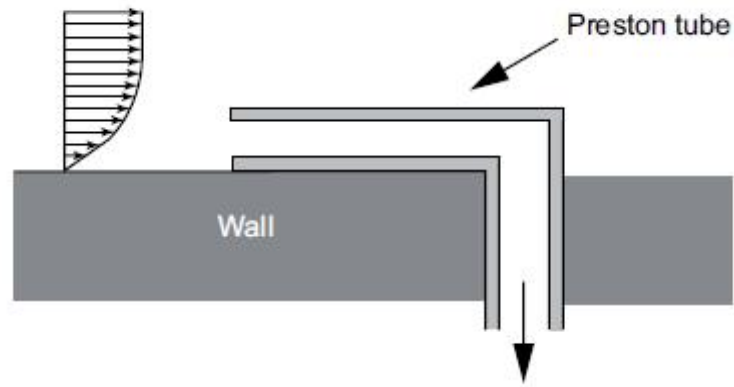


Figure 2.16 Preston tube technique.

The dimensionless diameter must lie in the logarithmic region for calibration curves of Patel (1965), or Head and Vasanta Ram (1971) use, while user-friendly calibration curves were suggested by Bechert (1995) and Zurfluh (1984). The accuracy of the Preston tube method is about $\pm 3\%$ and less for adverse pressure gradients (Patel 1965, Hirt and Thomann 1986). The main disadvantage of this technique is that it allows only the mean wall shear stress value measurement.

(4) Surface fence

Surface fence method has the advantage that it's easy to build and it needs only a precise manometer for pressure difference reading between the upstream and downstream of the fence (Figure 2.17). The surface fence or sublayer fence's first application for measuring the magnitude and direction of the wall shear-stress was carried out by Konstantinov and Dragnysh (1960).

Head and Rechenberg (1962) and Vagt and Fernholz (1973) describe in detail the use of this technique. Some constraints are required for its geometry, its height should not to exceed a value, corresponding to $y^+ = 5$, for measuring within the viscous sublayer and becoming in this way independent of the validity of the logarithmic law of the wall. The accuracy of a surface fence, used together with the Preston tube as a

calibration device, is about $\pm 4\%$ and it may decrease if the turbulence structure of the studied flow differs strongly from the turbulence structure of the calibration flow.

Meanwhile one of its disadvantages is that it can be used only for the Reynolds numbers between 0.25 and 25. In the same time, due to the small size of the fence and the manufacturing tolerances, a calibration is needed for each fence. Moreover, this technique together with the oil interferometry method have poor resolution.

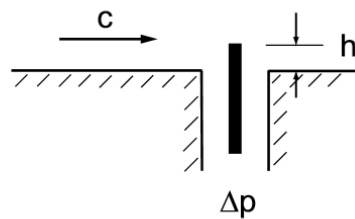


Figure 2.17 Surface fence technique.

(5) Wall pulsed wire

Wall pulsed wire consists in 3 wires parallel mounted in a plane parallel to the wall (Figure 2.18). The central wire is heated by a very short electrical pulse, which generates a heat tracer. The 2 sensors are operated as temperature sensors and note the arrival of the heat tracer. The flight time of the heat tracer is a measure of the instantaneous wall shear-stress value.

The principle of the wall pulsed-wire was described in detail by Bradbury and Castro (1971), while its first application was made by Ginder and Bradbury (1973). This technique is capable of measuring the instantaneous wall shear stress in highly turbulent flows with flow reversal, in the same way as oil-film interferometry or surface fences which, otherwise, have poor temporal resolution. The wall pulsed wire is usually calibrated with a Preston tube. The wall pulsed-wire probe is not well suited to obtain spectra due to its low sampling rate, about 40 Hz. The combined errors of calibration and time of flight measurement, the resolution of the time of flight counter having an

estimated error for high wall shear-stress values, typically 1% can lead to an overall error of about $\pm 4\%$.

Main disadvantage of this technique is that the range of the wall shear stress covered by the probe is limited by requirements that the probe should not extend the viscous sublayer. The range of wall shear stress of such a probe lies within $\pm 2\text{Pa}$. Another disadvantage is that the thick pulsed wire gives a strong signal, producing, in the same time, larger wake.

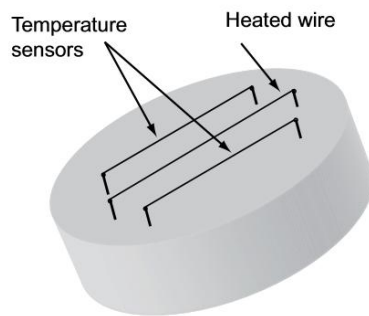


Figure 2.18 Wall pulsed wire technique.

(6) Hot-wire

This indirect technique consists in measuring the velocity gradient in a boundary layer very close to the wall. Shear stress is determined by applying Newton's law which links the flow deformation ratio and the shear stress. Wall shear-stress values obtained are instantaneous local values. For the flow velocity it is used, generally, the hot-wire anemometry (Figure 2.19).

The evaluation of the instantaneous wall shear-stress values by hot-wire measurements of the velocity gradient in the viscous sublayer is strongly affected by the proximity of the wall, while the distortion of the temperature field affects only the sensitivity of the probe, and not its frequency response. For correct results, the velocity measurement must be performed in the viscous sublayer of the boundary layer. Several studies were carried out for investigating the wall distance dependence of hot-wire probes (Janke

1987). It found a single relationship for correcting the mean flow velocity both in laminar and turbulent boundary layers, showing in this way that the mean response of the wall hot-wire probe is independent on the turbulence structure of the flow. Wall hot-wire probes are mainly used for their capacity of retaining their dynamic sensitivity and of their facility of adaptation for heat transfer effects to the wall (Wagner 1991).

Most common materials used for the wire are tungsten, platinum and their alloys. Tungsten wires, the most popular, are characterized by a high temperature coefficient of resistance, but their poor oxidation resistance makes them impossible of use at high temperatures in many gases. Platinum possesses a good temperature coefficient and a good oxidation resistance, but is very weak at high temperatures. The alloys have a good oxidation resistance, and they are more strength than platinum, but with a low temperature coefficient of resistance. Usually, a thin platinum is coated for improving bond with the plated ends and the support needles.

The wall hot wire calibration must be performed in a fixed position, against another instrument measuring the local wall shear-stress. A first approach was carried out by Bradshaw and Gregory (1959), who determined only the mean wall shear-stress value, while Alfredsson *et al.* (1987) used this instrument in a turbulent zero-pressure-gradient boundary layer, evidencing that at high Reynolds numbers, acceptable results both for the mean and for the RMS value of the wall shear stress are obtained. Meanwhile, the wall hot-wire probe sensitivity decreases with the Reynolds numbers decrease, leading to a limited maximum distance from the wall. This technique can be applied only for the cases where the viscous sublayers are thick enough, due to the difficulty of measuring the flow velocity by hot wire to a distance from the wall lower than 0.25 mm. The accuracy of the mean wall shear-stress value measured using this technique is about $\pm 4\%$ for an accuracy of the calibration device of $\pm 3\%$. Its main disadvantage is that it can't be mounted too close to the wall, for maintaining both its sensitivity and linearity.

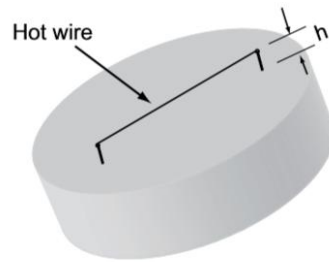


Figure 2.19 Hot wire technique.

2.2.2 Preston tube method

Direct measurement of the bed shear stress is not straightforward and in most cases not practical. The Preston tube method is one of the most commonly used techniques for wall shear stress measurements and relatively simple and convenient method. Most of indirect measurement techniques are also calibrated with the Preston tube method. In the open channel flow Preston tube method have been applied to measure the distributions of the wall shear stress (Thornton *et al.* 2008).

Preston (1954) suggested a linear relationship between the velocity at the boundary and the bed shear stress. Using a pitot-static tube to measure the velocity head near the bed, an indirect procedure was proposed to compute the boundary shear stress. Use of a pitot-static tube, or Preston tube, to measure boundary shear stress requires that a relationship between the boundary shear stress and velocity near the boundary be calibrated under similar conditions.

Calibration of the Preston tube requires collecting velocity data near the bed in a channel with known boundary shear stress. Preston (1954) suggested that once a relationship between shear stress and near boundary velocity under idealized conditions is developed, it can then be applied in a more general sense, to channels of similar characteristics. Fundamental theory for the Preston tube method presented below is summary of Thornton *et al.* (2008).

(1) Backwater Calculation

Computation of the water surface profiles involves finding the change in total head over some distance, dx. Total head consists of velocity head, pressure head, and elevation head as Figure 2.20.

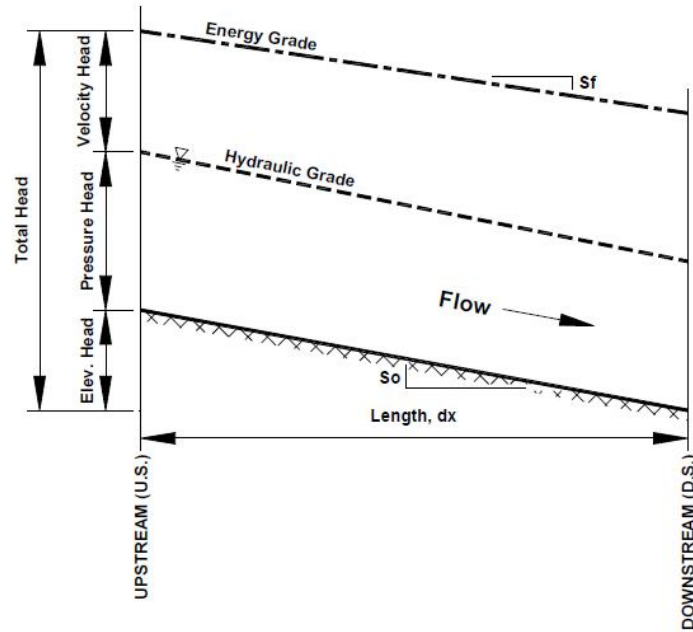


Figure 2.20 Water surface profile.

Total head can be defined as Equation 2.59, where H , P/γ , z , $V^2/2g$, γ , and g represent total head, pressure head, elevation head, velocity head, specific weight of water, and gravitational constant, respectively.

$$H = \frac{P}{\gamma} + z + \frac{V^2}{2g} \quad (2.59)$$

Differentiating Equation 2.59 with respect to x and rearranging, results in Equation 2.60.

$$\frac{\partial}{\partial x} \left(\frac{P}{\gamma} + \frac{V^2}{2g} \right) = \frac{\partial H}{\partial x} - \frac{\partial z}{\partial x} \quad (2.60)$$

Substituting the bed slope, $S_0 = \partial z / \partial x$ and the friction slope, $S_f = \partial H / \partial x$ results in the backwater Equation 2.61, which can be used to compute the change in water surface elevation over some distance.

$$\frac{\partial}{\partial x} \left(\frac{P}{\gamma} + \frac{V^2}{2g} \right) = S_0 - S_f \quad (2.61)$$

Water surface profiles can be computed using the standard step method, where the friction slope is computed by Equation 2.62.

$$S_f = \frac{n^2 V^2}{R^{4/3}} \quad (2.62)$$

where R and V represent hydraulic radius and cross sectional averaged velocity, respectively.

Exact matches between computed water surface profiles and known water surface profiles are not typically expected. For this reason, error associated between the computed profile and the known profile must be computed for each computational interval. One method for establishing the quality of fit is by summing the square differences between computed and known depth at each cross section. Adjustment of the computational model parameters can then be made to optimize the fit. In the case of backwater computations in the laboratory setting, where the discharge and cross sectional areas are well established, Manning's roughness and the starting water surface elevation are the primary parameters that can be adjusted to improve fit. As with any computational model, parameters that are calibrated to match expected results must still maintain a realistic sense of what the parameter is measuring.

(2) Calculation of boundary shear stress in the open channel flow

Boundary shear stress can be computed from a known water surface profile using fundamental principles of momentum conservation. Applying Newton's second law of motion to open channel flow systems, one can state "that the change of momentum per unit time in the body of water in a flowing channel is equal to the resultant of all the external forces that are acting on the body" (Chow 1959).

Practical use Newton's second law involves setting momentum flux through a control volume, as defined by the change in momentum (mass times velocity) per unit time, equal to the sum of the external forces acting upon that control volume. In defining the momentum flux through a typical control volume, it is convenient to assume a constant cross sectional geometry, constant discharge, constant water density, and gradually varied flow depth over the length, L , of the control volume. Equation 2.63 gives an expression of the momentum flux through a typical control volume with a width, b ; depth, y ; and length, L .

$$\dot{M} = \frac{\partial mV}{\partial t} = \Delta(\rho QV) = \rho Q(V_{DS} - V_{US}) = \rho q^2 b \left(\frac{1}{y_{DS}} - \frac{1}{y_{US}} \right) \quad (2.63)$$

where \dot{M} , m , V , V_{US} , V_{DS} , ρ , Q , and q represent momentum flux, mass of water within control volume, cross sectional averaged velocity, cross sectional averaged velocity at the upstream boundary, cross sectional averaged velocity at the downstream boundary, mass density of water, discharge, and discharge per unit width of channel, respectively.

Considering the typical control volume of some length, L , shown in Figure 2.21, four forces can be defined to be acting on the control volume; pressure acting on the upstream and downstream faces, weight of the fluid within the control volume, and the friction force acting opposite the flow direction.

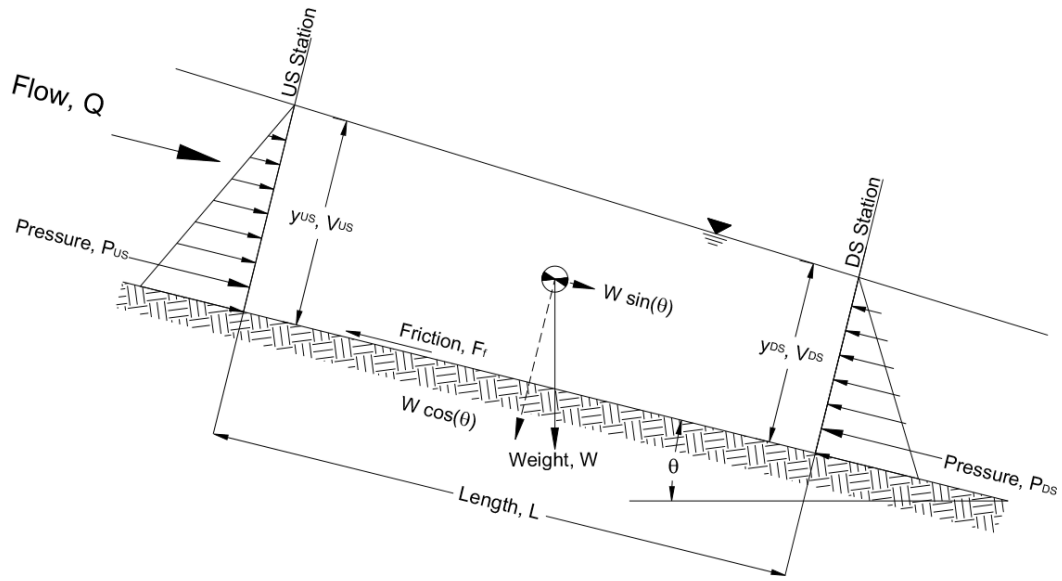


Figure 2.21 Forces acting on a typical open channel flow control volume.

From Figure 2.21 an expression, summing these four forces, can be created as shown in Equation 2.64.

$$\Sigma F_x = P_{US} - P_{DS} + W \sin \theta - F_f \quad (2.64)$$

where ΣF_x , P_{US} , P_{DS} , W , θ , and F_f represent Sum of the forces in the principle (x) direction of flow, pressure exerted on the upstream face of the control volume, pressure exerted on the downstream face of the control volume, weight of the fluid within the control volume, angle of the bed slope, and friction force acting on the bed surface, respectively.

Development of an expression for boundary shear stress in a rectangular channel can proceed by considering each one of the terms listed in Equation 2.64. If the flow depth across the control volume is gradually varied, and hydrostatic conditions persist, then the pressure can be expressed as a function of depth, shown in Equation 2.65.

$$P = \left[\frac{1}{2}(\gamma y) y b \right] \cos \theta \quad (2.65)$$

where P , y , and b represent pressure, flow depth and channel width, respectively.

Applying Equation 2.65 to upstream and downstream faces of the control volume results in Equation 2.66, an expression for the total depth as a function of depth.

$$P_T = P_{US} - P_{DS} = \frac{1}{2} \gamma b (y_{US}^2 - y_{DS}^2) \cos \theta \quad (2.66)$$

Applying Equation 2.66 to upstream and downstream faces of the control volume results in Equation 2.67, an expression for the total depth as a function of depth.

$$W = \gamma V_{ol} = \gamma (b \bar{y} L) = \gamma b L \frac{(y_{US} + y_{DS})}{2} \quad (2.67)$$

Friction force can be computed by the multiplication of the shear stress by the area of the surface that is in contact with the water. For a rectangular flume with plexiglass sides, the frictional force created by the bed is much greater than that created by the sides. Thus, the wetted perimeter for a rectangular plexiglass channel with a rough bed can be assumed to be the channel width. Equation 2.68 shows the equation for friction force within a typical control volume.

$$F_f = \tau_0 A = \tau_0 (P_w L) = \tau_0 (b L) \quad (2.68)$$

Equation 2.69 shows the result of combining Equation 2.66, Equation 2.67, and Equation 2.68.

$$\Sigma F_x = \frac{1}{2}\gamma b(y_{US}^2 - y_{DS}^2)\cos\theta + \gamma bL\frac{(y_{US} + y_{DS})}{2}\sin\theta + \tau_0(bL) \quad (2.69)$$

A final expression for the boundary shear stress can be derived from solving Equation 2.69 for the boundary shear stress and simplifying. This final expression is shown in Equation 2.70.

$$\tau_0 = \frac{1}{2}\gamma(y_{US} + y_{DS})\sin\theta + \frac{1}{L}\left[\frac{1}{2}\gamma(y_{US}^2 - y_{DS}^2)\cos\theta + \rho g^2\left(\frac{1}{y_{DS}} - \frac{1}{y_{US}}\right)\right] \quad (2.70)$$

It can also be shown that the boundary shear stress can be approximated from Equation 2.71. Equation 2.71 and Equation 2.70 differ only by a $\cos\theta$.

$$\tau_0 = \gamma R S_f \quad (2.71)$$

(3) pitot-static tube

Pitot-static tubes are used to measure velocity in a moving stream. Function of the pitot-static tube is based on Bernoulli's principle which states that for an incompressible, inviscid flow along a stream line the sum of the static head, dynamic head, and elevation head remains constant (Munson 1994). Bernoulli's principle can be applied to two points shown Figure 2.22 where point 1 is located within fully developed dimensional flow, undisturbed by the pitot-static tube and point 2 is located at a point very close to the pitot-static tube.

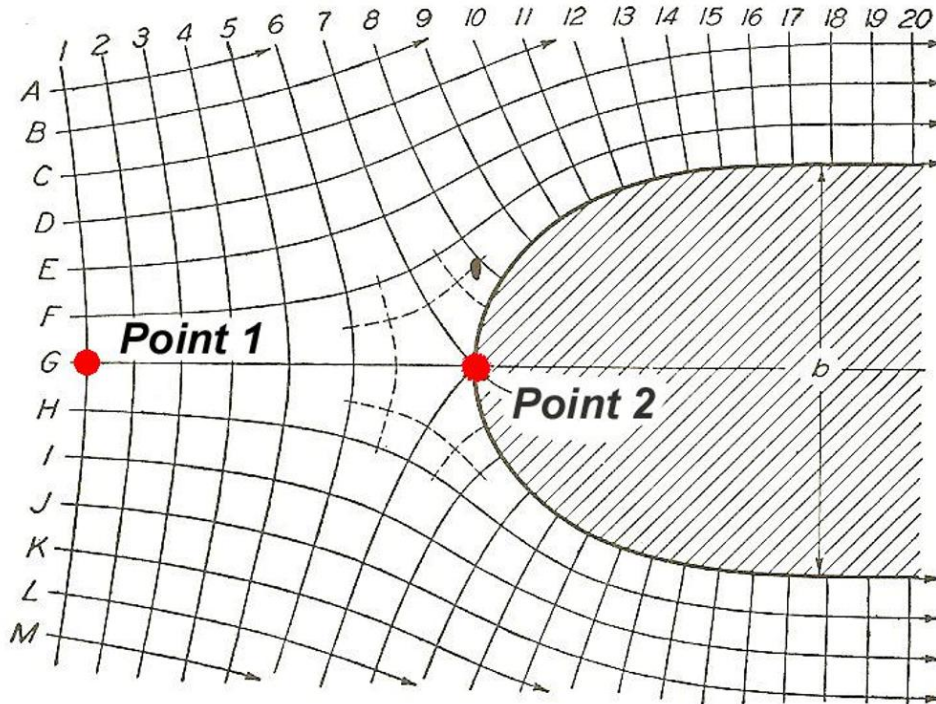


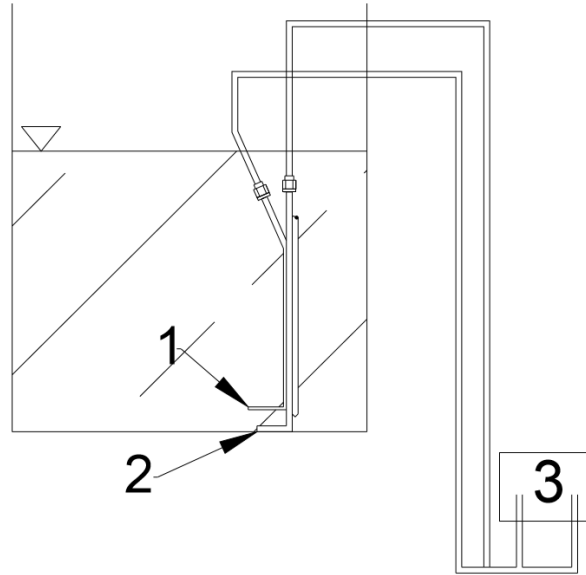
Figure 2.22 Flow approaching the pitot-static tube (Rouse 1978).

As a fluid approaches the opening of the total pressure port of a pitot-static tube, the velocity reduces to zero; this is the point of stagnation. Because the streamlines cannot go through solid objects, they must bend around the opening, causing a point of zero velocity very close to the opening. According to Bernoulli's principle the total head at point 1 must equal the total head at point 2, as expressed in Equation 2.72.

$$\frac{p_1}{\gamma} + \frac{V_1^2}{2g} = \frac{p_2}{\gamma} \quad (2.72)$$

Because the velocity at the pitot-static tube opening is zero, the head measured by the pitot tube is the total head. Figure 2.23 shows the components of a typical pitot-static tube. Point 2 measures the total pressure experienced at the stagnation point. Point 1 measures the static pressure within the normal flow field. Dynamic head can be

computed by subtracting the static head at point 1 from the total head at point 2, similar to Equation 2.72. The pitot-static tube, therefore, can be used to determine the velocity at any point within a uniform flow field.



1. Total pressure port on pitot-static tube.
2. Static pressure port on pitot-static tube.
3. High and low pressure connections on pressure transducer.

Figure 2.23 Schematic of pitot-static tube (Thornton *et al.* 2008)

(4) Literature review of the Preston tube

Ludwig and Tillmann (1950) presented results of research that used a method of determining the shear stress by measuring the amount of heat transfer from small element embedded in the surface of the wall. From boundary layer theory, the velocity profile next to the wall, in the fully turbulent zone, can be expressed as Equation 2.73.

$$\frac{u}{U_*} = a \log \left(\frac{U_* y}{\nu} \right) + b \quad (2.73)$$

where, a and b are both universal constants, and u , U_* , and ν represent velocity at

distance y from the boundary, shear velocity, and kinematic viscosity of water, respectively.

Approximation of the velocity profile can be made using a power law, as presented in Equation 2.16. Results of Ludwig and Tillman (1950) for various flow conditions on a horizontal plate are shown in Figure 2.24 where the solid line represents the universal law. Within the limits of the Ludwig and Tillmann (1950) tests, Figure 2.24 shows reasonable evidence in support of Equation 2.73 and Equation 2.74.

$$\frac{u}{U_*} = C \left(\frac{U_* y}{\nu} \right)^{1/n} \quad (2.74)$$

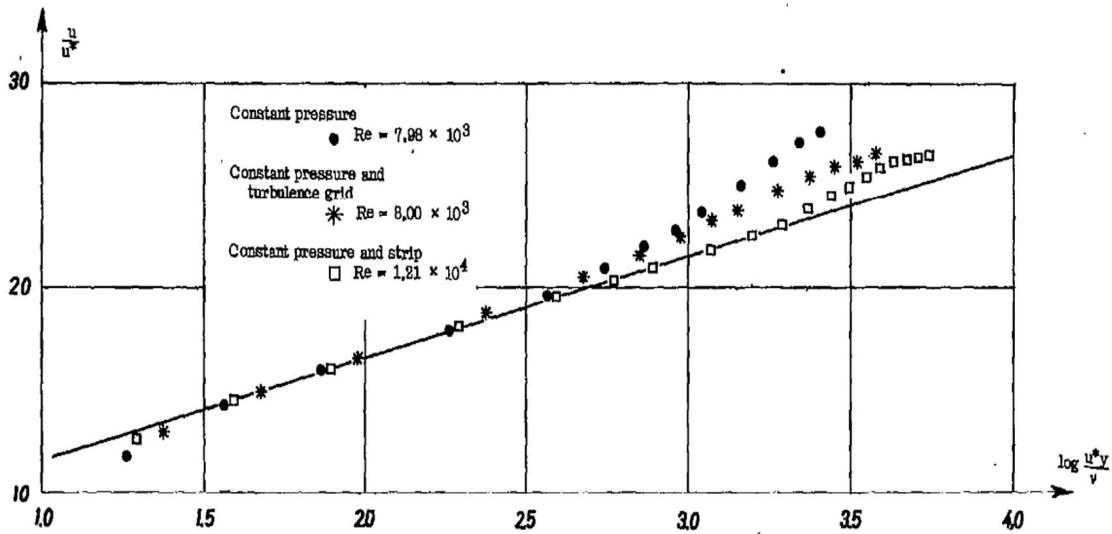


Figure 2.24 Measured velocity profiles (Ludwig and Tillmann 1950).

Preston (1954) intended to develop a simple method to deduce the skin friction that could be applied to surfaces in motion through air and water as well as physical laboratory models. Skin friction is a function of the velocity and the shear stress near the wall as shown in Equation 2.75.

$$c_f = \frac{\tau_0}{\frac{1}{2}\rho u^2} \quad (2.75)$$

where c_f , τ_0 , ρ , and u represent skin friction coefficient, boundary shear stress, density of water, and velocity near boundary, respectively.

Therefore, estimation of the skin friction requires an estimate of both the shear stress and velocity near the boundary. Using a pitot-static tube, the velocity near the bed can be determined by measuring the difference between the static and dynamic pressure. Further, substituting the relationship for shear velocity, presented in Equation 2.76, into Equation 2.74 from Ludwig and Tillman (1950), a modified relationship can be deduced as shown in Equation 2.77.

$$U_*^2 = \frac{\tau_0}{\rho} \quad (2.76)$$

$$\frac{(P-p_0)d^2}{\rho v^2} = F\left(\frac{\tau_0 d^2}{\rho v^2}\right) \quad (2.77)$$

where F , P , p_0 , and d represent representative linear function, dynamic pressure, static pressure, and pitot tube diameter taken as a representative length, respectively.

To determine the function, F , in Equation 2.77, calibration is required in a section of known boundary shear. In a circular pipe the boundary shear can be directly computed using Equation 2.78.

$$\tau_0 = (p_1 - p_2) \frac{D}{4L} \quad (2.78)$$

Four pitot tubes were used in Preston (1954) experimentation, corresponding to four tube diameters shown in Table 2.3.

Table 2.3 Diameters of pitot tubes in Preston (1954) experiment.

Tube Number		1	2	3	4
External diameter	inch	0.029	0.054	0.091	0.121
	mm	0.74041	1.3817	2.304	3.08
Internal diameter	inch	0.018	0.033	0.054	0.073
	mm	0.4	0.8	1.4	1.8
Ratio of internal/external diameter		0.600	0.603	0.599	0.598

Static pressures were measured from 0.02 inch diameter taps located at seven (7) inches, ten (10) inches, and sixteen (16) inches from the down stream end of the test section for p_0 , p_2 , and p_1 , respectively. Tests were performed in a 23-foot section of 2-inch internal diameter brass pipe with a polished smooth inner wall. Approximately 14 feet preceded the test section (89 pipe diameters). A schematic of the testing apparatus is shown in Figure 2.25.

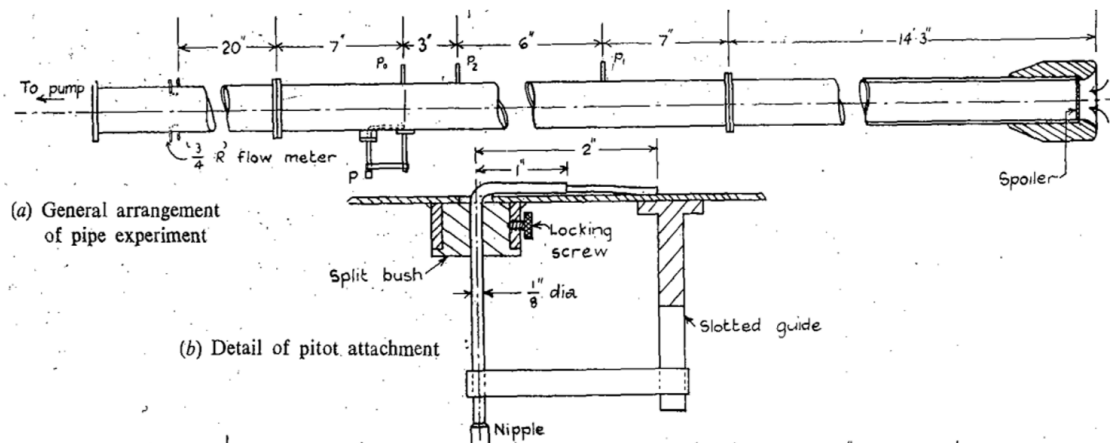


Figure 2.25 Schematic of Preston tube experiment (Preston 1954).

The velocity within the pipe was varied to achieve a range of Reynolds number of 10^4 to 10^5 for all four pitot tubes. The results of these tests are shown in Figure 2.26.

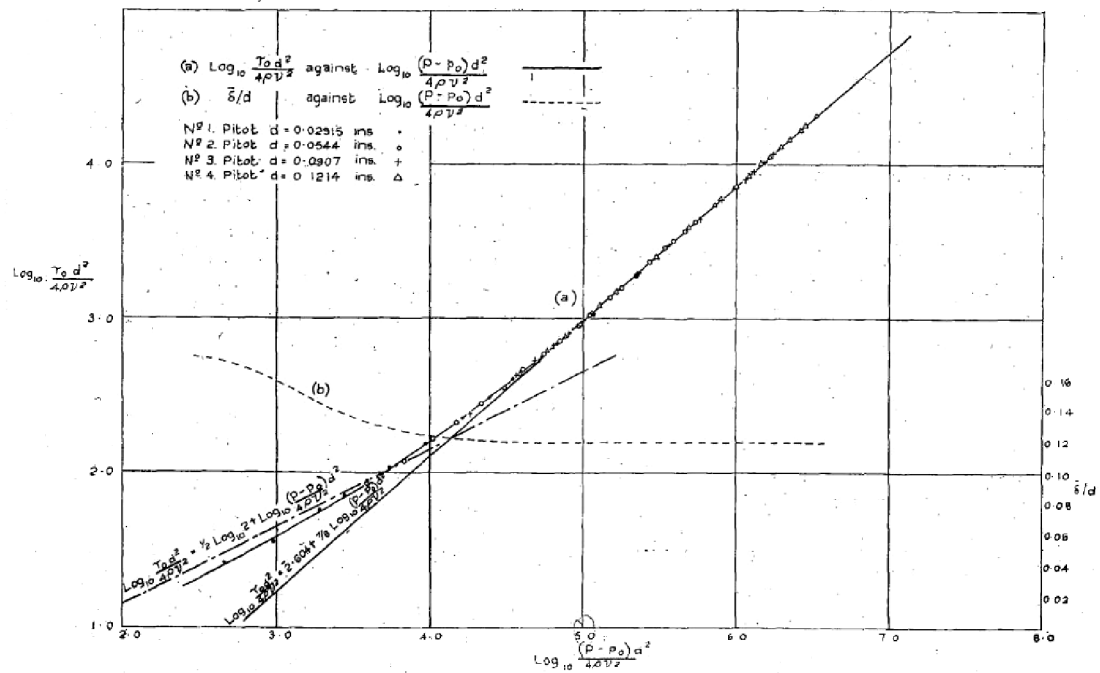


Figure 2.26 Results from Preston (1954).

The regression equation of the measured data shown in Figure 2.26 is presented as Equation 2.79.

$$\log_{10}\left(\frac{\tau_0 d^2}{4\rho\nu^2}\right) = -1.396 + \frac{7}{8} \log_{10}\left[\frac{(P-p_0)d^2}{4\rho\nu^2}\right] \quad (2.79)$$

Using known values for the properties of water and the pitot tube diameters presented in Table 2.3, Equation 2.21 can be reduced to a calibration equation for each size tube as shown in Table 2.4.

Table 2.4 Calibrated equations for tested pitot tubes (Preston 1954).

Pitot Tube Number	Inside Diameter(in)	Calibrated Equation τ_0 [psf], ΔH [in]
1	0.0175	$\tau_0 = 0.0644(\Delta H)^{7/8}$
2	0.0328	$\tau_0 = 0.0551(\Delta H)^{7/8}$
3	0.0543	$\tau_0 = 0.0486(\Delta H)^{7/8}$
4	0.0726	$\tau_0 = 0.0452(\Delta H)^{7/8}$

Additional tests were performed using round pitot tubes in a wind tunnel and a flat pitot tubes in the pipe. Traverses were made in both environments to determine the velocity profiles. Regression through the measured data indicated that the velocity profiles could be sufficiently described by a 1/7 power law when $\log Re_*$ is in the range of approximately 1.5 to 2.75. Equation 2.80 shows the resulting power relationship. The contribution of Preston (1954) was to develop, empirically, an equation to compute shear stress from a pitot-static tube reading.

$$\frac{u}{U_*} = 8.61 \left(\frac{U_* y}{\nu} \right)^{1/7} \quad (2.80)$$

Hsu (1955) develops a theoretical form of Equation 2.79 for smooth boundaries. A theoretical relationship between shear and pressure was developed by computing the total pressure acting on the tube; integrating over the area of tube opening. Equation 2.81 is obtained from performing this integration in the turbulent boundary layer, assuming that the velocity profile may be expressed as a 1/7th Power law (Preston 1954). Experiments run in a wind tunnel with a 1/16-inch pitot tubes demonstrated agreement with Equation 2.81. Data from Hsu (1955) were compared to the Preston (1954) calibration equation; but no new relationship was determined.

$$\log_{10}\left(\frac{\tau_0 d^2}{4\rho\nu^2}\right) = \log k + \frac{7}{8} \log_{10}\left[\frac{(P-p_0)d^2}{4\rho\nu^2}\right] \quad (2.81)$$

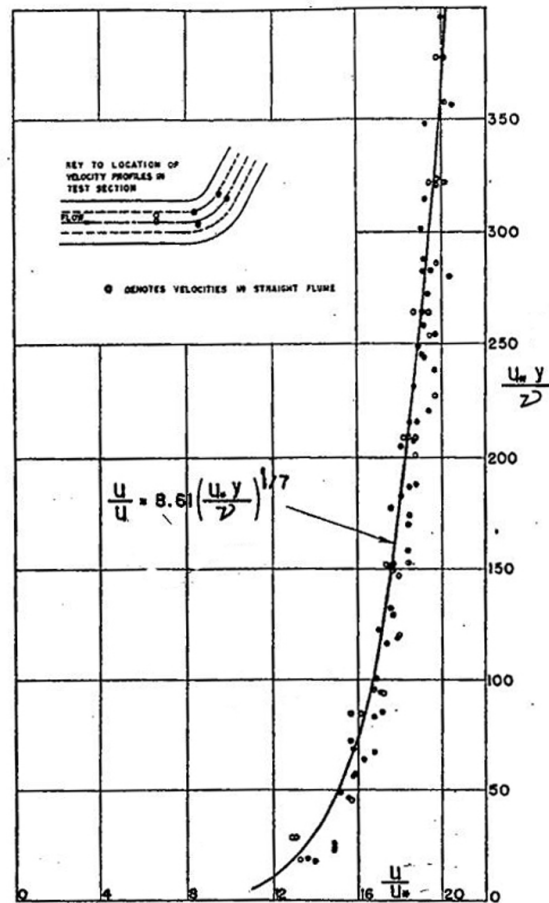


Figure 2.27 Velocity distribution of Ippen and Drinker (1960)

As part of a larger study of shear stress distributions of bends in an open channel, Ippen and Drinker (1960) sought to generally apply the methodology presented by Preston (1954) to both straight and curved free surface flow. To justify use of the pitot static tube (Preston tube) to free surface flow, six velocity profiles near the boundary were recorded using a pitot tube at various locations along the bend and in the straight

channel. From these velocity profiles, the shear velocity was computed from the boundary shear stress. Boundary shear stress was computed by using Preston's 1954 calibration (Equation 2.79). Figure 2.26 shows the collected data plotted with the empirically derived equation of the velocity profile presented in Equation 2.80 (Preston 1954). Agreement, shown in Figure 2.27, between the empirical equations for the velocity profile and the collected data provide supporting evidence to the validity of using Preston's 1954 calibrated equation, Equation 2.79, to compute the shear stress in free surface flow for smooth walled flumes with both straight and curved sections.

A 0.432-inch diameter pitot-static tube was then calibrated to measure boundary shear stress for free surface flow with rough boundaries. Within a straight flume, a 20 foot section of rough surface was installed. A 6-foot section near the downstream end was used for the test reach. Preston tube measurements were taken and plotted against the shear stress, which was computed as shown in Equation 2.82.

$$\tau_0 = \gamma y_0 S_f \quad (2.82)$$

Derivation of the turbulent shear relation for fully rough flow required including the roughness element height in the integration of pressure over the depth of the pitot tube dynamic port. This integration showed that $\tau_0 \propto \Delta p$ rather than $\tau_0 \propto \Delta p^{7/8}$. Regression of the collected data resulted in the relationship shown in Equation 2.83, where ΔH is in ft.

$$\tau_0 = 1.30 \Delta H \quad (2.83)$$

Heinz (2000) calibrated the Preston tube based on the Ippen and Drinker (1960), and which was involving use of the Preston tube on rough boundary. Ippen and Drinker's equation, presented in Equation 2.83 having a coefficient of 1.30, can be expressed in

general as shown in Equation 2.84.

$$\tau_0 = C\Delta H \quad (2.84)$$

A comparison was made between Preston tube measurements taken in the centerline of the constructed channel and shear stress computed as $\gamma y S_f$. Heinz (2002) prepared a computer model, using the Corps of Engineer's HEC-RAS computer software, simulating baseline conditions (with no obstructions in the channel). Within the HEC-RAS model of baseline conditions, the roughness coefficient was adjusted to minimize the sum of the square error between the computed profile and the measured profile collected during testing. Minimizing the error between computed and measured profiles resulted in a Manning's roughness coefficient of 0.017. Plotting the computed shear stress as a function of the Preston tube reading, and fitting a trend line through the data resulted in the calibrated Equation 2.85.

$$\tau_0 = 1.7397\Delta H \quad (2.85)$$

Thornton *et al.* (2008) calibrated the Preston tube in a 60-foot long, 4-foot wide, 2.5-foot tall flume with enough entrance transition, wave suppression, and dissipation to ensure fully developed flow. Calibration of the Preston tube in the 4-foot flume involved two bed materials, a 1/4-inch gravel bed and a brushed concrete cap. Preston tube data was collected over a one minute interval at a rate of 50 Hz and averaged over the minute before being used in calibration. Tests ranged from 2 cfs to 22 cfs with no backwater and from 5 cfs to 15 cfs with the backwater set at normal depth. A normalized profile was computed using standard step backwater procedures using a Manning's roughness that minimized the sum of the square errors between the measured profiles and the computed profile. From the normalized profile, momentum principles

were utilized to determine the shear stress. Computed shear stress values were plotted against the average Preston tube measurements for each surface condition, gravel bed and concrete cap.

Two distinct calibration equations were developed for the Preston tube, one for the gravel bed and one for the concrete cap. Preston tube calibration equations developed from tests in the 4-foot flume for the gravel bed and the concrete cap are presented in Equation 2.86 and Equation 2.87, respectively.

$$\tau_0 = 0.2968 dP \text{ (gravel bed)} \quad (2.86)$$

$$\tau_0 = 0.1644 dP \text{ (concrete cap)} \quad (2.87)$$

where, τ_0 and dP represent boundary shear stress in psf and Preston tube measured pressure difference in inches, respectively.

The Preston tube used for this experiment was made up of two stainless steel pipes; a larger pipe to measure the total pressure and a smaller pipe to measure the static pressure. A stainless steel housing was fabricated to attach the Preston tube to a point gage. Figure 2.28 illustrates the components of the Preston tube configuration. The outer diameter of the dynamic port of the Preston tube is 1/4 inch while the inside diameter of the dynamic port was 11/64 inch, creating an inside to outside diameter ratio of 0.69. Two static ports, each 1/32 inch in diameter, are located either side of a 1/8 inch diameter tube, creating a total of four static ports for the Preston tube. A distance of 13/16 inch separate the static and dynamic ports. Figure 2.29 illustrates the dimensions of the Preston tube static and dynamic ports and Figure 2.30 shows the picture of the Preston tube used in the measurement.

LEGEND

- 1. High Pressure Line
- 2. Low Pressure Line
- 3. Dynamic Port of Preston Tube
- 4. Static Port of Preston Tube
- 5. Preston Tube Housing
- 6. Point Gage

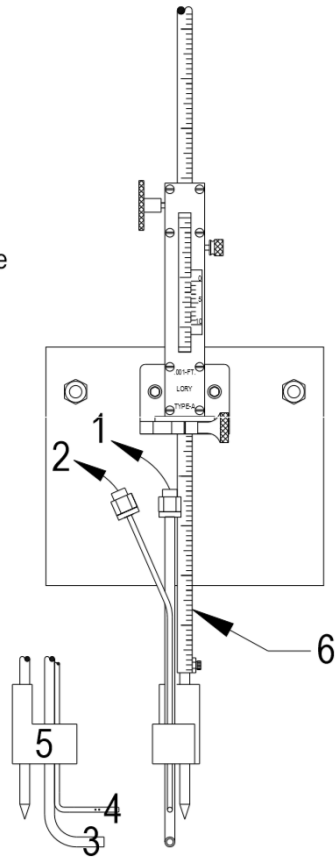


Figure 2.28 Preston tube configuration (Thornton *et al.* 2008).

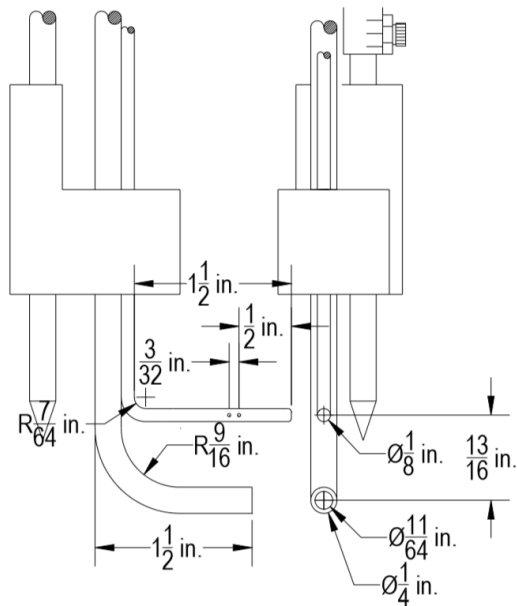


Figure 2.29 Dimension of the Preston tube (Thornton *et al.* 2008).



Figure 2.30 Picture of the Preston tube (Thornton *et al.* 2008).

2.3 Numerical Research

2.3.1 Turbulence Modelling

A brief review of the governing equations valid for constant-property Newtonian fluids under a constant gravitational field are presented in the followings. A detailed review of several turbulence models used to closure the Reynolds Averaged Navier-Stokes (RANS) equations and large eddy simulation (LES) are also presented, focusing on the main assumed hypotheses that can have impact on the numerical results.

Equations in the following subchapters use Cartesian index notation, where $i = 1$ is for x - direction (along the flow) and streamwise velocity component u , $i = 2$ is for y - direction (across the flow) and transversal velocity component v , and $i = 3$ is for z (orthogonal to the fluid bed) and vertical velocity component w .

(1) Governing Equations and Reynolds Averaging

The basic system of governing equations for incompressible fluid flows is based on the conservation laws of physics such as conservation of mass (i.e. continuity equation), and conservation of momentum (Newton's second law). The mass-conservation or continuity equation for an incompressible fluid can be expressed as Equation 2.88 (e.g. Pope 2000).

$$\nabla \cdot \mathbf{u} = \frac{\partial u}{\partial x} + \frac{\partial v}{\partial y} + \frac{\partial w}{\partial z} = 0 \quad \Leftrightarrow \quad \frac{\partial u_i}{\partial x_i} = 0 \quad (2.88)$$

The second equation, conservation of momentum, states that the rate of change of momentum equals the sum of the forces on a fluid element. For a constant-property (e.g. density and viscosity) Newtonian fluid and isothermal flow under a constant gravitational field can be written as Equation 2.89 (e.g. Pope 2000).

$$\frac{\partial u_i}{\partial t} + u_j \frac{\partial u_i}{\partial x_j} = -\frac{1}{\rho} \frac{\partial p}{\partial x_i} + \frac{\partial}{\partial x_j} \left(\nu \frac{\partial u_i}{\partial x_j} \right) + f_i \quad (2.89)$$

where p is instantaneous pressure field, ρ is the fluid density, ν is the fluid kinematic viscosity and f_i are body forces. Equations 2.89 are known as Navier-Stokes equations for constant property Newtonian fluids.

Equations 2.89 completely describe the laminar-turbulent field and may, in principle, be solved directly in so called direct numerical simulation (DNS). However, the numerical solution is extremely difficult, since the significantly different length and time scales in a turbulent field need to be resolved, and thus the stable solution requires such a fine mesh resolution that the computational effort grows rapidly with increasing Reynolds number. Thus, practically in most turbulent flows the flow-field variables are decomposed into the mean and fluctuating parts. This process is known as the Reynolds decomposition and can be expressed as Equation 2.90.

$$u_i = \overline{U}_i + u_i' \quad (2.90)$$

where u_i is the instantaneous velocity component, u_i' is the fluctuating part for which $\overline{u_i'} = 0$ and \overline{U}_i is the mean velocity. This mean value should be obtained from classic statistics knowing the probability density function of the random variable (velocity field). However, a very common approach, also adopted here, is to consider that the flow is statistically stationary that all statistics are invariant under a shift in time. This allows estimating the statistical mean by performing a time-average over a time interval. For statistically stationary flows, the time averaged value tends to the statistical mean value as the used time interval tends to infinity (Pope 2000). Substituting the decomposition Equation 2.90 for velocity and pressure into the continuity and momentum equations (Equation 2.88 and 2.89), and then by averaging all the terms in the equations the

Reynolds averaged Navier-Stokes equations (RANS) for constant-property Newtonian fluids are obtained (Pope 2000) as Equation 2.91 and Equation 2.92.

$$\frac{\partial U_i}{\partial x_i} = 0 \quad (2.91)$$

$$\frac{\partial U_i}{\partial t} + U_j \frac{\partial U_i}{\partial x_j} = -\frac{1}{\rho} \frac{\partial P}{\partial x_i} + \frac{\partial}{\partial x_j} \left(\nu \frac{\partial U_i}{\partial x_j} \right) - \frac{\overline{u_i' u_j'}}{\partial x_j} \quad (2.92)$$

For brevity, the over bars indicating the averaged values are dropped from U_i and P . The last term in Equation 2.92 is new compared to Equation 2.89. An extra term in Equation 2.92, $-\overline{u_i' u_j'}$ is the fluctuating contribution to the nonlinear convective acceleration term in the momentum Equation 2.89, also called the apparent stress arising from the fluctuating velocity field (Pope 2000). This apparent stress tensor is $-\overline{u_i' u_j'}$ which statistically represents the correlation matrix between fluctuating components of the velocity field, is also denominated the Reynolds stress tensor.

(2) Turbulence Modelling Method

Turbulence can either be resolved or modelled. Resolving implies proper solution of the governing equations at all length and time scales with no modelling or empirical assumptions. Modelling implies a solution that uses some degree of approximation and empiricism.

There are three levels of resolving turbulence: fully resolved, partially resolved, and unresolved. Direct Numerical Simulation (DNS) is one technique that attempts to fully resolve turbulent flow by solving the Navier-Stokes equations at all length and time scales. In DNS turbulence or empirical models are not required.

The ample variation in length and time scales is an important characteristic of

turbulent flows which is in part responsible for the difficulty encountered in the numerical and theoretical analysis of turbulent flows. The largest length scales (eddy sizes), given by L , in the flow account for most of the transport of momentum and energy. The size of these eddies is constrained by the physical boundaries of the flow. Thus, for compound channel flow the largest eddies can have the size of the channel width.

Kinetic energy from large eddies is transferred to the smaller eddies during the cascading process until it is dissipated into heat (Pope 2000). As we approach smaller and smaller length scales, the viscous effects become more important. Thus, the size of the smallest eddies, η , at which this energy is dissipated depends on the dissipation rate, ϵ , and viscosity, ν , and is defined as Equation 2.93.

$$\eta = \left(\frac{\nu^3}{\epsilon} \right)^{1/4} \quad (2.93)$$

This length scale is called the Kolmogorov length scale and it characterizes the smallest dissipative eddies. Therefore, it corresponds to the smallest length scale needed to properly resolve turbulent flow. The time scale, τ , of the smallest eddies is written as Equation 2.94.

$$\tau = \left(\frac{\nu}{\epsilon} \right)^{1/2} \quad (2.94)$$

The ratio of largest to smallest length scales and time scales in the flow is proportional to the Reynolds number raised to the 3/4 and 1/2 power, respectively. For example, in a flow with a Reynolds number of 10^5 , the ratio L/η is proportional to $10^{15/4}$. Thus, to resolve the entire range of length scales in 3D turbulent flow, we would need a computational domain that consists of at least 10^{10} grid points. The amount of

information resulting from such simulation would exceed the capacity of any existing computer. This becomes even clearer when the unsteady, transient nature of turbulence is considered. Thus, the problem with DNS is that it consumes enormous computational resources since the grid resolution must be on the order of the Kolmogorov scales.

Large Eddy Simulation (LES) attempts to partially resolve turbulence. The fundamental idea is that the small scales of turbulence (close to the Kolmogorov scales) can be modelled by a subgrid model, while the larger scales are resolved by the governing equations. Grid resolution is on the order of the turbulent scale that wants to be solved, in LES the computational demands are considerably smaller than in DNS. The LES has become more and more popular and shows good results when compared to experimental data (Thomas and Williams 1995, Cater and Williams 2008, Stoesser 2010, Kara *et al.* 2012). Nevertheless, its application to real problem is still impractical, due to the exceptionally high computational effort required compared with RANS.

The most practical and still the most popular method of dealing with turbulence is that based on RANS equations that only mean flow quantities are resolved. In the RANS method, all scales of turbulence are modelled and grid resolution is in the order of the mean flow scale, not a turbulent scale. This offers huge computational savings when compared to both DNS and LES. The complexity of RANS models ranges from purely algebraic or zero-equation models to a more complex Reynolds stress models.

Reynolds stresses appearing in RANS have to be related to the mean motion itself before the equations can be solved, since the number of unknowns and number of equations must be equal. From Equation 2.91 and 2.92 we have 10 unknowns (P , U_1 , U_2 , U_3 and six Reynolds stresses $-\overline{u_i' u_j'}$) and only 4 equations, which configures an unclosed mathematical problem. The absence of these additional equations is referred to the turbulence closure problem. To close these equations extra equations are introduced through the different turbulence models.

(3) Eddy Viscosity Models

In this part the eddy viscosity turbulence models are briefly discussed. The models can be divided in three categories; zero, one and two-equation models. These models use the Boussinesq eddy viscosity concept (Boussinesq 1877). In analogy to viscous stresses in laminar flow, the turbulent stresses are assumed to be proportional to the mean velocity gradients. The Reynolds stress tensor is then related to the mean flow field through Equation 2.95.

$$-\overline{u'_i u'_j} = \nu_t \left(\frac{\partial U_i}{\partial x_j} + \frac{\partial U_j}{\partial x_i} \right) - \frac{2}{3} k \delta_{ij} \quad (2.95)$$

where ν_t , δ_{ij} , and k are the eddy viscosity, the Kronecker delta, the turbulence kinetic energy defined as $k = \overline{u'_i u'_i} / 2$, respectively.

The primary object of many turbulence models is to find some estimation for the eddy viscosity to model the Reynolds stresses. These range from the relatively simple algebraic models to the more complex models such as the $k-\epsilon$ model, where two additional transport equations are solved in addition to the mean flow equations. Here only two-equation models are presented.

The two-equation models are the simplest complete models, since these models provide independent transport equations for both variables, the turbulence kinetic energy and the turbulence length scale, or some equivalent parameter. Kolmogorov (1942) and Prandtl (1945) suggested determining the distribution of k by solving a transport equation for this quantity, which can be obtained by introducing the Reynolds decomposition in the Navier-Stokes equations, multiplying by the velocity and taking time-average of the resulting equation (Pope 2000). The resulting transport equation for k can be written as Equation 2.96.

$$\frac{\partial k}{\partial t} + U_i \frac{\partial k}{\partial x_i} = - \frac{\partial}{\partial x_i} \left[\overline{u'_i \left(\frac{u'_j u'_j}{2} + \frac{p'}{\rho} \right)} \right] - \overline{u'_i u'_j} \frac{\partial U_i}{\partial x_j} - \nu \overline{\frac{\partial u'_i}{\partial x_j} \frac{\partial u'_i}{\partial x_j}} \quad (2.96)$$

Equation 2.96 is the exact k -equation and is of no use in the turbulence model since new unknown correlations appear in the turbulent transport and dissipation terms. To obtain a closed set of equations, model assumptions must be introduced for these terms. Thus, turbulent transport term is often modelled with a gradient-diffusion concept. Gradient-diffusion hypothesis is applicable to high Reynolds number flows and is not valid in certain flow regions, such as the viscous sublayer near walls. Assuming that the turbulent transport of k is proportional to the gradient of k (Rodi 1993), Equation 2.97 is introduced.

$$- \overline{u'_i \left(\frac{u'_j u'_j}{2} + \frac{p'}{\rho} \right)} = \frac{\nu_t}{\sigma_k} \frac{\partial k}{\partial x_i} \quad (2.97)$$

where σ_k is the turbulent Schmidt number that does not have a universal value and empirical values have been used in different studies in the range of 0.2 - 1.3 (Tominaga and Stathopoulos 2007). The selected value of σ_k has a significant effect on the prediction of the results. Thus, Tominaga and Stathopoulos (2007) recommended that σ_k should be determined by considering the dominant flow structures for each case. However, σ_k generally takes value around 1.0 (Nezu and Nakagawa 1993, Pope 2000, Rodi 1993). Taking into account the above assumptions in Equation 2.95 and 2.97, Equation (2.96) can be written as Equation 2.98.

$$\frac{\partial k}{\partial t} + U_i \frac{\partial k}{\partial x_i} = \frac{\partial}{\partial x_i} \left(\frac{\nu_t}{\sigma_k} \frac{\partial k}{\partial x_i} \right) + \nu_t \left(\frac{\partial U_i}{\partial x_j} + \frac{\partial U_j}{\partial x_i} \right) \frac{\partial U_i}{\partial x_j} - \epsilon \quad (2.98)$$

The choice of the second variable in two-equation models is arbitrary and many proposals have been presented. Davidov (1961), Harlow and Nakayama (1968) and Jones and Launder (1972) suggested an equation for the dissipation rate $\epsilon = k^{3/2}/l$, where l is a turbulence length-scale. Rotta (1951) proposed an equation for kl and Kolmogorov (1942) proposed an equation for the turbulence frequency $\omega = k^{1/2}/l$. Saffman (1970) proposed an equation for turbulence vorticity $\omega^2 = k/l^2$ and Speziale *et al.* (1992) proposed an equation for the turbulent time-scale $\tau = l/k^{1/2}$. Among these proposed variables, popular dependent variables for the second variable have been the dissipation rate ϵ and the specific dissipation rate ω .

The $k-\epsilon$ model is the best-known two-equation turbulence model and is incorporated in most commercial CFD codes. The most used formulation of the $k-\epsilon$ model, referred as the standard $k-\epsilon$ model, is the model of Jones and Launder (1972). The authors proposed the following transport equation for the dissipation rate.

$$\frac{\partial \epsilon}{\partial t} + U_i \frac{\partial \epsilon}{\partial x_i} = \frac{\epsilon}{k} (C_{\epsilon 1} P - C_{\epsilon 2} \epsilon) + \frac{\partial}{\partial x_i} \left(\frac{\nu_t}{\sigma_\epsilon} \frac{\partial \epsilon}{\partial x_i} \right) \quad (2.99)$$

where the eddy viscosity used in the model is defined as Equation 2.100.

$$\nu_t = C_\mu k^2 / \epsilon \quad (2.100)$$

Actually Equation 2.99 is not the exact transport equation for ϵ , but rather an entirely empirical equation that can account better for the fact that ϵ is determined by the large-scale motions (energy cascade) instead of motions in the dissipative range (Pope 2000). The $k-\epsilon$ model involves the five empirical constants C_μ , $C_{\epsilon 1}$, $C_{\epsilon 2}$, σ_k , and σ_ϵ . Their standard values for open-channel flows are presented in the Table 2.5. The choice

of these constants is based on the compatibility of the model to the logarithmic velocity distribution near the wall in channel flows with Von Kármán constant $\kappa = 0.41$ (Nezu and Nakagawa 1993).

In open-channel flows, vertical fluctuations, w' , are damped by the free-surface, which results in ν_t approaching to zero near the free-surface (Nezu and Nakagawa 1993). This damping phenomenon can be resolved in RANS where only mean properties of flow are accounted. This surface damping can be accounted for in the $k-\epsilon$ model by decreasing C_μ near the free-surface by means of damping functions, or surface-proximity function (Celik and Rodi 1984).

Table 2.5 Values of the constants in the $k-\epsilon$ model for open-channel flows (Nezu and Nakagawa 1993).

C_μ	$C_{\epsilon 1}$	$C_{\epsilon 2}$	σ_k	σ_ϵ
0.09	1.44	1.92	1.2	1.2

Another popular two-equation model is the $k-\omega$ model (being the turbulence frequency $\omega = \epsilon/k$), which is presented here in the form given by Wilcox (1988). The $k-\omega$ model solves the k -transport equation and a transport equation for ω , instead of the ϵ -equation. The k -transport equation, re-written replacing $\epsilon = k\omega$, and the transport equation for ω can be written as Equation 2.101 and Equation 2.102 (Wilcox 1988). The $k-\omega$ model involves five empirical constants and their standard values are presented in Table 2.6.

$$\frac{\partial k}{\partial t} + U_i \frac{\partial k}{\partial x_i} = \frac{\partial}{\partial x_i} \left(\frac{\nu_t}{\sigma_k} \frac{\partial k}{\partial x_i} \right) + P - \beta k \omega \quad (2.101)$$

$$\frac{\partial \omega}{\partial t} + U_i \frac{\partial k}{\partial x_i} = \frac{\partial}{\partial x_i} \left(\frac{\nu_t}{\sigma_\omega} \frac{\partial k}{\partial x_i} \right) + \alpha \frac{\omega}{k} P - \beta \omega \quad (2.102)$$

where eddy viscosity is given as Equation 2.103.

$$\nu_t = \frac{k}{\omega} \quad (2.103)$$

Table 2.6 Values of the constants in the $k-\omega$ model (Wilcox 1988).

β'	β	α	σ_k	σ_ω
0.09	1.44	1.92	1.2	1.2

Generally $k-\omega$ performs better near the wall region and $k-\epsilon$ performs better in the fully turbulent region. Menter (1994) proposed the Baseline (BSL) which combines the best behaviour of the $k-\epsilon$ and $k-\omega$ models. The BSL model proposed by Menter (1994) suggested a hybrid model using a transformation of the $k-\epsilon$ model into $k-\omega$ model in the near-wall region and the standard $k-\epsilon$ model in the fully turbulent region far from the wall. Thus, Wilcox model (Equation 2.101) is multiplied by a so called “blending function” F_1 and the transformed $k-\epsilon$ model by a function $(1-F_1)$. Close to the walls the blending function F_1 is equal to one (leading to a standard ω -equation) and decreases to a value of zero outside the boundary layer (corresponding to the standard ϵ - equation). The blending functions are used to achieve a smooth transition between the two models. The BSL model is written as Equation 2.104.

$$\frac{\partial \omega}{\partial t} + U_i \frac{\partial k}{\partial x_i} = \frac{\partial}{\partial x_i} \left(\frac{\nu_t}{\sigma_{\omega 3}} \frac{\partial k}{\partial x_i} \right) + \alpha_3 \frac{\omega}{k} P - \beta_3 \omega^2 + (1-F_1) \frac{2}{\sigma_{\omega 2} \omega} \frac{\partial k}{\partial x_i} \frac{\partial \omega}{\partial x_i} \quad (2.104)$$

An extra source term, called cross-diffusion term, appears on the right hand side (RHS), which arises during the transformation. The model constants, Φ_3 are related through a linear combination of a set of constants Φ_1 and Φ_2 where subscripts 1 and 2 correspond to constants of $k-\omega$ and of $k-\epsilon$ models presented in Table 2.6 and Table 2.5, respectively.

$$\Phi_3 = F_1 \Phi_1 + (1 - F_1) \Phi_2 \quad (2.105)$$

Blending function F_1 is defined as Equation 2.106.

$$F_1 = \tanh(\arg_1^4) \quad (2.106)$$

where \arg_1 is described as Equation 2.107.

$$\arg_1 = \min\left(\max\left(\frac{\sqrt{k}}{\beta' \omega z}, \frac{500\nu}{z^2 \omega}\right), \frac{4k}{CD_{k\omega} \sigma_{\omega 2} z^2}\right) \quad (2.107)$$

where z is the distance to the nearest wall and $CD_{k\omega}$ is defined as Equation 2.108.

$$CD_{k\omega} = \max\left(\frac{2}{\sigma_{\omega 2} \omega} \frac{\partial k}{\partial x_i} \frac{\partial \omega}{\partial x_i}, 10^{-10}\right) \quad (2.108)$$

All BSL constants are listed in the Table 2.7.

Table 2.7 Values of the coefficients in the BSL $k-\omega$ model (Menter 1994).

Φ_3	β'	β_3	α_3	σ_{k3}	σ_{w3}
Φ_2	β'	β_1	α_1	σ_{k1}	σ_{w1}
	0.09	0.075	5/9	2	2
Φ_1	β'	β_2	α_2	σ_{k2}	σ_{w2}
	0.09	0.0828	0.44	1	1/0.856

Another two-equation model which has become recently very popular is the Shear Stress Transport (SST) $k-\omega$ model proposed also by Menter (1993). The $k-\omega$ based SST model accounts for the transport of the turbulent shear stresses, according to modifications introduced to the original $k-\omega$ model by Menter. One of these modifications is referred to obtain a limiter for the formulation of the eddy viscosity, given by Equation 2.109.

$$\nu_t = \frac{a_1 k}{\max(a_1 \omega, S F_2)} \quad (2.109)$$

where $S = \sqrt{2S_{ij}S_{ij}}$, a_1 is a constant and F_2 is a blending function similar to F_1 .

$$F_2 = \tanh(\arg_2^2) \quad (2.110)$$

where \arg_2 is defined as Equation 2.111.

$$\arg_2 = \max\left(\frac{2\sqrt{k}}{\beta' \omega z}, \frac{500\nu}{z^2 \omega}\right) \quad (2.111)$$

A disadvantage of standard two-equation turbulence models is the excessive production

of turbulence kinetic energy (P). Therefore, another formulation of limiters for the production term in the turbulence equations was suggested by Menter (1994) as Equation 2.112.

$$P = \min(P, 10\beta' k\omega) \quad (2.112)$$

RANS two-equation models have proven that they perform reasonably well for a wide range of flows of engineering interest, with some limitations that may be accounted with the use of special bounding or damping functions. Their major advantage is the simplicity, and the low computational cost compared to more complex models, such as RSM or LES.

However, neither two-equation model, $k-\epsilon$ or $k-\omega$ model, is capable of giving quantitatively good results for more complicated flows. These models can fail drastically for flows with sudden changes in mean strain rate, curved surfaces, secondary motions, rotation, or if the flow is highly 3D (Wilcox 2006). Unfortunately, most flows of interest include some or all of these features. While two-equation models may be able to give qualitative results for such flows, generally a further level of complexity is needed in the model to obtain close agreement with experiments.

(4) Large eddy simulation (LES)

The basic equations for LES were first formulated by Smagorinsky (1963). Since computational resources were severely limited an alternative to resolving all the scales of motion had to be conceived. Based on the theory of Kolmogorov (1941), that the smallest scales of motion were uniform and the assumption that these small scales serve mainly to dissipate energy from the larger scales through the cascade process. Thus, the small scales could be successfully approximated. The large scales of motion, which contain most of the energy, do most of the transporting and are affected mainly by the

boundary conditions, should therefore be calculated directly, while the small scales are represented by a model. This is the basis of LES.

To separate the large scales of motion from the small scales, some kind of averaging must be done. In LES this averaging operator is not the ensemble average as in RANS, but a filter which is a locally derived weighted average of flow properties over a volume of fluid. One of the properties of the filtering process is the filter width, Δ , which is a characteristic length-scale and has the approximate effect that scales larger than Δ (resolved or super Grid Scales (GS)) are retained in the filtered flow field, while the contribution of scales smaller than Δ (Sub-Grid Scale (SGS)) must be modeled.

Flow variable, f , in LES is composed of a large scale and a small scale contribution as Equation 2.113.

$$f = \bar{f} + f' \quad (2.113)$$

where prime denotes the small scales and the over-bar denotes the larger scales that are also referred to as grid or resolved scales. To extract the large scale components a filtering operation is applied, which is defined as Equation 2.114.

$$\bar{f}(x) = \oint G(x, x'; \Delta) f(x') dx' \quad (2.114)$$

where Δ , in addition to being the filter width, is also proportional to the wavelength of the smallest scale retained by the filtering operation. $G(x, x'; \Delta)$, the filter kernel, is a localized function or function with compact support (i.e. the function is large only when x and x' are not far apart, that satisfies the following condition.

$$\oint G(x, x'; \Delta) dx' = 1 \quad (2.115)$$

A graphical representation of the filtering process is shown in Figure 2.31 with arbitrary filter kernel and a randomly fluctuating one-dimensional variable, f . The most common filter kernels that have been applied to LES are Gaussian filter, top-hat filter, and sharp Fourier cutoff filter.

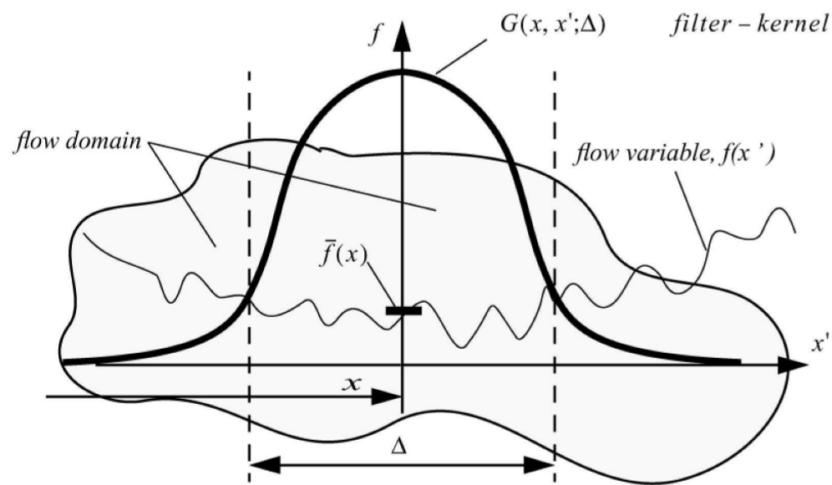


Figure 2.31 Representation of an arbitrary filter function (Villiers 2006).

The Gaussian filter is defined as Equation 2.116, which has the advantage of being smooth and differentiable.

$$G(x, \Delta) = \sqrt{\frac{6}{\pi \Delta^2}} \exp\left(-\frac{6x^2}{\Delta^2}\right) \quad (2.116)$$

The top-hat filter, which is simply an average over a rectangular region. It is the common choice for finite volume methods, primarily because the average is over a grid volume of the finite volume mesh where the flow variables are a piecewise linear function of x . This implies that if the filter width Δ is chosen to be equal to the

grid-spacing, the averaged and the local value of \bar{f} will be equal. The top-hat filter is defined as Equation 2.117.

$$G(x, \Delta) = \begin{cases} 1/\Delta & : \text{if } |x'| \leq \Delta/2 \\ 0 & : \text{otherwise} \end{cases} \quad (2.117)$$

It is evident that the filtering gives a value which is an average over a rectangular volume Δ^3 . A common choice for Δ is the cubic root of the volume of the local computational cell as following.

$$\Delta = \sqrt[3]{\Delta x \Delta y \Delta z} \quad (2.118)$$

The sharp Fourier cutoff filter, which is best defined in Fourier space and eliminates all the wave numbers above a chosen frequency. This filter is normally used in conjunction with spectral methods since it is difficult to apply to inhomogeneous flows and doesn't smooth the resolved scale field as the previously mentioned filters tend to do.

$$\hat{G}(x, \Delta) = \begin{cases} 1 & : \text{if wave number } k \leq \pi/\Delta \\ 0 & : \text{otherwise} \end{cases} \quad (2.119)$$

where \hat{G} denotes the Fourier coefficient of the filter function and k the wave number.

The shape of these three filters and their Fourier transforms are shown in Figure 2.32.

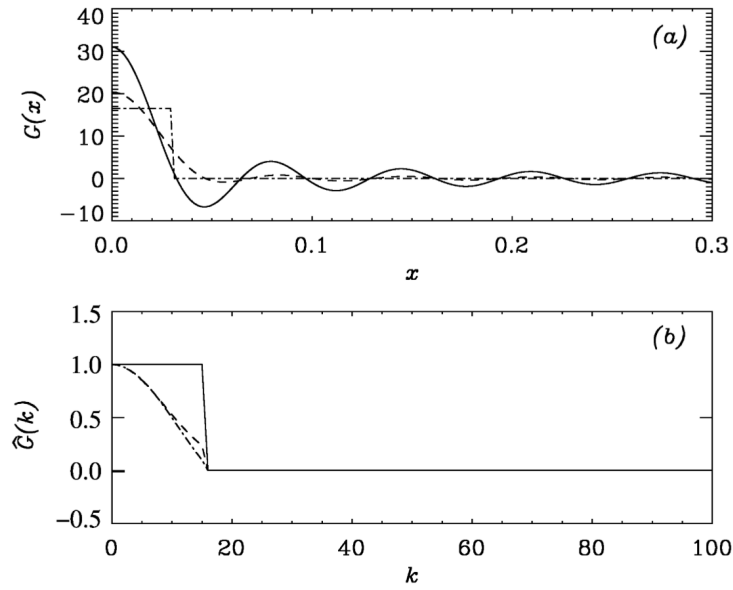


Figure 2.32 Shape of filter functions (Piomelli 1999). (solid line : sharp Fourier cutoff, dashed line : truncated Gaussian, chain line : top-hat, (a) Real space; (b) Fourier space)

By applying the filtering operation to the continuity equation and Navier-Stokes equations it is possible to derive conservation laws for the filtered flow variables. Due to the linearity of the continuity equation, applying the filtering is straightforward. The form of the equation remains unchanged as Equation 2.120.

$$\overline{\frac{\partial u_i}{\partial x_i}} = 0 \quad (2.120)$$

Filtering the Navier-Stokes equations results in the following.

$$\frac{\partial \overline{u_i}}{\partial t} + \frac{\partial}{\partial x_j} (\overline{u_i u_j}) = -\frac{\partial \overline{p}}{\partial x_i} + \nu \frac{\partial^2 \overline{u_i}}{\partial x_j \partial x_j} \quad (2.121)$$

The main complication is that the advection term cannot be expressed in terms of $\overline{u_i}$.

The common way to address this issue is to introduce the so called SGS stress tensor B_{ij} , the components of which are defined by Equation 2.122.

$$B_{ij} = \overline{u_i u_j} - \overline{u_i} \overline{u_j} \quad (2.122)$$

Inserting this into Equation 2.121 leads to Equation 2.123.

$$\frac{\partial \overline{u_i}}{\partial t} + \frac{\partial}{\partial x_j} (\overline{u_i u_j}) = - \frac{\partial \overline{p}}{\partial x_i} - \frac{\partial B_{ij}}{\partial x_j} + \nu \frac{\partial^2 \overline{u_i}}{\partial x_j \partial x_j} \quad (2.123)$$

In order to close this system of equations, B_{ij} has to be modelled. A various approaches to modelling B_{ij} has been developed. Only a small amount of the models proposed in the literature has been implemented in general-purpose CFD packages. The reason is that the implementation of some of the models is often difficult, or impossible, to combine with the general framework of the code or the discretization practices the code is based on. A common approach to SGS-modelling is to employ the Boussinesq assumption, which is the hypothesis that the SGS-stress can be modelled in a structurally similar way to the viscous stress. The analogous idea is also used in most RANS turbulence models (Sagaut 2006). It can be expressed as Equation 2.124.

$$B_{ij} = \frac{1}{3} B_{kk} \delta_{ij} + \nu_{sgs} \left(\frac{\partial \overline{u_i}}{\partial x_j} + \frac{\partial \overline{u_j}}{\partial x_i} \right) \quad (2.124)$$

where ν_{sgs} is the so called SGS viscosity which is to be computed from the filtered velocity field.

Assuming Equation 2.124, the task is then to obtain a way of calculating ν_{sgs} . In

order to be able to do that, one has to adopt the hypothesis, that a characteristic length scale l_{sgs} and time scale t_{sgs} are sufficient to describe the subgrid scale. Then, based on dimensional analysis, the SGS viscosity can be calculated as Equation 2.125.

$$\nu_{sgs} \sim \frac{l_{sgs}^2}{t_{sgs}} = u_{sgs} l_{sgs} \quad (2.125)$$

where u_{sgs} is the corresponding velocity scale. A natural choice for l_{sgs} is the filter cut-off width Δ . The choice of u_{sgs} is less obvious and different models use different approaches.

The Smagorinsky–Lilly SGS model builds on Prandtl’s mixing length model and assumes that we can define a kinematic SGS viscosity ν_{sgs} , which can be described in terms of one length scale and one velocity scale and is related to the dynamic SGS viscosity by $\nu_{SGS} = \mu_{SGS}/\rho$. Since the size of the SGS eddies is determined by the details of the filtering function, the obvious choice for the length scale is the filter cutoff width Δ . As in the mixing length model, the velocity scale is expressed as the product of the length scale Δ and the average strain rate of the resolved flow. Thus, the SGS viscosity is calculated as Equation 2.126. It is called Smagorinsky-Lilly SGS model.

$$\nu_{SGS} = (C_{SGS}\Delta)^2 |\bar{S}| = (C_{SGS}\Delta)^2 \sqrt{2\bar{S}_{ij}\bar{S}_{ij}} \quad (2.126)$$

where C_{SGS} is constant and $\bar{S}_{ij} = 1/2(\partial\bar{u}_i/\partial x_j + \partial\bar{u}_j/\partial x_i)$.

Lilly (1966, 1967) presented a theoretical analysis of the decay rates of isotropic turbulent eddies in the inertial subrange of the energy spectrum, which suggests values of C_{SGS} between 0.17 and 0.21. Rogallo and Moin (1984) reviewed work by other

authors suggesting values of $C_{SGS} = 0.19-0.24$ for results across a range of grids and filter functions. They also quoted early LES computations by Deardorff (1970) of turbulent channel flow, which has strongly anisotropic turbulence, particularly in the near-wall regions. This work established that the above values caused excessive damping and suggested that $C_{SGS} = 0.1$ is most appropriate for this type of internal flow calculation. The difference in C_{SGS} values is attributable to the effect of the mean flow strain or shear. This gave an early indication that the behaviour of the small eddies is not as universal as was surmised at first and that successful LES turbulence modelling might require case-by-case adjustment of C_{SGS} or a more sophisticated approach (Versteeg and Malalasekera 2007).

A model of the SGS Reynolds stresses based on the Boussinesq eddy viscosity hypothesis assumes that changes in the resolved flow take place sufficiently slowly that the SGS eddies can adjust themselves instantaneously to the rate of strain of the resolved flow field. An alternative strategy to case-by-case tuning of the constant C_{SGS} is to use the ideas of RANS turbulence modelling to make an allowance for transport effects. We keep the filter cutoff width Δ as the characteristic length scale of the SGS eddies, but replace the velocity scale $\Delta \times |\bar{S}|$ by one that is more representative of the velocity of the SGS eddies. For this we choose the square root of the SGS turbulent kinetic energy k_{SGS} as Equation 2.127.

$$\nu_{SGS} = C'_{SGS} \Delta \sqrt{k_{sgs}} \quad (2.127)$$

where C'_{SGS} is constant.

To account for the effects of convection, diffusion, production and destruction on the SGS velocity scale we solve a transport equation to determine the distribution of k_{SGS} as Equation 2.128. It is called one-equation eddy LES model.

$$\frac{\partial k_{sgs}}{\partial t} + \frac{\partial \overline{u_i k_{sgs}}}{\partial x_i} = 2\nu_{sgs} |\overline{D_{ij}}|^2 - C_e \frac{k_{sgs}^{3/2}}{\Delta} + \frac{\partial}{\partial x_i} \left(\nu_{sgs} \frac{\partial k_{sgs}}{\partial x_i} \right) + \nu \frac{\partial^2 k_{sgs}}{\partial x_i \partial x_i} \quad (2.128)$$

where $\overline{D_{ij}}$ is the filtered rate of strain tensor, and $C_e = 1.048$ is a constant. The expression for ν_{sgs} is then taken to be,

$$\nu_{sgs} = C_k \Delta \sqrt{k_{sgs}} \quad (2.129)$$

where $C_k = 0.094$.

Physically the four terms on the right-hand side of Equation 2.128 represent, respectively, the production of turbulence by the resolved scales, turbulent dissipation, turbulent diffusion, and viscous dissipation. When defined as Equation 2.129, ν_{sgs} does not exhibit correct behaviour near the wall. To rectify this problem a damping function can be employed. Generally van Driest damping function is applied and it has the following form.

$$f = \frac{\kappa}{C_\Delta} \left(1 - \exp\left(-\frac{y^+}{A^+}\right) \right) \quad (2.130)$$

where, $\kappa = 0.41$, is the von Karman constant, $C_\Delta = 0.158$, $A^+ = 26$, and y is the distance from a wall.

2.3.2 Brief review of OpenFOAM

The OpenFOAM computational tool box is a free, open-source software package capable of simulating a wide variety of fluid flow processes. The default tool box includes over 80 solver modules, each tailored to flows ranging from simple incompressible and

compressible flows to chemical reactions and fluid–structure interactions. In addition, over 170 utilities are available for grid generation and pre- and post-processing.

The popularity of OpenFOAM for various applications is rapidly growing. In recent years, OpenFOAM users worldwide have published several notable studies in the fields of computational fluid dynamics, computational heat transfer, fluid–structure interaction, and multiphase flow. The studies have focused on a wide range of application areas, such as atmospheric boundary layer modeling for wind turbine studies, propellant combustion modeling and diesel spray ignition, turbo machinery and industrial diffusers, cavitation in flow around a submarine hull, and 2-D flow around a bridge deck (Robertston et. al 2015).

OpenFOAM uses the finite volume method for numerical representation of the equations governing fluid motion and the message passing interface (MPI) method for parallel computing. The tool box features a range of numerical schemes, methods and turbulence models. The available turbulence models range from Reynolds averaged Navier–Stokes (RANS) to hybrid RANS/LES (HRL) to LES. It is also possible to resolve all scales using direct numerical simulation (DNS). The governing equations for incompressible fluid flow are the Navier–Stokes equations.

OpenFOAM provides three different pressure–velocity coupling methods for solving these equations: PISO (pressure implicit with split operator), SIMPLE (semi-implicit method for pressure linked equations), and PIMPLE, which is a hybrid of PISO and SIMPLE.

2.3.3 Literature Review of Simple Section Channel Flows

In the past open-channel flows have been modelled using one-dimensional (1D) Saint-Venant equations (Saint-Venant 1871). It is a simplification from two-dimensional shallow water equations, which are also known as the two-dimensional Saint-Venant equations. These 1D models contain high level of empiricism which has been

investigated experimentally, namely work carried out on the Flood Channel Facility (FCF) by Knight and Sellin (1987), Knight and Shiono (1990) and Knight (1992). Based on these experimental results a number of 1D methods were developed, such as Coherence Method (COHM) of Ackers (1993a, b), the Weighted Divided Channel Method (WDCM) of Lambert and Myers (1998) and the Shiono and Knight Method (SKM) of Shiono and Knight (1991). With advances in computer power, the interest has risen in applying more complex three-dimensional (3D) models. However, according to Wright (2001), most of the models applied to open-channel flow are either 1D or 2D with few applications of 3D models due to the inherent difficulties found in applying CFD in natural river channels.

The main focus of this research is the numerical modelling of compound channel flow. Most natural rivers have compound cross-section consisting of the main channel and one or more floodplains on the lateral sides.

Compound channel flow is characterized by complicated 3D flow structures. These structures are called secondary flows and have been classified into two categories by Prandtl (1952). He distinguished the secondary flows of the first kind, which are derived from the mean flow skewing and by the centrifugal forces in curved or meandering channels, and the secondary flows of the second kind, which are generated by the non-homogeneity and anisotropy of turbulence (Nezu and Nakagawa 1993).

There are several approaches for studying secondary flows (Nikora and Roy 2012). One of the approaches, which is widely used by researchers, is based on time averaged streamwise vorticity equation. This equation stems from Navier-Stokes (momentum) equation and can be derived by eliminating the pressure term through cross differentiation (Nezu and Nakagawa 1993). These authors focused their study of Prandtl's second kind secondary flows, based on equation for streamwise vorticity.

The magnitude of the secondary flows of the second type is about 2-3% of the maximum streamwise velocity (Nezu and Rodi 1985), however, they have a major

impact on the mean flow and turbulence structures.

In order to understand the behavior of these secondary flow structures, it is helpful to investigate simpler cases, such as the inbank flow in straight rectangular and trapezoidal open channels. Hence, the main aspects on numerical modelling of straight simple and compound channel flows are summarized in this part. However, it should be kept in mind that natural river channels are usually neither rectangular, nor prismatic.

In order to understand the more complex 3D turbulent structures of compound channel flow, a basic understanding of simple section flows is essential. The aspect ratio, B/H , defined as the ratio between the width of the channel B and the depth of the flow H , and the geometry have an impact on the flow structures in open-channel flows. The main characteristics of flow in straight simple section channels are briefly reviewed in this part.

(1) Rectangular open channels

The secondary currents in closed air ducts have been measured by several researchers, e.g. Brundrett and Bains (1964), Gessner and Jones (1965) and Perkins (1970) using Hot Wire Anemometer (HWA) and Melling and Whitelaw (1976) using a Laser Doppler Anemometry (LDA). These results contributed to the future development of Algebraic Stress Model (ASM) and Reynolds Stress Model (RSM).

Accurate measurements of secondary currents in rectangular open-channel flow have been carried out by Nezu and Rodi (1985). They have measured streamwise (u) and vertical (w) velocities using LDA and calculated the transverse velocity (v) from the equation of continuity for fully developed flow. The results are presented in Figure 2.33.

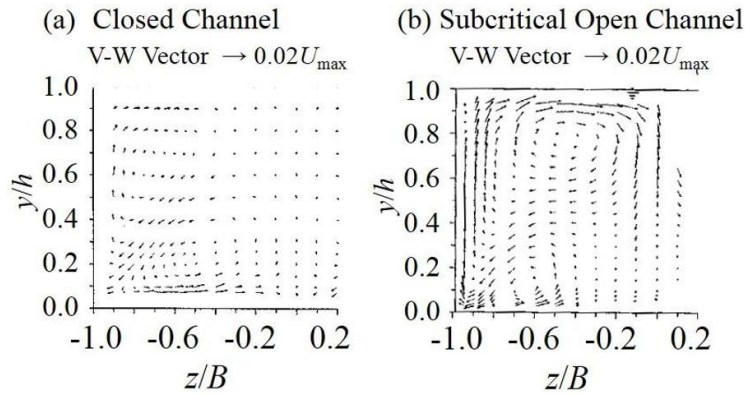


Figure 2.33 Measured secondary-current velocity vectors at a section in: (a) closed duct; (b) open-channel (Nezu 2005).

Secondary flow pattern in closed duct is symmetric, representing two symmetric contra-rotating secondary cells with regard to the corner bisector. In open-channel flow two main secondary cells are observed. Near the free surface ($z/h \geq 0.6$), a large-scale secondary-current cell called “free-surface vortex” is generated which transports momentum and energy from the side wall towards the channel centre. At the channel bottom, a smaller secondary cell called “bottom vortex” is formed which rotates in the opposite direction to the free-surface vortex.

Nezu and Rodi (1985) found that the cause for the velocity dip at the channel center is the free-surface vortex due to the transport of momentum from the free surface to the mid-depth of the channel. They also noticed that the pattern of the secondary flows depends on the aspect ratio, and hence classified rectangular channel as narrow ($B/H < 5$) or as wide ($B/H > 5$) channels.

Further investigations on the secondary currents in rectangular channels were followed up by Tominaga *et al.* (1989) using Hot Film Anemometry (HFA). They studied the effects of geometry and wall roughness on the pattern of secondary currents. Figure 2.34 shows the distribution of streamwise velocity and secondary currents in rectangular open-channel. These authors concluded that the streamwise velocity, the turbulence intensities, the Reynolds stresses and the boundary shear stress are affected by the

secondary currents. The maximum value of the secondary flows was nearly equal to $0.015U_{max}$.

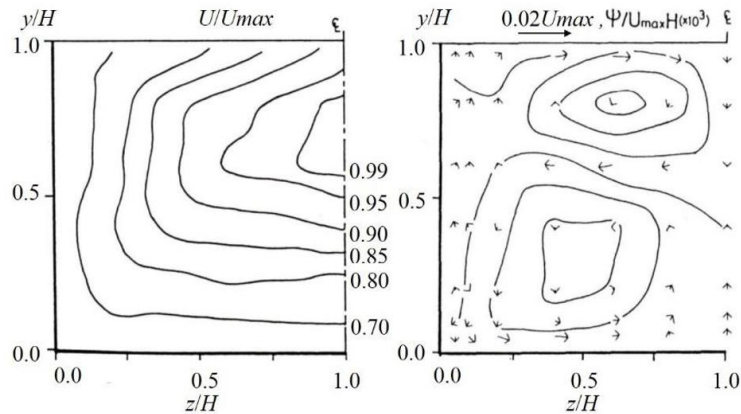


Figure 2.34 Isovels of streamwise velocity and secondary currents in rectangular open-channel for aspect ratio 2 (Tominaga *et al.* 1989).

Naot and Rodi (1982) simulated rectangular open-channel flows using the ASM and investigated the effect of the aspect ratio on the iso-velocities of the streamwise velocity and on the formation of the secondary currents. The calculated secondary current streamlines are illustrated in Figure 2.34. The pattern of secondary currents simulated by ASM shows a strong free-surface vortex, which transports high momentum from the water surface downwards, and a weak bottom vortex, which transports low momentum from near the walls towards the channel center. As the aspect ratio increases, the free-surface vortex becomes stronger and suppresses the lower bottom vortex. For aspect ratios below 2 the bottom vortex becomes dominant. When the aspect ratio is below 1, then the free-surface vortex splits into smaller and weaker vortices.

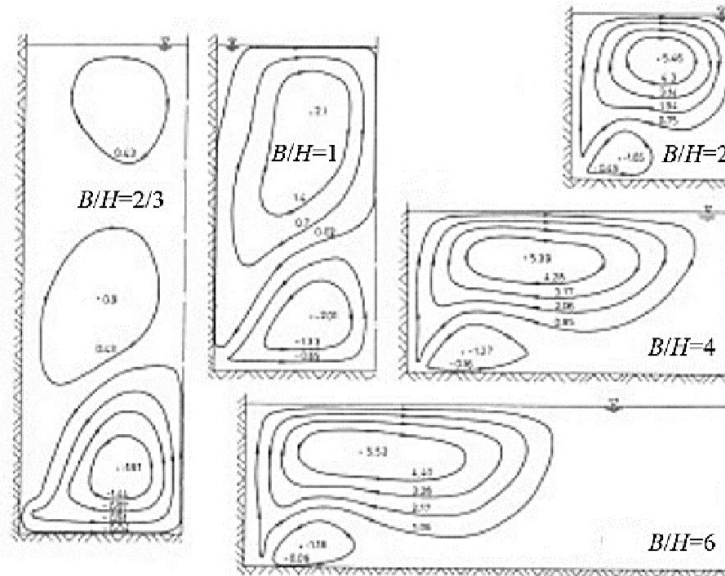


Figure 2.35 Calculated secondary current streamlines in open-channels under various aspect ratios (after Naot and Rodi 1982).

Following Naot and Rodi (1982), many researches simulated open-channel flows using ASM (Krishnappan and Lau 1986, Naot *et al.* 1993, Naot *et al.* 1996). For numerical simulations of 3D turbulent open-channel flows, the $k-\epsilon$ model has been the preferred choice (Fischer-Antze *et al.* 2001, Wu *et al.* 2000, Rameshwaran and Naden 2003). However, according to Pezzinga (1994) and Cokljat and Younis (1995) the $k-\epsilon$ model cannot reproduce secondary flows.

Reece (1977) was the first who simulated square duct and open-channel flow using RSM based on the work of Launder *et al.* (1975). Later, Cokljat and Younis (1995) have simulated rectangular open-channel flow for three aspect ratios using RSM and compared their results with the experimental data of Tominaga *et al.* (1989). The calculated and measured secondary velocity vectors are shown in Figure 2.36.

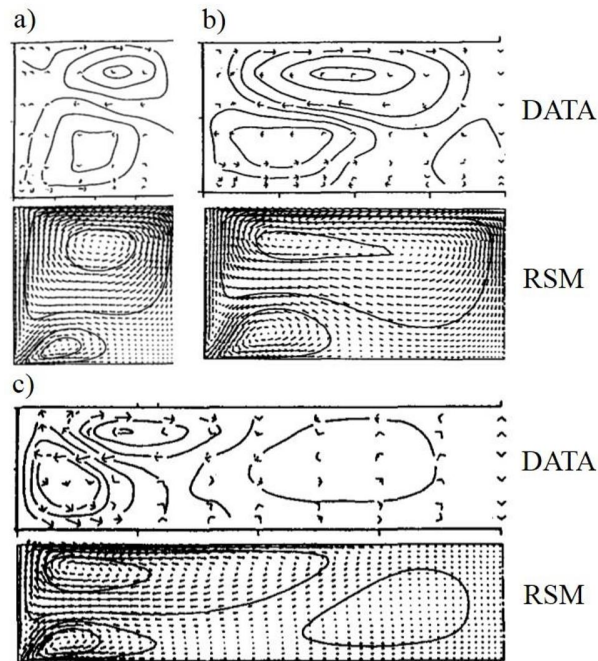


Figure 2.36 Predicted (RSM) and measured secondary flow in rectangular open-channel: Aspect ratios (a) 2; (b) 3.94; (c) 8 (Cokljat and Younis 1995).

The RSM model of Cokljat and Younis (1995) agrees well with the experimental data of Tominaga *et al.* (1989). This RSM was able to predict the number and the pattern of the secondary flows, namely free-surface vortex and bottom vortex. Cokljat and Younis (1995) noticed that with the increase of the aspect ratio the free-surface vortex elongates until it separates into two contra-rotating vortices. This behaviour was well captured by the experiment and reproduced by model. Cokljat and Younis (1995) also studied the effect of the secondary flows on the primary velocity field. Figure 2.37 presents the predicted and measured contours of the streamwise velocity.

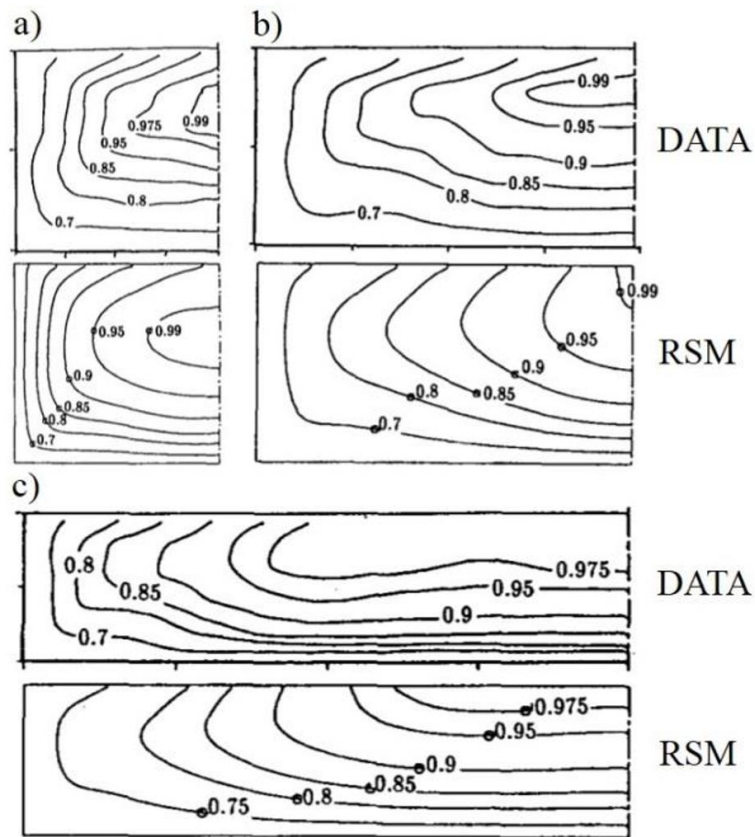


Figure 2.37 Contours of primary velocity in rectangular open-channel: Aspect ratios (a) 2; (b) 3.94; (c) 8 (Cokljat and Younis 1995).

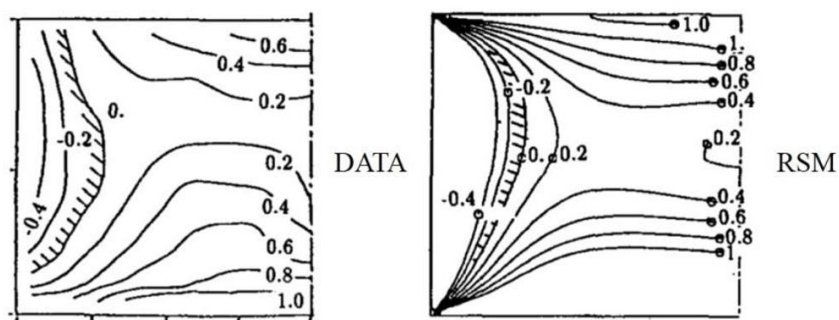


Figure 2.38 Predicted (RSM) and measured turbulence anisotropy for open rectangular channel with aspect ratio = 2 (Cokljat and Younis 1995).

The free-surface vortex transports the slow fluid from the vicinity of the side walls into the centre of the channel causing the distortion of the isovels, and thus, the

maximum velocity occurs below the free surface. In this study Cokljat and Younis (1995) have concluded that for $B/H = 2$ the position of the maximum velocity predicted by RSM was slightly over predicted in comparison to the experimental data, and that for higher aspect ratios the agreement was less satisfactory.

Cokljat and Younis (1995) also have studied the effect of the normal-stress anisotropy since the anisotropy is the driving force for the secondary current. They pointed out the shaded line in Figure 2.38, which is a zone where $\overline{v'v'}$ and $\overline{w'w'}$ are equal. They noticed that in closed ducts this line would lie along the corner bisector. But the presence of the free surface in the model adds an asymmetry to the flow. The position of this shaded line predicted by the model matched the measured one, however some over-prediction was observed near the free surface.

Besides the already known free-surface vortex and bottom vortex, Grega *et al.* (1995) and Hsu *et al.* (2000) have reported the existence of the inner secondary currents in the rectangular open-channels, which occur at the junction of the free surface and side wall. Despite the magnitude of this small-sized vortex is about 1% of the mean streamwise velocity, it affects the mean flow and turbulence structures (Grega *et al.* 1995).

Kang and Choi (2006a) continued the study of the rectangular open-channels using RSM. The purpose of their study was to develop a RSM that is capable to reproduce detailed mean flow and turbulence structure including inner vortex. The results, simulated by RSM of Kang and Choi (2006a), were compared with experimental data by Nezu and Rodi (1985) and also with another RSM results by Cokljat (1993) and with Large Eddy Simulation (LES) results by Shi *et al.* (1999).

The isovels of the streamwise mean velocity predicted by RSM of Kang and Choi (2006a) were in a good agreement with the experimental data and with other numerical models, and bulged towards the juncture between the sidewall and free surface (Figure 2.39). This bulging was due to the presence of the inner vortex that was not seen in other models and measurements.

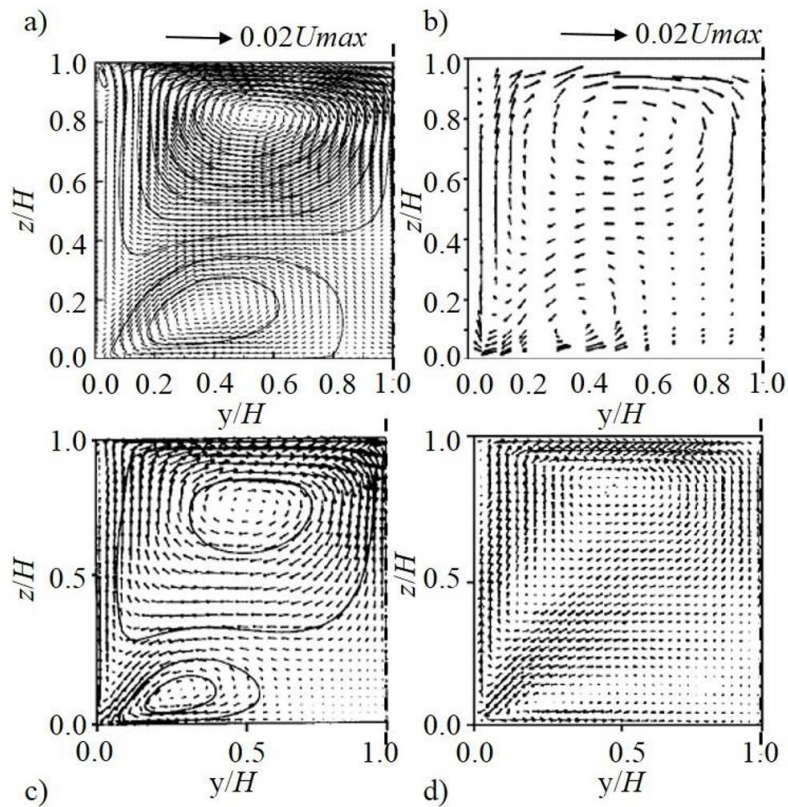


Figure 2.39 Secondary current vectors: (a) RSM by Kang and Choi (2006a); (b) experiment Nezu and Rodi (1985); (c) RSM by Cokljat (1993); and (d) LES by Shi *et al.* (1999) (Kang and Choi 2006a).

In the secondary current vectors (Figure 2.39) the free surface vortex and the bottom vortex are observed. The overall pattern and the magnitude of the secondary currents simulated by the Kang and Choi (2006a) RSM are in a good agreement with measured data and other RSM and LES models. The maximum magnitude of the secondary flows is around 2% of the maximum streamwise velocity, which is consistent with the previous studies by Naot and Rodi (1982), Tominaga *et al.* (1989) and Cokljat and Younis (1995).

However, the inner vortex is observed only in the RSM results produced by Kang and Choi (2006a). Experimental data and two other numerical models did not reveal this small inner vortex probably due to poor resolution in the experiments and coarse

computational grid (Hsu *et al.* 2000). A good agreement was also observed by Kang and Choi (2006a) between turbulence intensities u' and w' and experimental data. Profiles of the bed shear stress at the side wall were also analysed. The shear stress at the free surface was 60% higher than the mean value as a result of the inner secondary current occurring at that region, i.e. at the juncture of the free surface and the side wall.

(2) Trapezoidal open channels

In addition to the rectangular channels, Tominaga *et al.* (1989) also measured three dimensional flow in open smooth trapezoidal channels with different side slope angles (Figure 2.40).

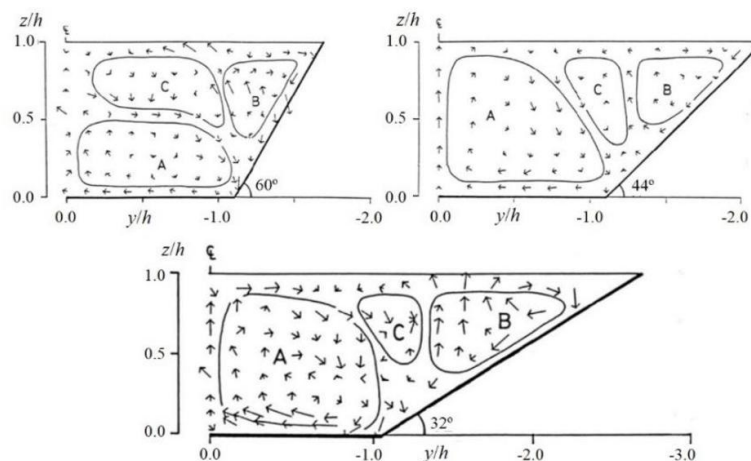


Figure 2.40 Secondary current vectors in smooth trapezoidal channels (Tominaga *et al.* 1989).

They observed that one more vortex is generated between the side wall and the free-surface vortex. Tominaga *et al.* (1989) concluded that when the side slope angle reduces, the free surface vortex gets weaker and the bottom vortex expands. They did not observe the velocity dip phenomenon observed in rectangular channels. It was revealed that the maximum value of the secondary currents was of the same magnitude

as that in the rectangular channel.

Knight *et al.* (2007) have applied the Shiono and Knight method (SKM) to calculating the lateral distributions of depth-averaged velocity U_d and boundary shear stress τ_b for flows in straight prismatic trapezoidal channels. During this study they obtained accurate distributions of U_d , however distributions of τ_b did not always match the experimental data due to the use of a constant value of friction factor, f . To achieve a high accuracy in the analytical τ_b results, Knight *et al.* (2007) have adopted linearly varying f values and two additional panels for the modelling. They also have concluded that the number of secondary current cells in a simple trapezoidal channel depends on the aspect ratio $2b/H$. For aspect ratios less than 2.2, three secondary current cells were observed; two of them were located at the side slope and one over the bottom of the channel. For $2b/H \geq 4$, the number of the secondary cells was found to be four, with two cells situated over the side slope and two over the flat bottom. The schematic representation of the pattern of the secondary current cells is presented in Figure 2.41.

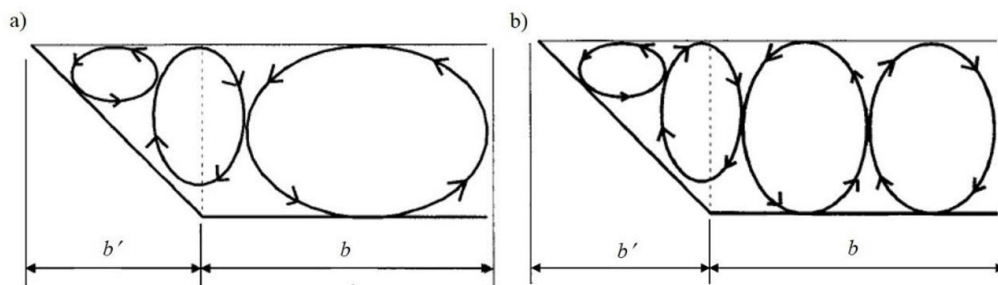


Figure 2.41 Secondary flow cells pattern in smooth trapezoidal channels with different aspect ratio: (a) $2b/H \leq 2.2$; (b) $2b/H \geq 4$ (Knight *et al.* 2007).

Knight *et al.* (2005) applied a state-of-the-art CFD workbench software to explore the physics within open-channel flows. In their research work they applied three different turbulent models, namely the $k-\epsilon$, Reynolds Stress model by Speziale, Sarkar and Gatski (SSG) by Speziale *et al.* (1991) and Reynolds Stress ω or SMC- ω (implemented

in ANSYS-CFX) models to trapezoidal channel. The three models were compared with LES by Wright *et al.* (2004). The results revealed that $k-\epsilon$ did not show any recirculation, while some bulging of the velocity isovels was observed in the SSG, and the bulging in the SMC- ω was found to be more prominent at the middle of the side slope; the three secondary cells were present for the Reynolds stress models. However, there was no evidence of the velocity dip phenomenon.

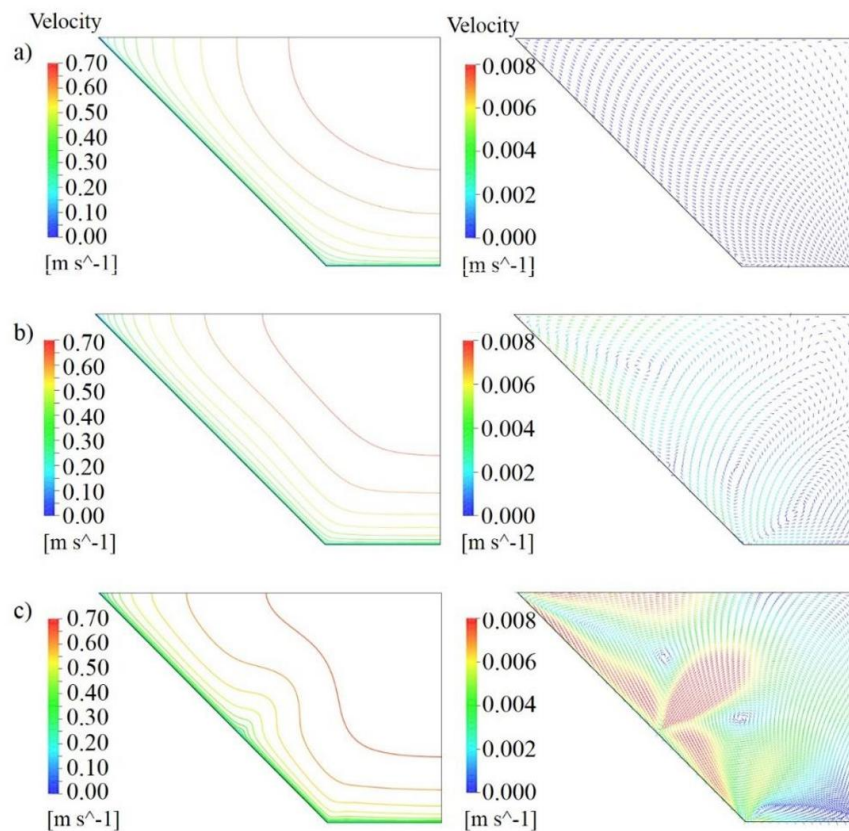


Figure 2.42 Velocity contours and secondary velocity vectors in smooth trapezoidal channels: (a) $k-\epsilon$; (b) SSG; (c) SMC- ω (Knight *et al.* 2005).

To overcome this issue, a modified free surface boundary condition was applied in their study, based on Celik and Rodi (1984), which yields a higher value for turbulent eddy dissipation and reduces turbulence kinetic energy near the free surface. The use of modified free surface boundary condition, affected the location of the secondary flows and the position of the bulging in SMC- ω was slightly shifted up than before. In the

SSG results was verified that the maximum of the velocity was beneath the water surface. The results from three models using the modified boundary condition are presented in Figure 2.42. The LES results showed a similar bulging of the isovels on the side slope of the trapezoidal channel as in the SMC- ω model. LES results also revealed an additional bulging near the bottom of the channel, and the magnitude of the v and w velocity components was greater than the results obtained by other models in this research.

2.3.4 Literature Review of Compound Open Channel Flows

Since the 1960s, compound channels have been studied intensively. The complexity of turbulent structures in compound channel flow is higher than in a single rectangular or trapezoidal open-channel. The straight compound channels are classified into symmetric or asymmetric, and according to the shape of the cross-section – into rectangular or trapezoidal.

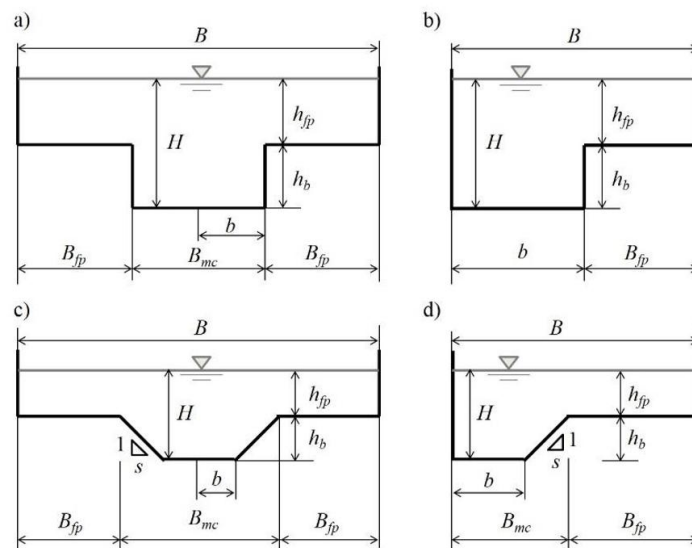


Figure 2.43 Schematic representation of compound channel:
 (a) symmetric rectangular compound channel; (b) asymmetric rectangular compound channel; (c) symmetric trapezoidal compound channel and (d) asymmetric trapezoidal compound channel (Shiono and Knight 1991).

A schematic representation of compound channels and the geometric variables are presented in Figure 2.36, namely, the total channel width, B ; the top main channel width, B_{mc} ; the floodplain width, B_{fp} ; the half of the main channel bottom width in symmetric channels and the main channel bottom width in asymmetric channels, b ; and the side slope of the main channel 1:s = vertical:horizontal. Furthermore, H and h_{fp} correspond to the main channel and the floodplain water depths, and h_b denotes the main channel bankfull height.

Figure 2.43 represents the typical hydraulic parameters and turbulent structures in symmetric prismatic compound channel (Shiono and Knight 1991). A strong lateral shear layer is present due to the difference between the faster flow in the deeper main channel and the slower flow in the shallower floodplain. This shear layer produces horizontal vortices with vertical axes at the edge between the main channel and the floodplain, which transport the high momentum fluid from the main channel towards the floodplain. These vertical vortices were first identified and photographed by Sellin (1964). There are also streamwise vortices (Prandtl's second kind secondary flows) with horizontal axes present in the main channel, which also contribute to the momentum exchange between the main channel and the floodplain.

Relative depth, $h_r = h_{fp}/H$, plays an important role in compound channel flows. Depending on the relative depth value, one form of the vortices may dominate another. Thus, for $h_r < 0.3$, the horizontal vortices are dominant, which can extend to the entire width of the floodplain, even in natural rivers (Knight 2013). For higher relative depths, that is, $h_r > 0.4$, the streamwise vortices tend to dominate the flow, thus making horizontal vortices smaller, as presented in Figure 2.44.

(1) Rectangular compound channels

Much research has focused on rectangular compound channels. This type of channel has been studied by many researches to understand the interaction mechanisms at the

interface region between the main channel and the floodplain.

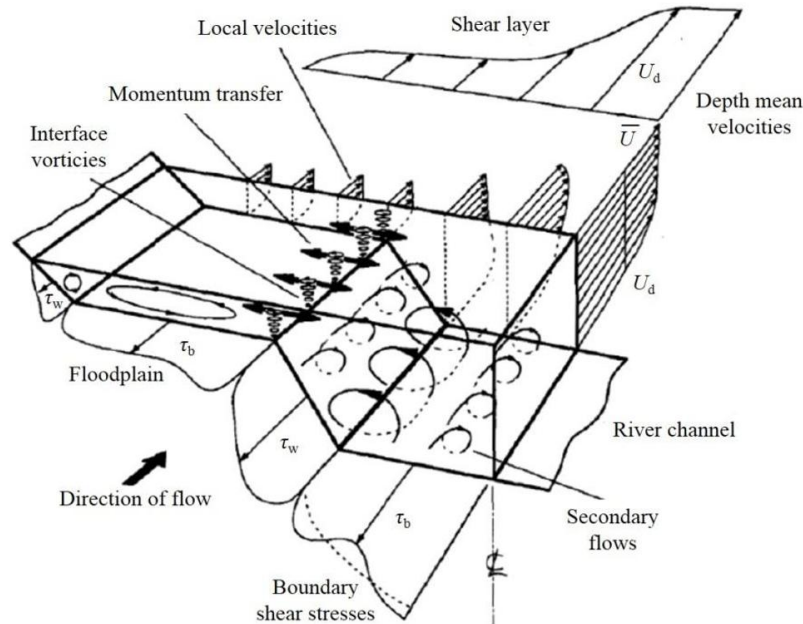


Figure 2.44 Hydraulic parameters associated with overbank flow in a trapezoidal compound channel (Shiono and Knight 1991).

Myers (1978) measured the shear stress distributions across the entire cross-section of the compound channel using a Preston tube. He considered the entire cross-section in equilibrium and identified the acting forces. Taking into account a momentum balance separately in the main channel and in the floodplain, Myers (1978) identified an additional shear stress acting in the vertical interface between the main channel and the floodplain due to momentum transfer from the main channel to the floodplain and called it apparent shear stress, τ_a . He also found that the apparent shear stress is higher at the lowest depth and suggested that the apparent shear stress may represent the intensity of the vorticity in the mixing region.

The apparent shear stress, τ_a , may be obtained by the integration over the width of a subsection, the floodplain or the main channel, of the depth-averaged momentum equation in the streamwise direction. In the vertical interface between the main channel

and the floodplain τ_a is defined as Equation 2.131.

$$\tau_a = -\rho \left(\overline{u_1 u_2} \right)_d \Big|_{B_{mc}} + \rho U_d V_d \Big|_{B_{mc}} \quad (2.131)$$

The first RHS term of Equation 2.90 represent the contribution of the shear layer to the overall shear stress in each subsection, and the second term represents the secondary flow contribution (Shiono and Knight 1991).

Tominaga and Nezu (1991) performed accurate measurements using fiber-optic two-component LDA and investigated the three-dimensional turbulent structure in rectangular compound channel. They have studied four cases, namely, three relative depths, $h_r = 0.25$; 0.5 and 0.75 , with smooth boundaries and one relative depth, $h_r = 0.5$, with rough floodplain.

For $h_r = 0.25$ and $h_r = 0.5$, a pair of longitudinal vortices was recognised near the interface region, namely a main channel and a floodplain vortex, as well as a free surface vortex observed near the side wall of the main channel. For $h_r = 0.75$, the floodplain vortex appeared stronger and reached the free surface. They found that the magnitude of the secondary flows reaches approximately 4% of the maximum streamwise velocity. This magnitude is higher than the magnitude of secondary currents observed in the simple section case, which reaches typically 2-3%. Turbulence intensities, Reynolds stresses and bed shear stress were also obtained. Using the results of turbulence intensities, they calculated the turbulence kinetic energy (TKE) and anisotropy of turbulence. The TKE results revealed that the total magnitude of turbulence increases in the vicinity of the interface between the main channel and the floodplain. The anisotropy of turbulence determines the structure of secondary currents driven by turbulence showing a complicated behaviour near the junction. Tominaga and Nezu (1991) concluded that the roughened floodplain did not affect the structure of the

secondary currents.

Nezu (1994, 1996) extended the study of Tominaga and Nezu (1991) to various geometries and roughness using fiber-optic two-component LDA. His results agree well with those of Tominaga and Nezu (1991).

Nezu *et al.* (1999) using LDA and Particle Image Velocimetry (PIV) measurements studied further the pattern and the strength of the coherent horizontal vortices for various relative depths between 0.16 and 0.67. They found that for relative depths higher than 0.375, a pair of horizontal vortices is observed near the junction. For lower h_r , a unique horizontal vortex develops at the interface region between the main channel and the floodplain (Figure 2.45).

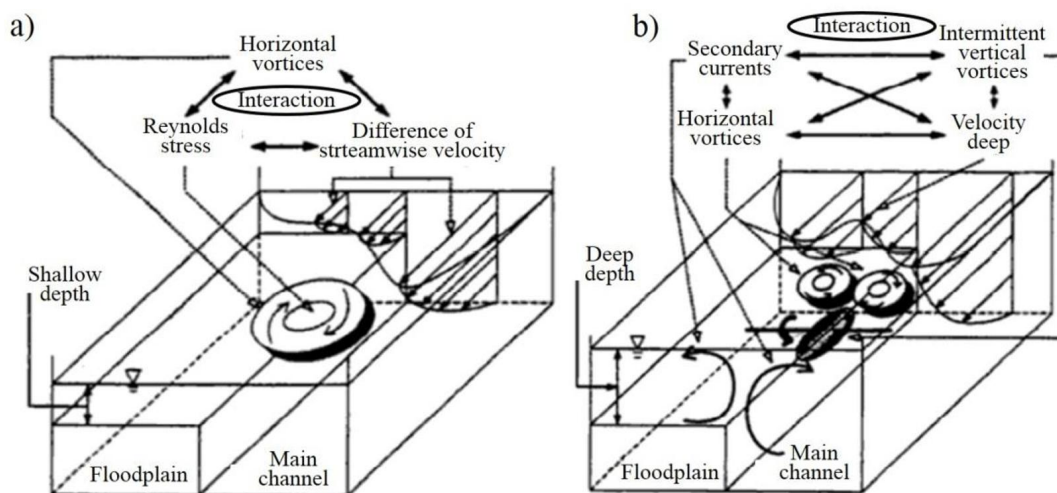


Figure 2.45 Schematic representation of flow field in: (a) a shallow depth flow; (b) deep depth flow (Nezu *et al.* 1999).

Keller and Rodi (1989) were the first to incorporate a two-dimensional depth-averaged form of the $k-\epsilon$ model in a numerical study to predict flow characteristics in compound channels. They modelled symmetric and asymmetric rectangular compound channels and compared the depth-averaged velocity and bed shear stress against the existing laboratory data. The agreement between the predicted distributions and the

experimental data was generally quite good. However, there was some deviation in the interaction region from the experimental data. They concluded that this deviation results from the under-prediction of transverse mixing in regions with an abrupt change in depth and that it cannot be accounted for correctly in their model.

The non-linear $k-\epsilon$ model, first proposed by Speziale (1987), has employed to predict secondary currents in compound channel flows by Pezzinga (1994), Lin and Shiono (1995) and Sofialidis and Prinos (1998). The latter used a low-Reynolds non-linear $k-\epsilon$ model. Although these models successfully predicted both streamwise velocity and the secondary currents, especially the two vortices generated at the interface between the main channel and the floodplain, they could not accurately simulate the velocity-dip phenomenon. The non-linear $k-\epsilon$ model also did not predict correctly the strength of the secondary currents. The measured and predicted isovels of the streamwise velocity are presented in Figure 2.46.

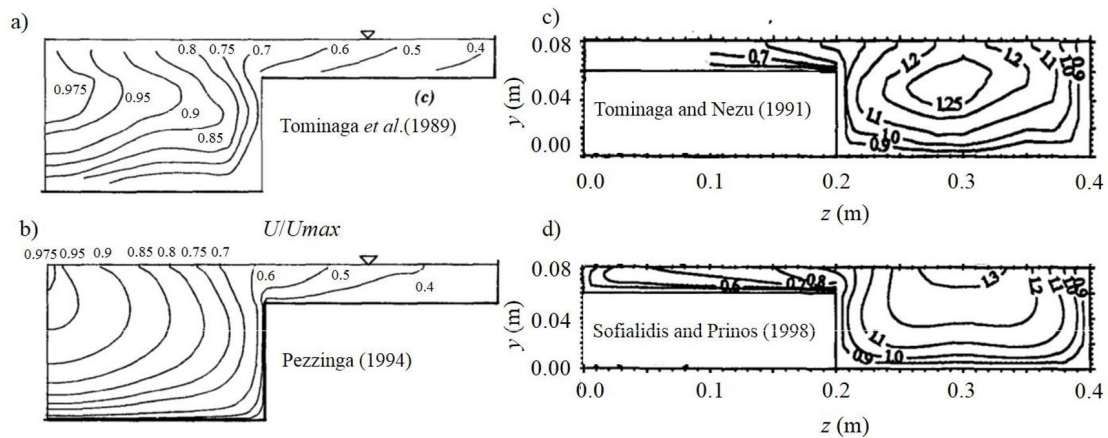


Figure 2.46 Experimental and computed contours of the streamwise velocity: (a) data by Tominaga *et al.* (1989); (b) model by Pezzinga (1994); (c) data by Tominaga and Nezu (1991) and (d) model by Sofialidis and Prinos (1998) (Filonivichi 2015).

Naot *et al.* (1993) extended the ASM of Naot and Rodi (1982) to simulate asymmetric rectangular compound channel flows with smooth and rough floodplain and

symmetric smooth and wide compound channels with relative depth ratios of $h_r = 0.25, 0.50, 0.75$. They compared the predicted results of streamwise velocity, wall shear stress distribution, TKE and secondary currents with experimental data of Tominaga and Nezu (1991). The results were in a good agreement although some differences were recognized in the secondary currents. For $h_r = 0.5$ comparison revealed that calculated values of k are too small due to the choice of the model coefficients adopted in their model.

Shiono *et al.* (2003) studied the effect of secondary flows on solute transport processes in a compound channel using linear $k-\epsilon$ model and the ASM by Launder and Ying (1973). The previous study by Lin and Shiono (1995), where they investigated solute transport in a compound channel comparing the linear and non-linear $k-\epsilon$ models, revealed a significant difference in solute distributions with and without secondary flows. Shiono *et al.* (2003) concluded that the streamwise velocity and secondary flow in the shear layer using ASM of Lin and Shiono (1995) were in a good agreement with the experimental data. However, the inclination angle of two vortices from the junction between the main channel and the floodplain was steeper than the measured one. The linear $k-\epsilon$ model did not predict secondary flows and gave poor quality predictions. For shallow flow, both models failed in predicting two concentration peaks. Shiono *et al.* (2003) highlighted the importance of secondary currents modelling in order to accurately predict the primary velocity.

Cokljat and Younis (1995) applied their RSM to symmetric and asymmetric compound channels. The experimental data from Tominaga and Ezaki (1988) and Tominaga and Nezu (1991) were used for the model validation. It was found that RSM captured the secondary currents and even smaller vortices. The position, where free surface and main channel vortices meet, was predicted almost exactly by the model. The effect that secondary currents have on the primary flow was well predicted, where a significant bulging of the isovels at the junction between the main channel and the

floodplain was present (Figure 2.47). The velocity-dip phenomenon was captured by the RSM. Cokljat and Younis (1995) suggested that the latter was not reproduced in the work of Naot *et al.* (1993) due to under prediction of the levels of turbulence anisotropy by that model. They also compared the predicted and measured boundary shear stress distribution for the symmetric compound channel. The correspondence was fairly satisfactory, especially for the floodplain, where the RSM reproduced the waviness of the experimental data. The variation of the total discharge with different relative depths was also well predicted.

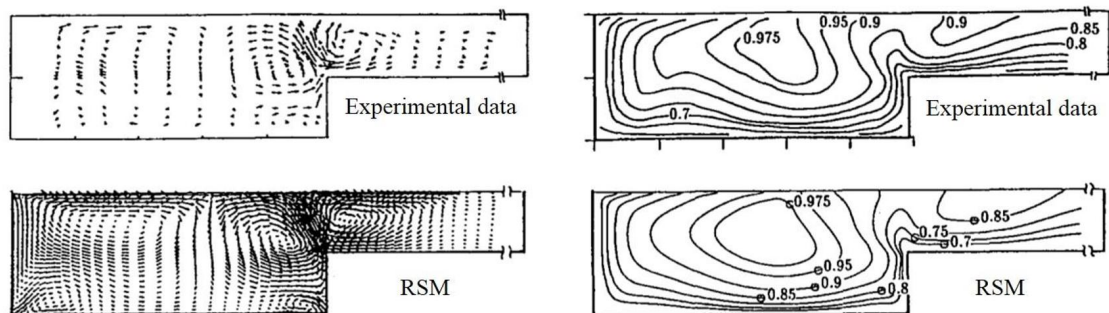


Figure 2.47 Vector plots of the secondary currents and contours of the primary velocity in asymmetric compound channels for $h_r = 0.5$ (Cokljat and Younis 1995).

Similar calculations have been made by Kang and Choi (2006b). Their RSM was capable of predicting the velocity dip, number and position of the secondary currents and the distribution of the streamwise velocity. It also produced results that were in good agreement with experimental data of Tominaga and Nezu (1991). The maximum magnitude of the secondary currents was about 3% for the $h_r = 0.5$. The authors have noticed that the secondary currents at the junction between the main channel and the floodplain become weakened as the relative depth decreases. This aspect is reflected in the angle of inclination of the upflow at the junction, which increases with decreasing the relative depth (Kang and Choi 2006b). For shallow flow, $h_r = 0.25$, the vertical

structure in the main channel becomes similar to that observed in the rectangular channel. The main channel vortex increases its intensity and the floodplain vortex decreases with the decrease of the relative depth. Kang and Choi (2006b) also compared the wall shear stress distribution and concluded that the RSM overestimates bottom shear stress in the main channel. However, in the floodplain, the simulated bottom shear stress was in a good agreement with the experimental data.

Thomas and Williams (1995a) were the first to apply LES to study the flow and turbulence structure in a compound open-channel. Their work has been complemented by the study of Cater and Williams (2008). Both of these studies simulated an asymmetric rectangular compound channel using LES for a relative depth of $h_r = 0.5$. The difference between these models lied in the longer calculation domain and in finer mesh for Cater and Williams (2008) in comparison to the model of Thomas and Williams (1995a). They have predicted mean streamwise velocity distribution, secondary currents, bed shear stress distribution, turbulence intensities, TKE, and calculated lateral distribution of apparent shear stress. In general, the results were in a good agreement with the experimental data of Tominaga and Nezu (1991).

However, some deviation from the data was observed. Namely, the bed shear stress predicted by LES, as well as the ASM of Naot *et al.* (1993), differ significantly from the experimental data. The position and number of secondary currents was captured by LES in both studies. The maximum magnitude of the secondary flows was around 3.7% of the maximum primary velocity. The upflow at the junction between the main channel and the floodplain was inclined at the angle of 20° from the vertical. The authors of both studies have noticed that the distortion of the isovels is more pronounced in the experimental data (Figure 2.48).

The previous studies of Thomas and Williams (1995a) and Cater and Williams (2008) have been complemented by the work of Kara *et al.* (2012). The latter have employed LES to study the effects of the floodplain depth on the flow in an asymmetric compound channel. They have studied two relative depths, namely, $h_r = 0.25$ and 0.5 . With an increase in recent years in the computational power, this study was run with finer mesh compared to the previous cases. Kara *et al.* (2012) predicted secondary

currents, the time-averaged streamwise velocity, distribution of shear Reynolds stresses and bed shear stress distribution.

Overall a good agreement between the experimental data of Tominaga and Nezu (1991) and simulated results was obtained, confirming the accuracy of the method for these flows (Figure 2.48). Kara *et al.* (2012) compared the depth-averaged streamwise velocities obtained by LES with calculated by analytical solution of Shiono and Knight Method (SKM), and concluded that the analytical approach to their problem requires calibration of the lateral eddy viscosity coefficient and the secondary current parameter. The authors have examined the terms contributing to the lateral momentum transport and quantified the anisotropy, generation term of streamwise vorticity and apparent shear stress.

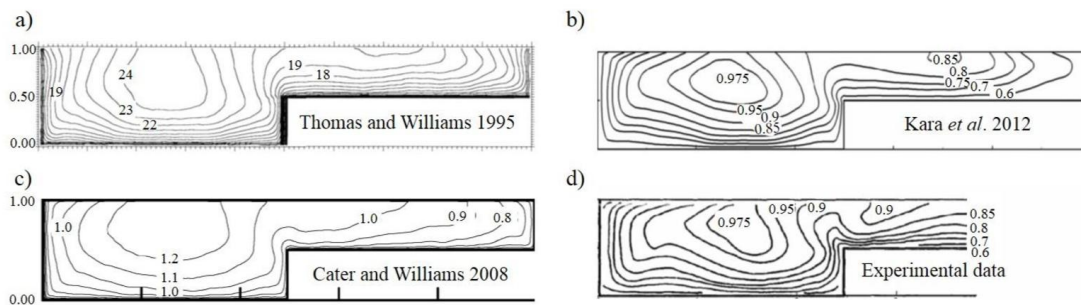


Figure 2.48 Contours of the streamwise velocity in asymmetric compound channels for $h_r/hr = 0.5$ (adapted from Thomas and Williams 1995a, Cater and Williams 2008, Kara *et al.* 2012).

Kara *et al.* (2012) demonstrated that the anisotropy in compound channel at the interface between the main channel and the floodplain leads to the formation of a vortex pair. The apparent shear stress was greater for the shallow floodplain case. The generation term was found to be more significant at the interface for shallow case, where the peak values extend to the free surface. The authors suggested that the extent and magnitude of the secondary current generation term influences the angle of inclination of secondary currents.

Furthermore, recently Xie *et al.* (2013) used LES to simulate asymmetric rectangular compound channel. In this study the distributions of the mean velocity and secondary

flows, boundary shear stress, turbulence intensities, TKE and Reynolds stresses were in a good agreement with the experimental data. They investigated the instantaneous flow fields and large-scale vortical structures, and concluded that a stronger turbulent flow occurs in the near wall region and a significant lateral transport of momentum is present.

(2) Trapezoidal compound channels

For the purposes of establishing an experimental database for validating open-channel flow phenomena in numerical models, the Science and Engineering Research Council (SERC) built the Flood Channel Facility (FCF) in 1986 at Hydraulic Research Ltd., located in Wallingford, UK. A large number of detailed measurements of various channel geometries, including trapezoidal compound channel, were carried out at the FCF flume. For the details of the facility and on the experiments the reader can consult Knight and Sellin (1987).

One of the first outputs of this program was the work presented by Knight and Shiono (1990). This study includes highly accurate measurements of the primary velocity, the turbulent intensities, TKE and the Reynolds stresses. One of the main conclusions of their study was the significance of the secondary currents contribution to the lateral transfer of momentum despite their small values. Longitudinal vortices have been found by those authors to be important for relative depths as low as 0.25. The vertical distribution of the shear stress was found to be highly non-linear in the interface zone, indicating strong secondary currents development. With an increase of the relative depth, the spreading of the shear layer onto the floodplain decreases.

Very recently, Azevedo *et al.* (2012) have measured the streamwise and vertical velocity components and turbulent intensities, using a 2D Laser Doppler Velocimetry (LDV) in asymmetric compound channel with trapezoidal cross-section.

Since the introduction of the analytical SKM by Shiono and Knight (1988), a number of studies have been carried out to show its accuracy in predicting lateral distributions of the depth-averaged velocity and the boundary shear stress distribution. In this SKM Shiono and Knight (1988) ignored the secondary flow effects. Shiono and Knight (1991)

improved their earlier work by including the effects of secondary flow.

SKM has been among the most popular methods used by researchers (Lambert and Sellin 1996, Ervine *et al.* 2000, Bousmar and Zech 2004, Rezaei and Knight 2009, Yang *et al.* 2013). Previous research (e.g. Knight and Shiono 1996, Abril and Knight 2004, McGahey *et al.* 2006) has demonstrated that the SKM is capable of determining the lateral distributions of depth averaged velocity and boundary shear stress across rivers and channels of various cross-sections both accurately and with a minimum of computational effort (Sharifi *et al.* 2009).

However, for a successful simulation using SKM, in addition to the inputs of the shape of cross-section, number of sub-areas (panels) and longitudinal bed slope, correctly specified values of three parameters are required, namely, the lateral distribution of friction factor, dimensionless eddy viscosity, and a sink term which represents the effect of the secondary flow. The calibration of these parameters had to be done for different types of channels. Based on the experimental studies, Knight and Abril (1996) and Abril and Knight (2004) derived equations for estimating the value of f , λ and Γ in compound channels; Chlebek and Knight (2006) provided initial guidance on choosing suitable parameters for prismatic rectangular channels. Based on the analysis of the calibration results, Knight *et al.* (2007) and Sharifi *et al.* (2008, 2009) provided guidelines for calculating the values of the calibration parameters for hydraulically smooth trapezoidal channels.

A two-dimensional depth-averaged $k-\epsilon$ model has been applied to trapezoidal compound channel by Keller and Rodi (1988). They calculated the depth-averaged velocity and the bed shear stress distributions. The agreement between the predicted distributions and the experimental data were quite good. However, some deviations were present in the interaction region between the main channel and the floodplain due to not sufficient transverse mixing and too low eddy viscosity, which can cause under-prediction of turbulence generation. To account for this production a more refined bed shear stress and turbulence model is required.

A LES was used to calculate velocity and bed shear stress distribution and secondary currents in symmetric compound channel of trapezoidal cross-section by Thomas and

Williams (1995b). The results were compared with experimental data from the SERC-FCF. The pattern of the secondary cells was in close agreement with data of Shiono and Knight (1990) for the lower relative depth, $h_r = 0.15$. The predicted bed shear stress distribution was in a good agreement with the experimental data. Meanwhile the streamwise velocity was over predicted at most by approximately 8% and deviated from the logarithmic profile. The authors concluded that the main deficiency in their simulation was too coarse mesh spacing in streamwise direction of the flow due to the limitations in their computational resources at the moment.

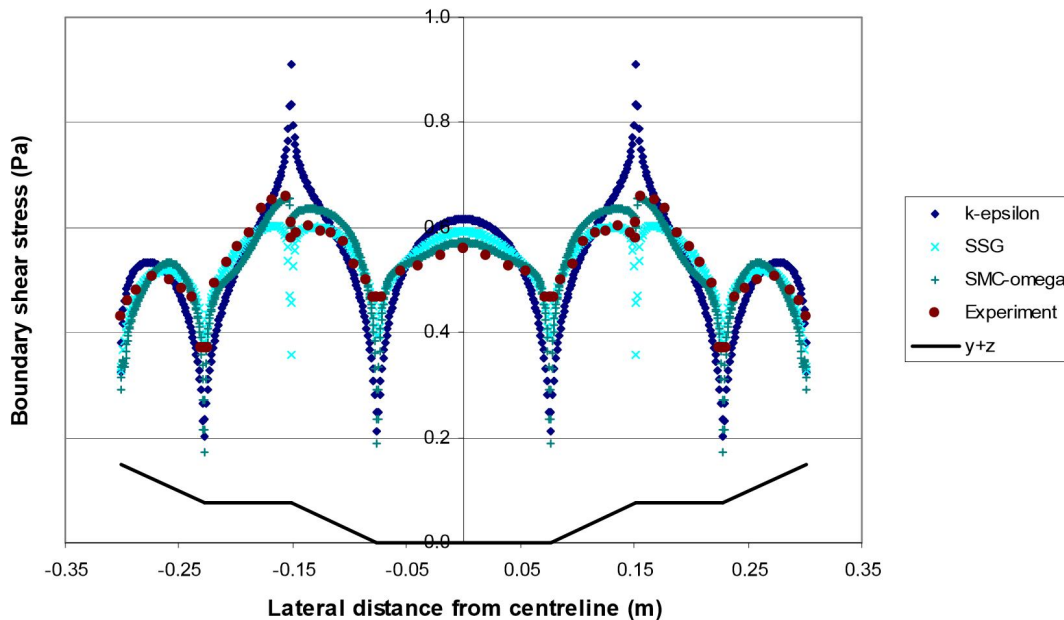


Figure 2.49 Boundary shear stress in symmetric compound channel with trapezoidal cross-section (Knight *et al.* 2005).

Knight *et al.* (2005) continued their research work in applying state-of-the-art CFD workbench software to compound channel flow. They have tested $k-\epsilon$ model, SSG and SMC- ω model and compared the predicted streamwise velocity and boundary shear stress distributions with experimental data by Yuen (1989). Both models, SSG and SMC- ω , predict the presence of four secondary cells where the strongest is located about the junction between the main channel and the floodplain. In the case of bed boundary shear stress distribution, the SMC- ω predictions were in the closest match to the experimental data (Figure 2.49). The authors have noticed that the predicted mass

flow rate was higher than the experimental value. This is due to the fact that whilst the experiments were considered with relatively smooth walls, there was still some roughness to account for. This was reflected in CFD simulations through applying a small roughness (0.5 mm) in the cases of $k-\epsilon$ and SSG model. The introduction of roughness did not have any impact on the velocity contours or the boundary shear stress profiles. The $k-\epsilon$ model failed in predicting secondary currents and overestimated the boundary shear stress. The main conclusion from this research work has been that there are limitations as to what can be achieved with a turbulence model in the case of steady uniform flow (Knight *et al.* 2005).

Evidence gathered from the literature review permits to assume that besides DNS, much more complex models, such as LES, are necessary for simulating the fully 3D multi-scale phenomena in open-channel flows. However, despite the fact that LES produces accurate results, it increases computational cost further beyond typical engineering time and resource framework, which often leads to rejection of this method. Thus, a compromise is needed between capturing the complexity of anisotropic 3D secondary flows with accuracy and using moderate computational cost yet. Accessible computational cost may dictate the usefulness or not of new models to develop engineering analyses for which, for example, design optimization is mandatory and hundreds or even thousands of simulations are required before determining the best solution. For such a purpose several turbulence models are studied to compound channel flow, compare numerical results to experimental data and discuss the advantages and drawbacks of the used models.

CHAPTER 3

LABORATORY EXPERIMENTS ON WALL SHEAR STRESS

3.1 Experimental Setup

The Preston tube is used for measurement of the wall shear stress. The Preston tube used for this study is made up of two stainless steel pipes. In a large pipe the total pressure is measured and in a smaller pipe the static pressure is measured. Figure 3.1 illustrates the Preston tube configuration.

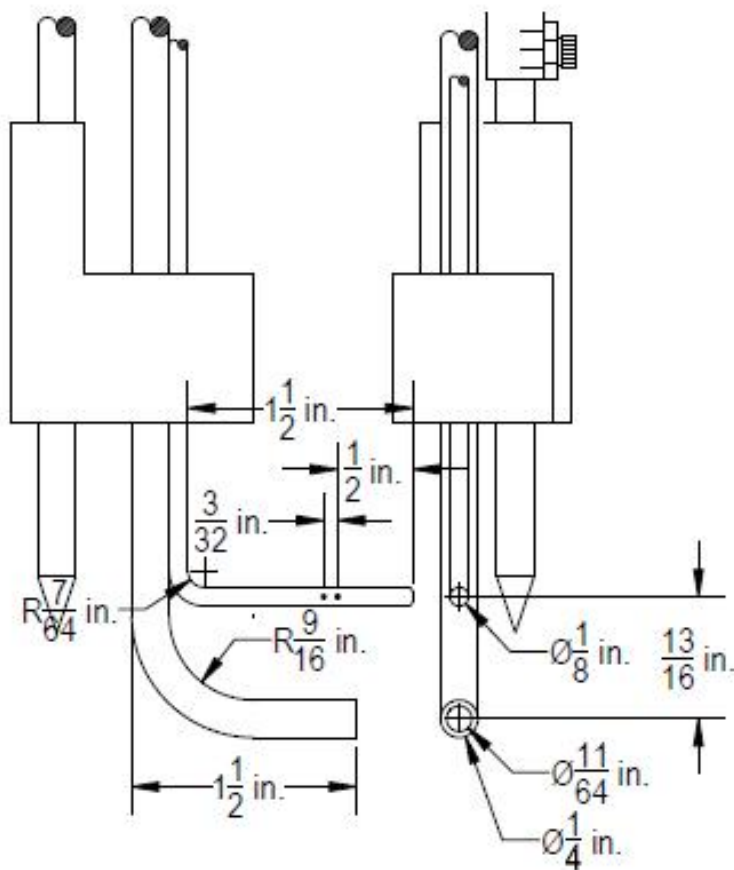


Figure 3.1 Preston tube configuration.

The outer diameter of the dynamic port of the Preston tube is 1/4 inch while the inside diameter of the dynamic port is 11/64 inch, creating an inside to outside diameter ratio of 0.69. Two static ports, each 1/32 inch in diameter, are located either side of a 1/8 inch diameter tube, creating a total of four ports for the Preston tube. A distance of 13/16 inch separate the static and dynamic ports.

The Preston tube is connected to the pressure gauge that measures pressure difference between the dynamic pressure and the static pressure. The pressure gauge is connected to data logger that gathers time series of the pressure difference. The pressure gauge used in this study is model LD 300 of the Smar company and the data logger is model GL220 of the Graphtec company.



Figure 3.2 The pressure gauge (LD300).



Figure 3.3 The data logger (GL220).

Calibration of the Preston tube and wall shear experiments are performed in a straight 0.8 m wide by 0.5 m tall by 8 m long flume. Water is delivered to the headbox of the flume entrance through the weir box. Figure 3.4 shows a schematic of the experimental channel.

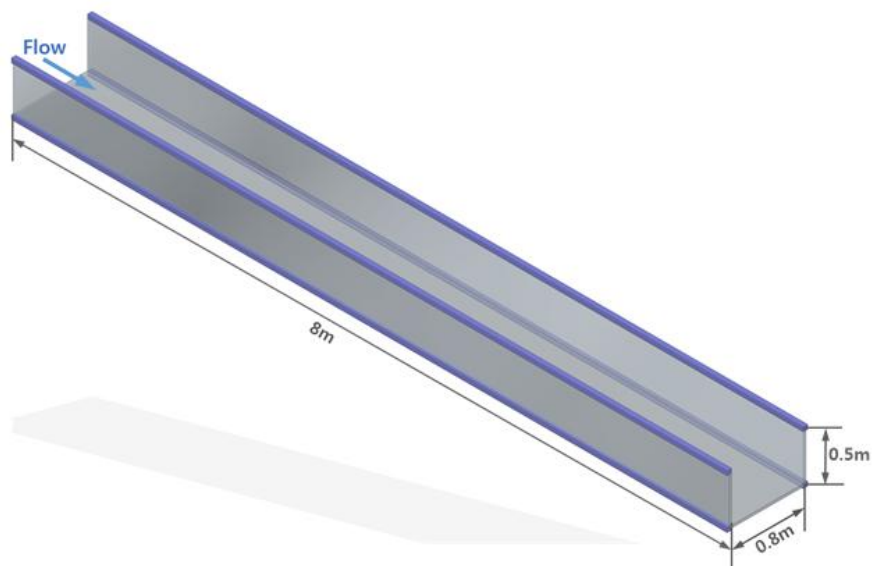


Figure 3.4 Schematic of the experimental channel.



Figure 3.5 Setup of the pressure gauges.



Figure 3.6 Measurement of water depth.



Figure 3.7 Measurement of wall shear stresses.

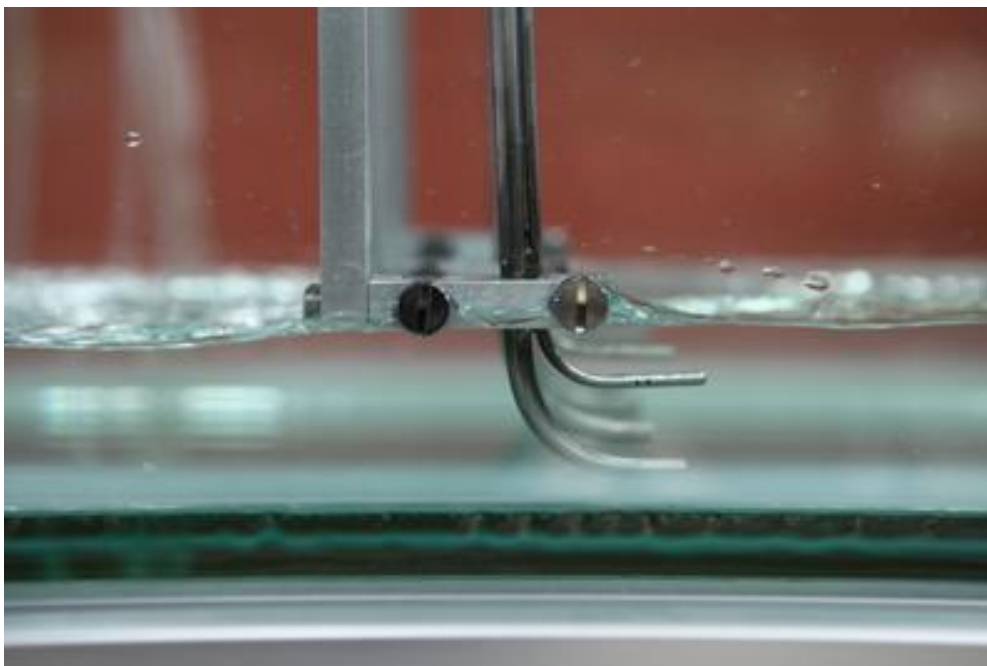


Figure 3.8 Picture of the Preston tube measuring wall shear.

3.2 Calibration of Preston Tube

Preston tube data are collected with corresponding shear stress computations. The procedure of the calibration test is presented in Figure 3.9. In order to achieve the range of Preston tube readings required for calibration, the discharge and tail gate are varied during the test.

The discharge ranges from 0.0116 m³/sec to 0.0504 and the corresponding mean velocity ranges from 0.28 m/sec to 1.61 m/sec. The discharge is measured in the inlet weir by water elevation and discharge relationship and the water depth in the channel is measured in the middle of the test section located 4 m downstream of the inflow boundary.

Pressure difference is measured at the same location by Preston tube in length scale. Pressure difference used in this study is time averaged value that is calculated from the time series of the measured pressure difference for 180 seconds (Figure 3.10 ~ Figure 3.13). Friction slope (S_f) is calculated from measured water depth and then wall shear stress (τ_0) is calculated by $\gamma h S_f$.

Results of the calibration test are presented in Table 3.1. Total 24 cases are performed for the calibration. Wall shear stress ranges from 0.52 N/m² to 17.58 N/m² and Reynolds number ranges from 51,000 to 220,000.

Calibration curve is created from the collected Preston tube data and the computed wall shear stress and the results for the calibration of the Preston tube are presented in Figure 3.14. Calibration equation is developed as Equation 3.1 with an r-squared value of 0.9929.

$$\tau_0 = 0.2097 \Delta p \quad (3.1)$$

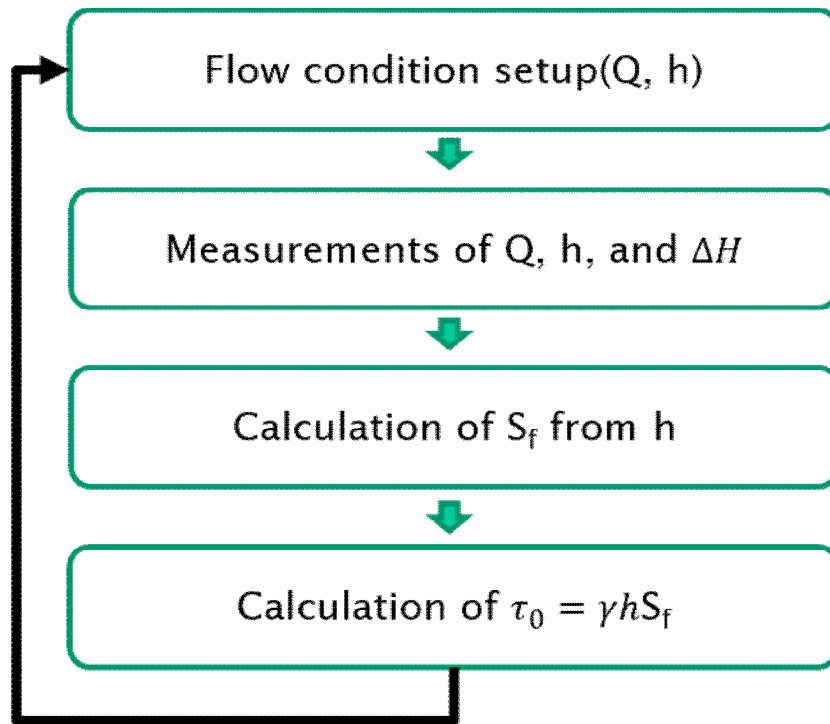


Figure 3.9 Procedure of the calibration test.

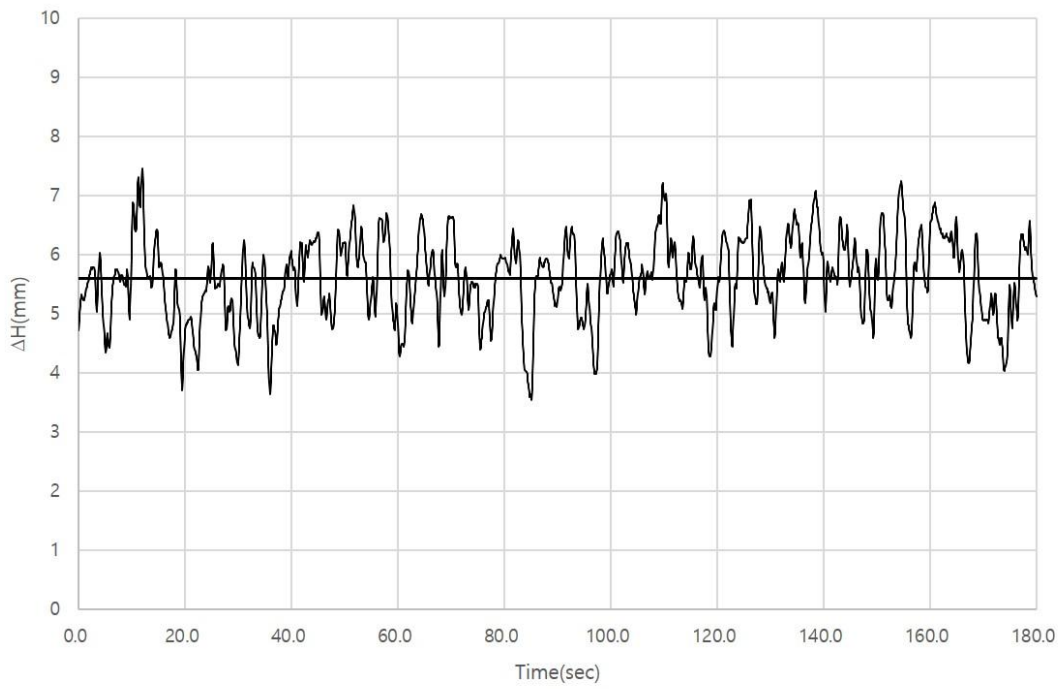


Figure 3.10 Measurement of the pressure difference (case01).

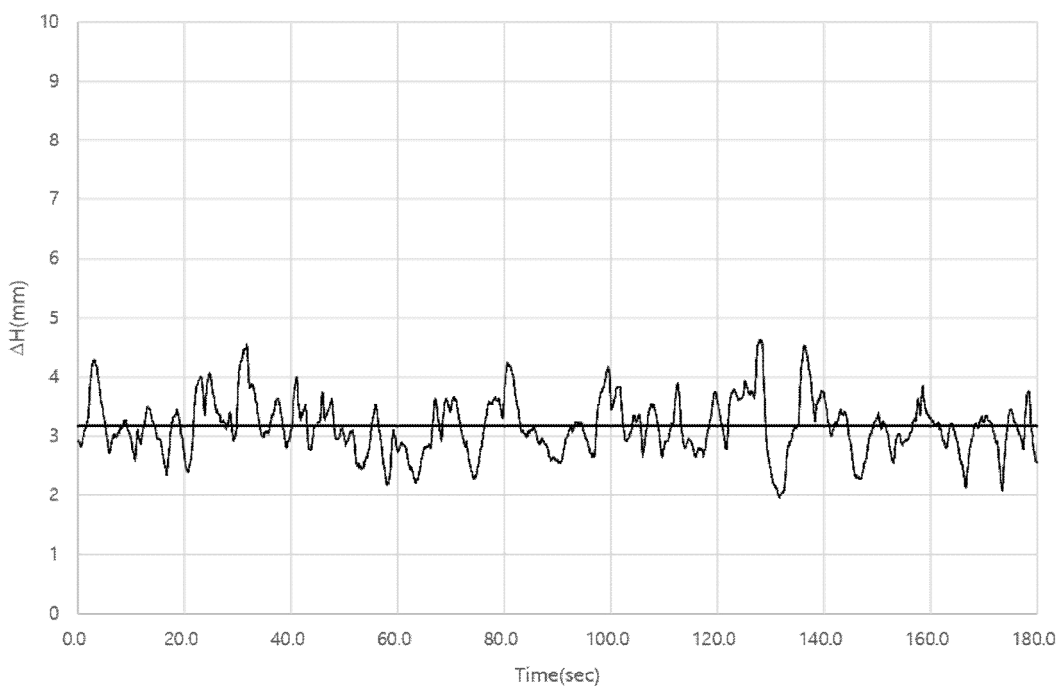


Figure 3.11 Measurement of the pressure difference (case02).

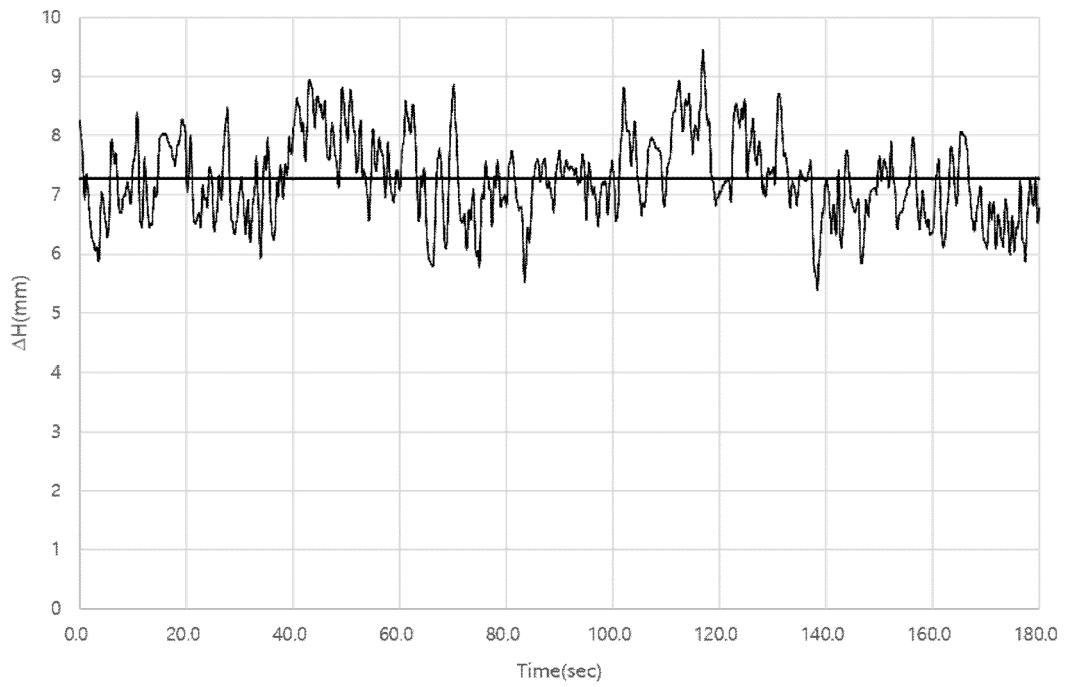


Figure 3.12 Measurement of the pressure difference (case03).

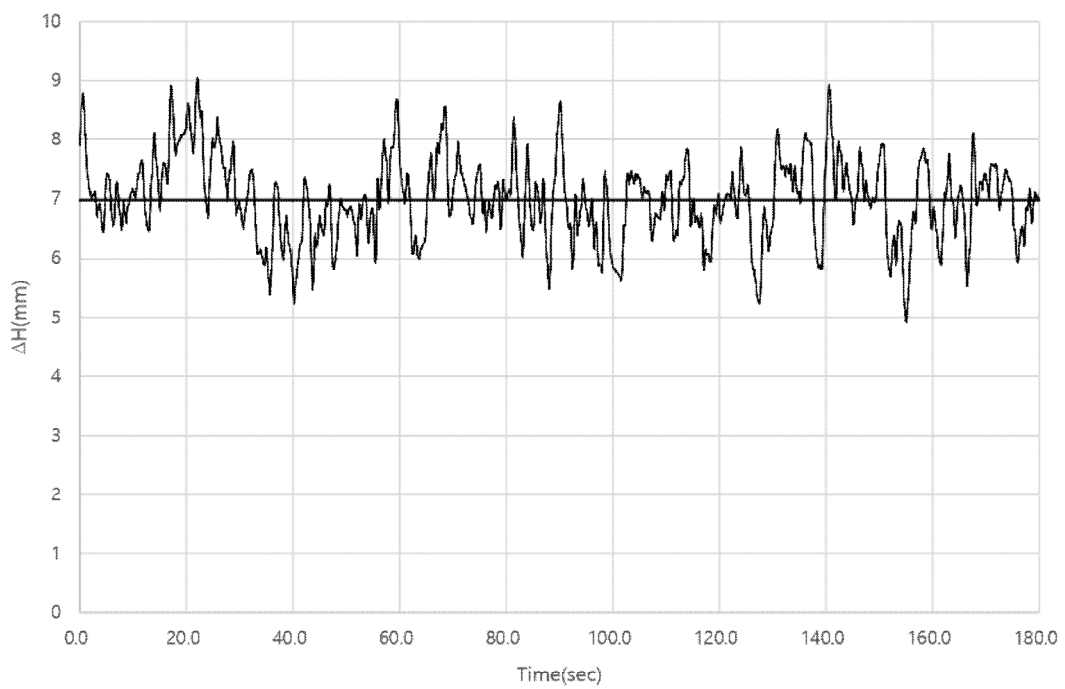


Figure 3.13 Measurement of the pressure difference (case04).

Table 3.1 Results of the calibration test.

Case	Pressure difference (mm)	Discharge (m ³ /sec)	Mean velocity (m/sec)	Depth (m)	S_f	Wall shear (N/m ²)	Re
01	5.60	0.0378	0.51	0.093	0.00184	1.36	153,465
02	3.16	0.0378	0.35	0.134	0.00060	0.59	141,552
03	7.28	0.0483	0.59	0.102	0.00224	1.79	192,449
04	6.99	0.0436	0.56	0.097	0.00215	1.64	175,548
05	2.14	0.0116	0.29	0.050	0.00120	0.52	51,559
06	2.99	0.0153	0.34	0.056	0.00142	0.69	67,038
07	1.94	0.0153	0.28	0.069	0.00075	0.43	65,206
08	4.90	0.0248	0.43	0.071	0.00179	1.06	105,248
09	9.67	0.0483	0.61	0.099	0.00243	1.89	193,467
10	12.59	0.0483	0.76	0.080	0.00478	3.11	201,334
11	32.51	0.0483	1.08	0.056	0.01450	6.98	211,819
12	25.94	0.0483	0.97	0.062	0.01056	5.55	209,109
13	38.39	0.0483	1.09	0.055	0.01514	7.21	212,172
14	46.45	0.0483	1.27	0.048	0.02449	10.20	215,851
15	49.91	0.0483	1.25	0.048	0.02338	9.86	215,514
16	81.10	0.0483	1.61	0.038	0.05232	17.58	220,795
17	10.14	0.0483	0.60	0.100	0.00237	1.86	193,177
18	9.55	0.0483	0.58	0.105	0.00206	1.67	191,336
19	8.32	0.0483	0.52	0.116	0.00152	1.34	187,304
20	8.06	0.0504	0.54	0.117	0.00159	1.42	194,877
21	9.86	0.0504	0.59	0.107	0.00210	1.74	198,758
22	9.91	0.0504	0.60	0.104	0.00228	1.85	199,881
23	10.75	0.0504	0.62	0.102	0.00245	1.95	200,873
24	10.77	0.0504	0.62	0.101	0.00250	1.98	201,125

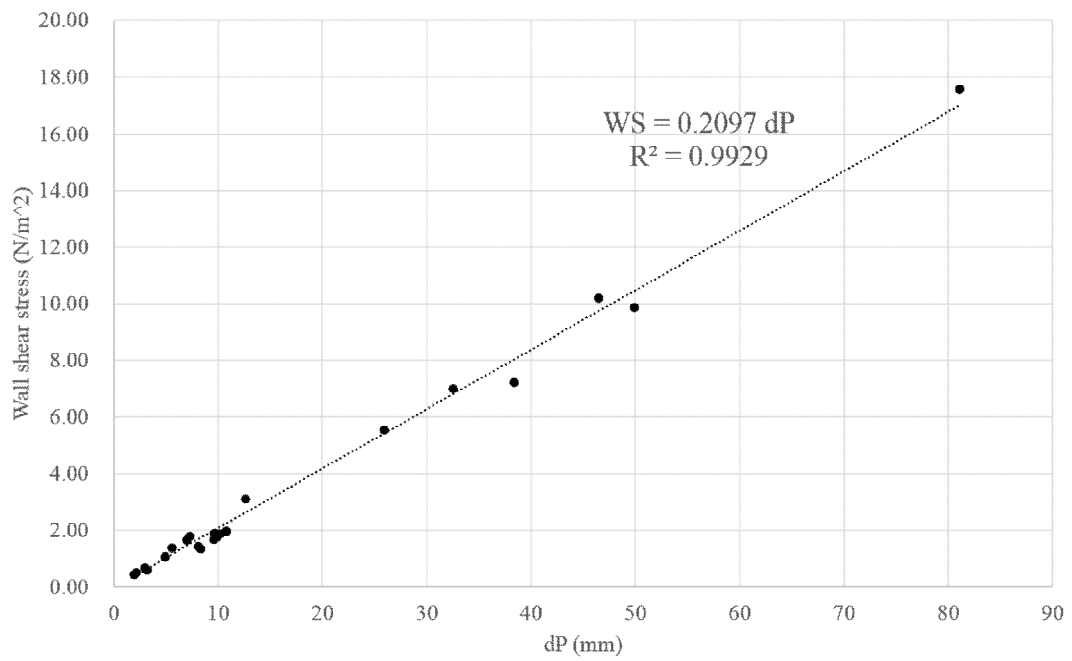


Figure 3.14 Results of the calibration test.

3.3 Experimental Results in the Compound Open Channel

3.3.1 Experimental Conditions

The experiments are conducted in the experiment channel (Figure 3.4). The bed and sidewalls are composed of glass. A fully developed and uniform flow is established at the test section 4 m downstream from the entrance of the channel. Unsymmetrical compound open channels are composed of a main channel and a floodplain and the floodplain is made of opaque acrylic panels on one side in the flume. The nomenclature used in this paper is indicated in Figure 3.15. H and h are the flow depth of the main channel and of the floodplain, respectively. B and b are the total channel width and the floodplain width, respectively. B and b are fixed with values of 0.8 m and 0.4 m, respectively in the experiment.

Experimental conditions are shown in Table 3.2. Mean wall shear stress is evaluated from the measured wall shear stresses. Five experiments are conducted in this study. The cases CR01Ex, CR02Ex, and CR03Ex have the floodplain height of 0.16 m and the cases CR11Ex and CR12Ex have the floodplain height of 0.12 m. The conditions of geometry and water elevation are shown from Figure 3.16 to 3.20.

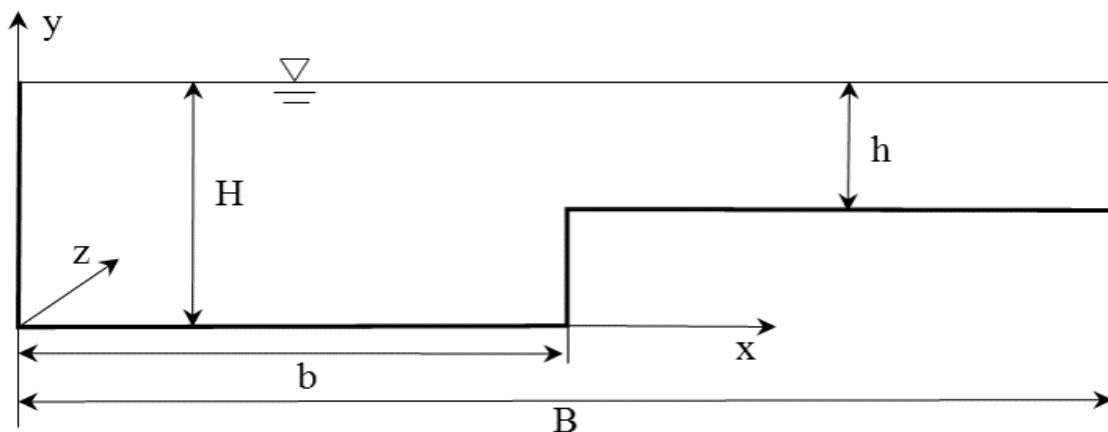


Figure 3.15 Schematic description of floodplain open channel flow.

Table 3.2 Experimental conditions

Case	H (m)	h (m)	h/H	Mean velocity (m/sec)	Mean Wall shear (N/m ²)	Re
CR01Ex	0.191	0.031	0.16	0.231	0.908	95,488
CR02Ex	0.304	0.144	0.47	0.170	0.471	112,009
CR03Ex	0.366	0.286	0.78	0.175	0.448	133,053
CR11Ex	0.180	0.060	0.33	0.231	1.572	96,417
CR12Ex	0.240	0.120	0.50	0.335	0.857	185,538

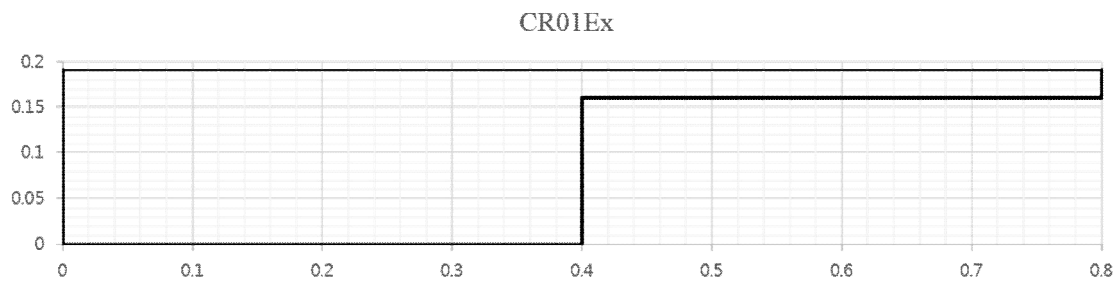


Figure 3.16 Geometry and water elevation of the case CR01Ex.

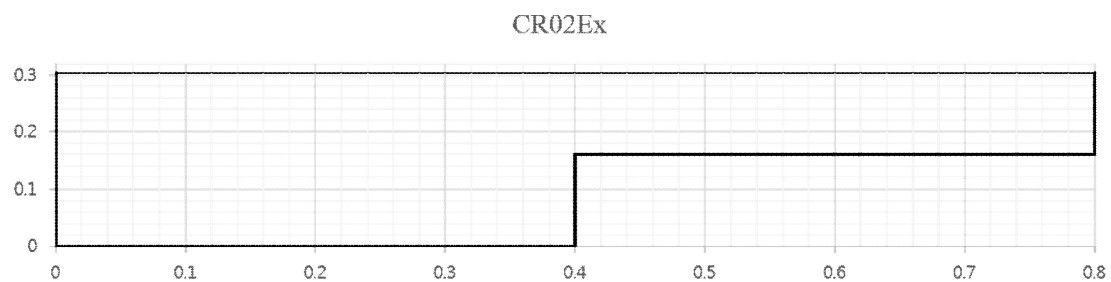


Figure 3.17 Geometry and water elevation of the case CR02Ex.

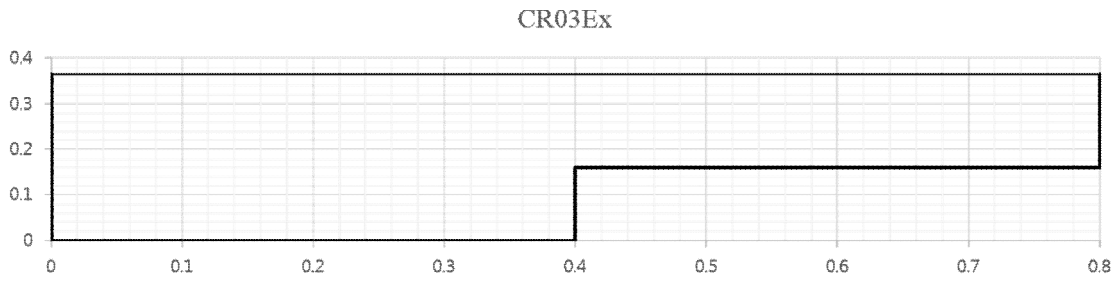


Figure 3.18 Geometry and water elevation of the case CR03Ex.

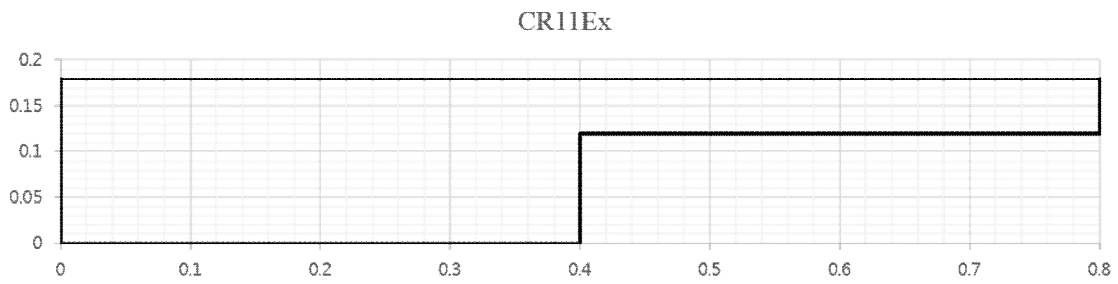


Figure 3.19 Geometry and water elevation of the case CR11Ex.

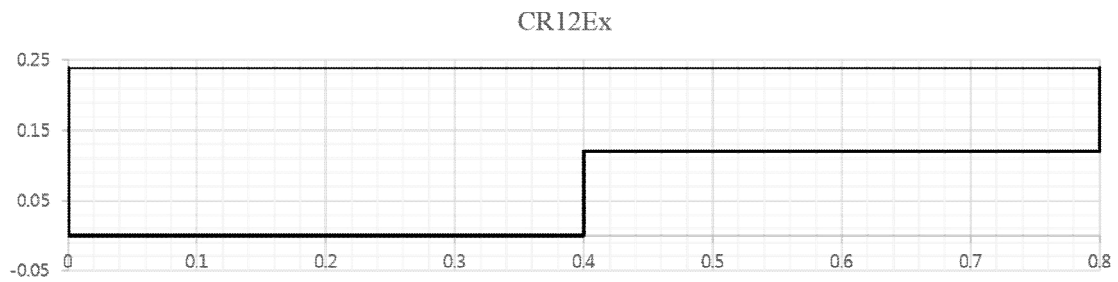


Figure 3.20 Geometry and water elevation of the case CR12Ex.

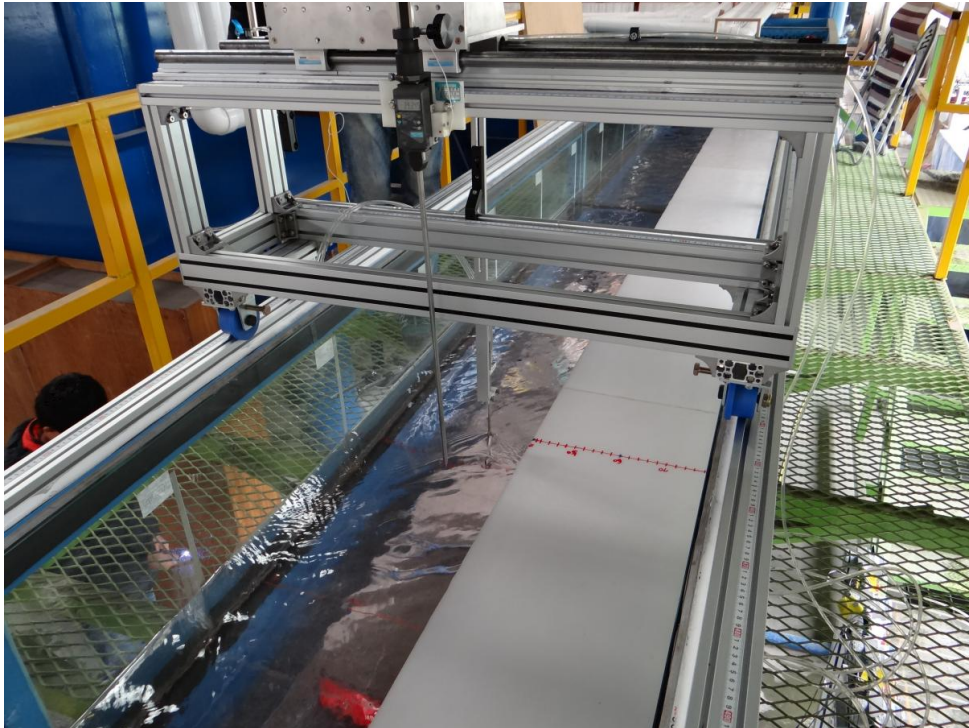


Figure 3.21 Experiment in the compound open channel (CR01Ex).

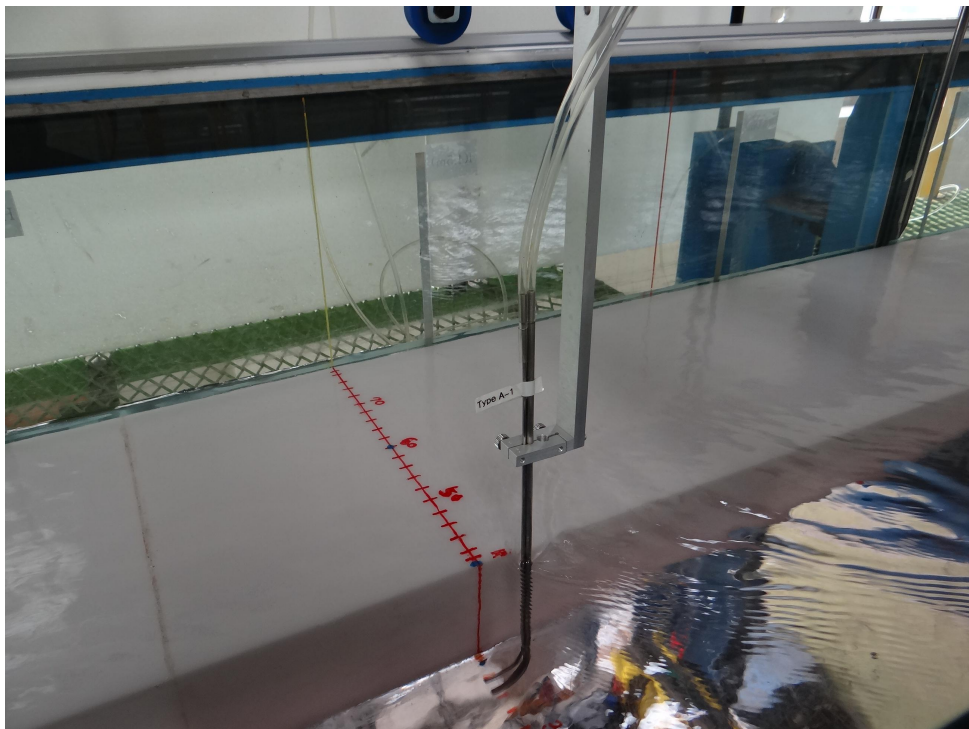


Figure 3.22 Experiment in the compound open channel (CR11Ex).

3.3.2 Experimental Results

Wall shear stresses are measured by the calibrated Preston tube and the measured wall shear stresses are presented from Table 3.3 to Table 3.7. The wall shear stress distributions normalized by the average wall shear stress are shown from Figure 3.23 to 3.27. The average wall shear stress is calculated by averaging all measured shear stresses because the measurement is conducted at the uniform distributed points.

In CR01Ex case ($h/H = 0.16$) overall distribution of the wall shear stress appears that high shear stresses are seen in the main channel and low shear stresses are seen in the floodplain. Normalized average values in the main channel and the floodplain are 1.27 and 0.71, respectively. Maximum value is seen near the middle of the main channel with 1.55 and relatively low values are seen at the 0.12 m and 0.28 in the main channel. In the junction of the floodplain and the main channel, normalized shear stress is 0.98 and the value decrease to 0.79 along the lateral distance.

In CR02Ex case ($h/H = 0.47$) overall distribution of the wall shear stress appears that little high shear stresses are seen in the main channel and little low shear stresses are seen in the floodplain, however, the difference is small. Normalized average values in the main channel and the floodplain are 1.01 and 0.99, respectively. Maximum value is seen near the middle of the main channel with 1.22 and relatively low values are seen at the 0.12 m and 0.28 in the main channel. In the junction of the floodplain and the main channel, normalized shear stress is 1.03 and the value decrease slightly to 0.79 along the lateral distance.

In CR03Ex case ($h/H = 0.78$) overall distribution of the wall shear stress appears similar to CR02Ex case that little high shear stresses are seen in the main channel and little low shear stresses are seen in the floodplain. Normalized average values in the main channel and the floodplain are same values with 1.00. Maximum value is seen near the middle of the main channel with 1.20 and relatively low values are seen at the 0.08 m in the main channel. In the junction of the floodplain and the main channel,

normalized shear stress is 1.01 and the value decrease slightly to 0.88 along the lateral distance.

In CR11Ex case ($h/H = 0.33$) overall distribution of the wall shear stress appears that little high shear stresses are seen in the main channel and little low shear stresses are seen in the floodplain. Normalized average values in the main channel and the floodplain are 1.03 and 0.96, respectively. Maximum value is seen near the middle of the main channel with 1.34 and relatively low values are seen at the 0.10 m in the main channel. In the junction of the floodplain and the main channel, normalized shear stress is 1.25 and the value decrease to 0.65 along the lateral distance.

In CR11Ex case ($h/H = 0.50$) overall distribution of the wall shear stress appears that little high shear stresses are seen in the floodplain and little low shear stresses are seen in the main channel. Normalized average values in the main channel and the floodplain are 0.98 and 1.02, respectively. The Maximum value is seen near the junction of the floodplain with 1.41 and the maximum value in the main channel is 1.24. Normalized shear stress in the floodplain decrease to 0.66 along the lateral distance.

The experimental results show the general tendency with depth ratio increase that normalized wall shear stress in the floodplain increases with depth ratio increase. Average values of the main channel and floodplain are similar over the depth ratio of 0.33. Maximum values are seen in the main channel excluding the CR12Ex case.

The results are compared with Tominaga and Nezu (1991) from Figure 3.28 to Figure 3.30. In the depth ratio of 0.25 and 0.50 present experiments show the good agreement with Tominaga and Nezu's experiments. However, In the depth ration of 0.75, lager difference in the floodplain is seen from the comparison. Present experiment shows the low shear stresses in the floodplain and Tominaga and Nezu's experiment shows much higher values in the floodplain. It may be due to the difference of the experimental condition and measuring method, expecially difference in Reynolds number.

Table 3.3 Experimental result of wall shear stress (CR01Ex).

Lateral distance (m)	Pressure difference (mm)	Measured wall shear stress (N/m ²)	Normalized wall shear stress
0.00	3.47	2.53	0.80
0.01	4.58	4.40	1.06
0.02	5.31	5.92	1.23
0.04	5.25	5.78	1.21
0.06	5.80	7.05	1.34
0.08	5.85	7.17	1.35
0.10	6.34	8.42	1.46
0.12	5.56	6.48	1.28
0.14	5.52	6.38	1.27
0.16	6.71	9.45	1.55
0.18	6.21	8.09	1.43
0.20	6.12	7.85	1.41
0.22	6.07	7.74	1.40
0.24	6.20	8.07	1.43
0.26	6.05	7.69	1.40
0.28	5.48	6.30	1.27
0.30	6.05	7.67	1.40
0.32	5.86	7.20	1.35
0.34	5.85	7.17	1.35
0.36	5.88	7.24	1.36
0.38	5.02	5.28	1.16
0.39	4.22	3.73	0.97
0.40	3.59	2.70	0.83
0.40	4.23	3.75	0.98
0.41	4.11	3.54	0.95
0.42	4.26	3.81	0.98
0.44	3.80	3.03	0.88
0.46	3.58	2.69	0.83
0.48	3.42	2.46	0.79
0.50	3.37	2.38	0.78
0.52	3.15	2.08	0.73
0.54	3.07	1.98	0.71
0.56	3.02	1.91	0.70
0.58	3.03	1.92	0.70
0.60	2.74	1.58	0.63
0.62	2.85	1.71	0.66
0.64	2.88	1.74	0.66
0.66	2.72	1.55	0.63
0.68	2.78	1.62	0.64
0.70	2.69	1.51	0.62
0.72	2.71	1.54	0.63
0.74	2.60	1.42	0.60
0.76	2.49	1.30	0.57
0.78	2.27	1.08	0.53
0.79	2.11	0.93	0.49

Table 3.4 Experimental result of wall shear stress (CR02Ex).

Lateral distance (m)	Pressure difference (mm)	Measured wall shear stress (N/m ²)	Normalized wall shear stress
0.00	1.50	0.47	0.67
0.01	2.01	0.85	0.90
0.02	2.25	1.06	1.00
0.04	2.02	0.86	0.90
0.06	2.22	1.03	0.99
0.08	2.23	1.04	0.99
0.10	2.21	1.02	0.98
0.12	2.37	1.17	1.05
0.14	2.43	1.24	1.08
0.16	2.58	1.39	1.15
0.18	2.56	1.38	1.14
0.20	2.72	1.55	1.21
0.22	2.29	1.10	1.02
0.24	2.73	1.57	1.22
0.26	2.69	1.52	1.20
0.28	2.30	1.11	1.02
0.30	2.73	1.56	1.21
0.32	2.44	1.25	1.09
0.34	2.28	1.09	1.01
0.36	2.00	0.84	0.89
0.38	2.05	0.88	0.91
0.39	2.09	0.91	0.93
0.40	1.70	0.61	0.76
0.40	2.32	1.13	1.03
0.41	2.25	1.07	1.00
0.42	2.53	1.34	1.13
0.44	2.49	1.30	1.11
0.46	2.23	1.04	0.99
0.48	2.39	1.19	1.06
0.50	2.41	1.22	1.07
0.52	2.26	1.07	1.00
0.54	2.29	1.10	1.02
0.56	2.36	1.16	1.05
0.58	2.28	1.09	1.01
0.60	2.24	1.05	0.99
0.62	2.26	1.07	1.01
0.64	2.13	0.95	0.95
0.66	2.19	1.01	0.97
0.68	2.03	0.86	0.90
0.70	1.93	0.78	0.86
0.72	2.07	0.90	0.92
0.74	2.15	0.97	0.95
0.76	2.06	0.89	0.92
0.78	2.09	0.92	0.93
0.79	1.83	0.70	0.81

Table 3.5 Experimental result of wall shear stress (CR03Ex).

Lateral distance (m)	Pressure difference (mm)	Measured wall shear stress (N/m ²)	Normalized wall shear stress
0.00	1.53	0.49	0.72
0.01	1.91	0.77	0.90
0.02	1.66	0.58	0.78
0.04	2.01	0.85	0.94
0.06	2.19	1.01	1.03
0.08	1.89	0.75	0.89
0.10	2.24	1.06	1.05
0.12	2.26	1.08	1.06
0.14	2.33	1.14	1.09
0.16	2.49	1.30	1.17
0.18	2.33	1.13	1.09
0.20	2.42	1.23	1.13
0.22	2.47	1.28	1.16
0.24	2.39	1.20	1.12
0.26	2.24	1.05	1.05
0.28	2.55	1.37	1.20
0.30	2.24	1.05	1.05
0.32	2.42	1.23	1.14
0.34	2.11	0.93	0.99
0.36	2.08	0.91	0.98
0.38	1.92	0.77	0.90
0.39	1.91	0.77	0.90
0.40	1.67	0.59	0.78
0.40	2.16	0.98	1.01
0.41	2.11	0.94	0.99
0.42	2.27	1.08	1.06
0.44	2.33	1.13	1.09
0.46	2.38	1.19	1.12
0.48	2.14	0.96	1.00
0.50	2.37	1.18	1.11
0.52	2.22	1.04	1.04
0.54	2.03	0.86	0.95
0.56	2.12	0.95	1.00
0.58	2.11	0.93	0.99
0.60	2.21	1.02	1.03
0.62	2.20	1.01	1.03
0.64	2.12	0.95	1.00
0.66	2.24	1.05	1.05
0.68	2.11	0.94	0.99
0.70	1.98	0.82	0.93
0.72	1.92	0.77	0.90
0.74	1.98	0.82	0.93
0.76	1.95	0.80	0.91
0.78	1.93	0.78	0.90
0.79	1.89	0.75	0.88

Table 3.6 Experimental result of wall shear stress (CR11Ex).

Lateral distance (m)	Pressure difference (mm)	Measured wall shear stress (N/m ²)	Normalized wall shear stress
0.00	4.23	3.75	0.56
0.01	5.50	6.35	0.73
0.02	6.52	8.93	0.87
0.04	6.93	10.07	0.92
0.06	6.97	10.19	0.93
0.08	7.07	10.49	0.94
0.10	6.08	7.75	0.81
0.12	7.07	10.47	0.94
0.14	8.48	15.10	1.13
0.16	8.46	15.01	1.13
0.18	9.34	18.31	1.25
0.20	9.23	17.88	1.23
0.22	8.90	16.63	1.19
0.24	9.49	18.90	1.27
0.26	9.96	20.78	1.33
0.28	10.05	21.19	1.34
0.30	9.38	18.46	1.25
0.32	9.29	18.10	1.24
0.34	8.90	16.60	1.19
0.36	8.64	15.64	1.15
0.38	6.96	10.15	0.93
0.39	6.53	8.94	0.87
0.40	4.23	3.75	0.56
0.40	9.40	18.52	1.25
0.41	9.04	17.13	1.21
0.42	8.32	14.51	1.11
0.44	8.63	15.63	1.15
0.46	7.96	13.30	1.06
0.48	7.81	12.79	1.04
0.50	7.78	12.70	1.04
0.52	7.70	12.44	1.03
0.54	6.87	9.89	0.92
0.56	7.78	12.70	1.04
0.58	7.45	11.64	0.99
0.60	7.61	12.16	1.02
0.62	7.50	11.80	1.00
0.64	7.30	11.18	0.97
0.66	7.21	10.91	0.96
0.68	6.83	9.77	0.91
0.70	6.63	9.22	0.88
0.72	6.53	8.94	0.87
0.74	5.48	6.29	0.73
0.76	5.51	6.36	0.73
0.78	4.91	5.06	0.66
0.79	4.87	4.97	0.65

Table 3.7 Experimental result of wall shear stress (CR12Ex).

Lateral distance (m)	Pressure difference (mm)	Measured wall shear stress (N/m ²)	Normalized wall shear stress
0.00	2.21	1.03	0.54
0.01	3.34	2.34	0.82
0.02	3.73	2.92	0.91
0.04	3.10	2.02	0.76
0.06	3.51	2.58	0.86
0.08	3.50	2.58	0.86
0.10	3.54	2.63	0.87
0.12	3.85	3.10	0.94
0.14	4.28	3.84	1.05
0.16	4.39	4.05	1.07
0.18	4.73	4.68	1.16
0.20	4.53	4.30	1.11
0.22	4.56	4.36	1.12
0.24	4.99	5.21	1.22
0.26	4.80	4.82	1.17
0.28	4.95	5.13	1.21
0.30	5.07	5.38	1.24
0.32	4.66	4.55	1.14
0.34	4.49	4.22	1.10
0.36	4.24	3.76	1.04
0.38	3.80	3.03	0.93
0.39	3.34	2.34	0.82
0.40	2.21	1.03	0.54
0.40	5.59	6.56	1.37
0.41	5.49	6.33	1.34
0.42	5.74	6.92	1.41
0.44	5.44	6.20	1.33
0.46	4.80	4.83	1.17
0.48	5.58	6.53	1.36
0.50	4.70	4.63	1.15
0.52	5.01	5.27	1.23
0.54	4.54	4.31	1.11
0.56	4.49	4.23	1.10
0.58	4.12	3.56	1.01
0.60	4.05	3.44	0.99
0.62	4.09	3.51	1.00
0.64	3.77	2.98	0.92
0.66	3.28	2.25	0.80
0.68	3.47	2.52	0.85
0.70	3.11	2.03	0.76
0.72	3.13	2.06	0.77
0.74	3.17	2.11	0.78
0.76	2.96	1.83	0.72
0.78	2.89	1.75	0.71
0.79	2.70	1.53	0.66

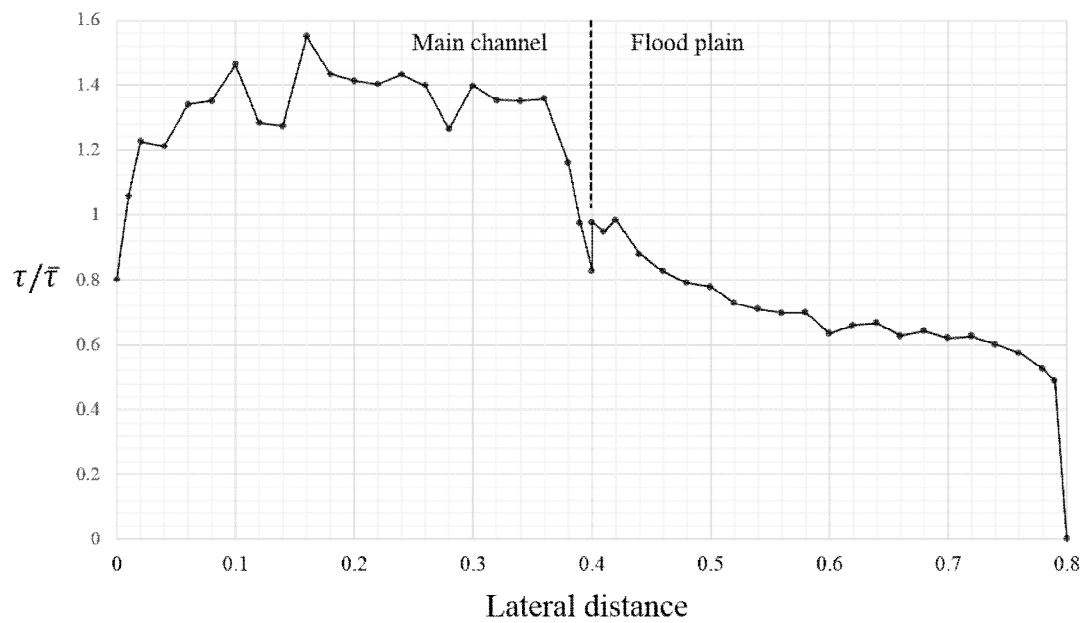


Figure 3.23 Results in the compound open channel (CR01Ex).

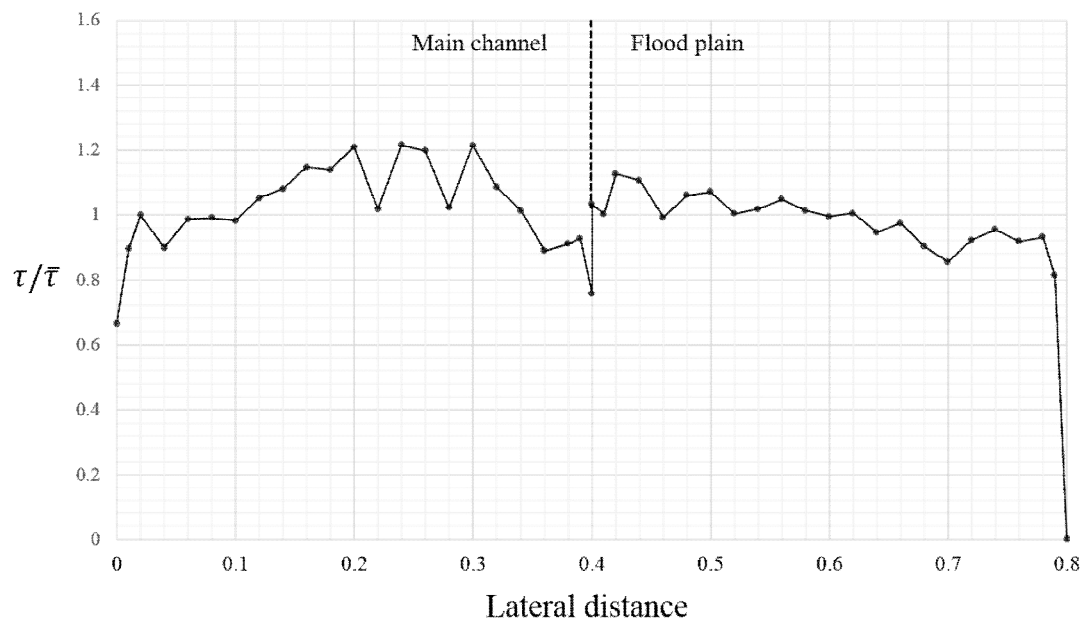


Figure 3.24 Results in the compound open channel (CR02Ex).

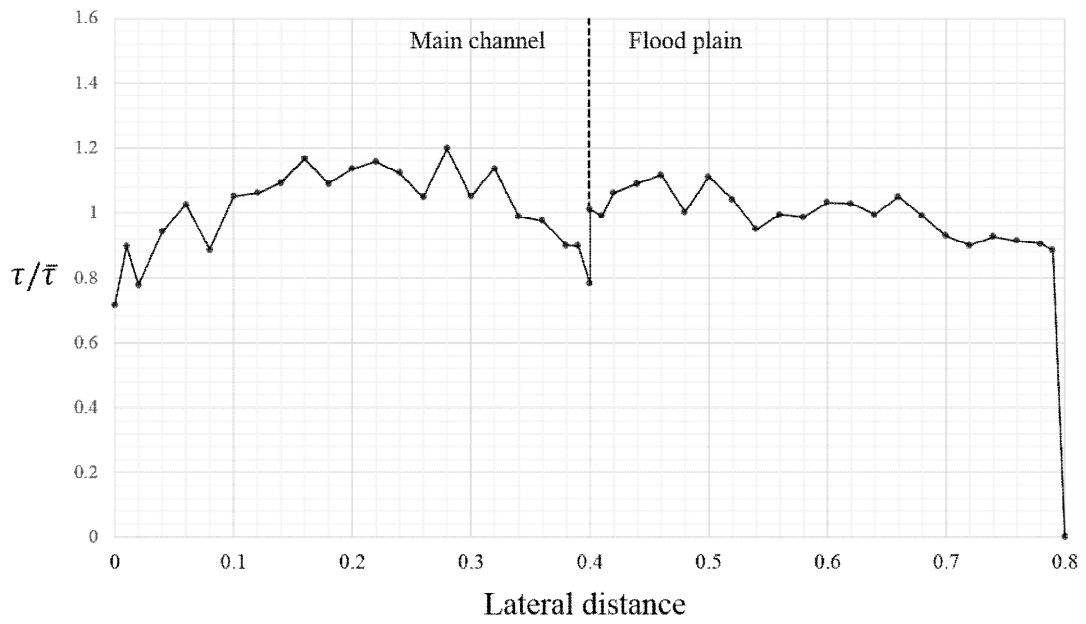


Figure 3.25 Results in the compound open channel (CR03Ex).

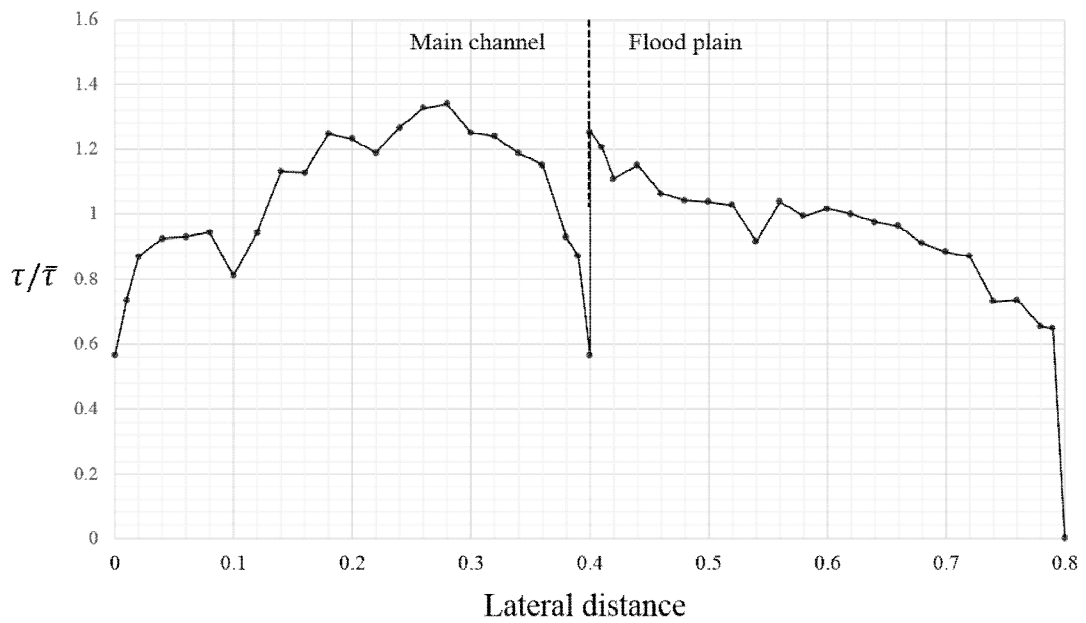


Figure 3.26 Results in the compound open channel (CR11Ex).

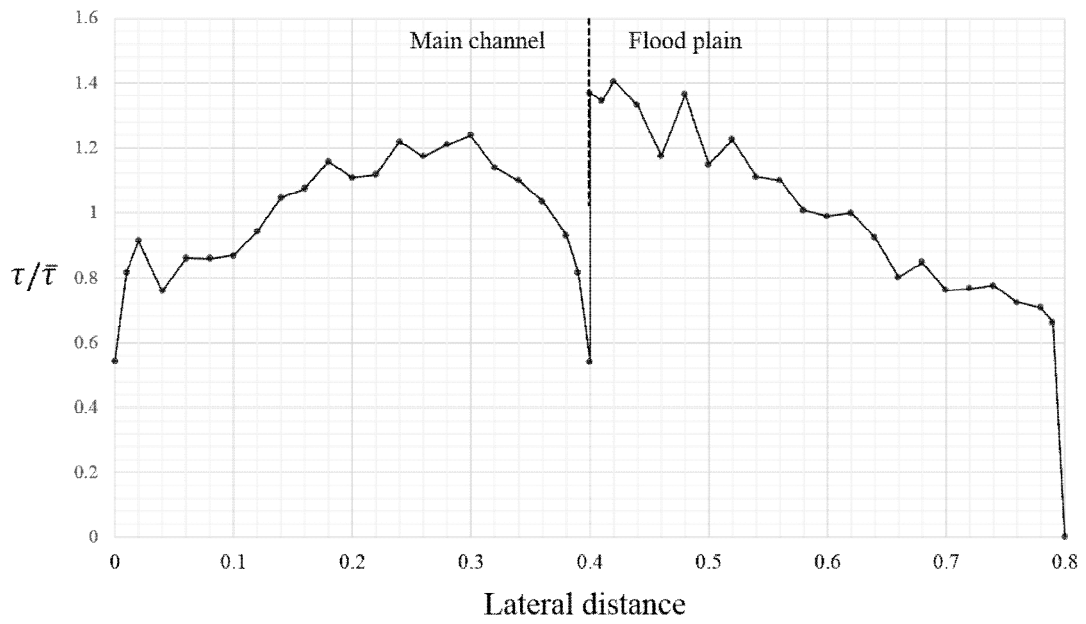


Figure 3.27 Results in the compound open channel (CR12Ex).

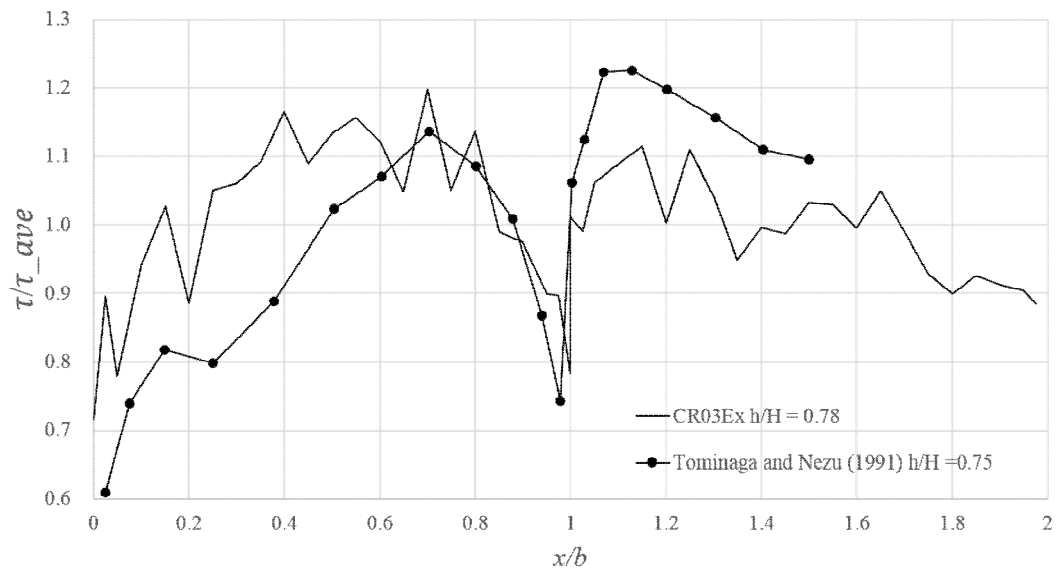


Figure 3.28 Comparison with Tominaga and Nezu ($h/H = 0.75$).

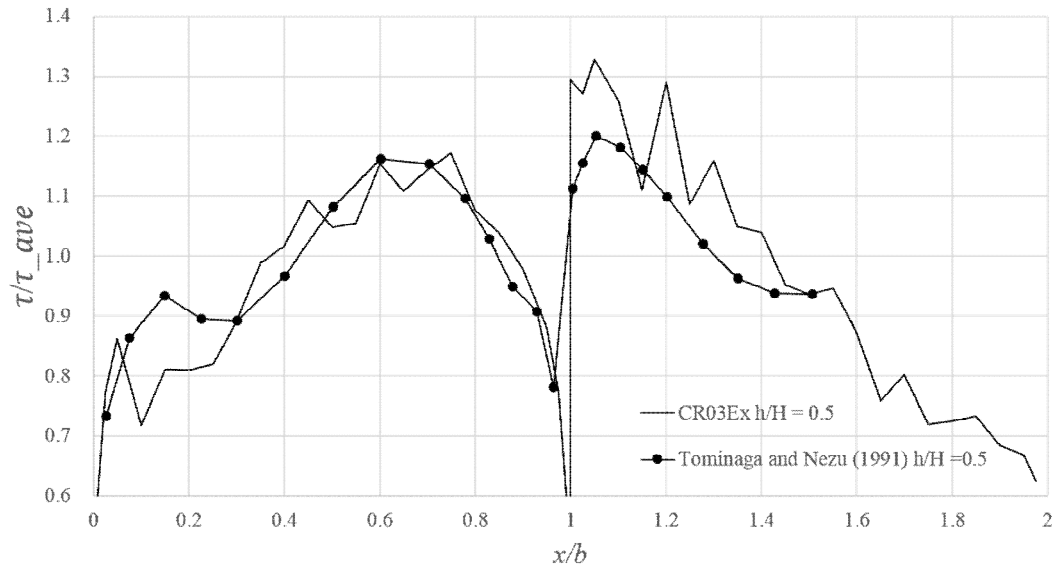


Figure 3.29 Comparison with Tominaga and Nezu ($h/H = 0.5$).

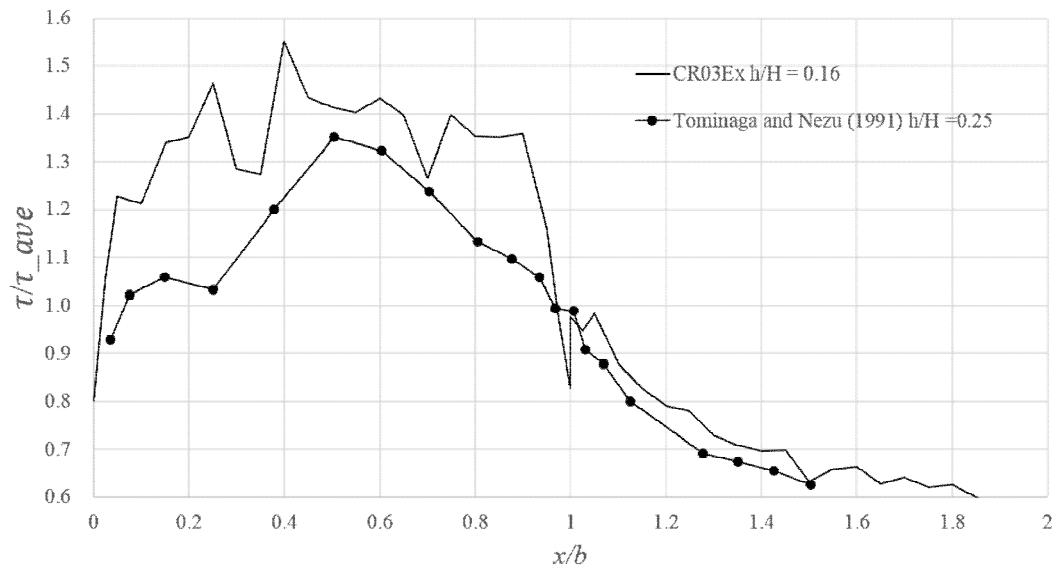


Figure 3.30 Comparison with Tominaga and Nezu ($h/H = 0.25$).

CHAPTER 4

NUMERICAL SIMULATION OF COMPOUND OPEN CHANNEL

4.1 Verification of OpenFOAM Model in Compound Open Channel

4.1.1 Numerical Setup

The LES code of OpenFOAM is used in this study solving the filtered continuity and momentum equations for incompressible flow on a Cartesian grid with the finite volume method. The one equation sub grid scale model is employed to calculate the SGS eddy viscosity.

The numerical model setup was chosen to correspond to the experiments by Tominaga and Nezu (1991), thereby allowing for the validation of sub grid modelling of the OpenFOAM's LES method for the compound open channel flows. Three different floodplain depths were considered with cases of $h/H = 0.75$, 0.5 and 0.25 that are smooth cases of the Tominaga and Nezu (1991) where h is the variable floodplain depth and H is the main channel depth of 0.080 m. The main channel width $B = 0.20$ m and the floodplain width were equal and B/H is constant with 2.5 . Schematic and variables of the cases are presented as Figure 4.1. The Reynolds numbers $Re = 4U_b R/\nu$ based on the bulk(or average) velocity $U_b = Q/A$ and the hydraulic radius R were $67,200$, $54,500$, and $45,600$. respectively as shown in Table 4.1.

Figure 4.2 shows the computational setup and the boundary conditions for $h/H = 0.5$. The length of the domain in the streamwise direction is $6H$ that is nearly the recommended value of $2\pi H$ for straight smooth channels. This ensures the capture of all relevant large-scale turbulence structures confirmed by two-point correlations. In LES, the flow is statistically homogeneous in the streamwise direction and cyclic boundary conditions are employed in this direction. For smooth walls, the no-slip wall boundary condition is used. The free surface is set as a frictionless rigid lid treated as a plane of

symmetry.

Table 4.1 Verification cases and flow conditions (Tominaga and Nezu 1991)

Case	Main channel Depth(mm)	Floodplain depth(mm)	Maximum velocity (m/s)	Friction velocity (m/s)	Mean velocity (m/s)	Reynolds Re
S1	80.3	60.3	0.409	0.0164	0.368	67,200
S2	80.0	40.0	0.389	0.0164	0.349	54,500
S3	80.5	20.5	0.358	0.0141	0.288	45,600

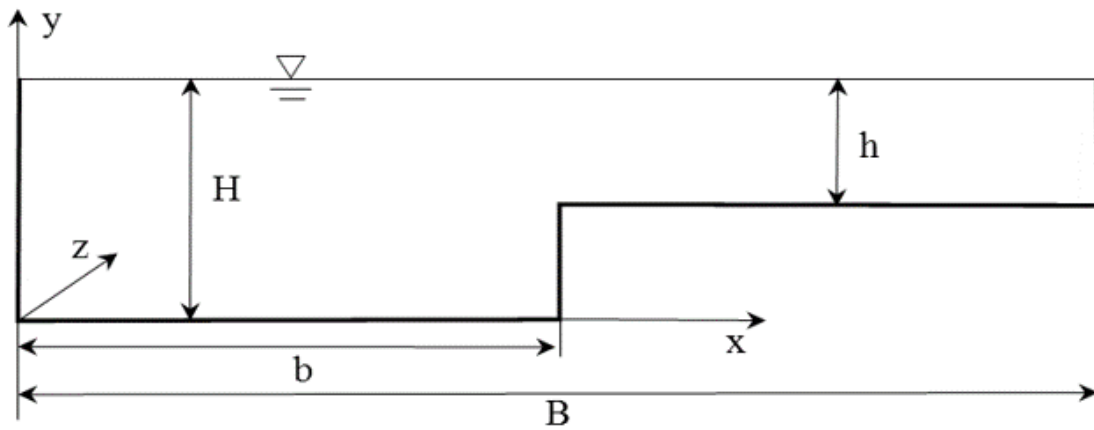


Figure 4.1 Schematic of compound open channels.

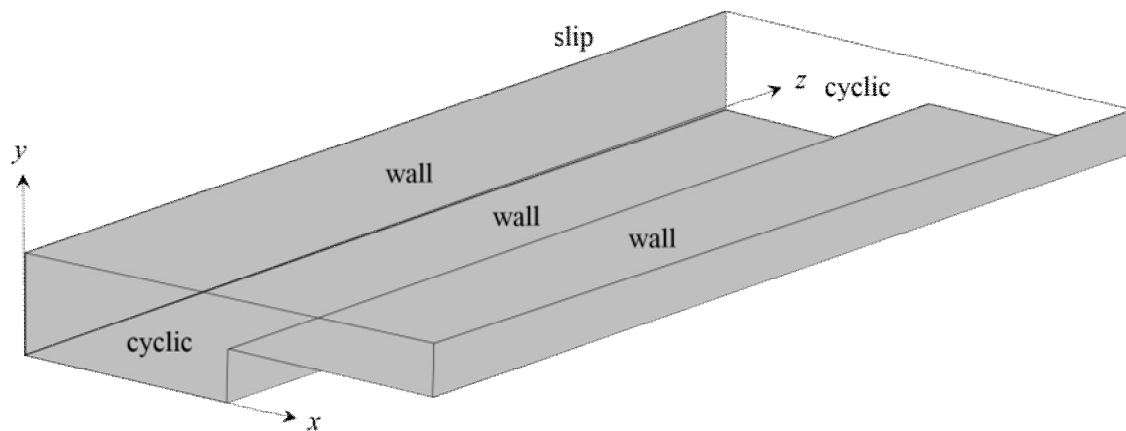


Figure 4.2 Computational setup and boundary conditions for LES.

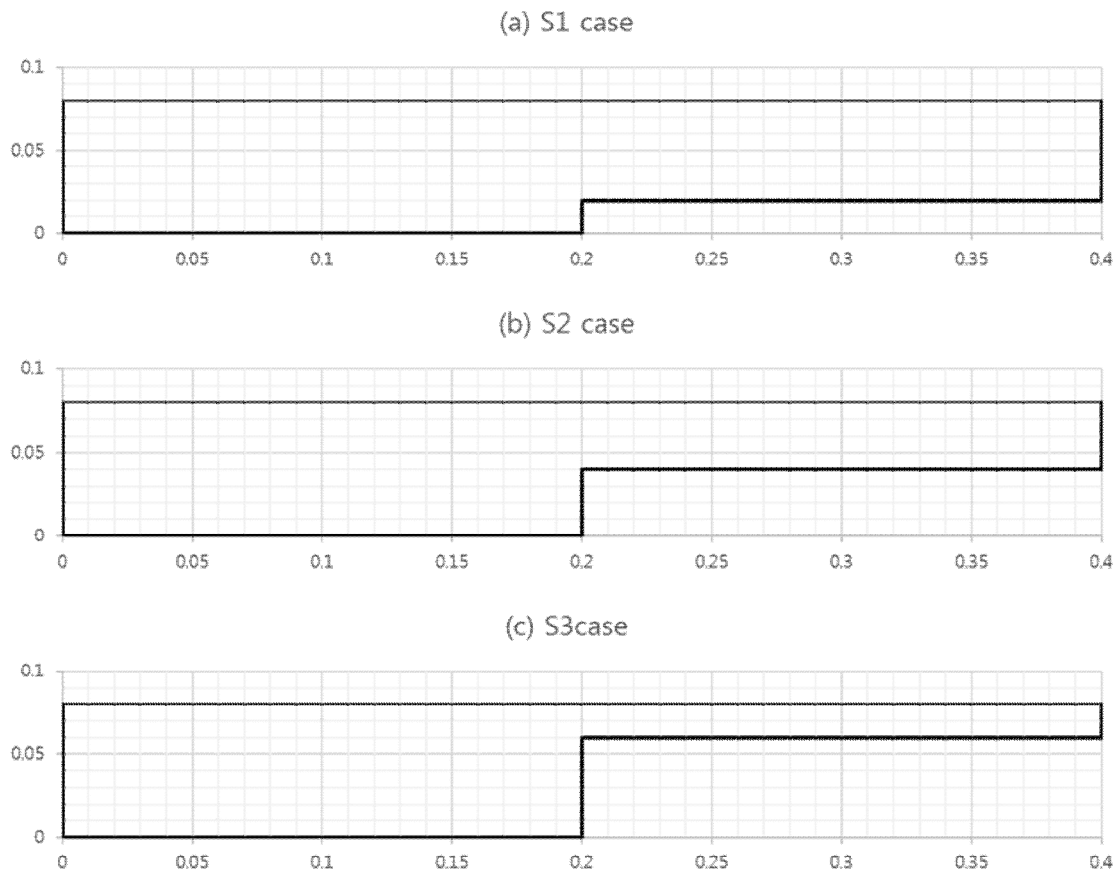


Figure 4.3 Geometry of compound channels in verification tests.

Geometry of the cases in cross sectional plane are shown as Figure 4.3. The computational domain is discretized with a fine non-uniform grid in x and y direction and a fine uniform grid in z direction (Figure 4.4 and Figure 4.5). Non-uniform grid is used in near region of the walls and interface of main channel and floodplain. This combination of non-uniform grid and uniform grid enables the efficient computation of small eddies near the walls and enhances the accuracy of the simulation.

The domain is composed of three sub domains that are lower main channel, upper main channel and floodplain (Figure 4.5). Discretization summary of the computational domains in the three cases is presented as Table 4.2. In S1 case, the domain is discretized with $64 \times 24 \times 128$ grid points for the lower main channel, $64 \times 32 \times 128$ grid points for the upper main channel and $64 \times 32 \times 128$ grid points for the floodplain in the

lateral (x), vertical (y), and streamwise (z) directions, respectively. The corresponding grid spacing in wall units are provided in Table 4.3.



Figure 4.4 Discretization of the computation domain (S2 case).

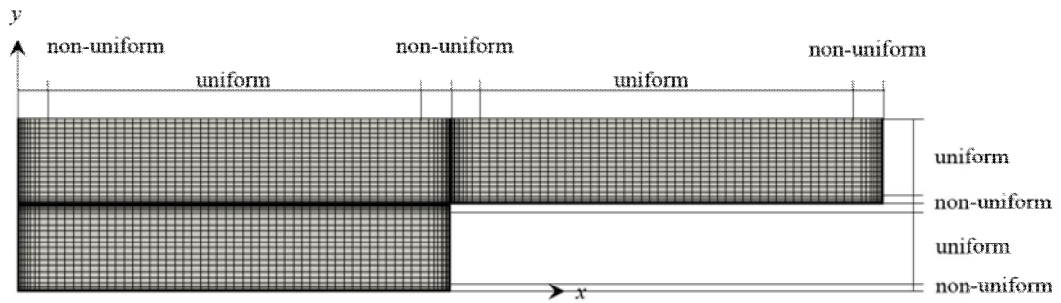


Figure 4.5 Composition of cross sectional grid points (S2 case).

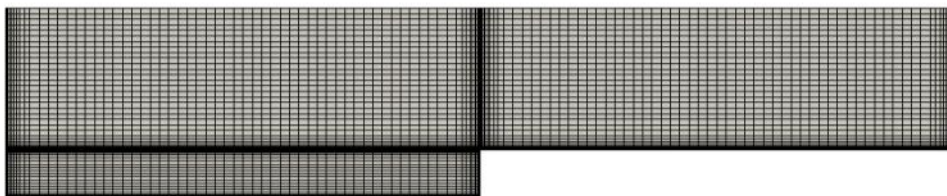


Figure 4.6 Composition of cross sectional grid points (S1 case).

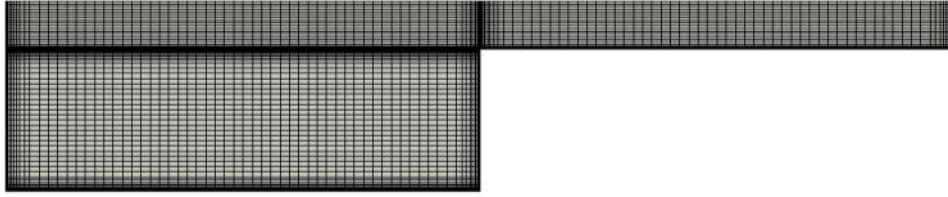


Figure 4.7 Composition of cross sectional grid points (S3 case).

Table 4.2 Domain discretization in verification tests.

Case	Discretization ($\Delta x \times \Delta y \times \Delta z$)			Grid points			
	Lower main channel	Upper main channel	Floodplain	Lower main channel	Upper main channel	Flood plain	Total
S1	64×24×128	64×32×128	64×32×128	196,608	262,144	262,144	720,896
S2	64×24×128	64×22×128	64×22×128	196,608	180,224	180,224	557,056
S3	64×44×128	64×22×128	64×22×128	360,448	180,224	180,224	720,896

Table 4.3 Wall distances in verification tests.

Case	Lower main channel				Floodplain				Δz^+
	First grid		Max grid		First grid		Max grid		
	Δx^+	Δy^+	Δx^+	Δy^+	Δx^+	Δy^+	Δx^+	Δy^+	
S1	5.7	1.9	54.7	43.7	5.7	4.3	34.3	25.5	61.5
S2	5.7	3.7	54.7	43.7	5.7	3.7	54.7	43.7	61.5
S3	4.9	2.5	47.0	37.6	4.9	1.6	47.0	37.6	52.9

The simulation is started an initial constant profile without any artificial turbulence field. It is integrated over time for about $160H/u_\tau$ keeping the convection Courant number $u\Delta t/\Delta x$ below 0.5. The flow is considered fully developed when the

successive values of the bed shear stress has converged and then run for another 30 H/u_τ to gather final turbulence statistics.

4.1.2 Results and Analysis

(1) Mean velocity distribution

Figure 4.8 to Figure 4.10 show simulated and measured isovel lines of the streamwise mean velocity U normalized by U_{\max} .

Measured data of S2 case (Figure 4.9 (b)) show that isovel lines bulge significantly upward in the vicinity of the junction edge along the inclined line that is formed by the strong secondary currents generated from the junction edge toward the free surface (Figure 4.12 (b)). The velocity in this edge region is decelerated due to momentum transport by the secondary currents away from the wall. On the both sides of this decelerated region, the isovel lines bulge toward the wall (the bed of the flood plain and the sidewall at the junction), due to high momentum transport by the secondary currents (Tominaga and Nezu 1991). The maximum velocity tends to appear below the free surface even in the central region of the main channel. The isovels near the junction in the case S1 bulge upward over a wide region. In spite of the large flow depth of the floodplain, the deceleration due to momentum transport from the junction edge extends to the free surface. Meanwhile the isovel lines for case S3 no longer bulge from the junction toward the free surface, but rather toward the sidewalls of the main channel in the same manner as with rectangular open channels. The velocity dip phenomenon becomes more remarkable as the value of h/H decrease.

The simulation results agree well with the experiments, especially in the main channel. The velocity bulge is observed in the simulation, but the intensity of the bulge is more weaker than measured data. It seems due to the effect of secondary flow. The formation of the secondary currents in the junction region is well agreed with the measured data, however, weakness of the magnitude of the secondary currents results

the more weak intensity of the velocity bulge. This velocity bulge is more pronounced in the deep floodplain cases, because the angle of inclination of the secondary vectors is smaller in the deep than in the shallow floodplain flow. The simulations slightly underestimate the secondary currents and consequent low velocity bulge and it is also founded other LES and RSM simulations (e.g. Thomas and Williams 1995, Kang and Choi 2006, Kara *et al.* 2011).

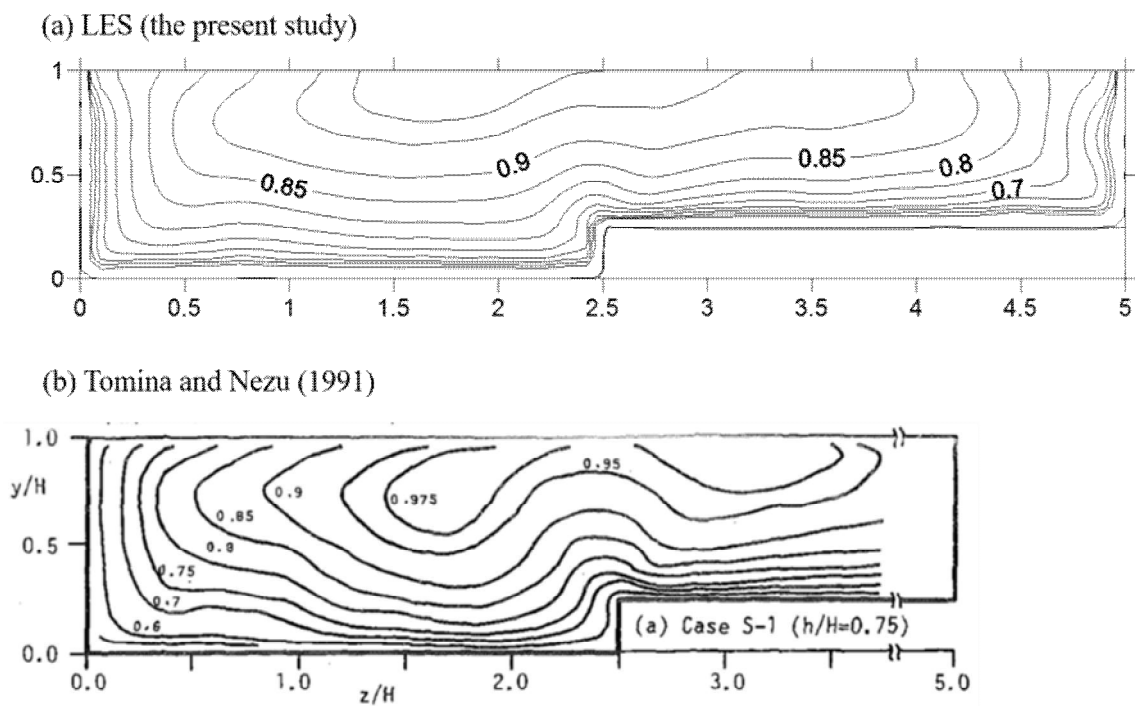


Figure 4.8 Streamwise mean velocity ($\overline{u}/\overline{u_{\max}}$) for S1 case.

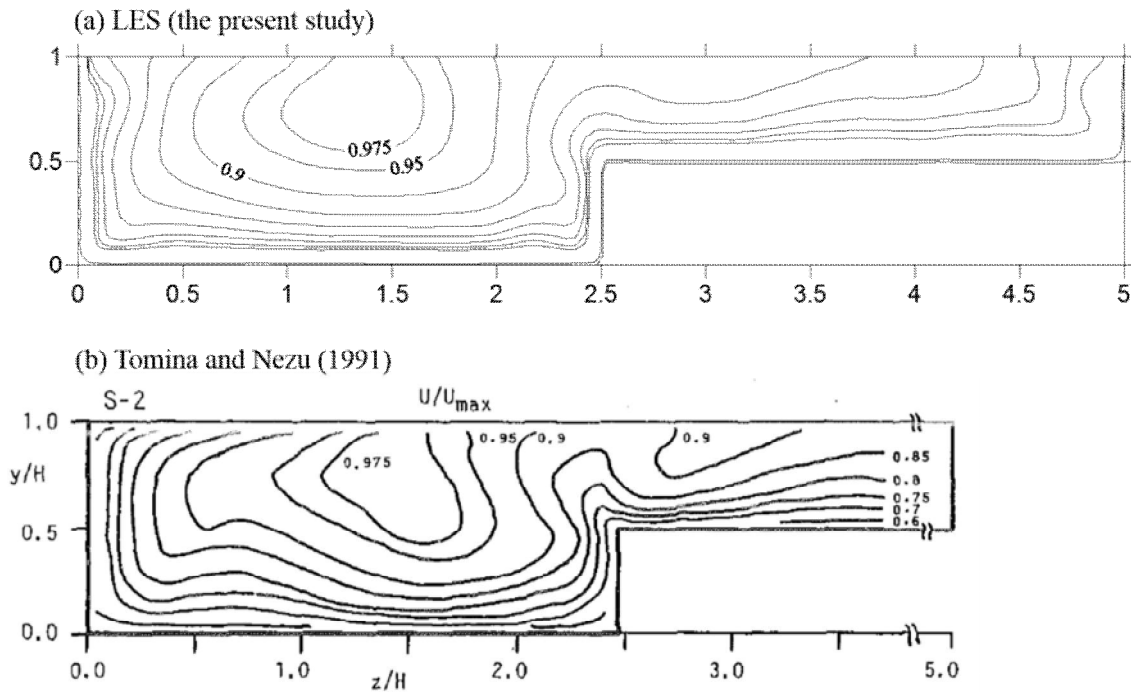


Figure 4.9 Streamwise mean velocity ($\overline{u}/\overline{u_{max}}$) for S2 case.

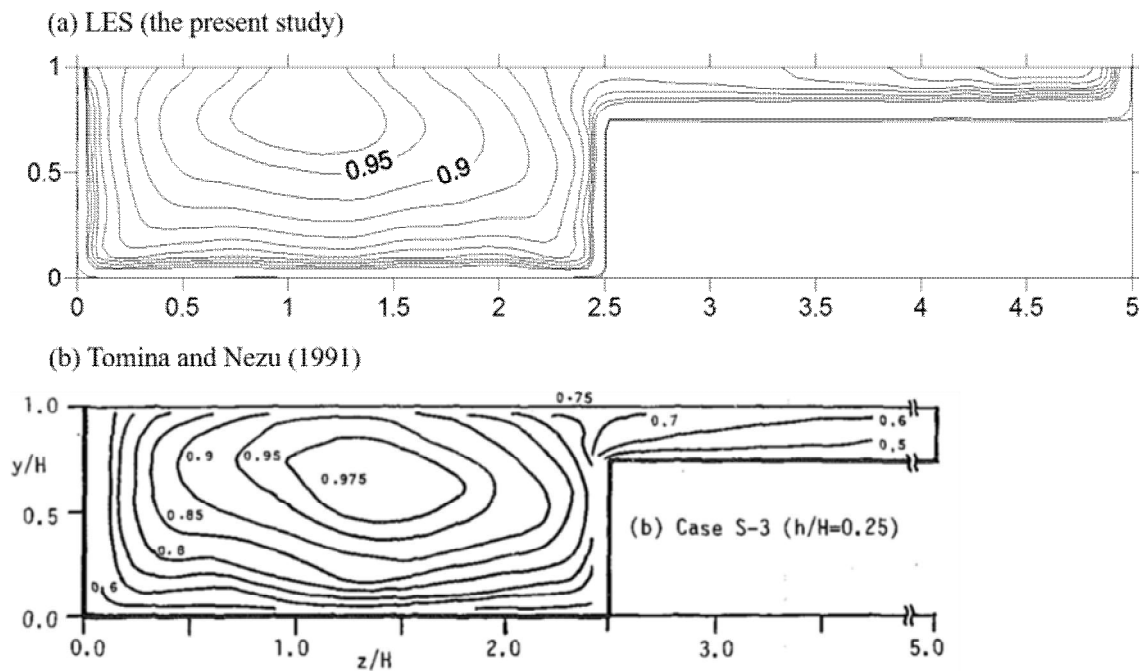


Figure 4.10 Streamwise mean velocity ($\overline{u}/\overline{u_{max}}$) for S3 case.

(2) Secondary flows

Figure 4.11 to Figure 4.13 show the vector description of the secondary flow in the case of S1, S2 and S3 compared with measured data.

Measured data show that the strong inclined secondary currents are generated from the junction of edge toward the free surface. The maximum magnitude of secondary flow is about 4% of U_{\max} . This value is slightly greater than the maximum magnitude of the secondary flow observed near the free surface in rectangular open channels, as indicated by Nezu and Rodi (1985), Tominaga *et al.* (1989), and Nezu *et al.* (1989), the magnitude is 2-3% of U_{\max} . A pair of outlines of secondary currents are recognized on both sides of the inclined upflow. These currents is known as longitudinal vortices. The vortex on the side of the floodplain is called the "floodplain vortex," whereas the vortex on the side of the main channel is called the "main-channel vortex." Both of the vortices reach the free surface and cover the junction region of $1.6 < z/H < 3.0$ in the spanwise direction.

In the sidewall region of the main channel ($z/H < 1.5$), a horizontal flow from the sidewall to the center of the main channel appears clearly at the free surface, and its flow forms the longitudinal vortex, the so-called free surface vortex. This free-surface vortex is generated because of the anisotropy of turbulence caused by the existence of the free surface and the sidewall, which have been observed by Nezu and Rodi (1985). Tominaga *et al.* (1989), and Nezu *et al.* (1989) in a rectangular open-channel. All of the mentioned researchers found that the spanwise scale of the free-surface vortex in rectangular open channels reaches about $2H$, when the aspect ratio B/H is greater than 5. Therefore, the free-surface vortex meets the main channel vortex at the central region of the main channel (i.e., at about $z/H = 1.6$). The bottom vortex, which exists in the corner of rectangular channels, can also be recognized in the region $z/H < 0.8$.

Overall the agreement of the simulated vortex with the measurements is satisfying. The difference in location and shape of the secondary cells may be a results of LES

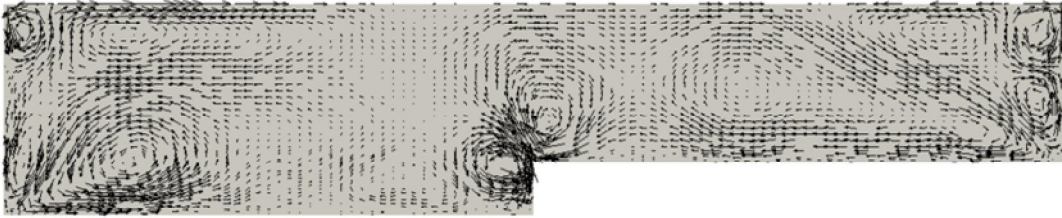
modelling (SGS modelling, rigid lid assumption) or due to flow development (finite domain in the experiment, infinite domain in the LES). In the measurement of case S2, five secondary vortex such as main channel vortex, floodplain vortex, free surface vortex, bottom vortex and junction bottom vortex are definitely observed. In the simulation, other vortex such as flood plain surface vortex and inner vortex are detected.

The size of the interface vortex pair at the junction is determined by the floodplain depth. The deeper the floodplain depth, the larger the floodplain vortex and the large the vortex in the main channel. Actually the floodplain depth controls the size and location of all vortex. It is natural to assume that flow structure is close to the rectangular open channel in the case of shallow floodplain depth and it is close to the wide rectangular open channel in the case of deep floodplain depth. In the case S3 (shallow floodplain depth), vortex formation in main channel is analogous to the vortex formation in the rectangular channel. The size of main channel vortex is larger in the S3 case and the size becomes smaller with floodplain depth increase. The interface in which the main channel vortex and free surface vortex meet moves toward to the floodplain with floodplain depth increase.

The main channel vortex size controls the size of the counter-rotating corner vortex (or junction bottom vortex) underneath. For the S3 case, the main channel vortex is flat and the junction bottom vortex is considerably larger than S1 and S2 cases.

The previous LES simulations of compound open channels haven't show the definite inner vortex near the side walls (side walls of main channel, junction edge, and floodplain). In the present LES simulations nonuniform grid is applied to refine the region near the bottom and side walls. Therefore the inner vortex can be captured in the present LES simulations. It is reasonable that the inner vortex exist near the side walls comparing with the vortex structure in the rectangular channels.

(a) LES (the present study)



(b) Tomina and Nezu (1991)

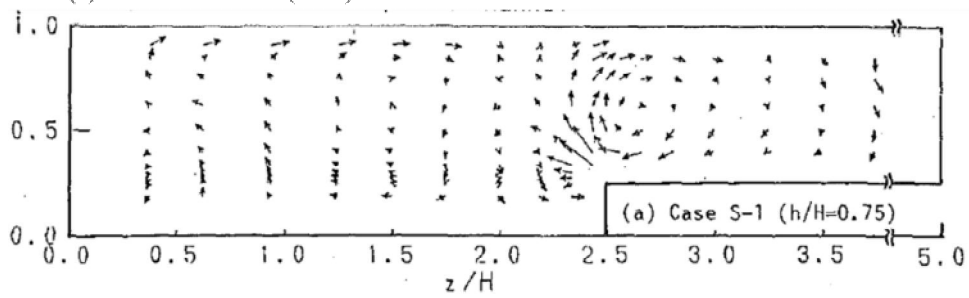
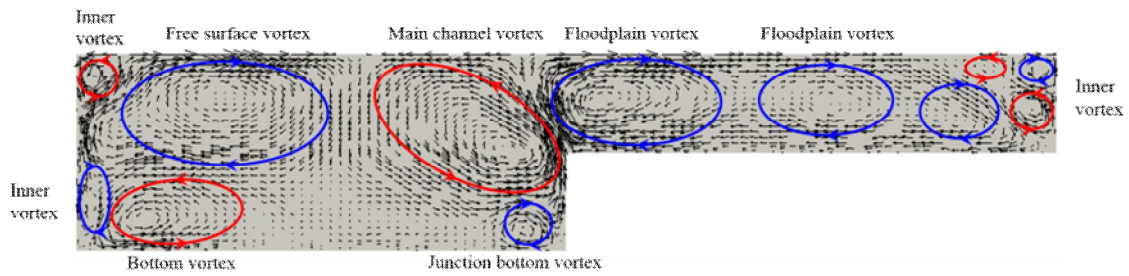


Figure 4.11 Secondary currents in S1.

(a) LES (the present study)



(b) Tominaga and Nezu (1991)

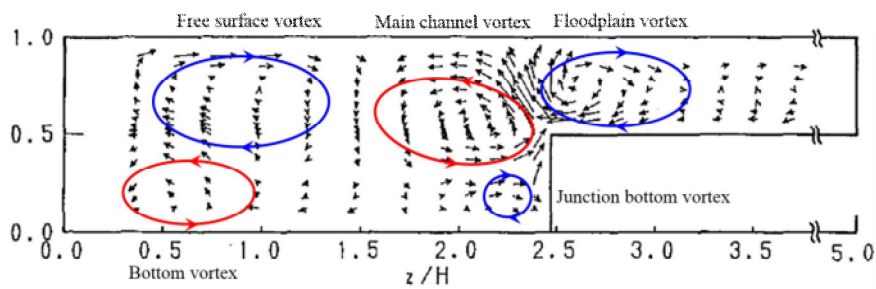
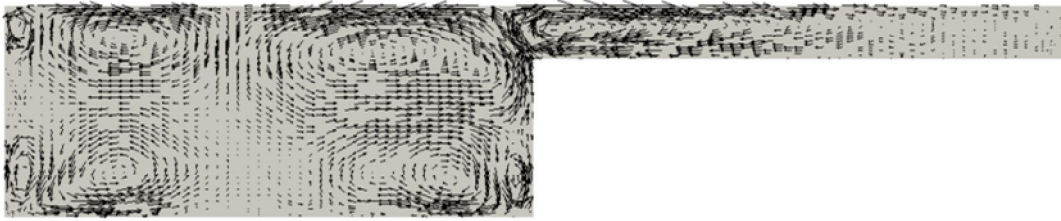


Figure 4.12 Secondary currents in S2.

(a) LES (the present study)



(b) Tominaga and Nezu (1991)

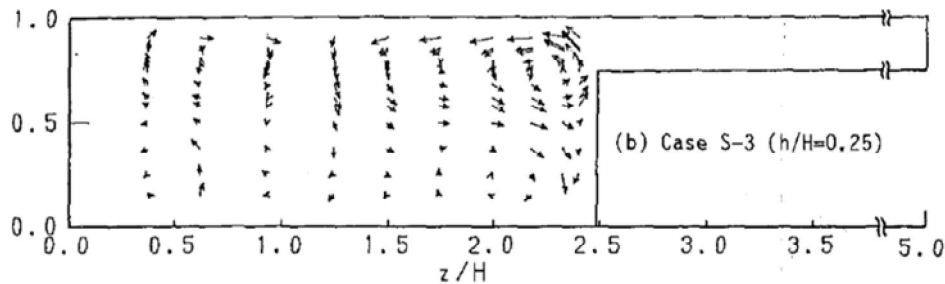


Figure 4.13 Secondary currents in S3.

(3) Turbulence statistics

Figures 4.14 to 4.16 show the isolines of three components of the root mean square (rms) turbulence intensities u' , v' , and w' , which are normalized by the averaged friction velocity \overline{U}_* in S2 case. The averaged friction velocity of the simulation is calculated from the wall shear stress distribution.

There is good qualitative agreement between the simulation and the measured data. The general shapes of the distributions of the turbulence intensity broadly follow that of the average streamwise velocity. However, the regions of greatest turbulent intensity occur at the sidewalls and bed surface. The influence of the free surface can be seen in that the streamwise and the lateral turbulence intensity are spread parallel to the surface whereas the vertical turbulence intensity reduce rapidly as the free surface is approached.

The streamwise component of the direct turbulent stress is a maximum in regions farthest from the submerged surfaces. This term constitutes the largest term in the turbulence intensity for the flow, but plays a relatively small part in the motion of fluid

to and from the flood plain. Fluctuations in the vertical velocity are associated with the relatively small scales generated at the vertical walls and peak in the near wall regions (Cater and Williams 2008).

All three components of turbulence intensity increase in the vicinity of the junction edge as expected, but the behavior of isolines of u' , v' , and w' somewhat differs. The isolines of u' seem to bulge from the junction edge in both the vertical and spanwise direction. On the other hand, the isolines of v' tend to bulge in the vertical direction in the main-channel region beside the junction, whereas those of w' tend to bulge in the lateral direction near the junction edge. This implies that the effect of convection due to the secondary currents on turbulence intensities is much more complicated than those of the primary mean energy. Consequently, the pattern of v' near the junction is quite different from that of w' . This means that the turbulence near the junction indicates a strong anisotropic behavior. Such significant differences in the distributions of u' , v' , and w' represent an anisotropic redistribution of turbulence energy into three components from mean flow energy (Tominaga and Nezu 1991).

Figure 4.17 shows the isolines of the difference between the normal stresses $(\overline{w'^2} - \overline{v'^2})$. The $(\overline{w'^2} - \overline{v'^2})$ represent anisotropy of turbulence and thus determine the structure of secondary currents driven by turbulence. The anisotropy in the main channel decreases with y/H increase and has the minimum at $y/H = 0.6-0.7$. Then, it increase again toward the free surface. This anisotropy of turbulence is known to generate the free surface vortex and bottom vortex (Tominaga *et al.* 1989, Nezu *et al.* 1989). The $(\overline{w'^2} - \overline{v'^2})$ becomes negative and shows the complicated behaviors near the junction coner. These behaviors are known to generate an inclined upflow in the same mechanism as the corner secondary current (Tominaga 1991).

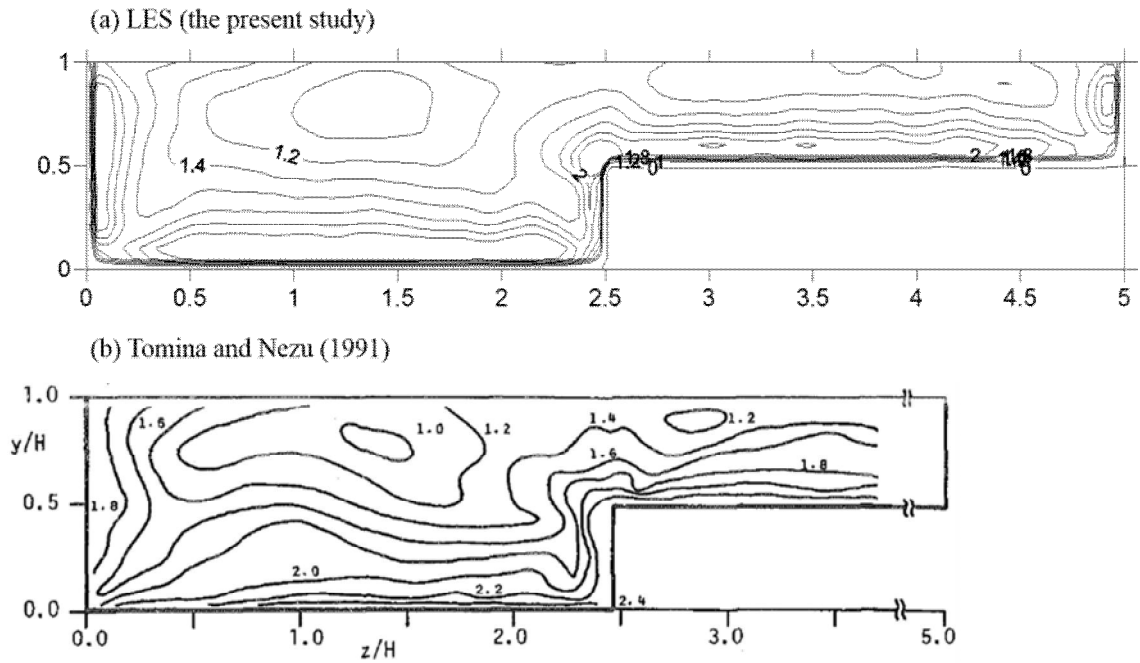


Figure 4.14 Streamwise turbulence intensity (u'/\overline{U}_*) of S2.

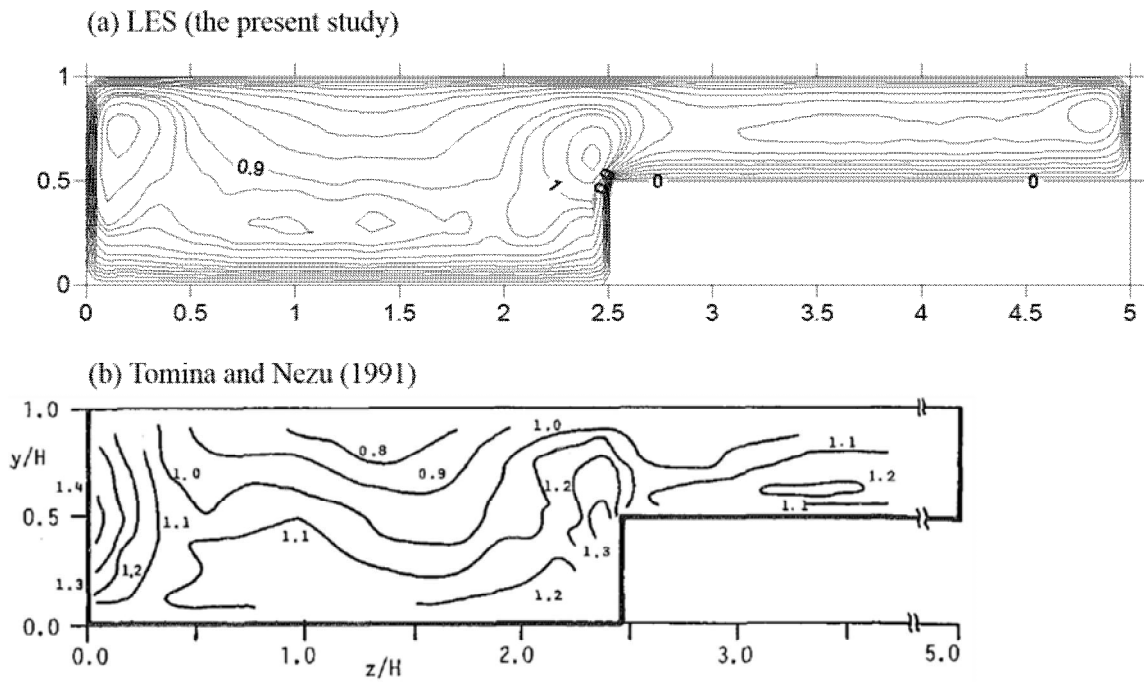


Figure 4.15 Vertical turbulence intensity (v'/\overline{U}_*) of S2.

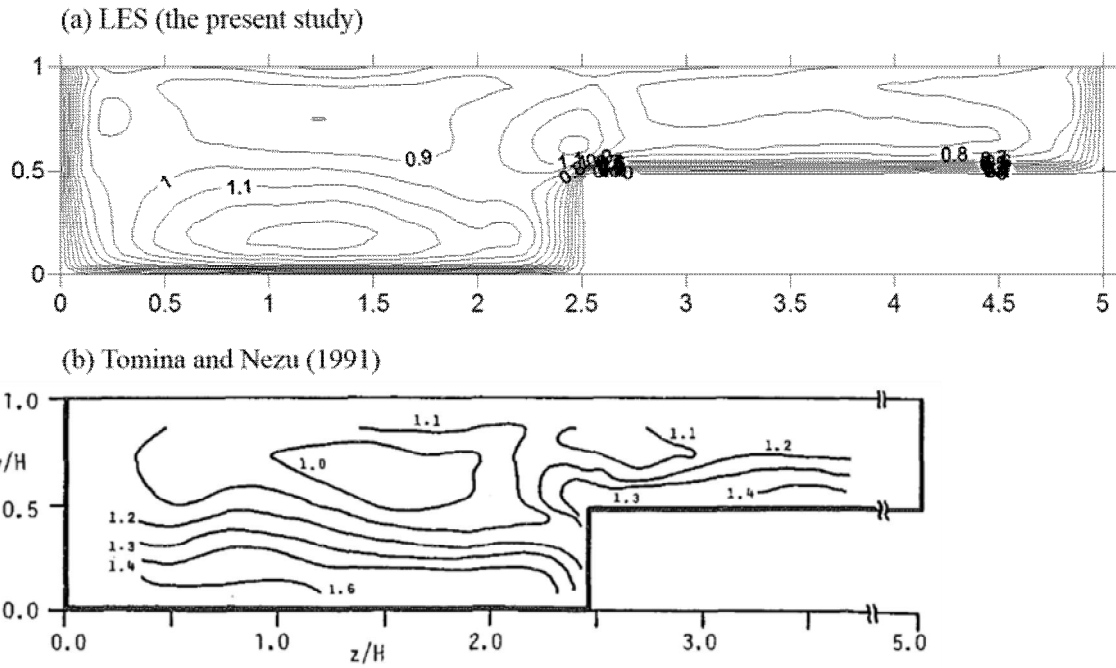


Figure 4.16 Lateral turbulence intensity (w'/\overline{U}_*) of S2.

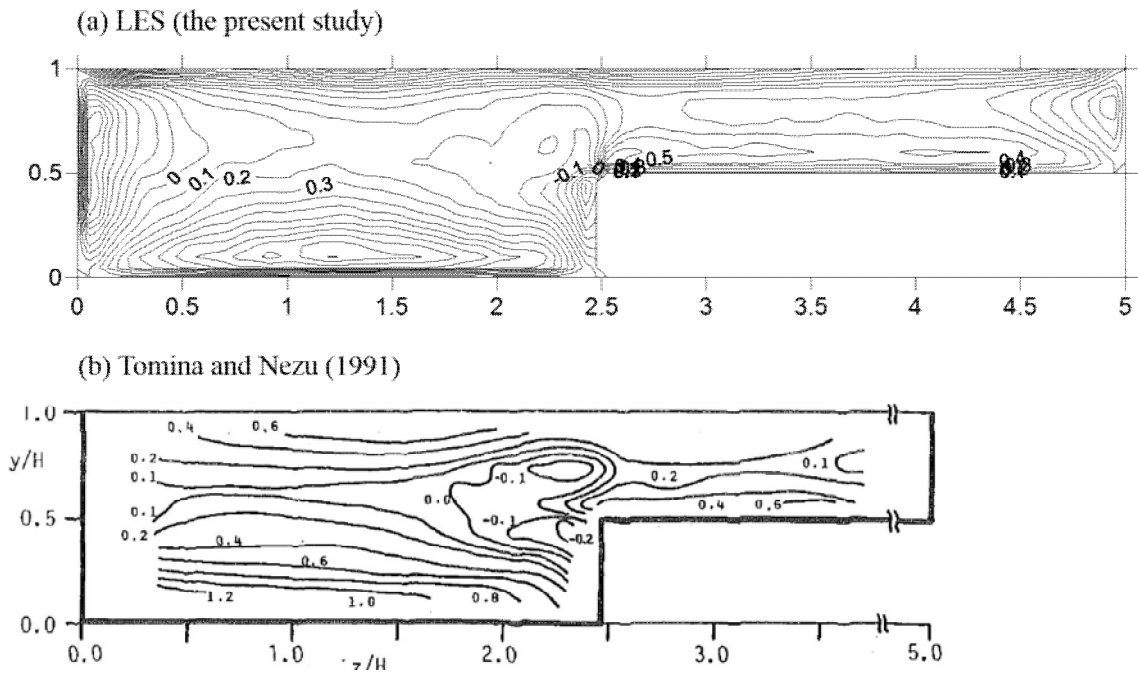


Figure 4.17 Anisotropy of turbulence $(\overline{w'^2} - \overline{v'^2})/\overline{U}_*^2$ of S2.

(4) Reynolds stress distributions

Figures 4.18 and 4.19 show the isolines of Reynolds stresses $-\overline{u'v'}$ and $-\overline{u'w'}$

normalized by the averaged friction velocity \overline{U}_* in the S2 case. The Reynolds shear stresses are generally related to gradients of the primary mean velocity. There is good qualitative agreement between the simulation and the measured data.

The negative value of $-\overline{u'v'}$ appears in a region below the outline of the inclined upflow and also in a free-surface region. These negative region of $-\overline{u'v'}$ corresponds well to the region where dU/dy is negative. In the floodplain, the value of $-\overline{u'v'}$ increases just above the junction edge adjacent to the negative region, and it decreases to be minimum at a position a little away from the junction edge.

The value of $-\overline{u'w'}$ becomes zero at about $z/H = 1.5$, and the sign of $-\overline{u'w'}$ is positive in the side of the main-channel sidewall, whereas it is negative in the opposite side. Of particular significance is that the value of $-\overline{u'w'}$ in the vicinity of the junction attains a negative peak on the side of the main channel, whereas it attains a positive peak on the sidewall of the floodplain. This implies that there exists momentum transport from the main channel toward the floodplain. The sign of $-\overline{u'w'}$ also corresponds to that of dU/dx .

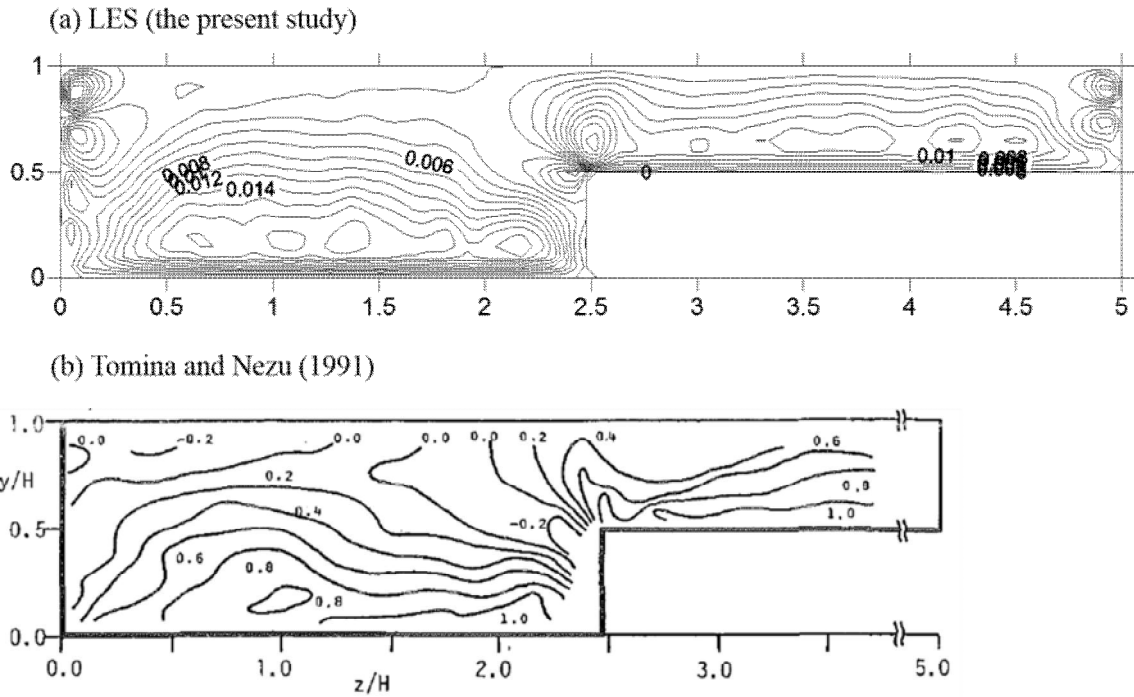


Figure 4.18 Reynolds stress distribution of $-\overline{u'v'}$ in S2 case.

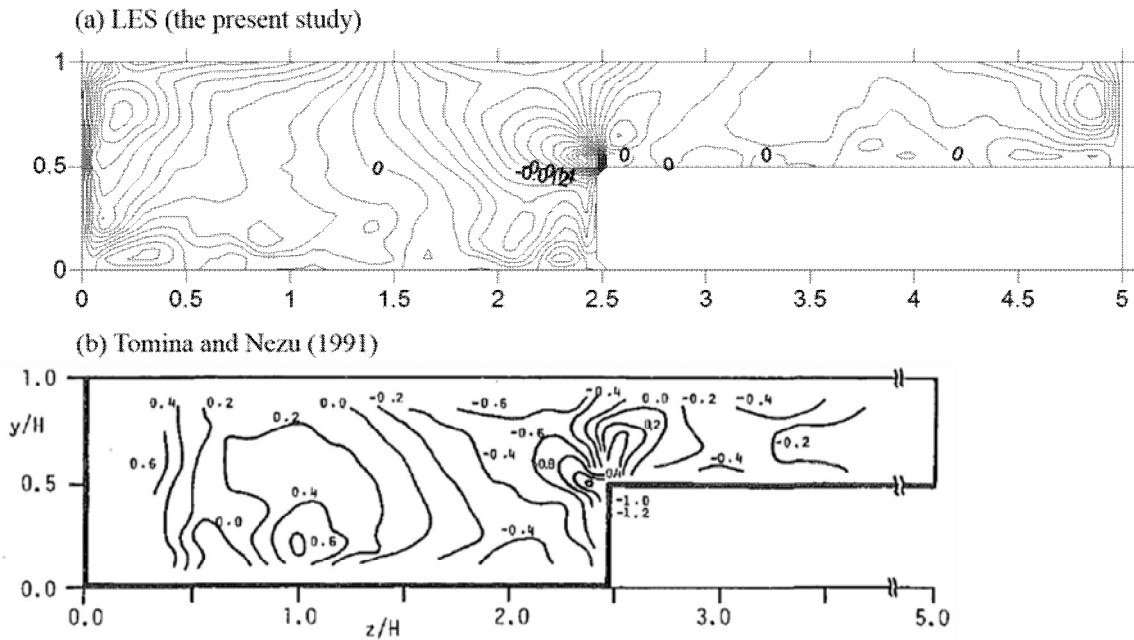


Figure 4.19 Reynolds stress distribution of $-\overline{u'w'}$ in S2 case.

(5) Bed shear stress distributions

Figure 4.20 to 4.23 show the distributions of bed shear stress on the main-channel and the floodplain beds, which are normalized by the averaged shear stress $\bar{\tau}$. Although the simulations have some difference with the measured data especially near the junction of main channel and floodplain, overall simulation results agree well with the experiments. Comparing with previous LES simulations on compound open channels (Thomas and Willams 1995, Cater et al 2008, Kara et al 2011), present LES simulations show fairly good results with the experiments.

The bed shear stress on the floodplain increases as the junction edge is approached. Rajaratnam and Ahmadi (1981) suggested that these increases of the bed shear stress on the floodplain indicated the amount of lateral momentum transport from the main channel. Overall simulations show higher bed shear stresses near the sidewall and junction edge of main channel, and adjacent to junction edge of the floodplain and these local high shear stresses are not seen in the measured data. The effect of these local high shear stresses mainly due to the side wall effect decreases with increase of floodplain depth (h/H). Except these local high shear stresses the simulations agree well with the measured data especially in the S1 and S2 cases.

Higher difference with the measured data is seen in the floodplain of S2 case. The reason of this difference is somewhat debatable and unclear because it is due to the limitation of the present LES simulation, or limitation of the experimental measurement, or both. In the measured data by Tominaga and Nezu (1991) the local friction velocity u_* was evaluated from the measured velocity near the wall assuming the log-law vertical velocity distribution and nondimensional wall unit y^+ was about 30 for main channel and floodplain. In the present LES y^+ are below 5.7 which are near the viscous sublayer or below sublayer along the cases. This difference in the wall unit can be main reason of the shear stress difference.

Figure 4.23 shows the simulated shear stress distribution along the floodplain depth.

The shear stresses in the center of main channel increase and the shear stresses in the floodplain decrease with the increase of floodplain depth as expected. Meanwhile, the measured shear stresses in the floodplain show similar values near the junction in the floodplain.

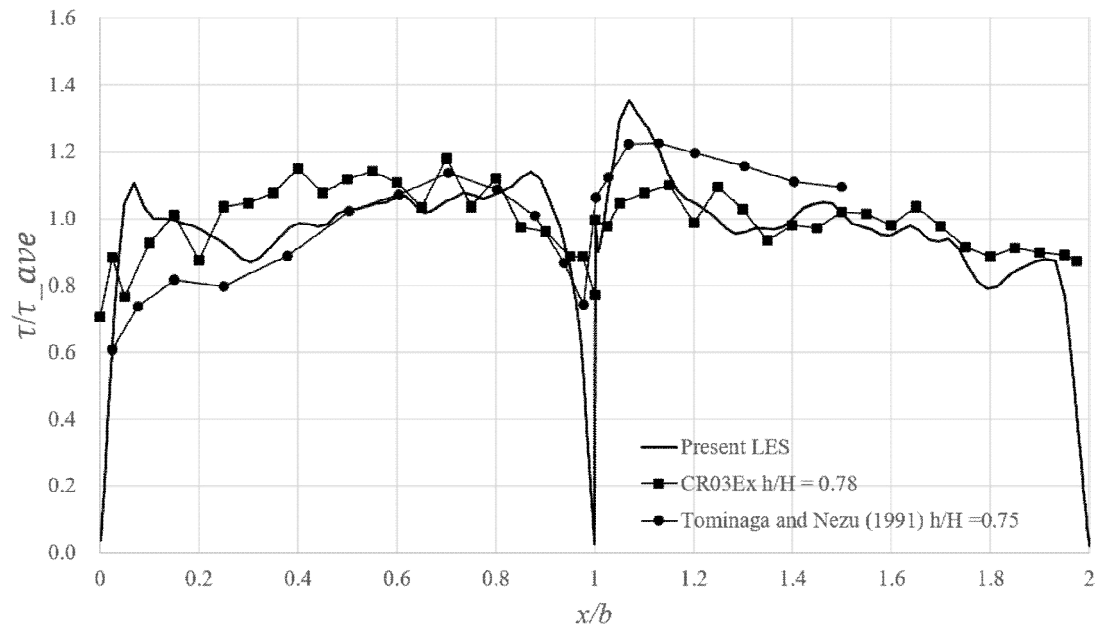


Figure 4.20 Wall shear stress distribution of S1.

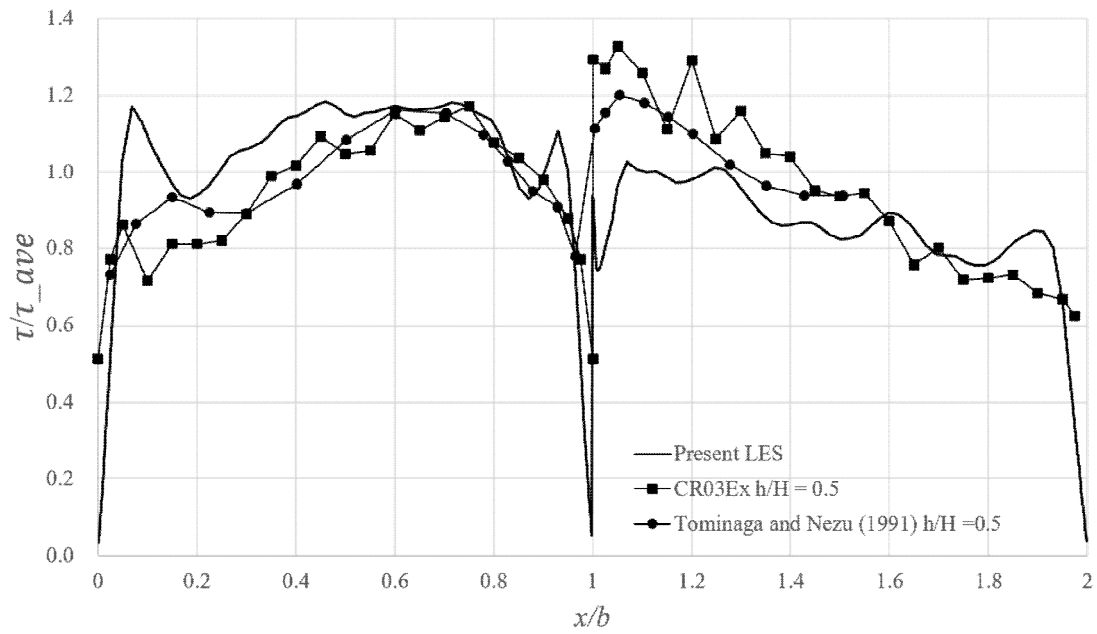


Figure 4.21 Wall shear stress distribution of S2.

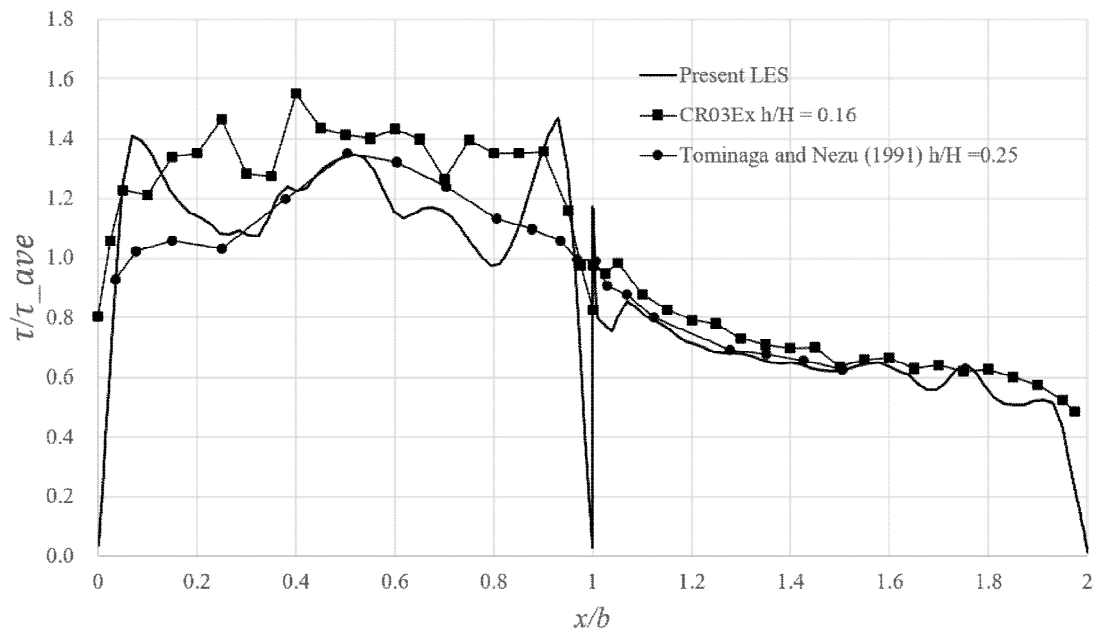


Figure 4.22 Wall shear stress distribution of S3.

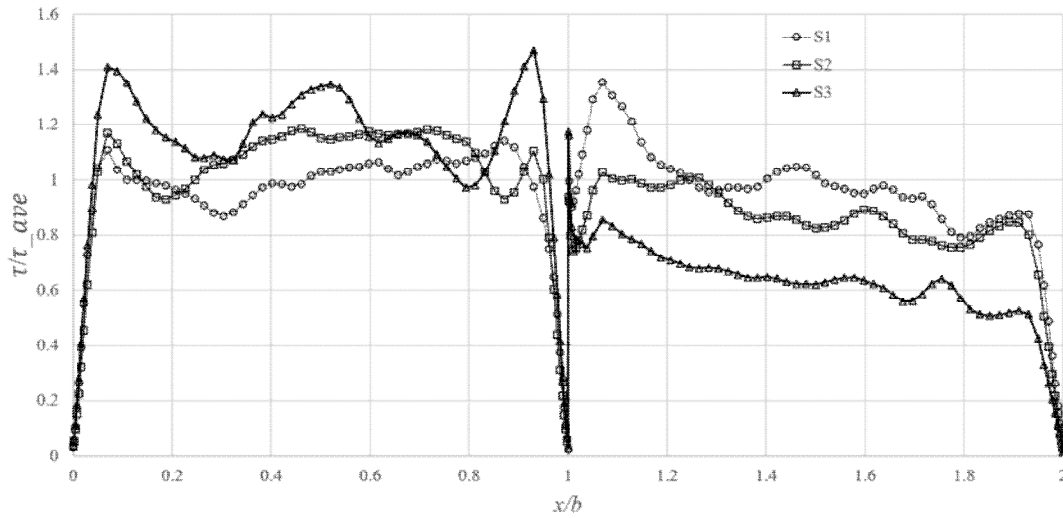


Figure 4.23 Wall shear stress distribution of the present LES (S1, S2 and S3).

4.2 Rectangular Compound Open Channels

4.2.1 Simulation cases

Total 12 cases of rectangular compound open channels are simulated for various depth ratio and width ratio (Table 4.4 and Figure 4.24 – 4.26). Depth ratio (h/H) of the cases range from 0.25 to 0.75 and width ratio (b/B) of the cases range from 0.500 to 0.875, covering the narrow, wide, shallow and deep shapes of the floodplain. Mean velocity is imposed as driving force ranging from 0.288 to 0.368. Corresponding Reynolds numbers range from 48,000 to 150,000. Boundary conditions coincide with those of verification test cases. Cases of CR01, CR11 and CR21 are exactly same cases of S2, S3, and S1 presented in section 4.1, respectively. The computational domain is discretized with a fine non-uniform grid in x and y direction and a fine uniform grid in z direction (from Figure 4.27 to 4.35).

Table 4.4 Simulation cases of rectangular compound channels.

Case	H (m)	h (m)	B (m)	b (m)	h/H	b/B	Mean velocity (m/s)	Reynolds Re
CR01	0.08	0.04	0.4	0.20	0.50	0.500	0.349	69,800
CR02	0.08	0.04	0.4	0.25	0.50	0.625	0.349	87,250
CR03	0.08	0.04	0.4	0.30	0.50	0.750	0.349	104,700
CR04	0.08	0.04	0.4	0.35	0.50	0.875	0.349	122,150
CR11	0.08	0.02	0.4	0.20	0.25	0.500	0.288	48,000
CR12	0.08	0.02	0.4	0.25	0.25	0.625	0.349	72,708
CR13	0.08	0.02	0.4	0.30	0.25	0.750	0.349	87,250
CR14	0.08	0.02	0.4	0.35	0.25	0.875	0.349	101,792
CR21	0.08	0.06	0.4	0.20	0.75	0.500	0.368	85,867
CR22	0.08	0.06	0.4	0.25	0.75	0.625	0.368	107,333
CR23	0.08	0.06	0.4	0.30	0.75	0.750	0.368	128,800
CR24	0.08	0.06	0.4	0.35	0.75	0.875	0.368	150,267

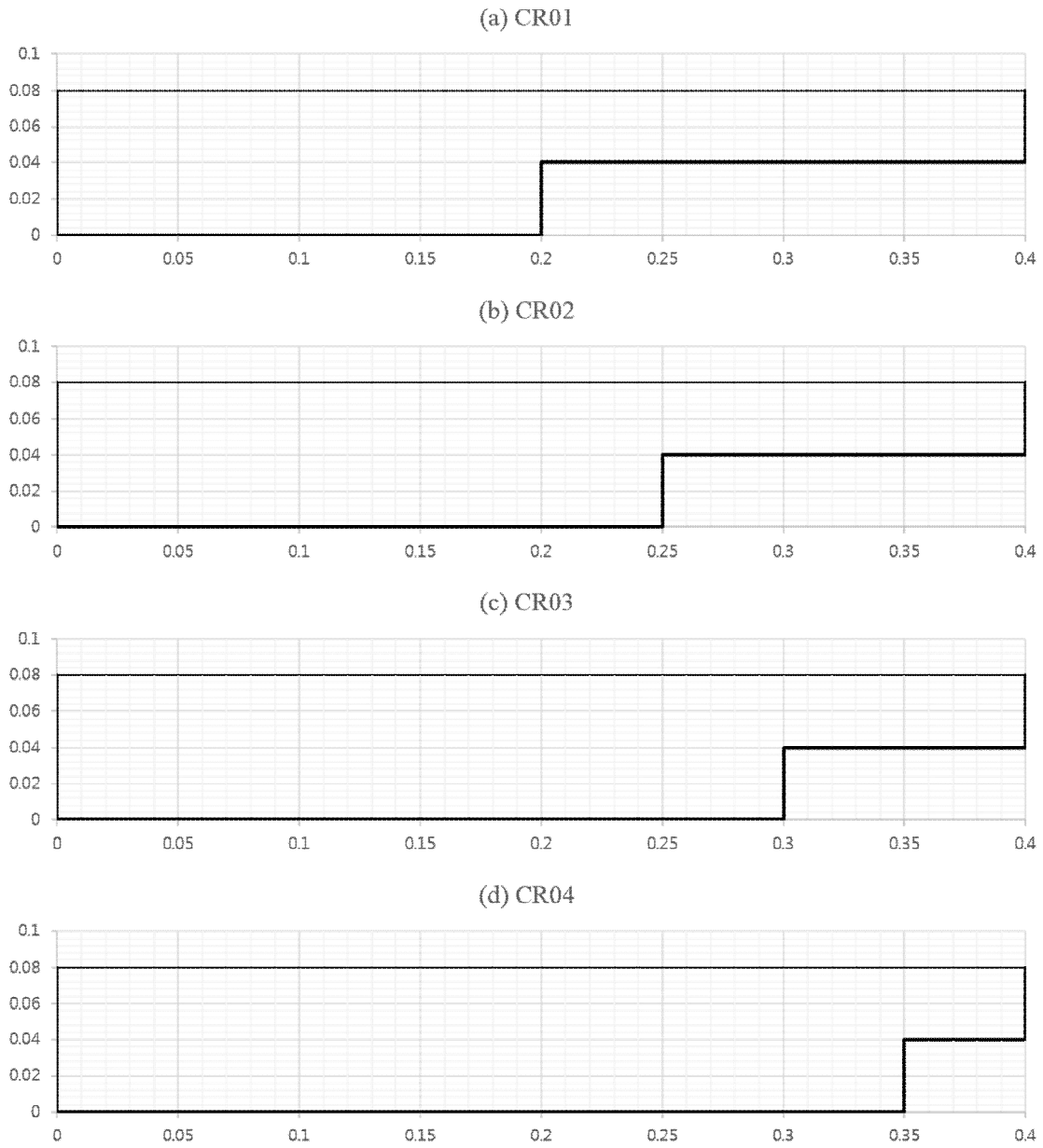


Figure 4.24 Geometry of the simulation cases (CR01, CR02, CR03 and CR04).

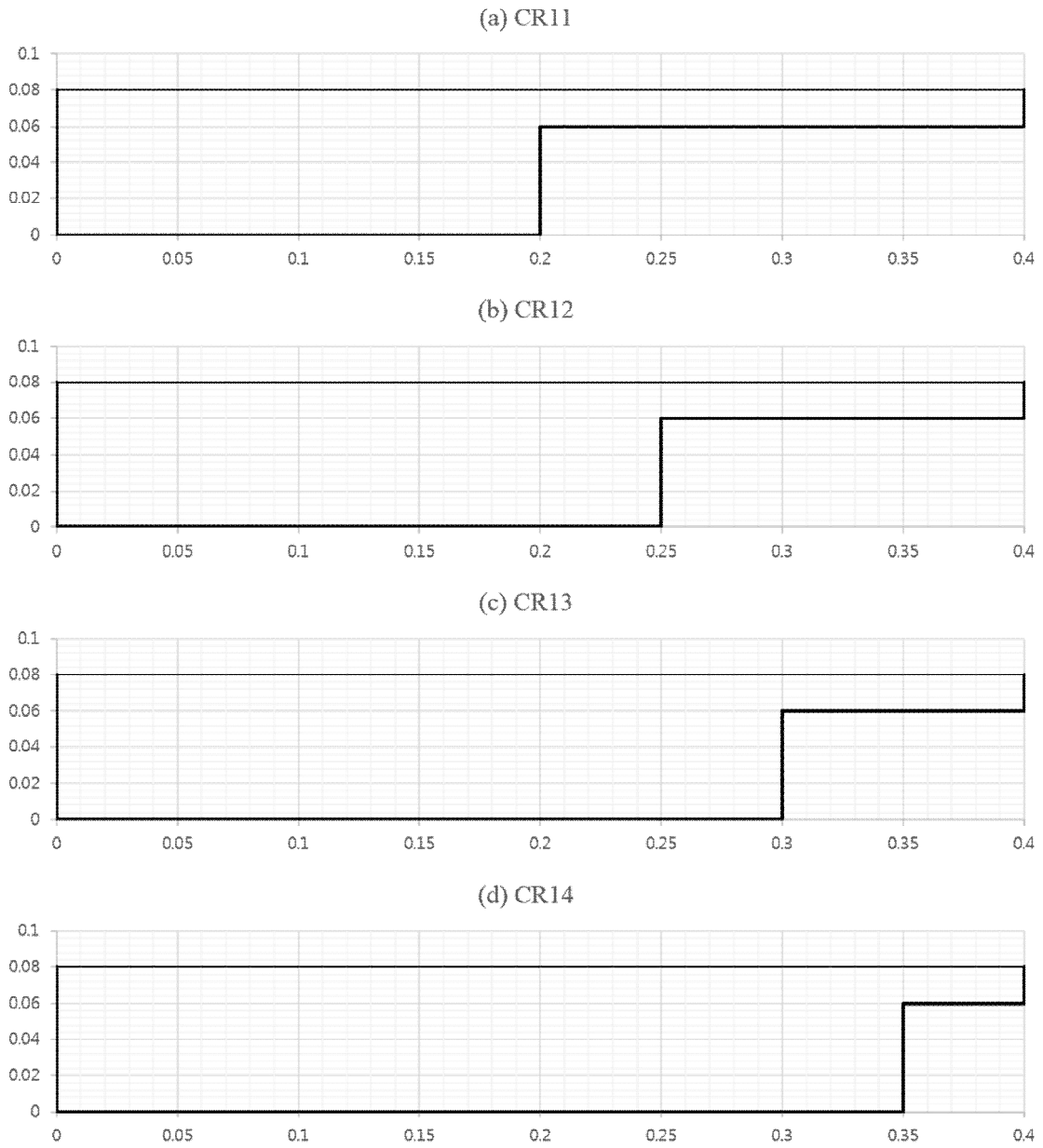


Figure 4.25 Geometry of the simulation cases (CR11, CR12, CR13 and CR14).

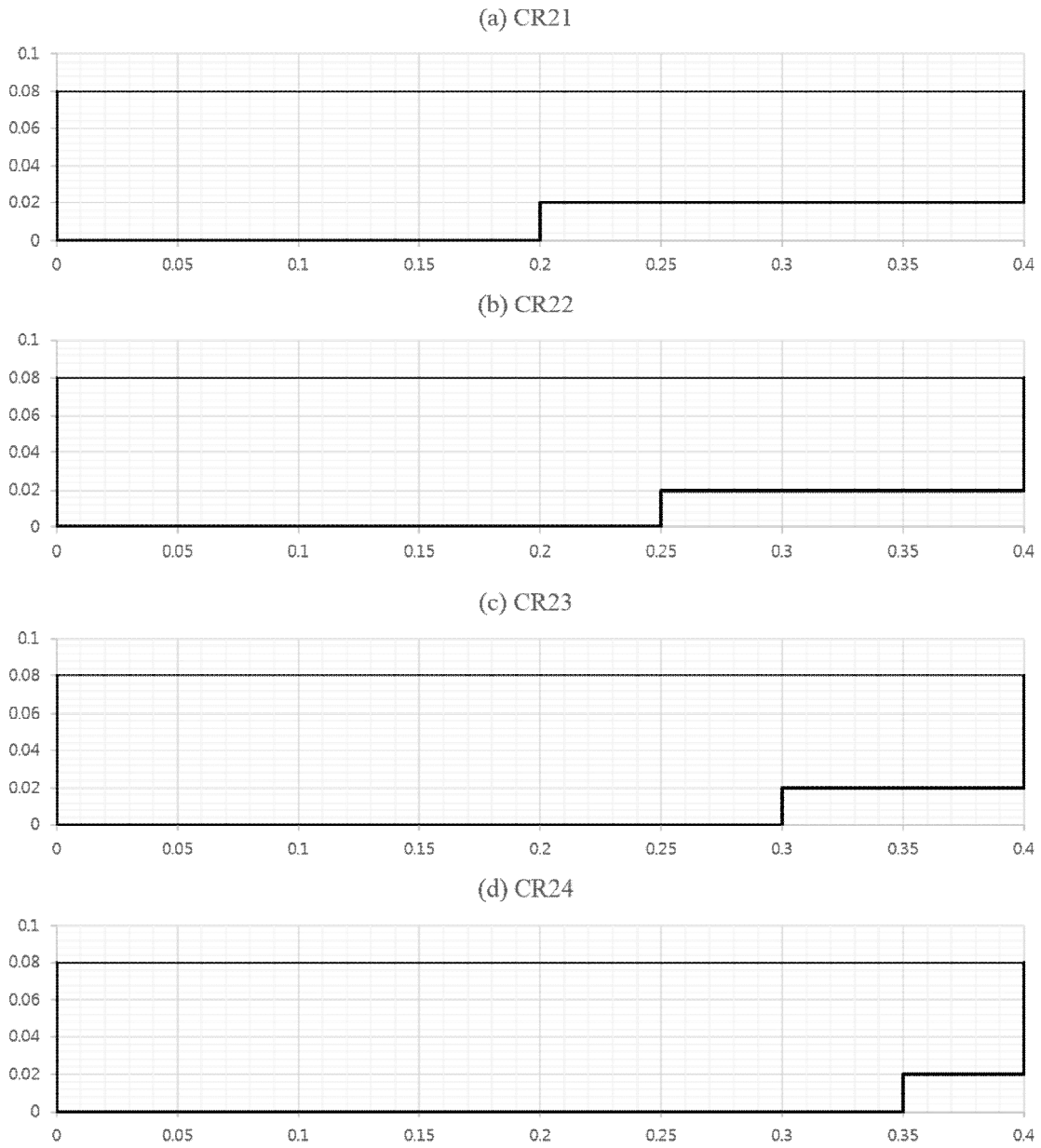


Figure 4.26 Geometry of the simulation cases (CR21, CR22, CR23 and CR24).

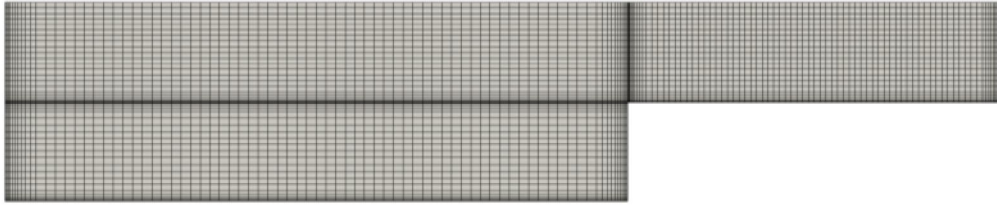


Figure 4.27 Geometry and mesh of case CR02.

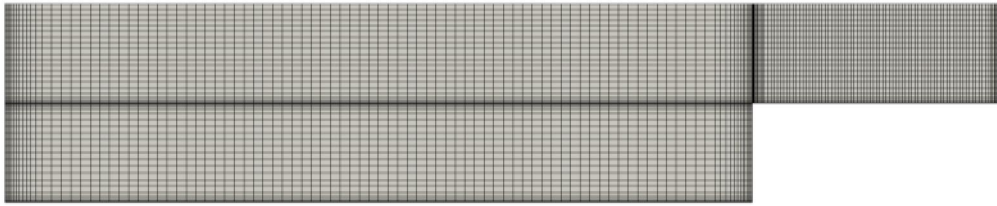


Figure 4.28 Geometry and mesh of case CR03.

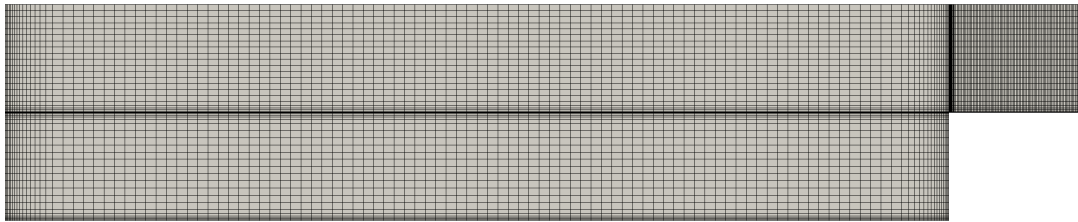


Figure 4.29 Geometry and mesh of case CR04.

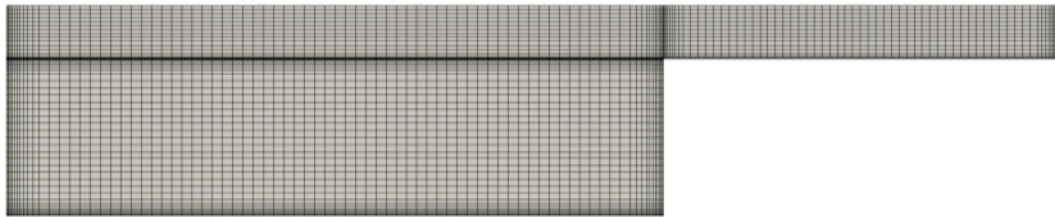


Figure 4.30 Geometry and mesh of case CR12.

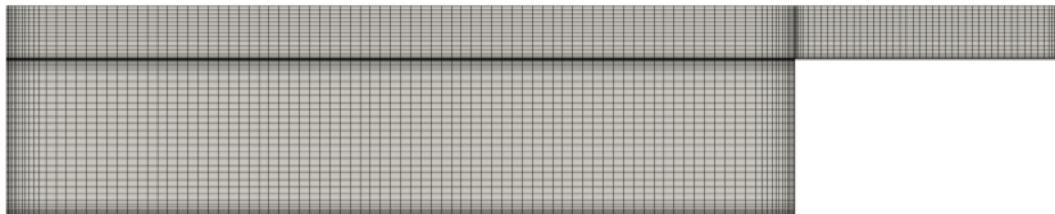


Figure 4.31 Geometry and mesh of case CR13.

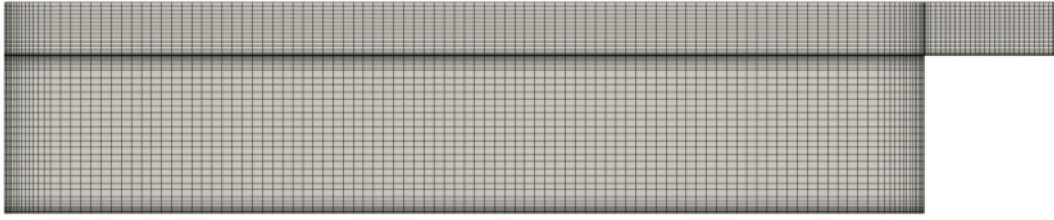


Figure 4.32 Geometry and mesh of case CR14.

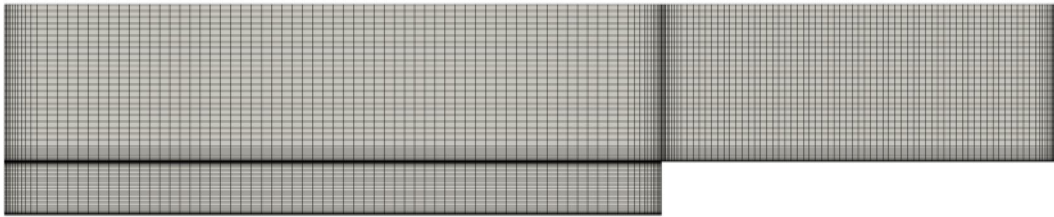


Figure 4.33 Geometry and mesh of case CR22.

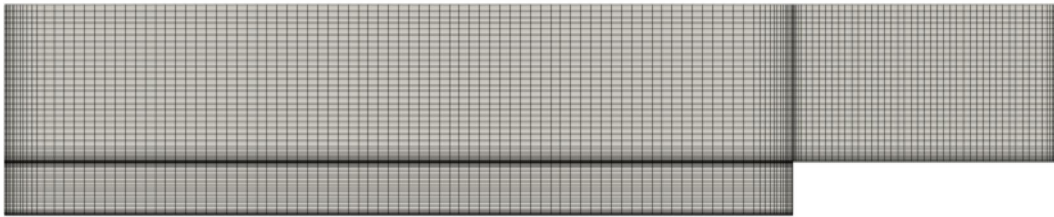


Figure 4.34 Geometry and mesh of case CR23.

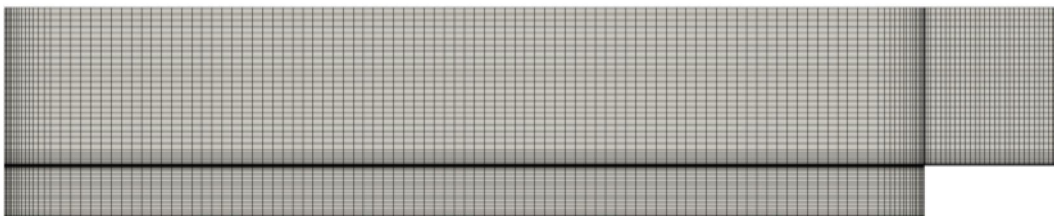


Figure 4.35 Geometry and mesh of case CR24.

4.2.2 Results and Analysis

(1) Mean velocity distribution

Figure 4.36 to Figure 4.47 show simulated isovel lines of the streamwise mean velocity U normalized by U_{\max} .

Velocity dip in the main channel is more distinct in the shallow floodplain cases and it becomes unclear in the deep floodplain cases. In the shallow floodplain cases, flow

condition in the main channel is more close to the condition in the narrow rectangular channels, thus the side wall effect of the junction region is dominant to velocity distribution in the main channel. In the deep floodplain cases, flow condition in the main channel approach to the condition in the wide rectangular channels, thus the side wall effect of the junction region is restricted and the bed wall effect is dominant.

Lateral position of the high velocity region in the main channels moves to the floodplain with floodplain depth increase. Velocity bulge near the junction region is more distinct in the deep floodplain cases, and it becomes weak in the shallow floodplain cases.

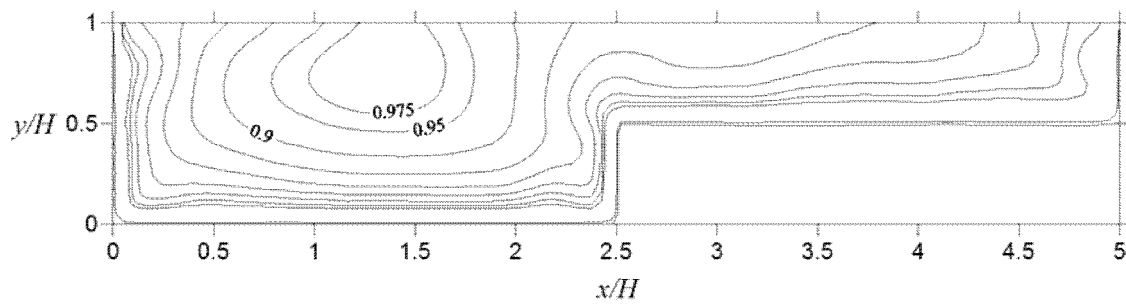


Figure 4.36 Streamwise mean velocity in case CR01.

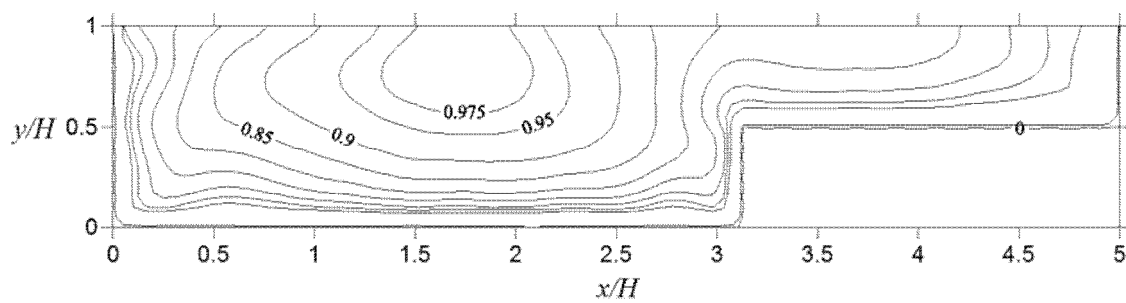


Figure 4.37 Streamwise mean velocity in case CR02.

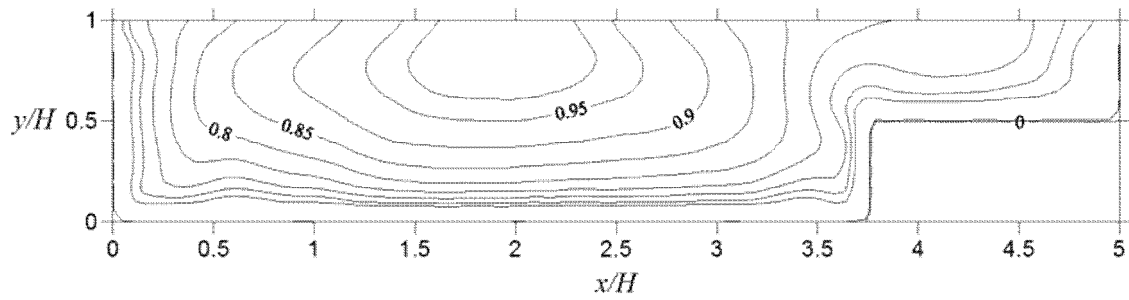


Figure 4.38 Streamwise mean velocity in case CR03.

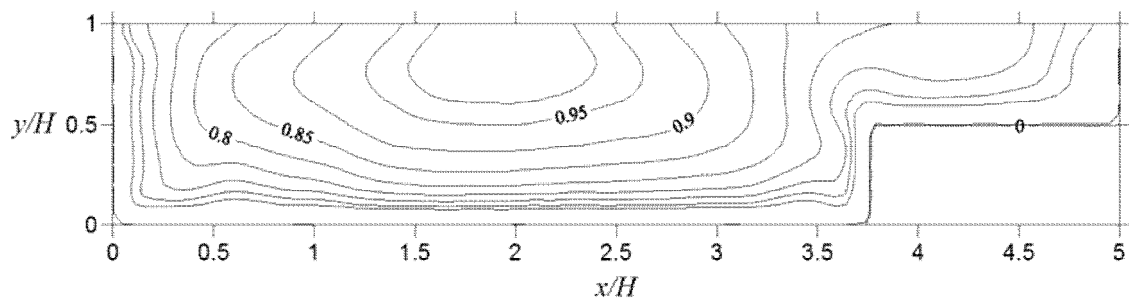


Figure 4.39 Streamwise mean velocity in case CR04.

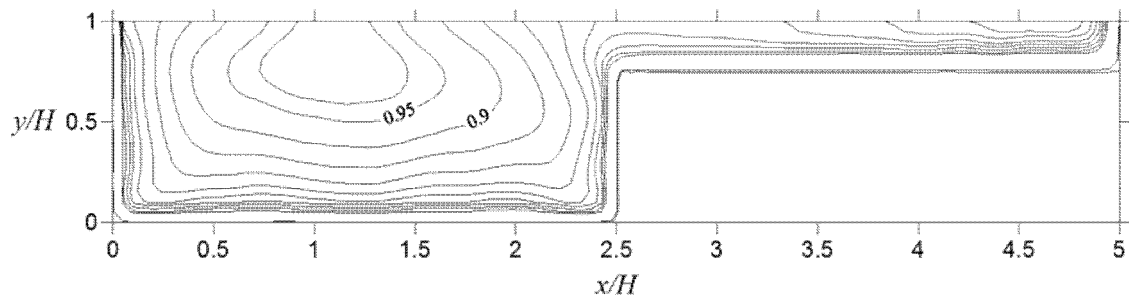


Figure 4.40 Streamwise mean velocity in case CR11.

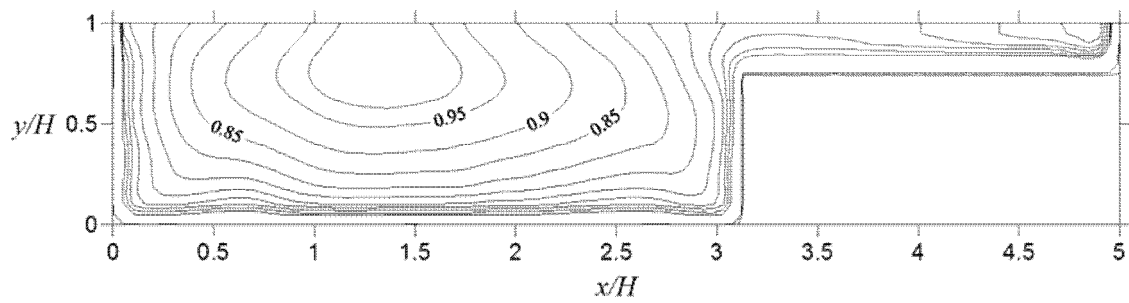


Figure 4.41 Streamwise mean velocity in case CR12.

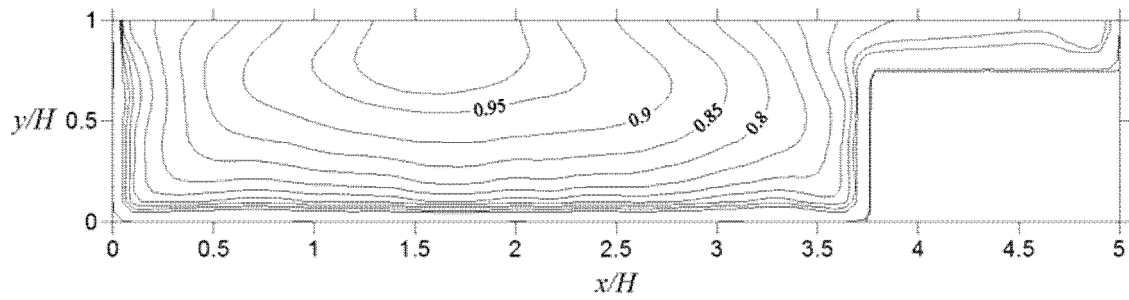


Figure 4.42 Streamwise mean velocity in case CR13.

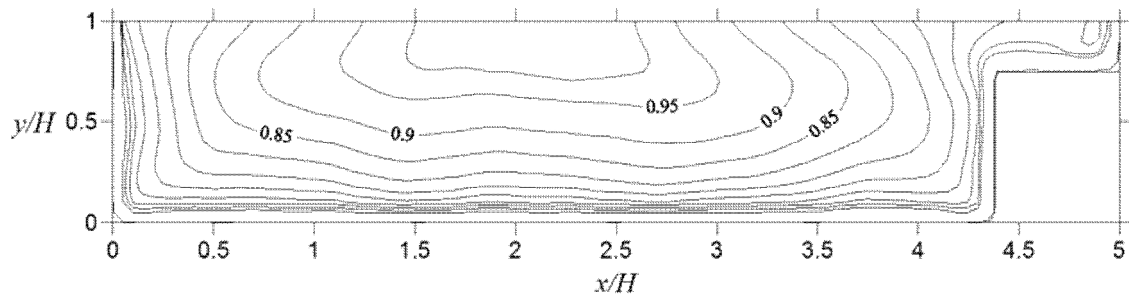


Figure 4.43 Streamwise mean velocity in case CR14.

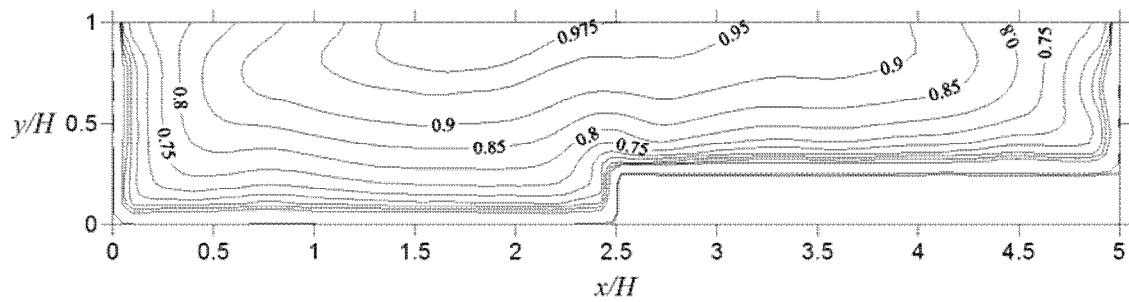


Figure 4.44 Streamwise mean velocity in case CR21.

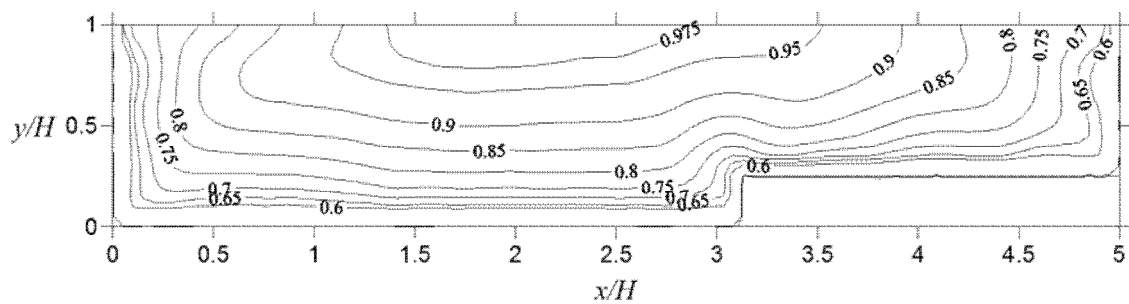


Figure 4.45 Streamwise mean velocity in case CR22.

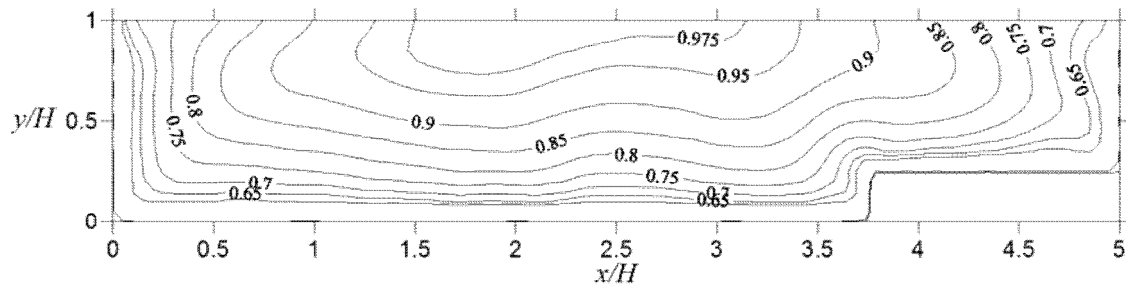


Figure 4.46 Streamwise mean velocity in case CR23.

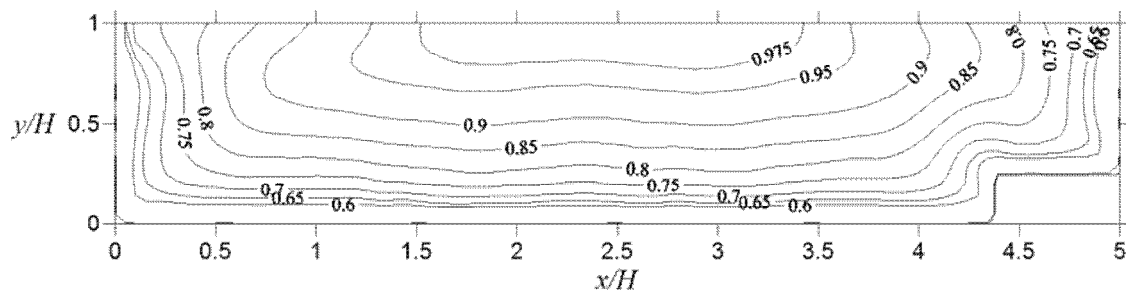


Figure 4.47 Streamwise mean velocity in case CR24.

(2) Secondary currents

Figure 4.48 to Figure 4.59 show the vector description of the secondary currents in the rectangular open channel cases.

In the same floodplain depth conditions, the secondary currents show analogous patterns in the side wall of main channel and the junction region of main channel and floodplain. The secondary currents in the side wall of floodplain also show analogous patterns in the same floodplain depth conditions. The main difference with change of floodplain width is observed in floodplain vortex. In $h/H = 0.5$, region of the floodplain vortex is decreased and the boundary between floodplain vortex and inner vortex formed in the side wall of floodplain becomes unclear with floodplain depth increase. Finally in case CR04, the floodplain vortex is dominant in the floodplain region and the inner vortex in the floodplain side wall decreases.

In $h/H = 0.25$, magnitude of the secondary currents changes with the floodplain width. In case CR11, secondary current decreases definitely near the side wall of the

floodplain. Meanwhile in case CR12, CR13 and CR14 magnitude of the secondary current in the surface and bed of the floodplain is nearly constant.

In $h/H = 0.75$, the secondary currents shows more complicated changes in the floodplain with floodplain depth increase. In case CR21, five vortex are observed definitely in the floodplain. Two floodplain vortex are observed in the junction and middle of the floodplain. Free surface vortex is observed near the side wall of the floodplain and the three inner vortex are observed adjacent to the side wall and coner of the floodplain. However the free surface vortex formed in the middle of the floodplain diminishes with floodplain width decrease and finally disappears in the case CR23. Surface vortex formed near the side wall also diminishes and disappears with floodplain width decrease. Meanwhile, two inner vortex formed adjacent to the side wall maintain with the floodplain decrease.

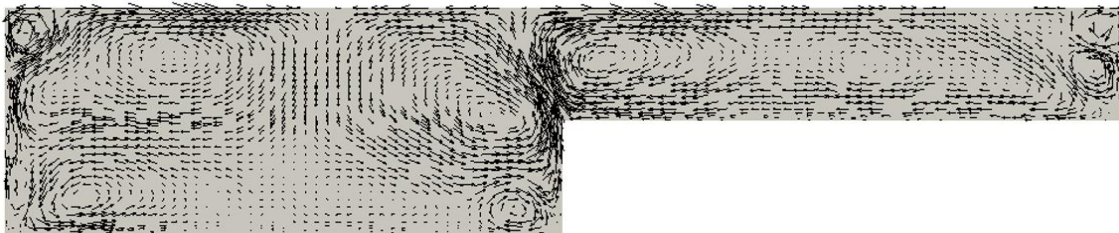


Figure 4.48 Secondary flows in case CR01.

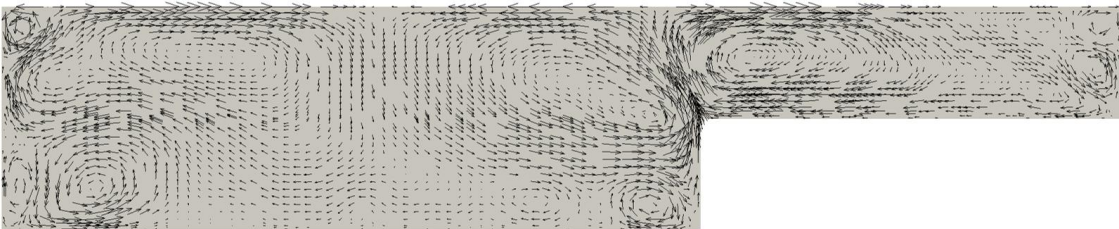


Figure 4.49 Secondary flows in case CR02.

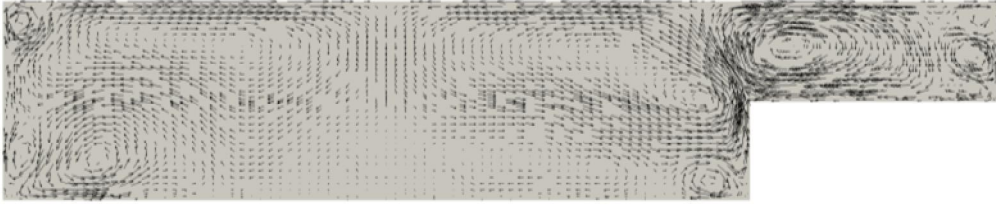


Figure 4.50 Secondary flows in case CR03.

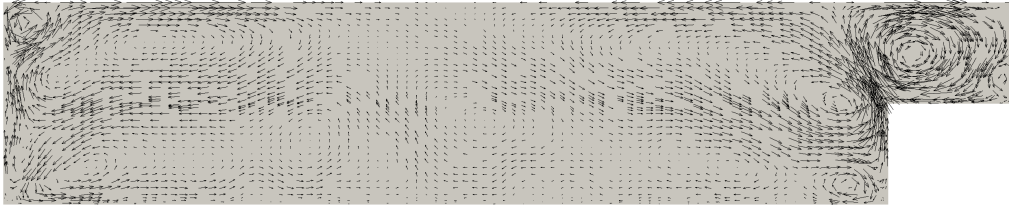


Figure 4.51 Secondary flows in case CR04.

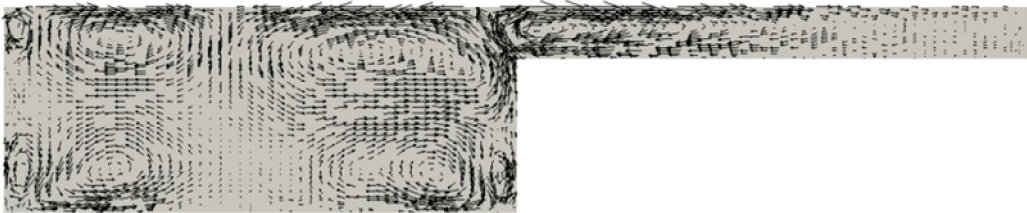


Figure 4.52 Secondary flows in case CR11.

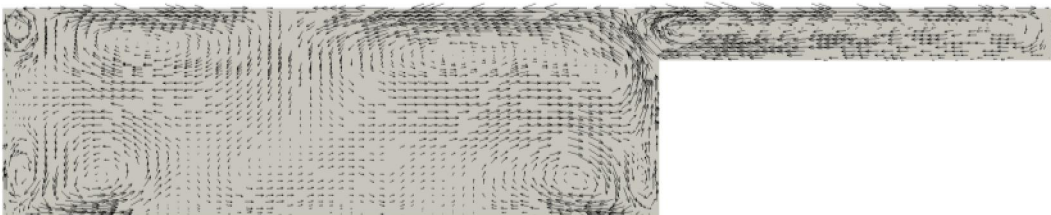


Figure 4.53 Secondary flows in case CR12.

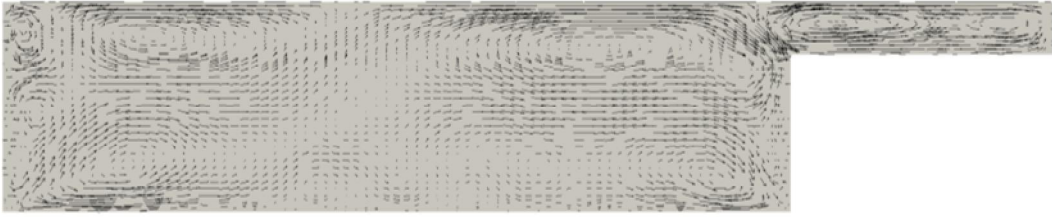


Figure 4.54 Secondary flows in case CR13.

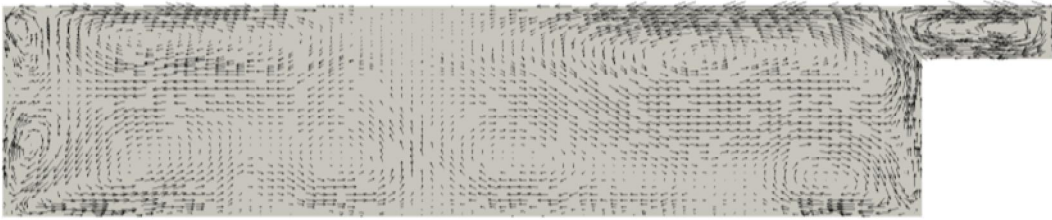


Figure 4.55 Secondary flows in case CR14.

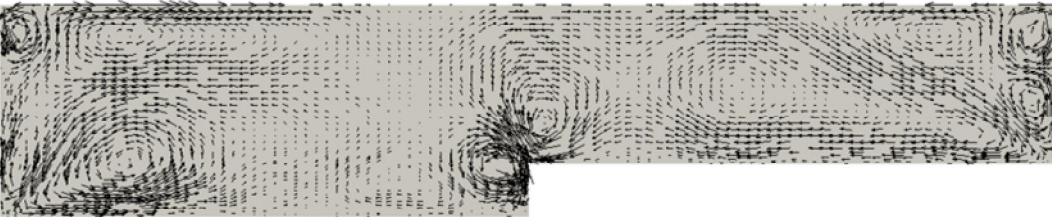


Figure 4.56 Secondary flows in case CR21.

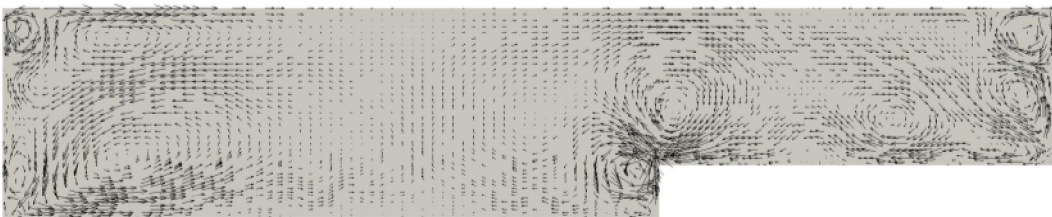


Figure 4.57 Secondary flows in case CR22.

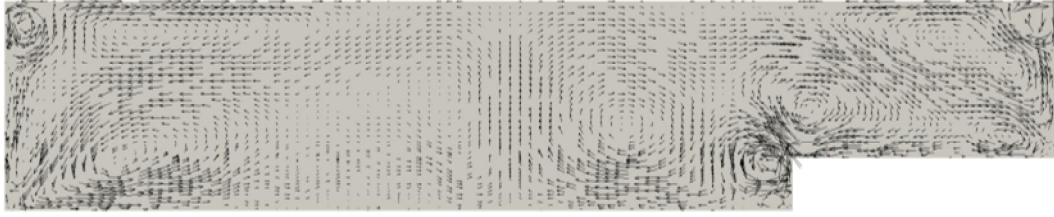


Figure 4.58 Secondary flows in case CR23.

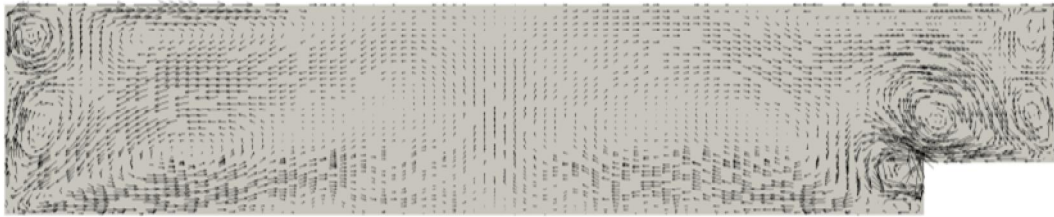


Figure 4.59 Secondary flows in case CR24.

(3) Wall shear stress distribution

Figure 4.60 to Figure 4.71 show wall shear stress distribution normalized by the averaged shear stress $\bar{\tau}$ in the rectangular compound channels. Overall distribution of the wall shear stress distribution show some degree of the consistency.

In $h/H = 0.5$, relatively high shear stresses are seen near side walls and in the middle of the main channel, and at the junction edge and near the junction and side wall of the floodplain. In case CR01, although maximum shear stress is seen in the middle of the main channel, high shear stresses are seen near the side walls of the main channel, due to the secondary currents formed in the corners of the main channel. In the floodplain, high shear stresses are seen near the junction and they decrease in the lateral direction. High shear stresses seen near the side walls of the main channel decrease and high shear stresses are dominant in the middle of the main channel with floodplain width decrease. Meanwhile locally high shear stress seen at the junction edge increase with floodplain width decrease and it becomes larger than maximum shear stress of the floodplain in cases of CR02, CR03 and CR04. Overall shear stresses in

the floodplain decrease and the locally high shear stresses formed near the side wall of the floodplain decrease much more with floodplain width decrease.

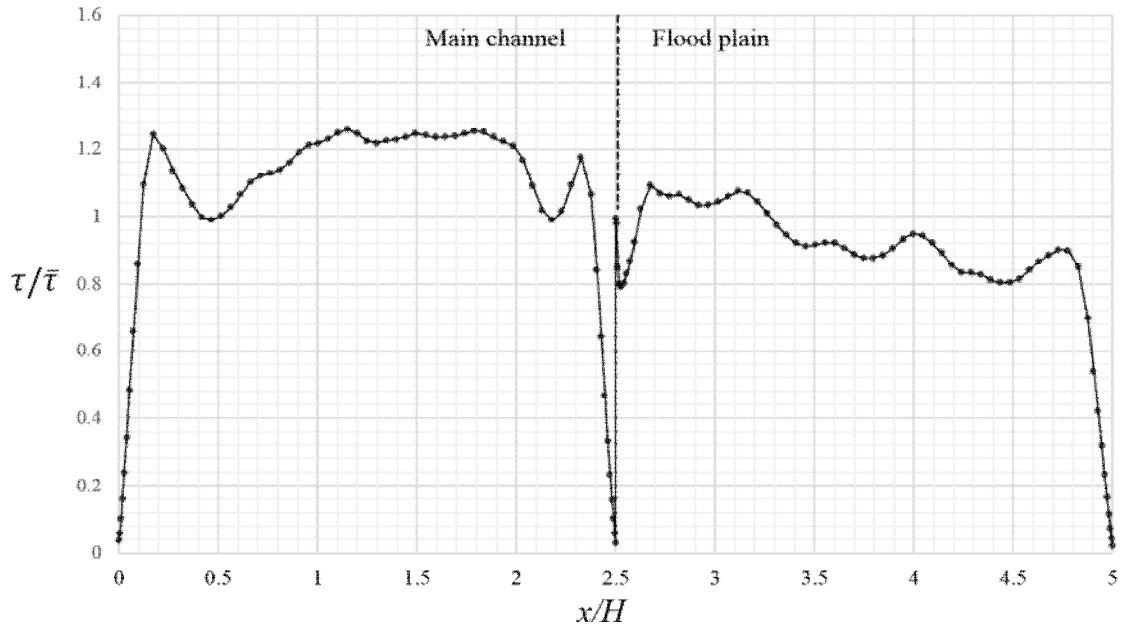


Figure 4.60 Wall shear distribution in case CR01.

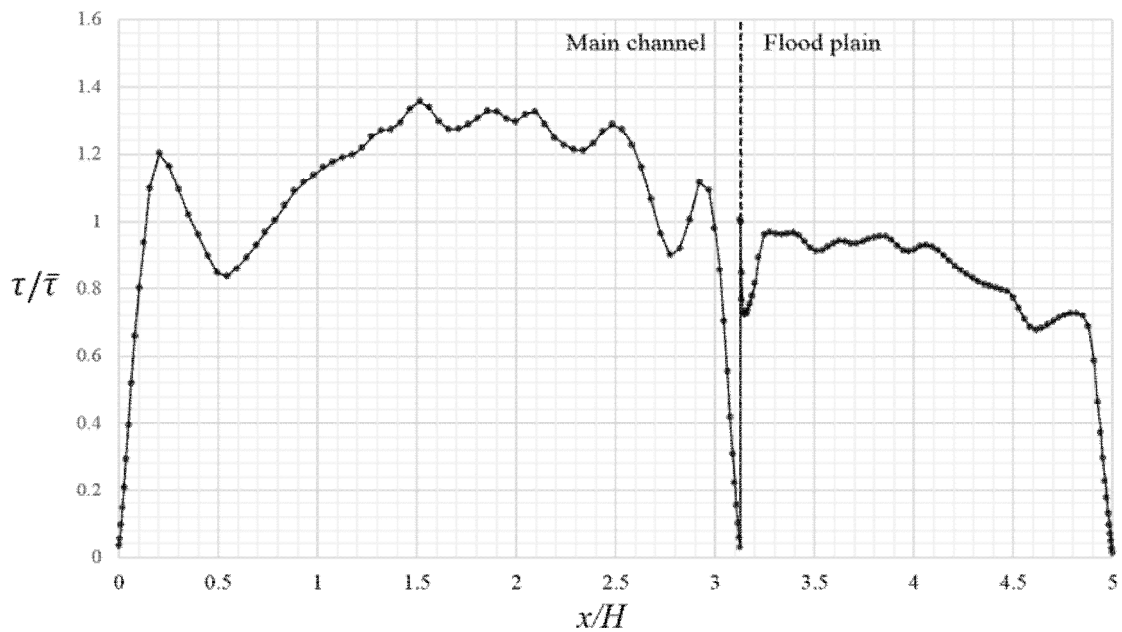


Figure 4.61 Wall shear distribution in case CR02.

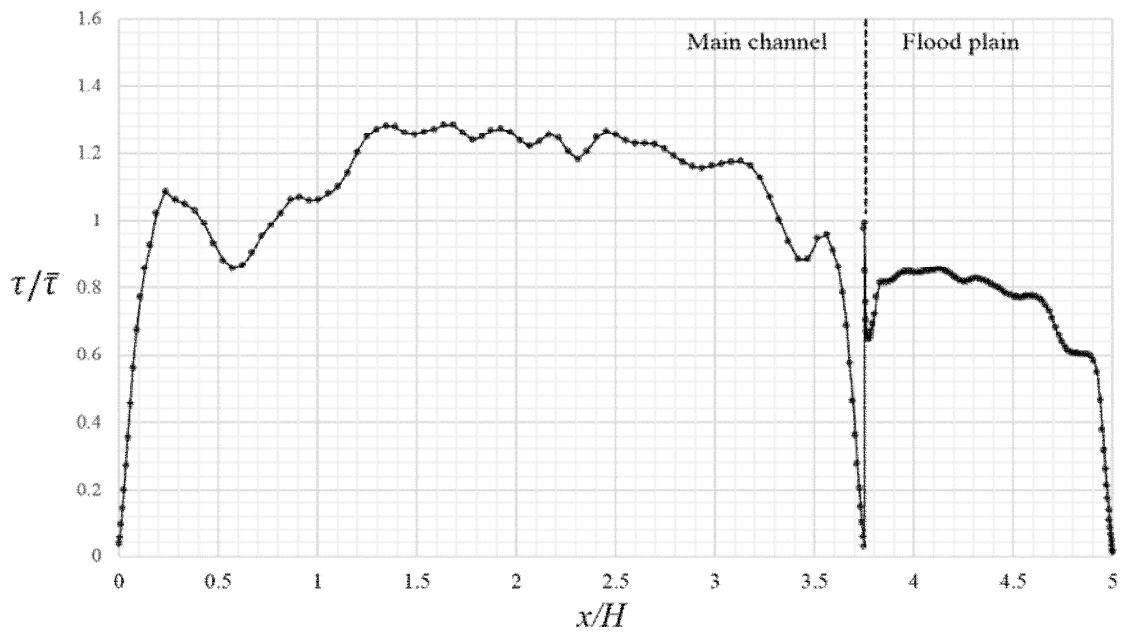


Figure 4.62 Wall shear distribution in case CR03.

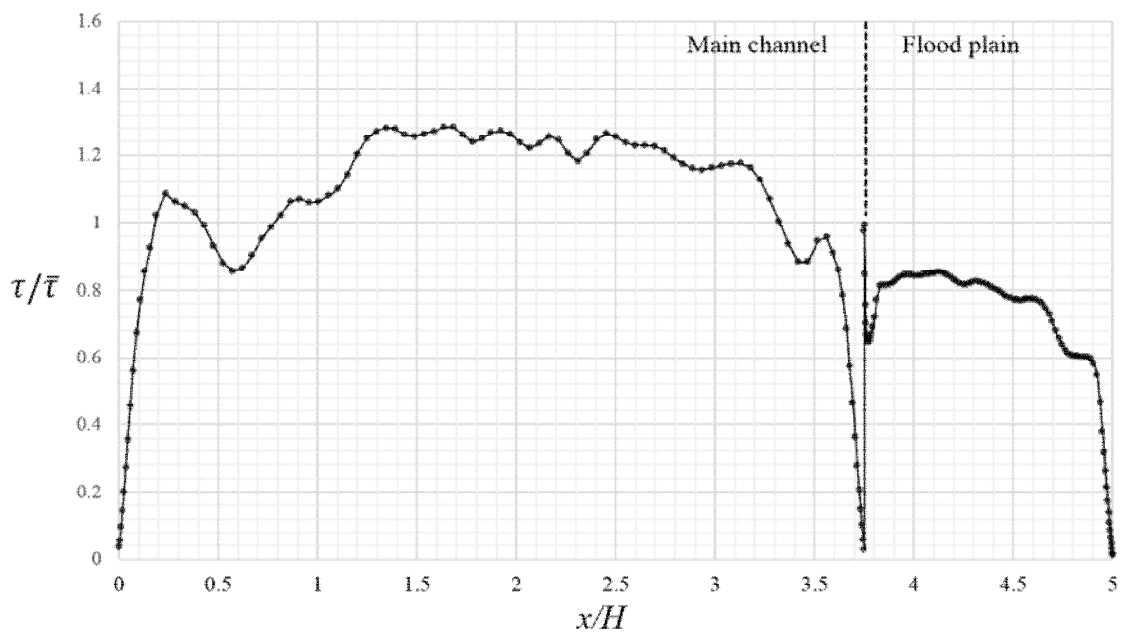


Figure 4.63 Wall shear distribution in case CR04.

In $h/H = 0.25$, shear stresses are relatively high in the main channel compared with $h/H = 0.25$ and 0.75 , because the flow is concentrated to the main channel by shallow floodplain. Relatively high shear stresses are seen near side walls and in the middle of the main channel, and at the junction edge and near the junction and side wall of the floodplain. In case CR11, although high shear stresses are seen in the middle of the main channel, maximum shear stresses are seen near the side walls of the main channel, due to the secondary currents formed in the corners of the main channel. In the floodplain, high shear stresses are seen near the junction and they decrease in the lateral direction. High shear stresses seen near the side walls of the main channel decrease and high shear stresses are dominant in the middle of the main channel with floodplain width decrease. Local high shear stress seen at the junction edge decreases with floodplain width decrease. Comparing with $h/H = 0.5$ and 0.72 , the effect of the main channel corner vortex is dominant and the effect of inner vortex formed near the side wall of floodplain is also dominant in $h/H = 0.25$. In the narrow floodplain case CR14, the shear stress distribution in the floodplain shows the concave pattern due to the local high shear stresses generated by the inner vortex of the floodplain side wall.

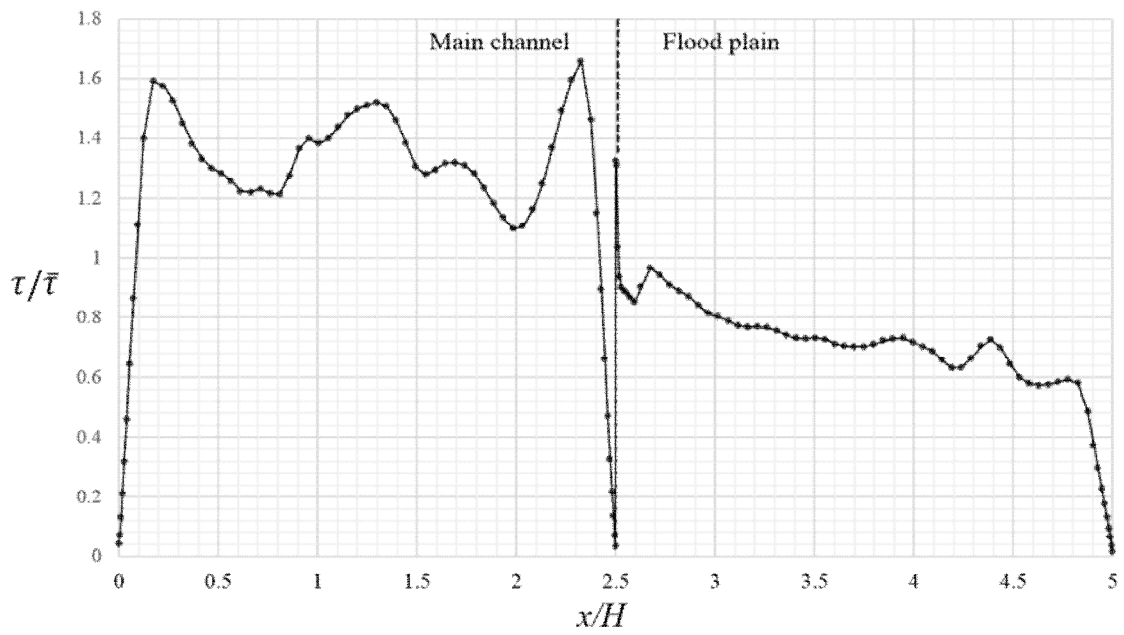


Figure 4.64 Wall shear distribution in case CR11.

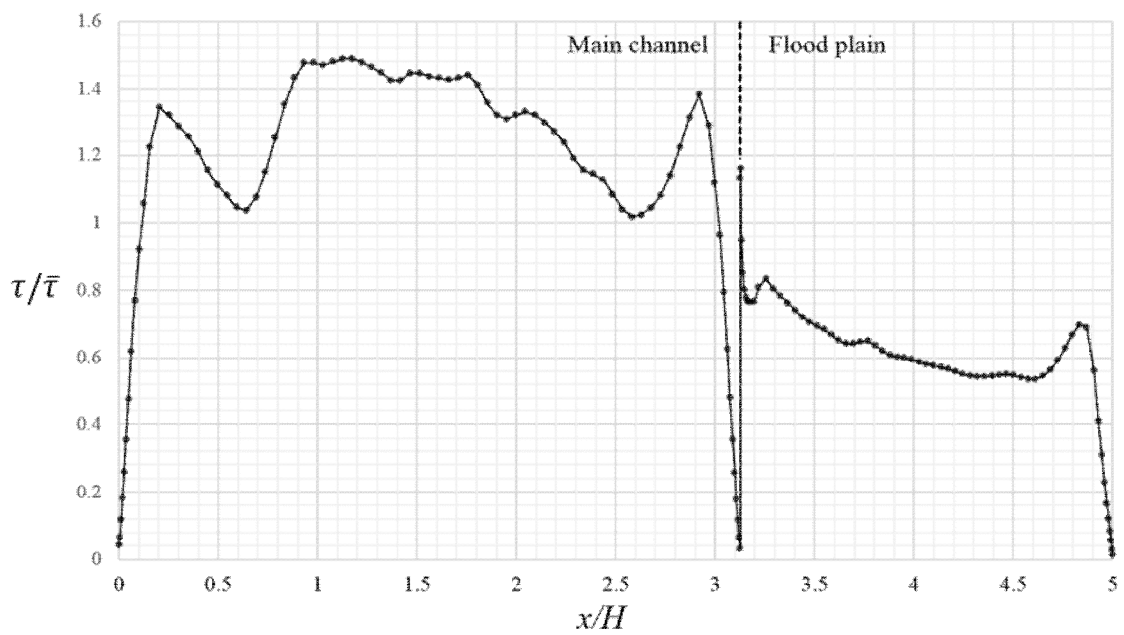


Figure 4.65 Wall shear distribution in case CR12.

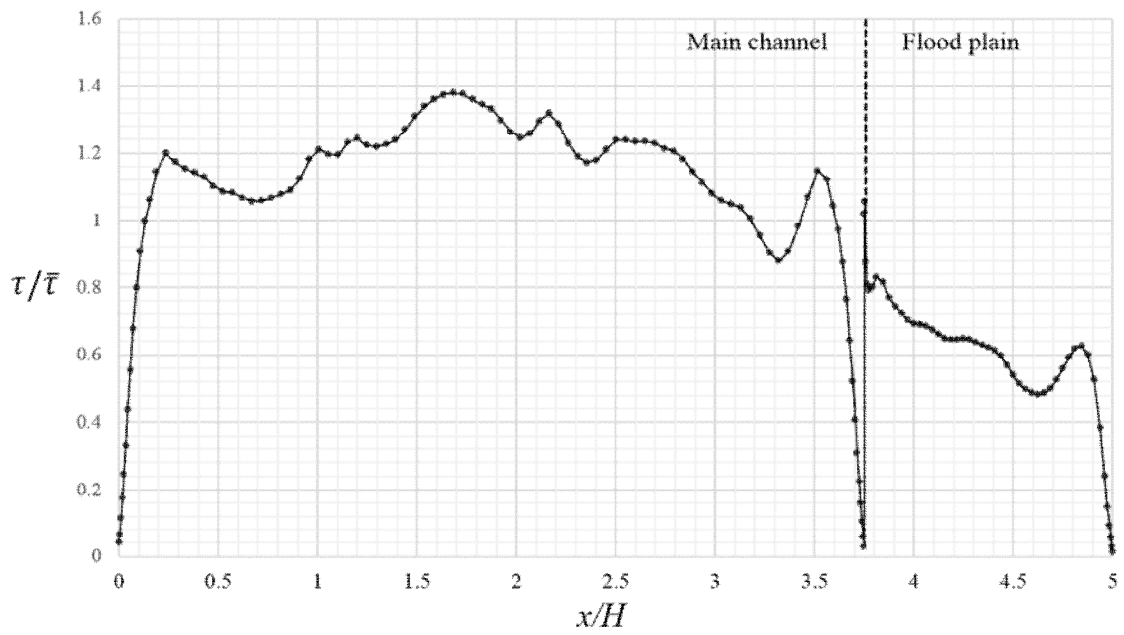


Figure 4.66 Wall shear distribution in case CR13.

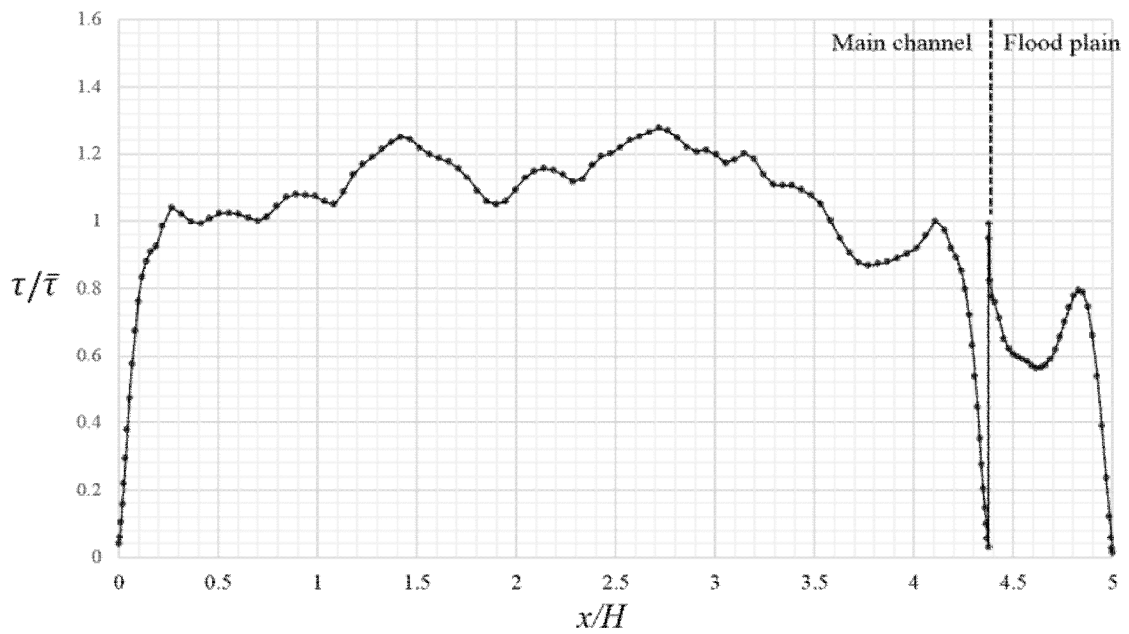


Figure 4.67 Wall shear distribution in case CR14.

In $h/H = 0.75$, relatively high shear stresses are seen near the junction of floodplain and conner vortex effect near the side wall of floodplain is diminished. Local high shear stress at the junction edge is also diminished. In case CR11, maximum shear stress is seen near the junction of floodplain and it decreases along lateral direction of the floodplain and minimum shear stress is seen near the side wall of the floodplain. This maximum shear stress in the floodplain decreases with the floodplain width decrease. In case CR12, shear stresses in the main channel increase slightly and shear stresses in the floodplain decrease slightly compared with case CR11.

In case CR12, maximum shear stresses in the main channel and floodplain have similar values. Finally, in case CR13 maximum shear stress in the main channel is over the maximum value in the floodplain.

With decrease of the floodplain width, difference between maximum and minimum shear stresses in the floodplain decrease.

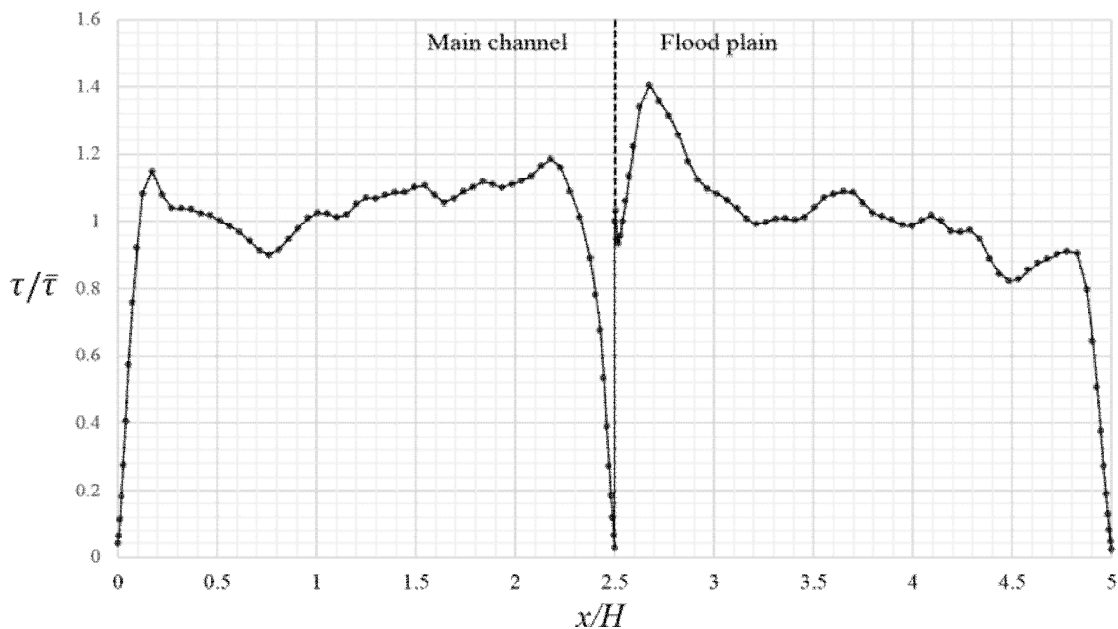


Figure 4.68 Wall shear distribution in case CR21.

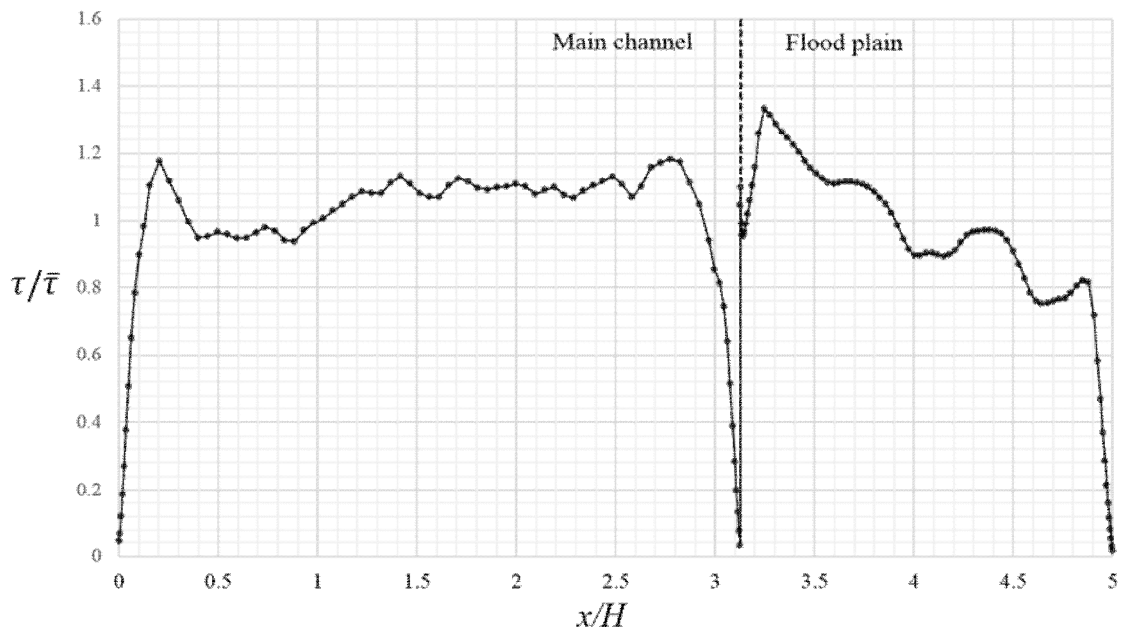


Figure 4.69 Wall shear distribution in case CR22.

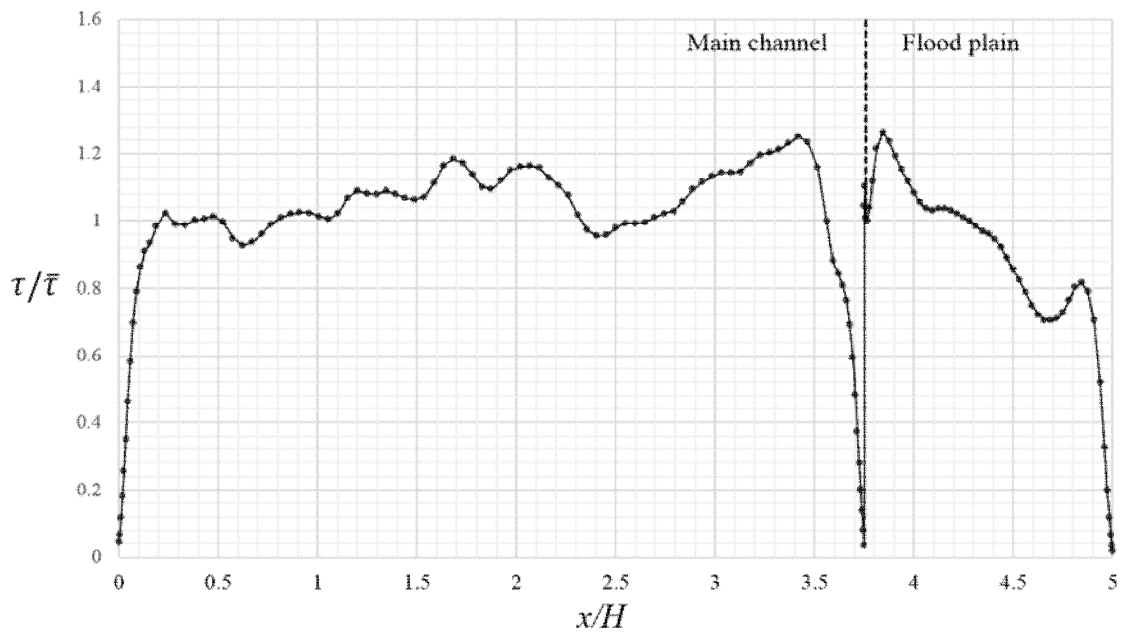


Figure 4.70 Wall shear distribution in case CR23.

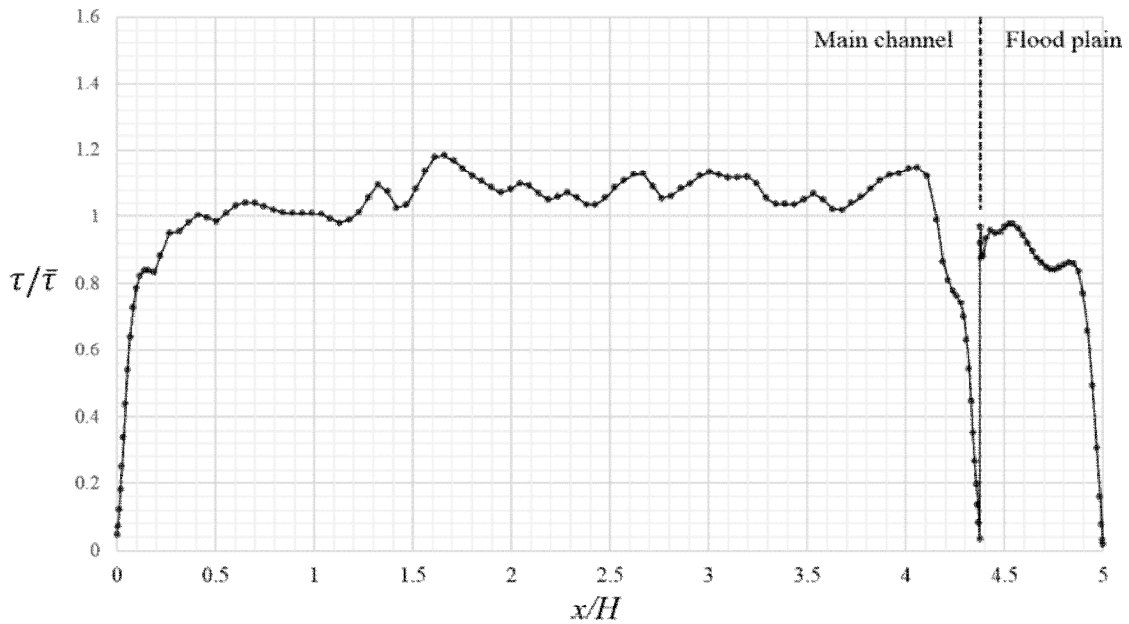


Figure 4.71 Wall shear distribution in case CR24.

4.3 Trapezoidal Compound Open Channels

4.3.1 Simulation cases

Total 9 cases of trapezoidal compound open channels are simulated for various depth ratio and width ratio (Table 4.5 and Figure 4.72 – 4.80). Depth ratio (h/H) of the cases range from 0.25 to 0.75 and width ratio (b/B) of the cases range from 0.500 to 0.750, covering the narrow, wide, shallow and deep shapes of the floodplain. Side wall slopes of main channel and floodplain are fixed with 1:1. Mean velocity is imposed as driving force ranging from 0.288 to 0.368. Corresponding Reynolds numbers range from 48,000 to 128,800. Boundary conditions coincide with those of verification test cases. The computational domain is discretized with a fine non-uniform grid in x and y direction and a fine uniform grid in z direction.

Table 4.5 Simulation cases of trapezoidal compound channels.

Case	H (m)	h (m)	B (m)	b (m)	h/H	b/B	Mean velocity (m/s)	Reynolds Re
CT01	0.08	0.04	0.4	0.20	0.50	0.500	0.349	69,800
CT02	0.08	0.04	0.4	0.25	0.50	0.625	0.349	87,250
CT03	0.08	0.04	0.4	0.30	0.50	0.750	0.349	104,700
CT11	0.08	0.02	0.4	0.20	0.25	0.500	0.288	48,000
CT12	0.08	0.02	0.4	0.25	0.25	0.625	0.349	72,708
CT13	0.08	0.02	0.4	0.30	0.25	0.750	0.349	87,250
CT21	0.08	0.06	0.4	0.20	0.75	0.500	0.368	85,867
CT22	0.08	0.06	0.4	0.25	0.75	0.625	0.368	107,333
CT23	0.08	0.06	0.4	0.30	0.75	0.750	0.368	128,800

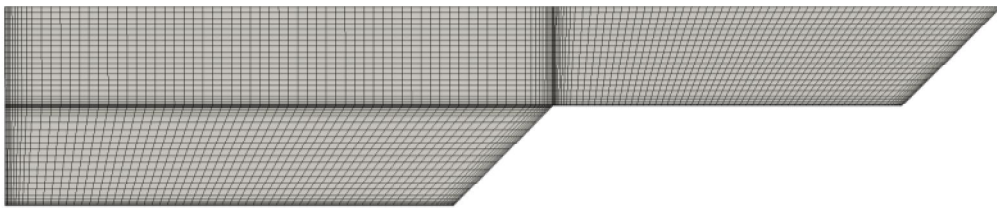


Figure 4.72 Geometry and mesh of case CT01.

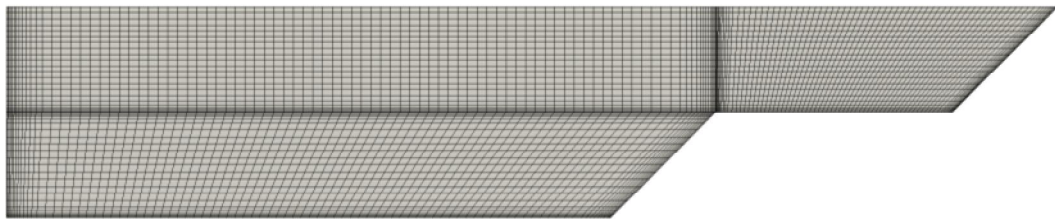


Figure 4.73 Geometry and mesh of case CT02.

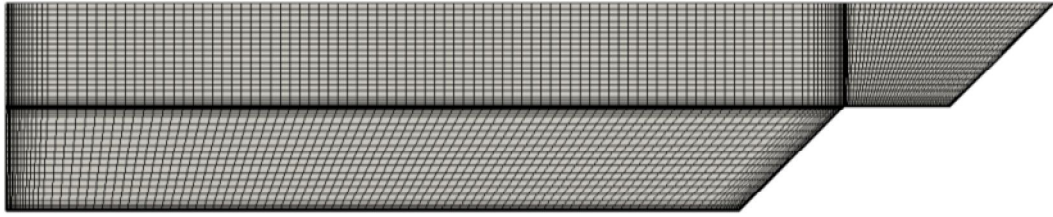


Figure 4.74 Geometry and mesh of case CT03.

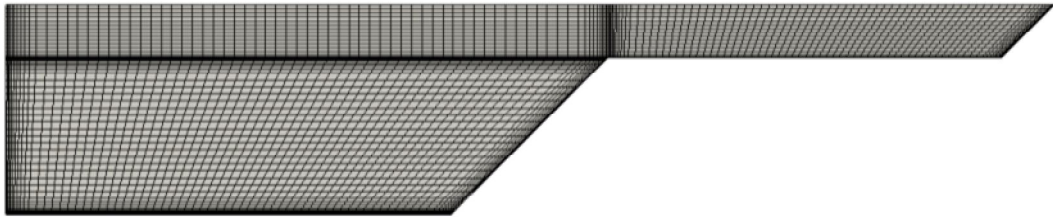


Figure 4.75 Geometry and mesh of case CT11.

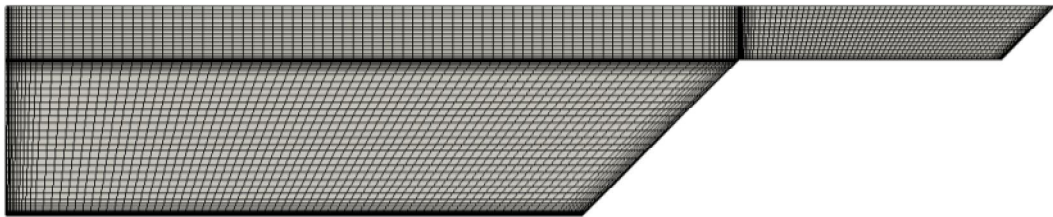


Figure 4.76 Geometry and mesh of case CT12.

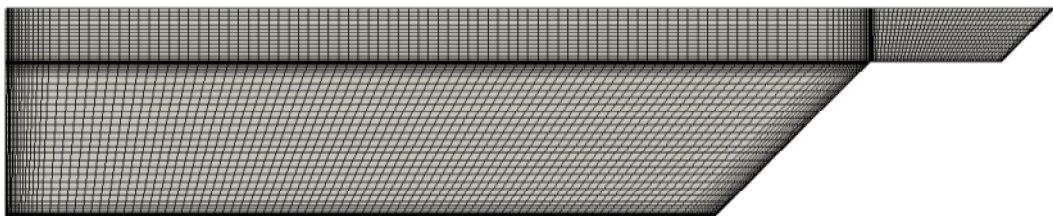


Figure 4.77 Geometry and mesh of case CT13.

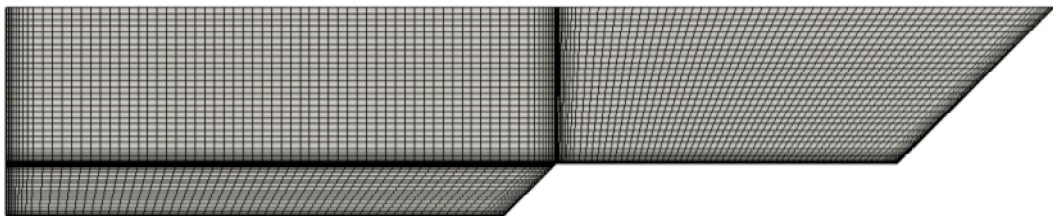


Figure 4.78 Geometry and mesh of case CT21.

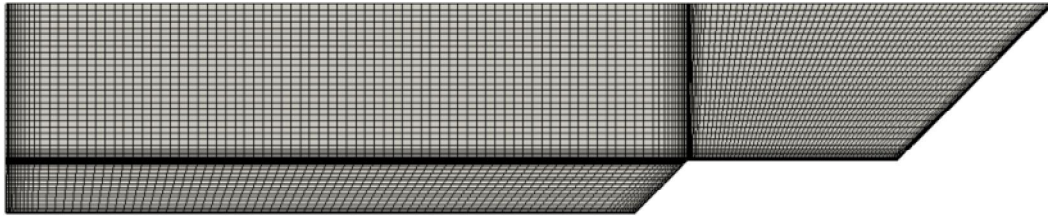


Figure 4.79 Geometry and mesh of case CT22.

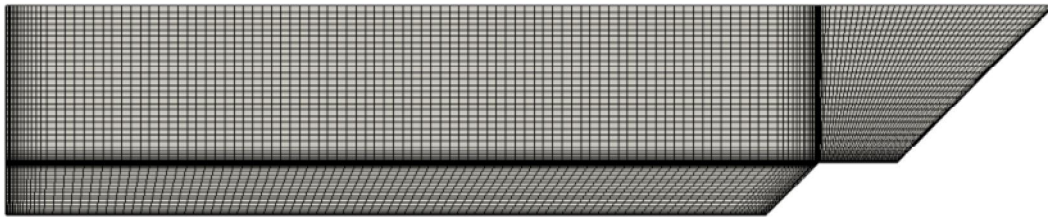


Figure 4.80 Geometry and mesh of case CT23.

4.3.2 Results and Analysis

(1) Mean velocity distribution

Figure 4.81 to Figure 4.89 show simulated isovel lines of the streamwise mean velocity U normalized by U_{\max} .

Overall mean velocity distributions of rectangular and trapezoidal compound channel show similar patterns, however some differences are seen. In rectangular cases contour lines are distorted slightly to the left side wall, on the other hand, in the trapezoidal cases contour lines are distorted slightly to the floodplain. This difference is due to resistance of the junction of the main channel and floodplain. More resistance due to the junction is produced in the rectangular cases than in the trapezoidal cases, hence the main channel velocity near the junction decreases in the rectangular cases.

Velocity bulge in the junction also decreases in the trapezoidal cases due to the decrease of the wall resistance. This decrease of the wall resistance in the trapezoidal cases is due to the decrease of the junction angle.

Velocity bulge in the sidewall of the floodplain is seen in the both of the rectangular and trapezoidal cases. This velocity bulge is more clear in the rectangular cases and this

seem to be related to the formation of the inner vortex in the sidewall of the floodplain.

Velocity dip in the main channel is more distinct in the shallow floodplain cases and it becomes unclear in the deep floodplain cases. Velocity bulge in the junction is seen in the case CT01, CT02, CT03, CT21, CT22 and CT23 and velocity bulge in the side wall of the floodplain is also seen in the case CT01, CT02, CT21 and CT22. The bulge phenomena is seen in the cases with deep and wide floodplain conditions, which means that generation of the velocity bulge is related to the size and strength of the secondary currents formed in the floodplain. Lateral position of the high velocity region in the main channels moves to the floodplain with floodplain depth increase.

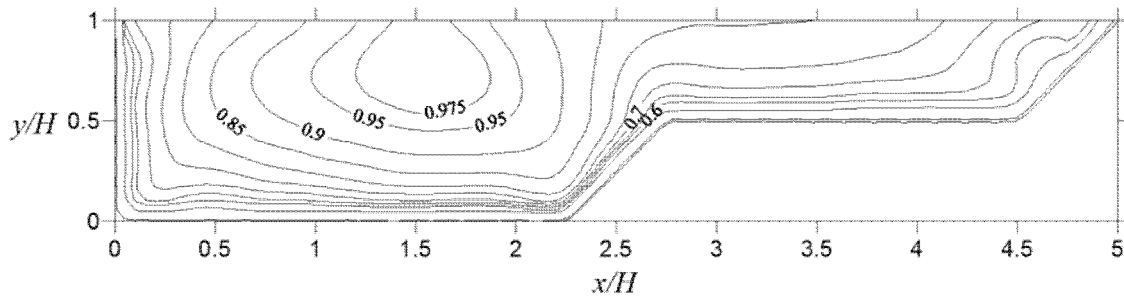


Figure 4.81 Streamwise mean velocity in case CT01.

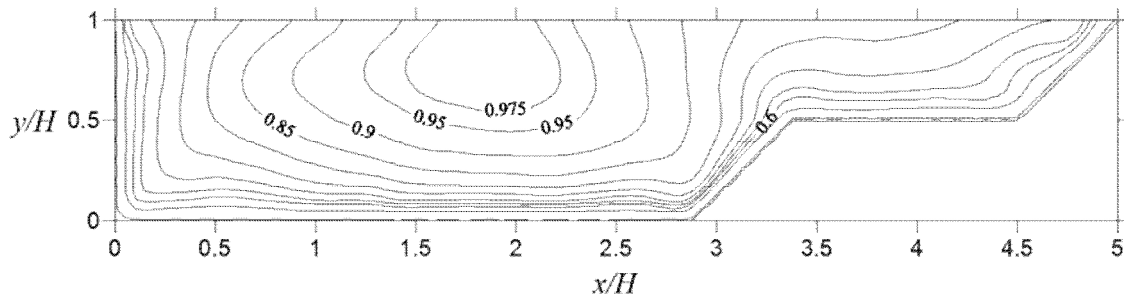


Figure 4.82 Streamwise mean velocity in case CT02.

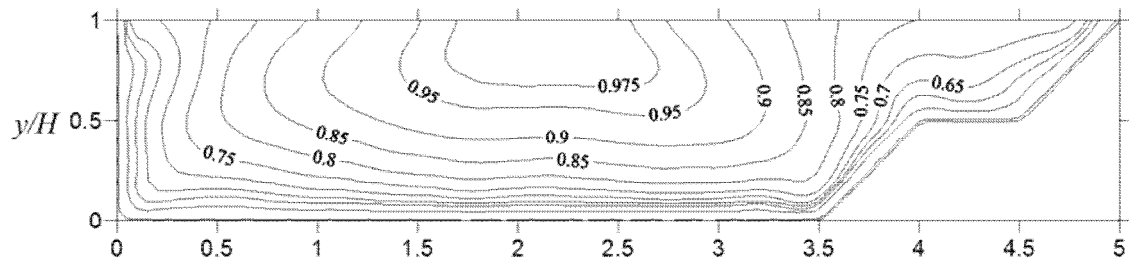


Figure 4.83 Streamwise mean velocity in case CT03.

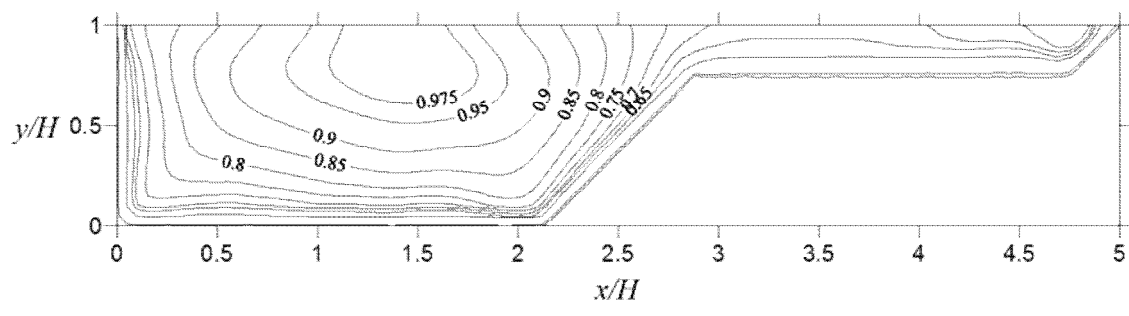


Figure 4.84 Streamwise mean velocity in case CT11.

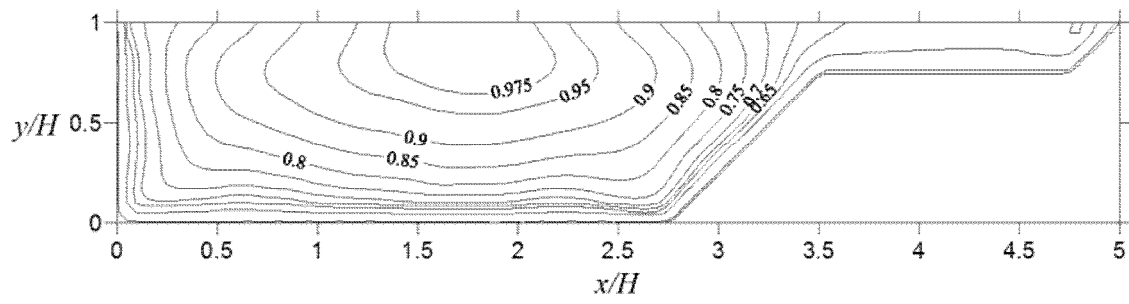


Figure 4.85 Streamwise mean velocity in case CT12.

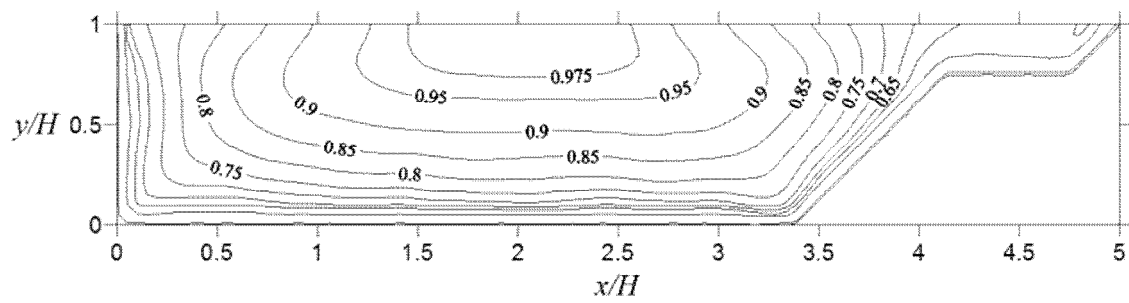


Figure 4.86 Streamwise mean velocity in case CT13.

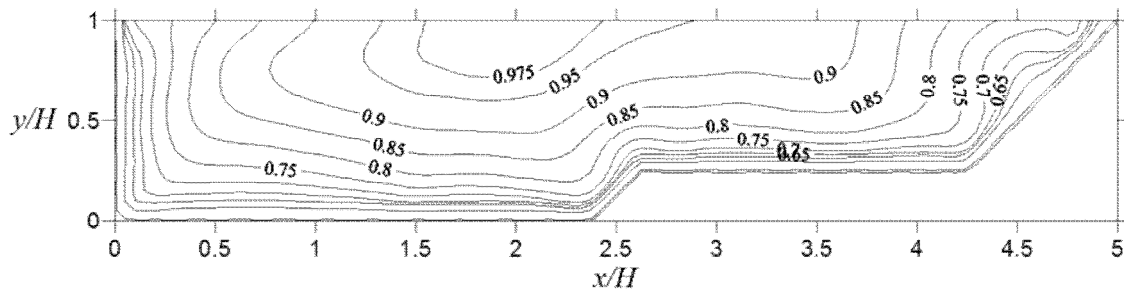


Figure 4.87 Streamwise mean velocity in case CT21.

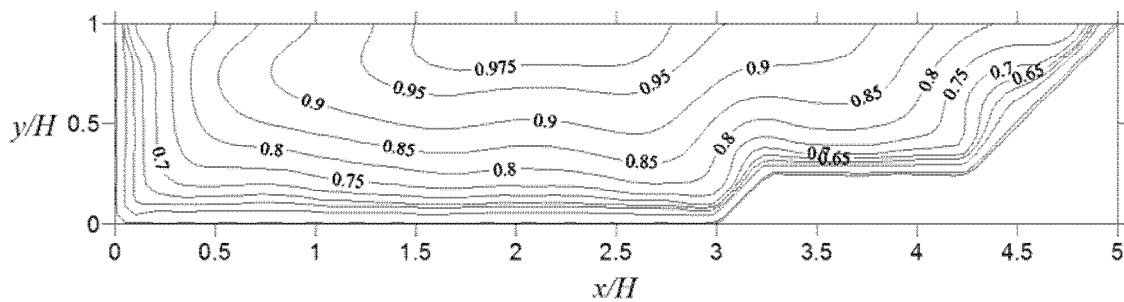


Figure 4.88 Streamwise mean velocity in case CT22.

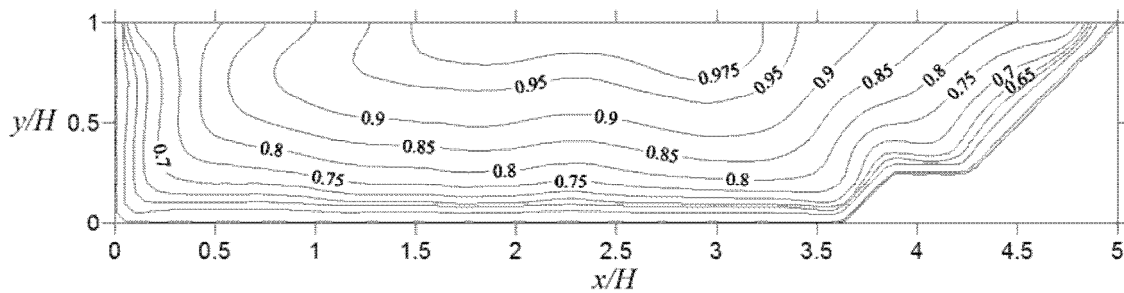


Figure 4.89 Streamwise mean velocity in case CT23.

(2) Secondary flow

Figure 4.90 to Figure 4.98 show the vector description of the secondary currents in the trapezoidal compound channel cases.

In the same floodplain depth conditions, the secondary currents show analogous patterns in the side wall of main channel and the junction region of main channel and floodplain. The secondary currents in the side wall of floodplain also show analogous patterns in the same floodplain depth conditions. The main difference with change of

floodplain width is observed in floodplain vortex. In $h/H = 0.5$, region of the floodplain vortex is decreased and the boundary between floodplain vortex and inner vortex formed in the side wall of floodplain becomes unclear with floodplain depth increase. In the case CT03, the floodplain vortex is dominant in the floodplain region and the inner vortex in the floodplain side wall decreases.

In $h/H = 0.25$, magnitude of the secondary current in the surface and bed of the floodplain is nearly constant. In $h/H = 0.75$, the secondary currents shows more complicated changes in the floodplain with floodplain depth increase. In case CT21, three vortex are observed definitely in the floodplain. One floodplain vortex is observed in the junction and middle of the floodplain. Side wall vortex is observed near the side wall of the floodplain and one inner vortex is observed adjacent to the coner of the floodplain. However the free surface vortex formed in the middle of the floodplain diminishes with floodplain width decrease and finally becomes unclear in the case CT23. Surface vortex formed near the side wall also diminishes and disappears with floodplain width decrease.

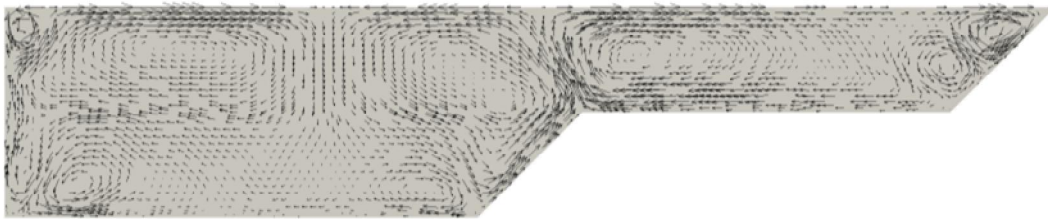


Figure 4.90 Secondary flows in case CT01.

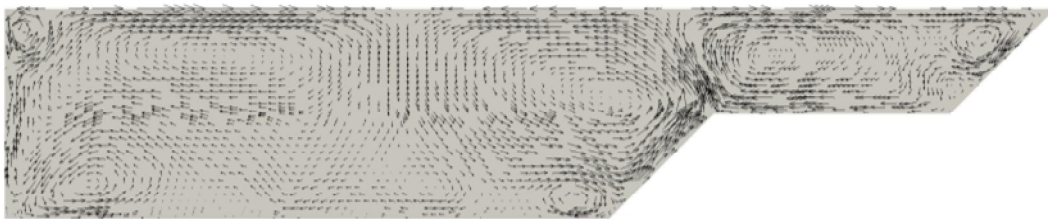


Figure 4.91 Secondary flows in case CT02.

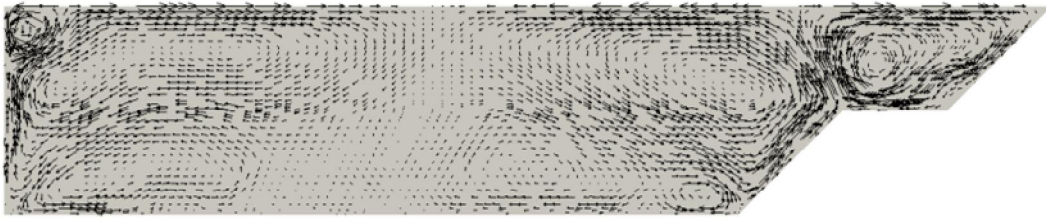


Figure 4.92 Secondary flows in case CT03.

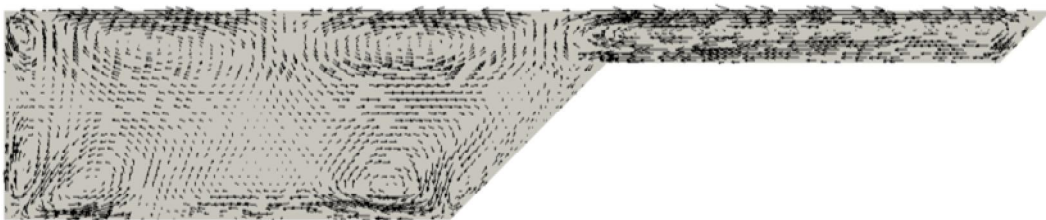


Figure 4.93 Secondary flows in case CT11.

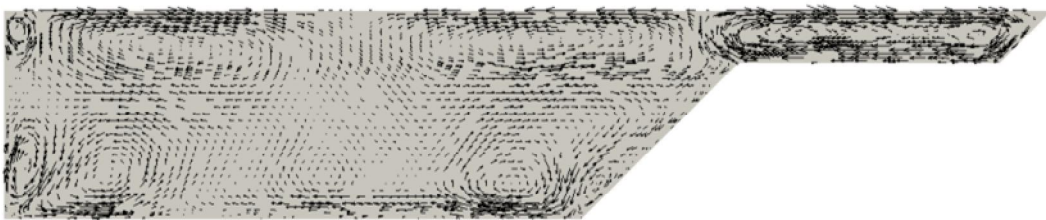


Figure 4.94 Secondary flows in case CT12.



Figure 4.95 Secondary flows in case CT13.



Figure 4.96 Secondary flows in case CT21.

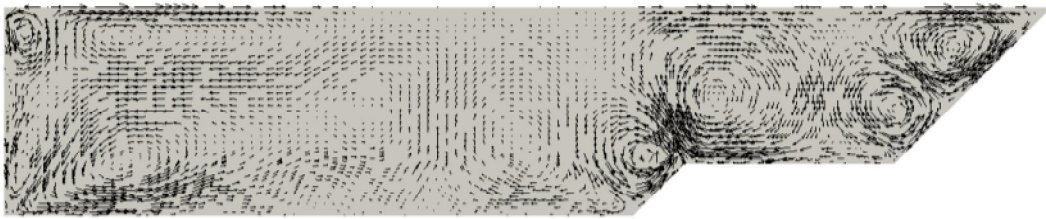


Figure 4.97 Secondary flows in case CT22.

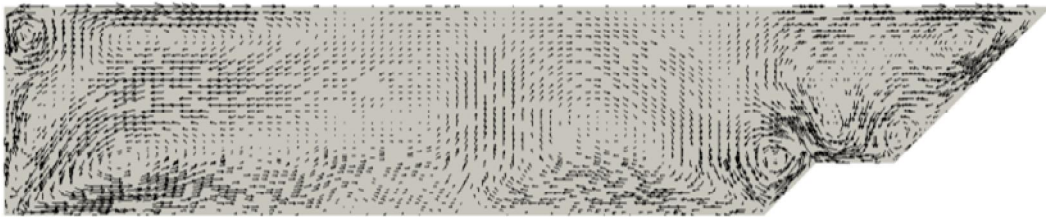


Figure 4.98 Secondary flows in case CT23.

(3) Wall shear distribution

Figure 4.99 to Figure 4.107 show wall shear stress distribution normalized by the averaged shear stress $\bar{\tau}$ in the trapezoidal compound channels.

In $h/H = 0.5$, relatively high shear stresses are seen near the junction of the main channel and floodplain and the maximum shear stresses are seen in the lower part of the bank. Shear stresses in the levee is somewhat greater than the values of floodplain. With the decrease of the floodplain width, maximum shear stresses in the bank, shear stresses in the floodplain and levee decrease.

In $h/H = 0.25$, relatively high shear stresses are also seen near the junction of the

main channel and floodplain and the maximum shear stresses are seen near the junction of the main channel. High shear stresses are also seen in the lower part of the bank and shear stresses in the levee is rather greater than the values in the floodplain. Shear stresses in the floodplain decrease rapidly with lateral direction. With the decrease of the floodplain width, maximum shear stresses in the bank, shear stresses in the floodplain and levee decrease.

In $h/H = 0.75$, relatively high shear stresses are seen in the junction of the main channel and floodplain, and the junction of the floodplain and levee. The maximum shear stresses are seen near the junction of the main channel. High shear stresses are also seen in the lower part of the bank, the junction of the floodplain, and the levee, but the magnitudes changes greatly with change of the floodplain width. In the case CT21, maximum shear stress is seen in the junction of the main channel, and the high shear stress in the bank is lower than the high values in the floodplain. However, in the case CT22, maximum shear stress is seen in the bank. In the case CT23, maximum shear stress in the main channel and floodplain is similar.

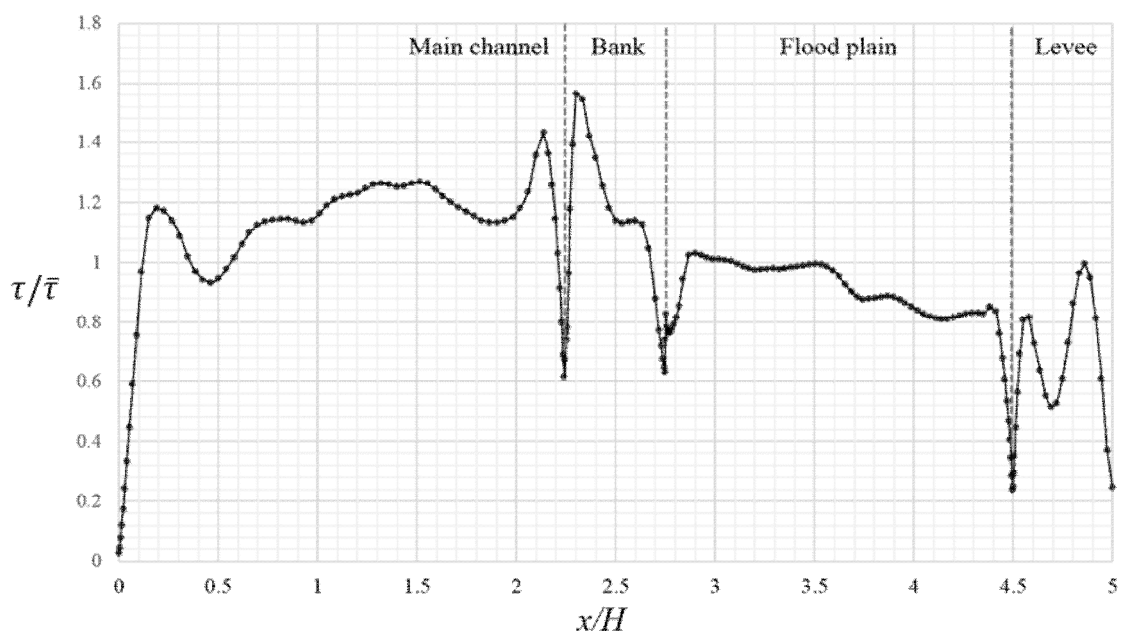


Figure 4.99 Wall shear distribution in case CT01.

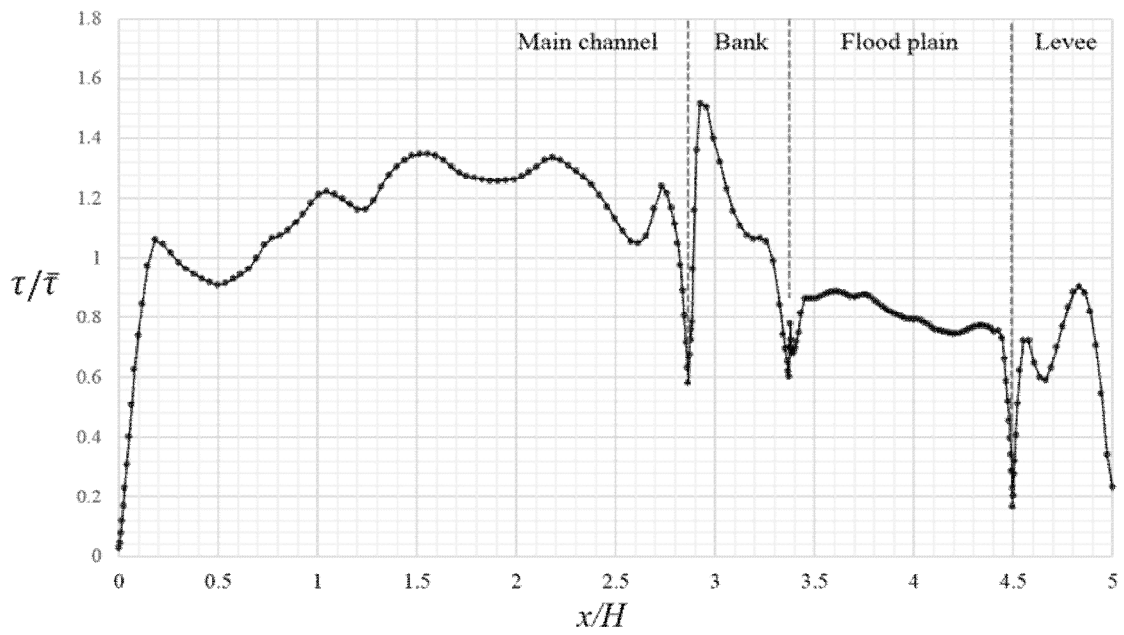


Figure 4.100 Wall shear distribution in case CT02.

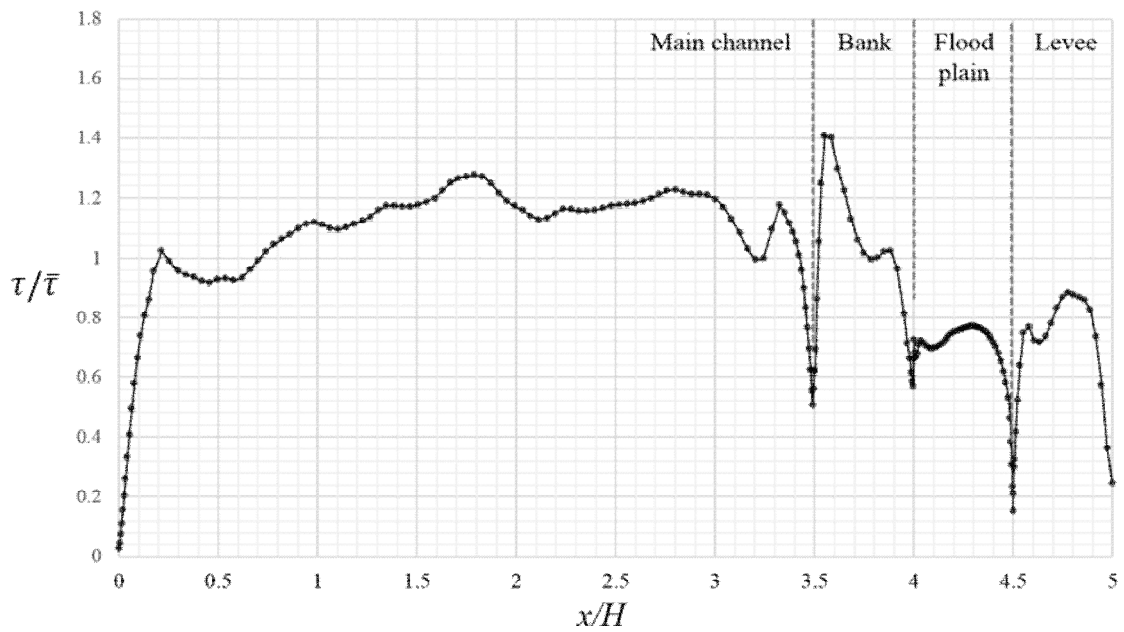


Figure 4.101 Wall shear distribution in case CT03.

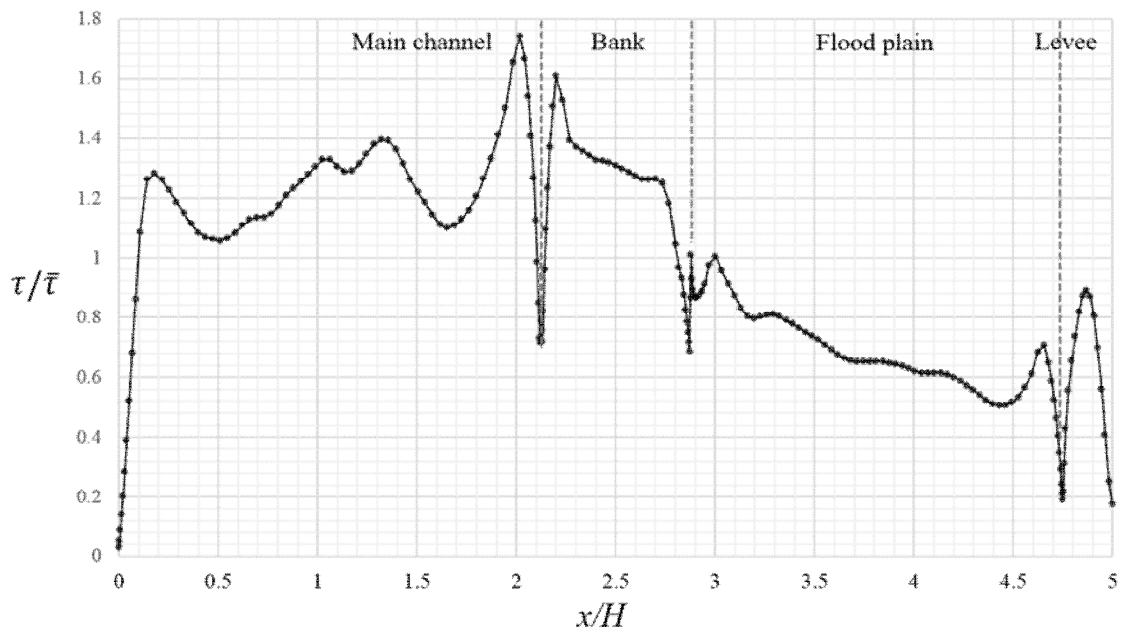


Figure 4.102 Wall shear distribution in case CT11.

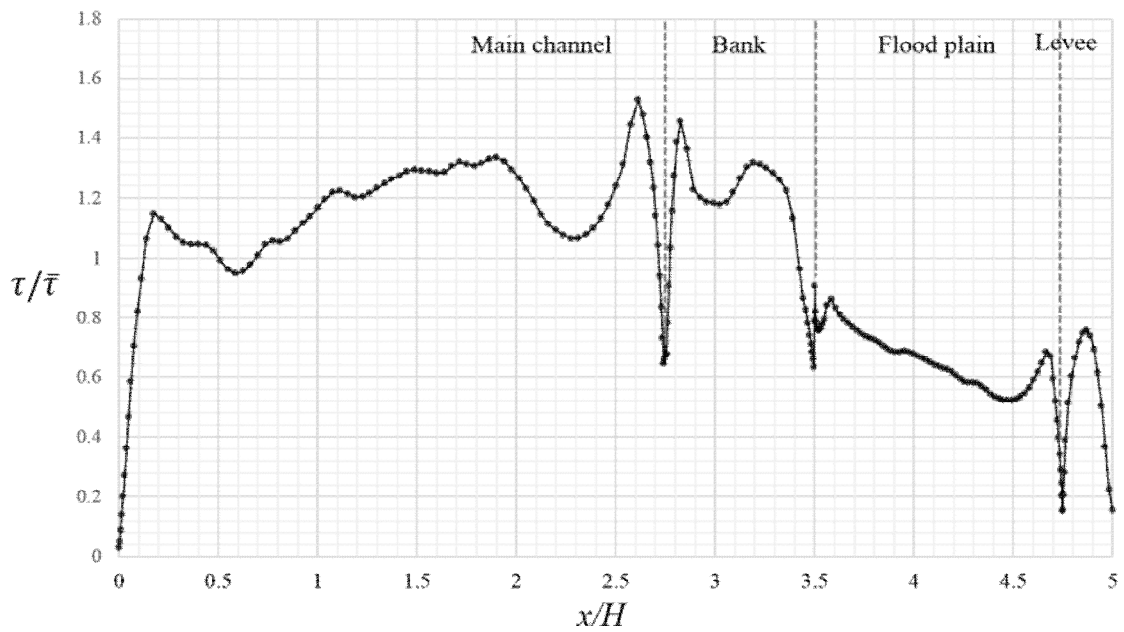


Figure 4.103 Wall shear distribution in case CT12.

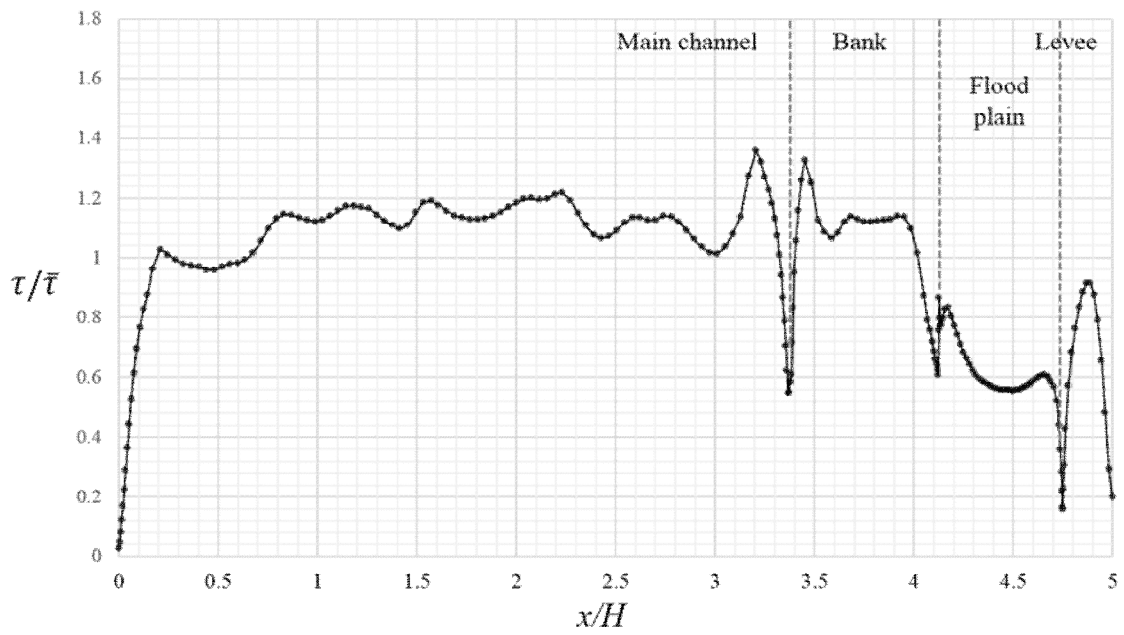


Figure 4.104 Wall shear distribution in case CT13.

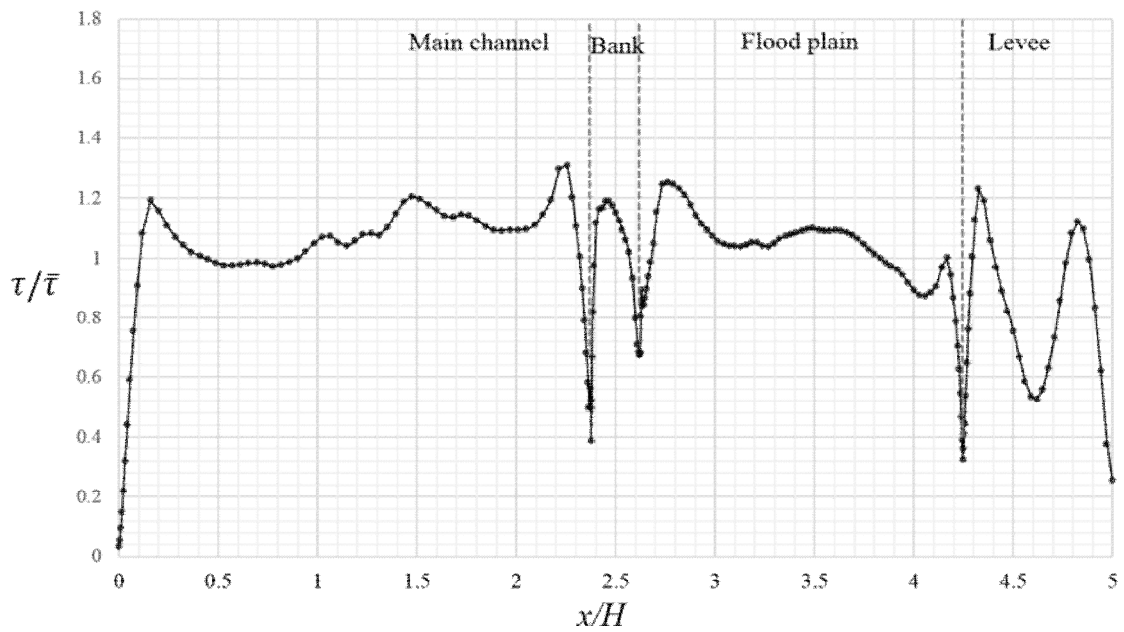


Figure 4.105 Wall shear distribution in case CT21.

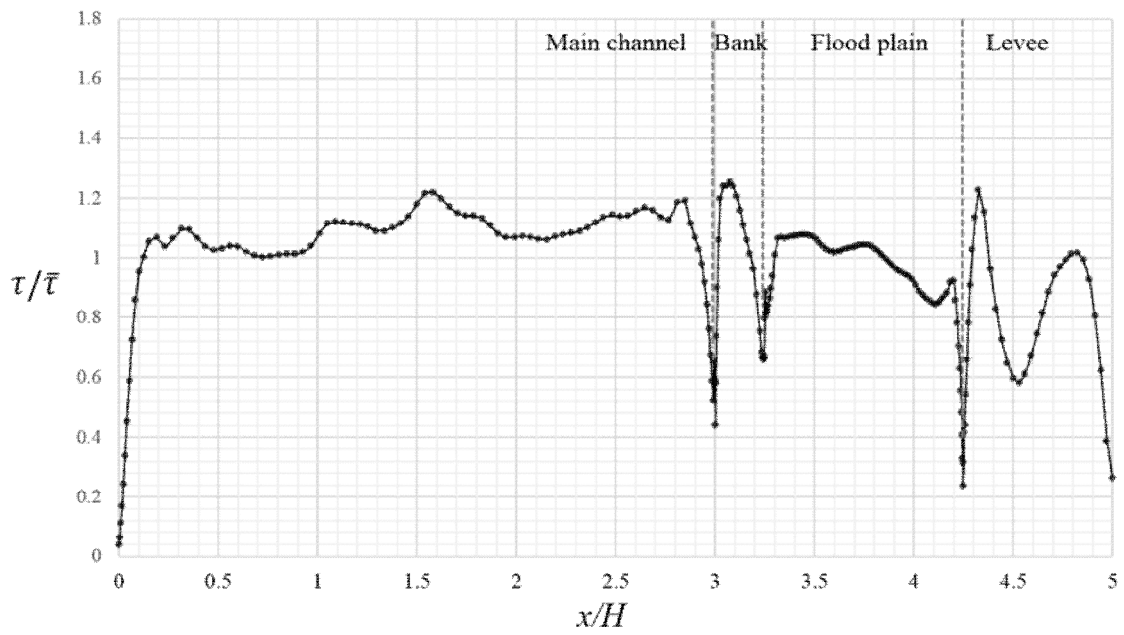


Figure 4.106 Wall shear distribution in case CT22.

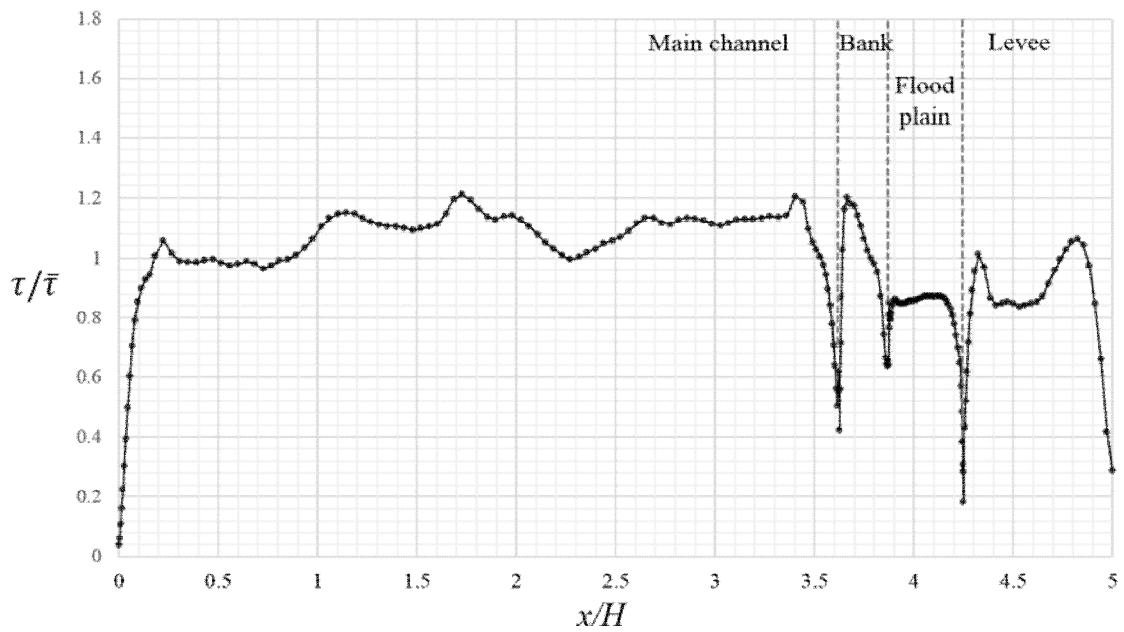


Figure 4.107 Wall shear distribution in case CT23.

CHAPTER 5

METHODS FOR DETERMINING DESIGN

TRACTIVE FORCES

5.1 Strategy for the Evaluation Methods

Tractive forces evaluation is needed in the channel and river design and it can be calculated from various hydraulic analysis. However, practical methods for design tractive forces of compound open channels are not proposed definitely and proposed practical methods have some disadvantages and limitations as introduced in chapter 2.

In this study, practical methods for design tractive force in compound open channels are suggested based on the numerical simulation results of various compound open channels. In the methods the main factors affecting the distribution of the shear stress are floodplain depth ratio and floodplain width ratio.

In the first method, design factors are suggested as multiplying factors of channel parts (main channel, bank, floodplain, and levee) to cross sectional averaged shear stress considering the compound open channel shapes as the depth ratio and width ratio.

In the second method, design factors are suggested as the friction factors of the channel parts to the depth averaged velocity also considering the compound open channel shapes as the depth ratio and width ratio.

5.2 Design factors for cross sectional averaged shear stress

5.2.1 Rectangular compound channels

In this section, the design factors mean the normalized maximum shear stresses in the channel part and the factors can be used as multiplying factors to cross sectional averaged shear stress to produce the design shear stress.

The design factors for main channel and floodplain in rectangular compound channels are provided as Table 5.1 and 5.2. The values are selected from the LES simulation results of the chapter 4 and they are maximum normalized shear stresses of main channel and floodplain with different depth and width ratio. The design factors are also plotted with changes of depth and width ratio as Figure 5.1 to Figure 5.7. Overall design factors show some consistency with depth and width ratio, however, local reversal relations are also seen due to the local vortex formations.

In the main channel, all factors are over 1.1 and the factors decrease with depth and width ratio increase. Maximum factor in the main channel is seen in the narrow and shallow floodplain as expected and the value is 1.52. Minimum factor in the main channel is seen in the deep floodplain and the value is 1.12.

In the floodplain, overall factors are lower than the factors in the main channels. The maximum value is seen in the narrow and deep floodplain and the value is 1.40. The factors in the floodplain increase with depth ratio increase and decrease with width ratio increase as expected. Minimum factor is seen in the wide and shallow floodplain and the value is 0.79.

The design factors with various combinations of width ratio and depth ratio can be easily selected from the Figure 5.5 and Figure 5.6.

Table 5.1 The design factors in rectangular compound channels (main channel).

b/B	h/H		
	0.25	0.5	0.75
0.500	1.52	1.26	1.12
0.625	1.49	1.36	1.13
0.750	1.38	1.28	1.18
0.875	1.28	1.23	1.17

Table 5.2 The design factors in rectangular compound channels (floodplain).

b/B	h/H		
	0.25	0.5	0.75
0.500	0.96	1.09	1.40
0.625	0.83	0.97	1.33
0.750	0.81	0.85	1.26
0.875	0.79	0.80	0.98

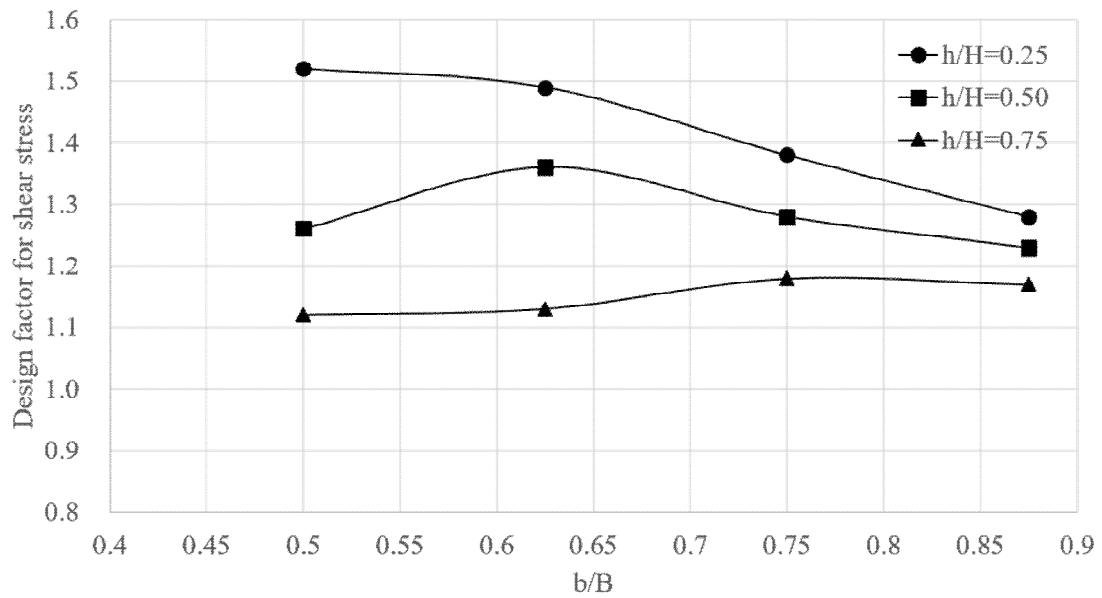


Figure 5.1 The design factors for rectangular compound channels with b/B (main channel).

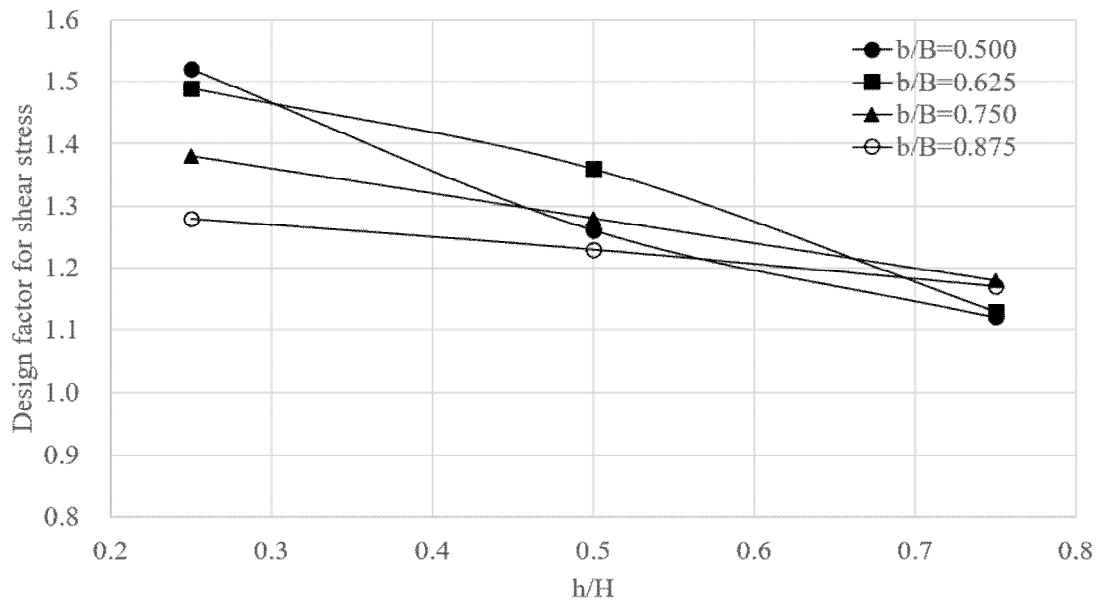


Figure 5.2 The design factors for rectangular compound channels with h/H (main channel).

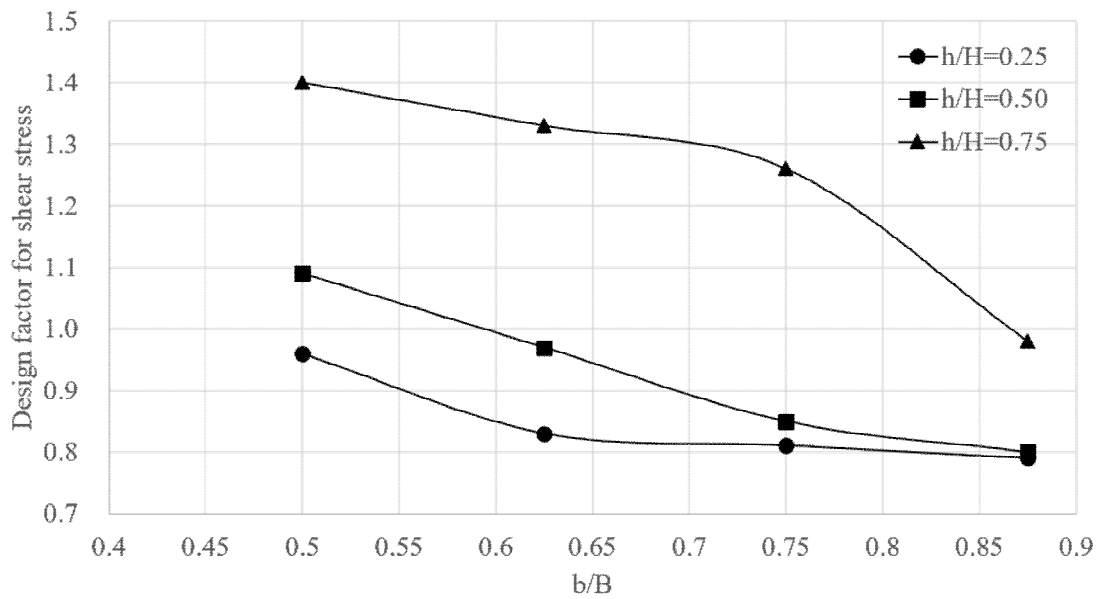


Figure 5.3 The design factors for rectangular compound channels with b/B (floodplain).

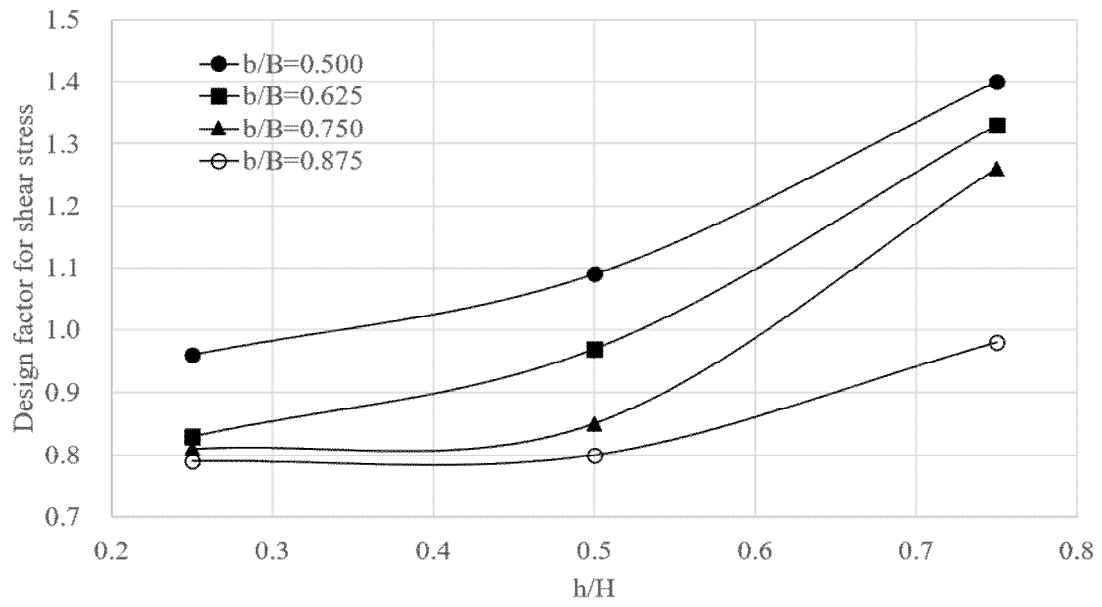


Figure 5.4 The design factors for rectangular compound channels with h/H (floodplain).

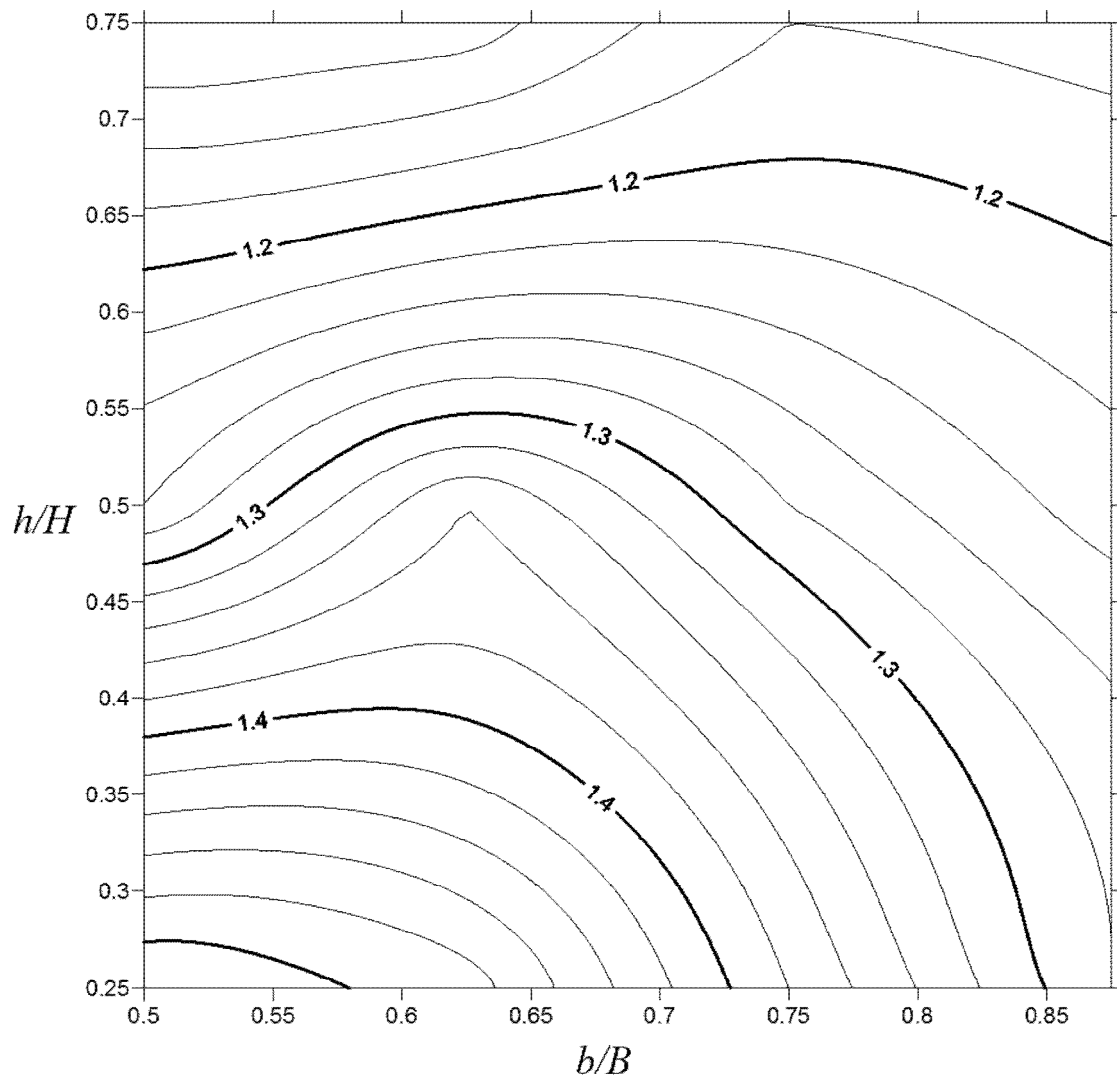


Figure 5.5 The design factors for rectangular compound channels with b/B and h/H (main channel).

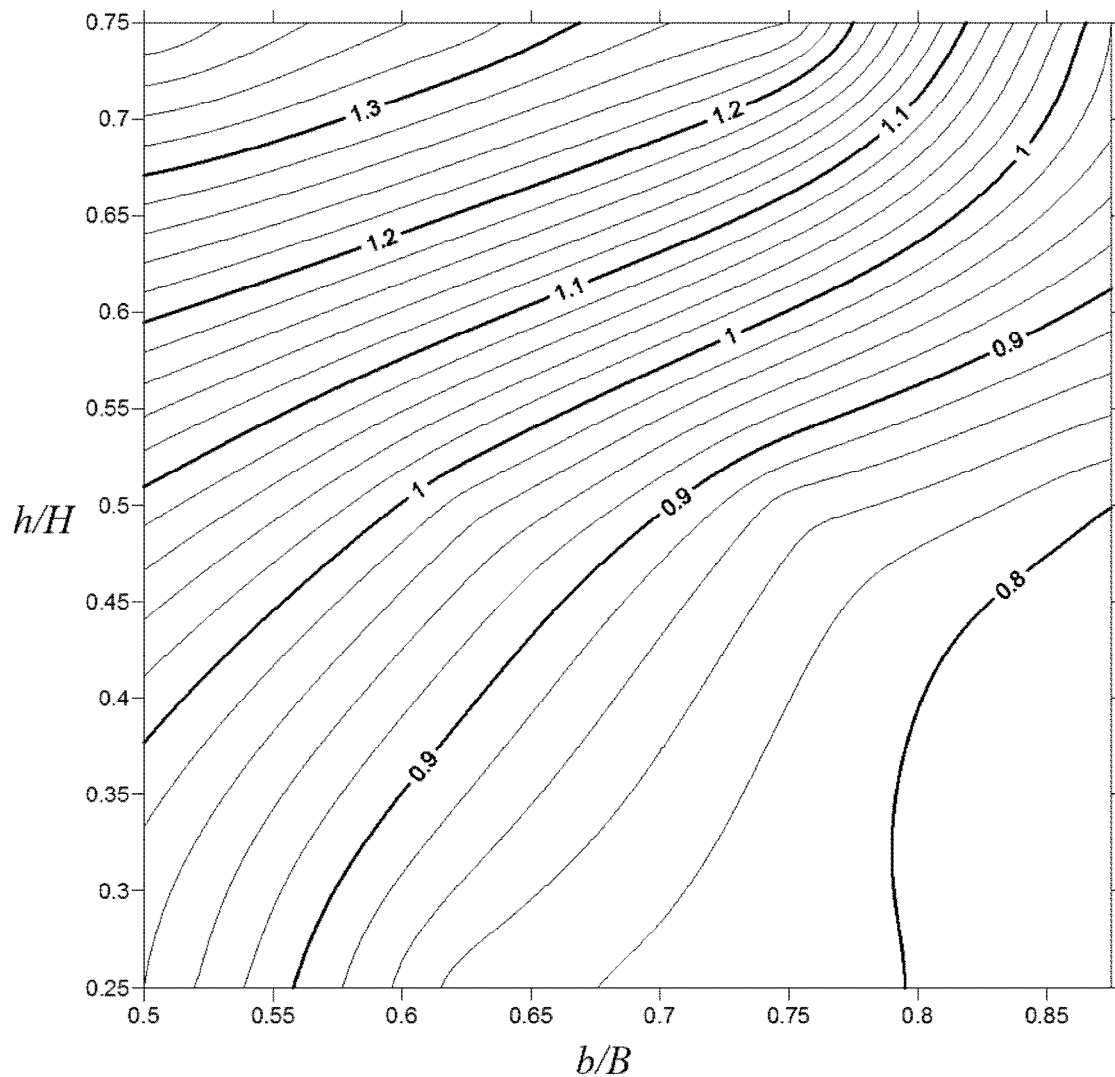


Figure 5.6 The design factors for rectangular compound channels with b/B and h/H (floodplain).

5.2.2 Trapezoidal compound channels

In this section, the design factors mean the normalized maximum shear stresses in the channel part and the factors can be used as multiplying factors to cross sectional averaged shear stress to produce the design shear stress.

The design factors for main channel and floodplain in rectangular compound channels are provided as Table 5.1 and 5.2. The values are selected from the LES simulation results of the chapter 4 and they are maximum normalized shear stresses of main

channel and floodplain with different depth and width ratio. The design factors are also plotted with changes of depth and width ratio as Figure 5.1 to Figure 5.7. Overall design factors show some consistency with depth and width ratio, however, local reversal relations are also seen due to the local vortex formations.

In the main channel, all factors are over 1.1 and the factors decrease with depth and width ratio increase. Maximum factor in the main channel is seen in the narrow and shallow floodplain as expected and the value is 1.52. Minimum factor in the main channel is seen in the deep floodplain and the value is 1.12.

In the floodplain, overall factors are lower than the factors in the main channels. The maximum value is seen in the narrow and deep floodplain and the value is 1.40. The factors in the floodplain increase with depth ratio increase and decrease with width ratio increase as expected. Minimum factor is seen in the wide and shallow floodplain and the value is 0.79.

The design factors with various combinations of width ratio and depth ratio can be easily selected from the Figure 5.5 and Figure 5.6.

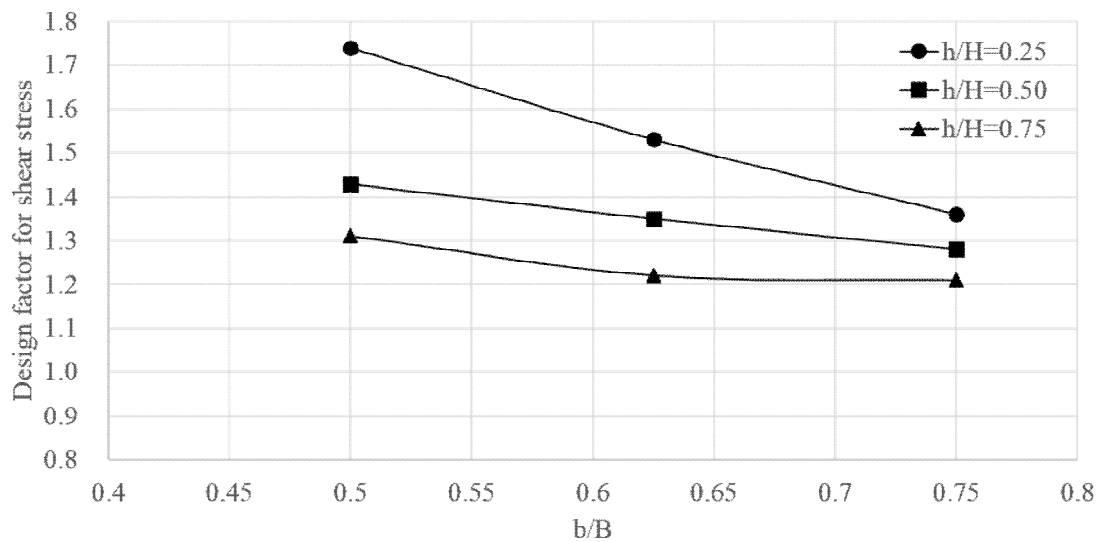


Figure 5.7 The design factors for trapezoidal compound channels with b/B (main channel).

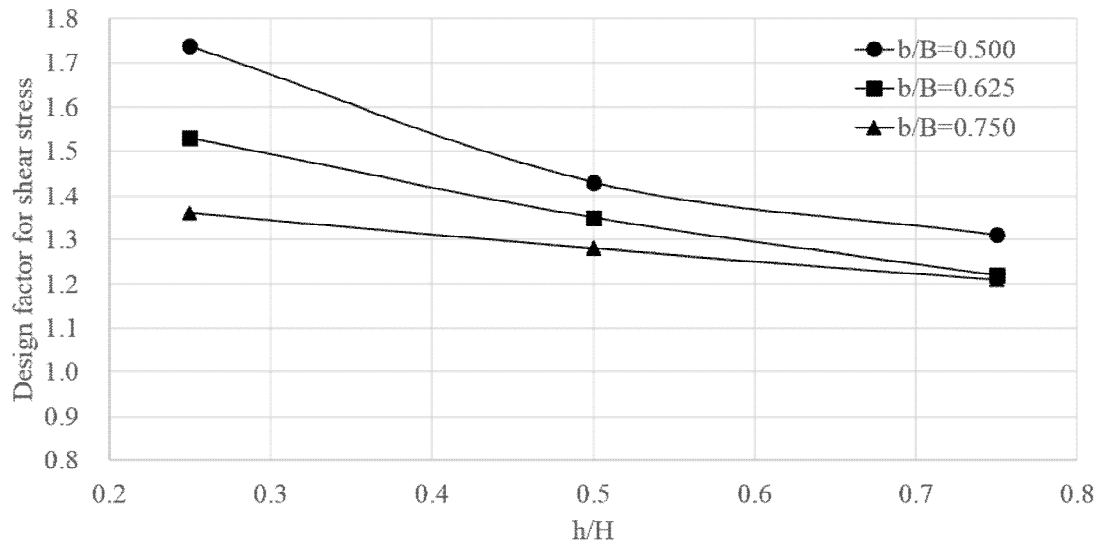


Figure 5.8 The design factors for trapezoidal compound channels with h/H (main channel).

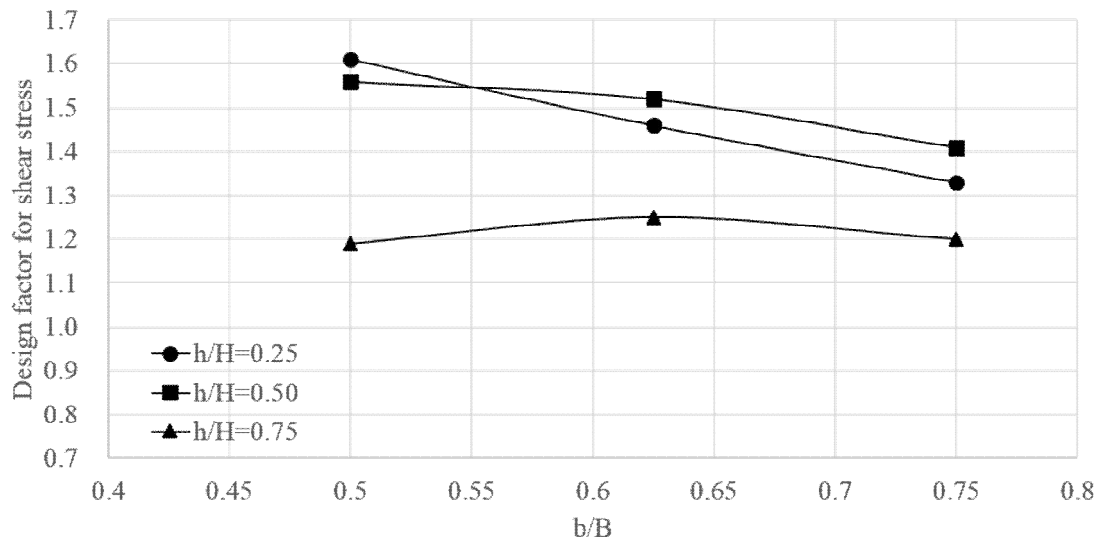


Figure 5.9 The design factors for trapezoidal compound channels with b/B (bank).

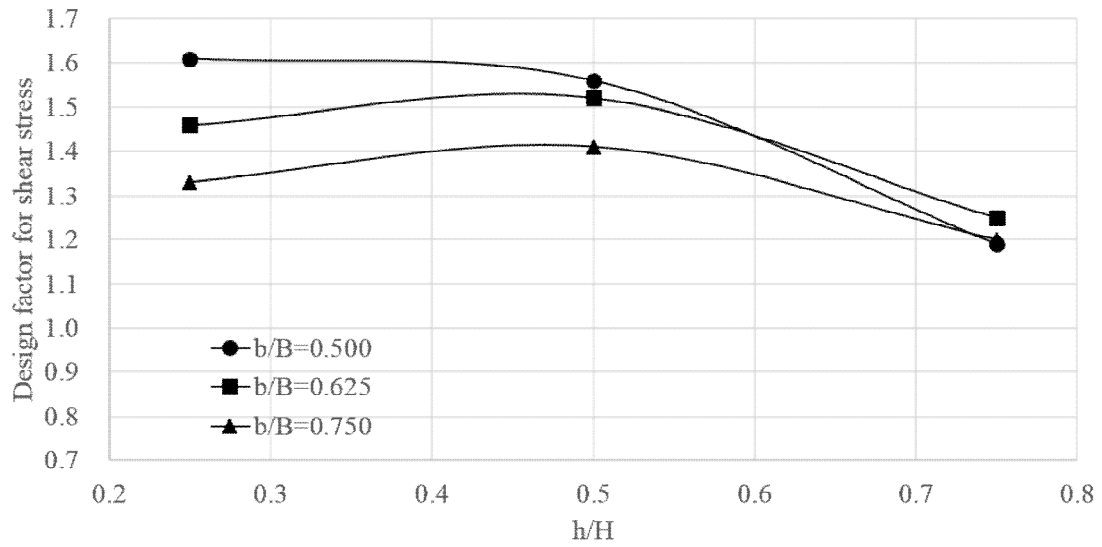


Figure 5.10 The design factors for trapezoidal compound channels with h/H (bank).

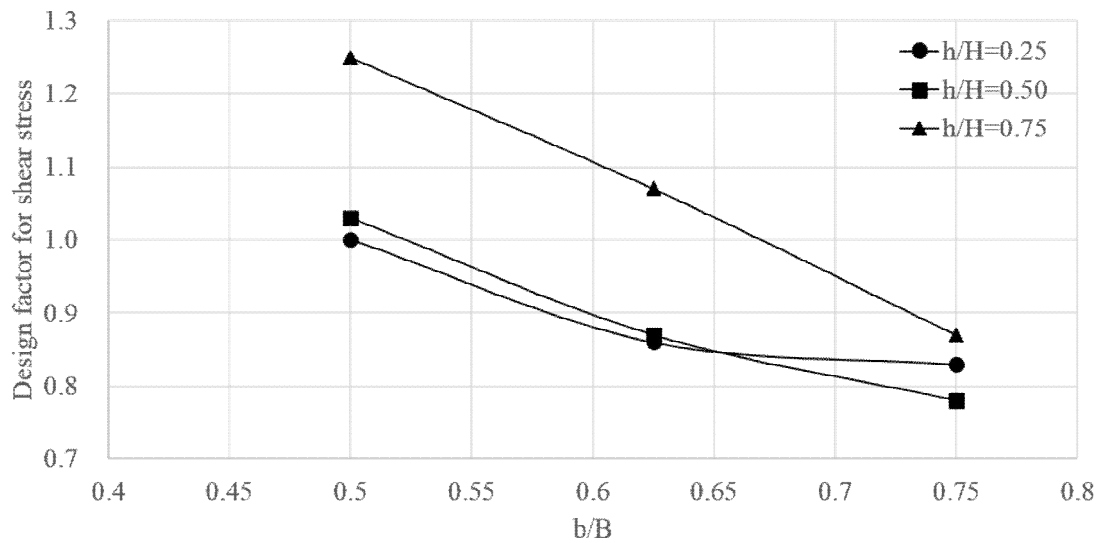


Figure 5.11 The design factors for trapezoidal compound channels with b/B (floodplain).

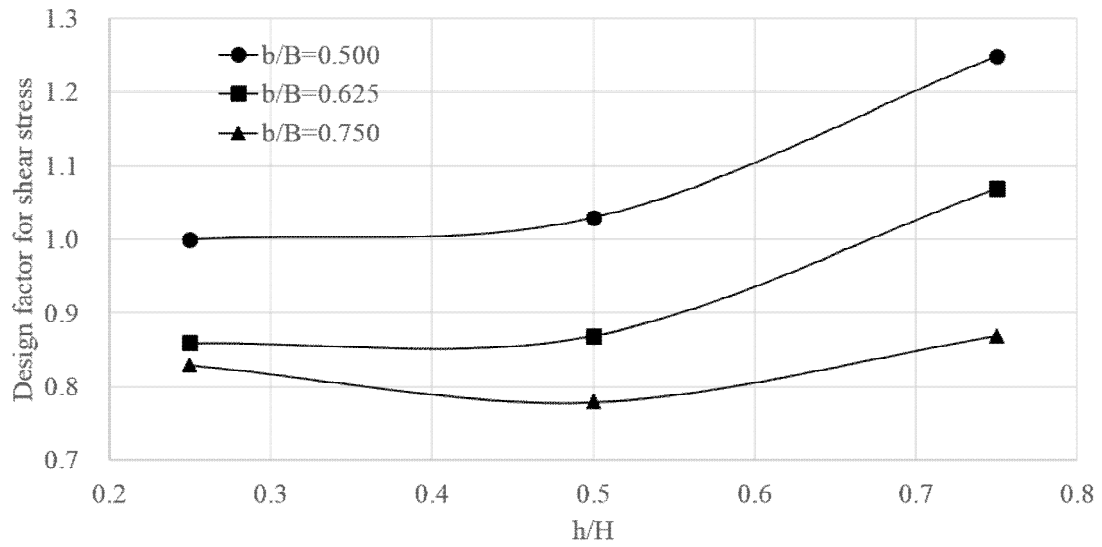


Figure 5.12 The design factors for trapezoidal compound channels with h/H (floodplain).

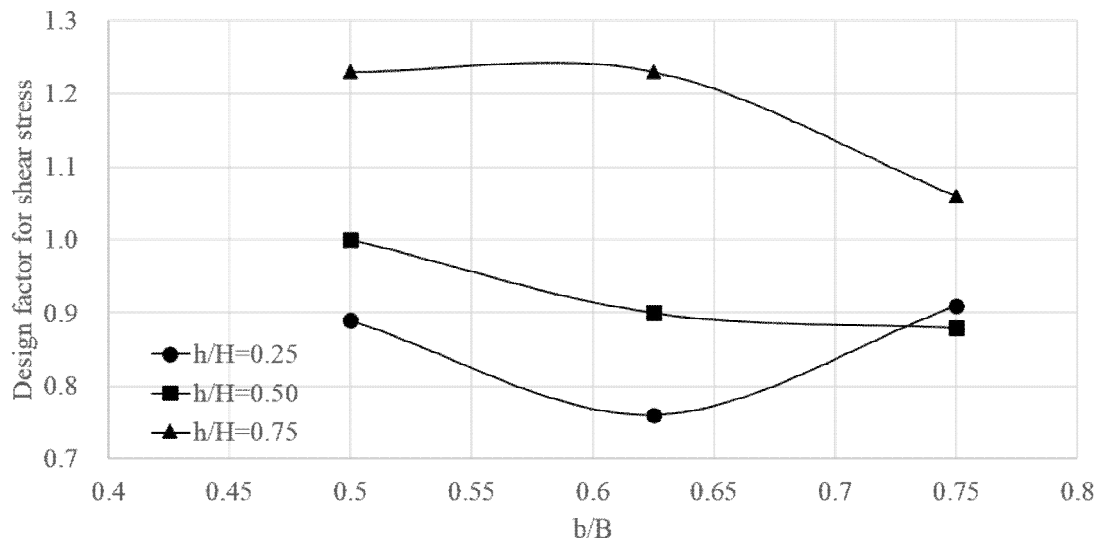


Figure 5.13 The design factors for trapezoidal compound channels with b/B (levee).

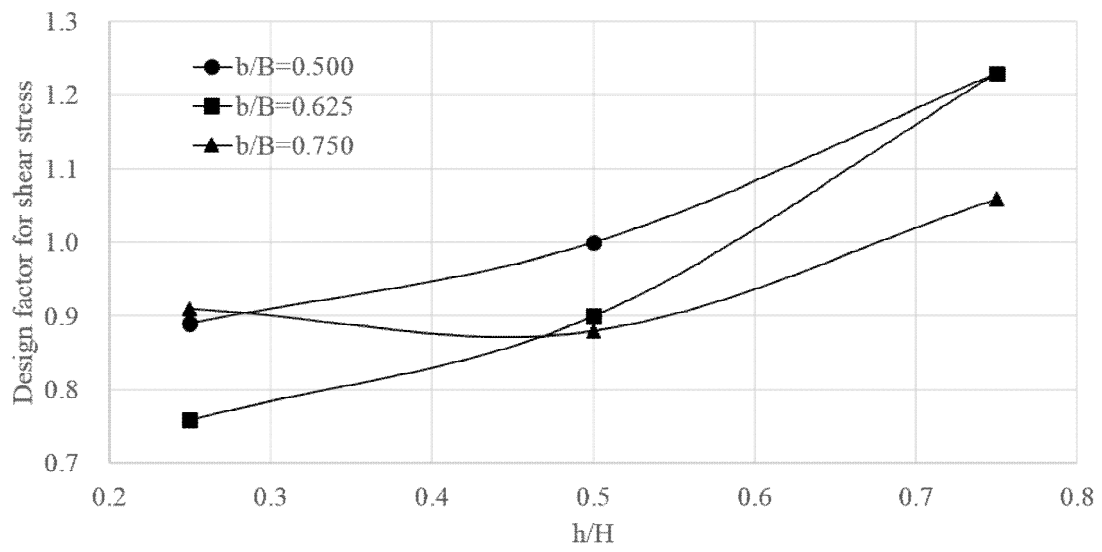


Figure 5.14 The design factors for trapezoidal compound channels with h/H (levee).

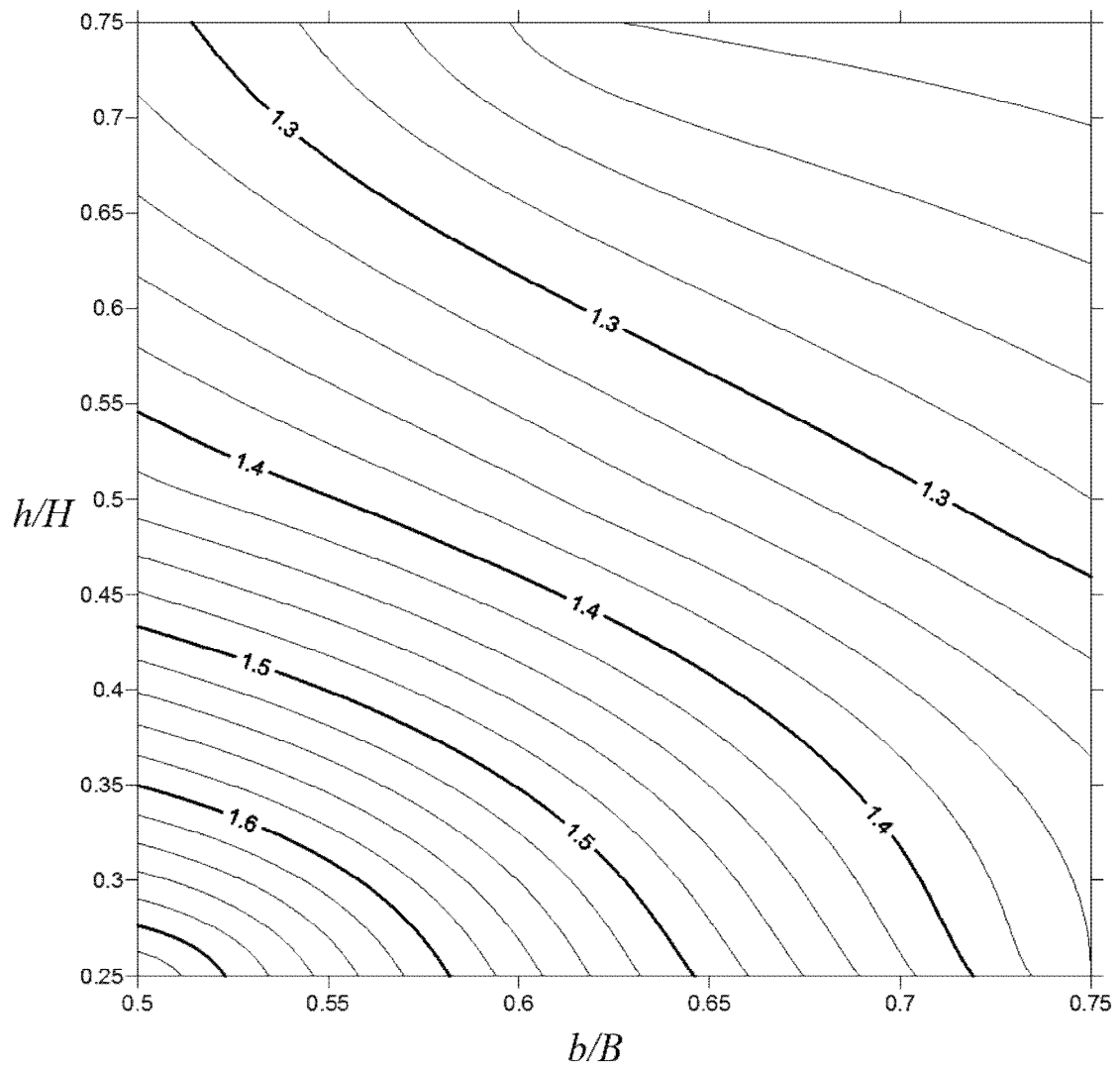


Figure 5.15 The design factors for trapezoidal compound channels with b/B and h/H (main channel).

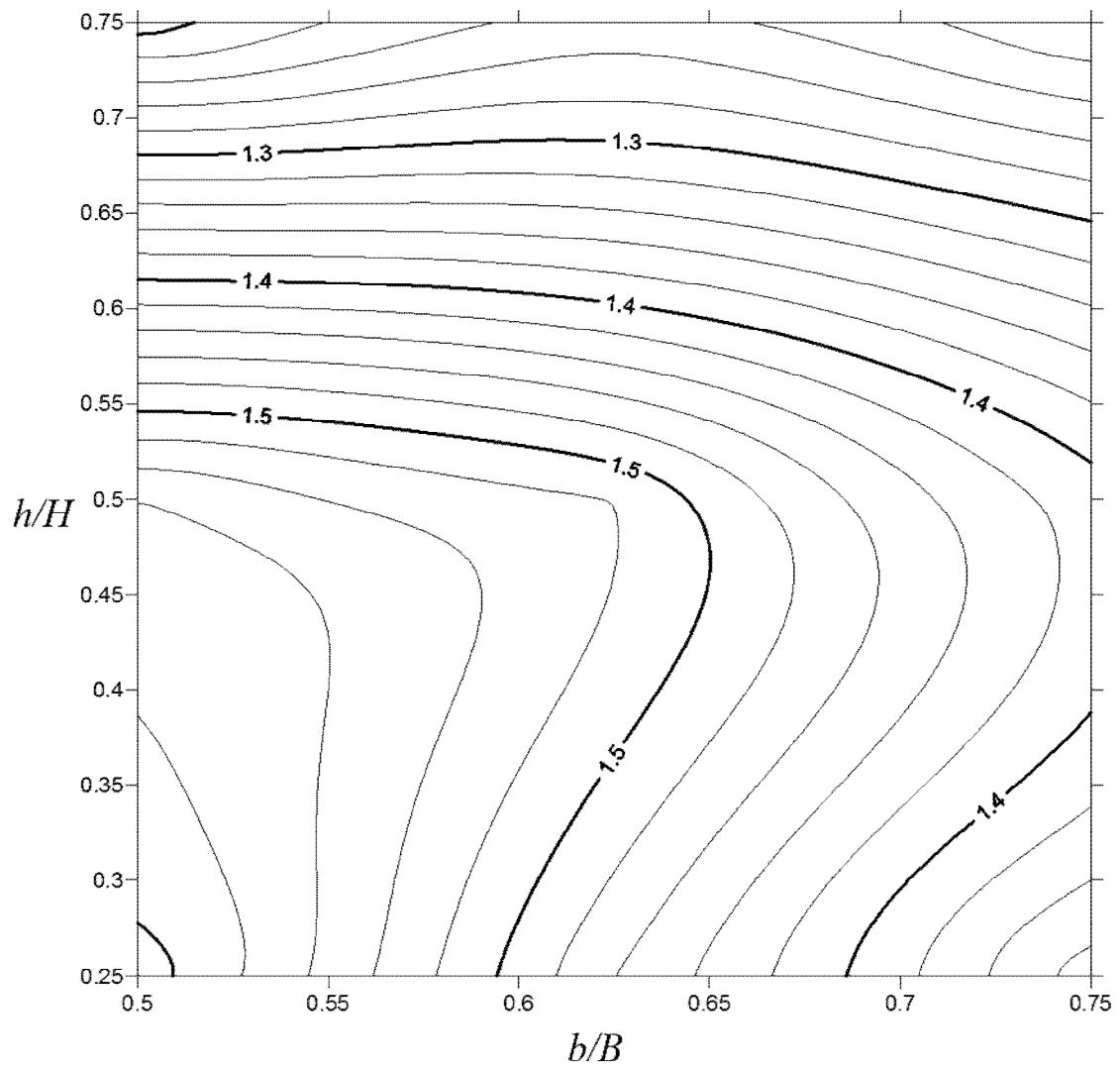


Figure 5.16 The design factors for trapezoidal compound channels with b/B and h/H (bank).

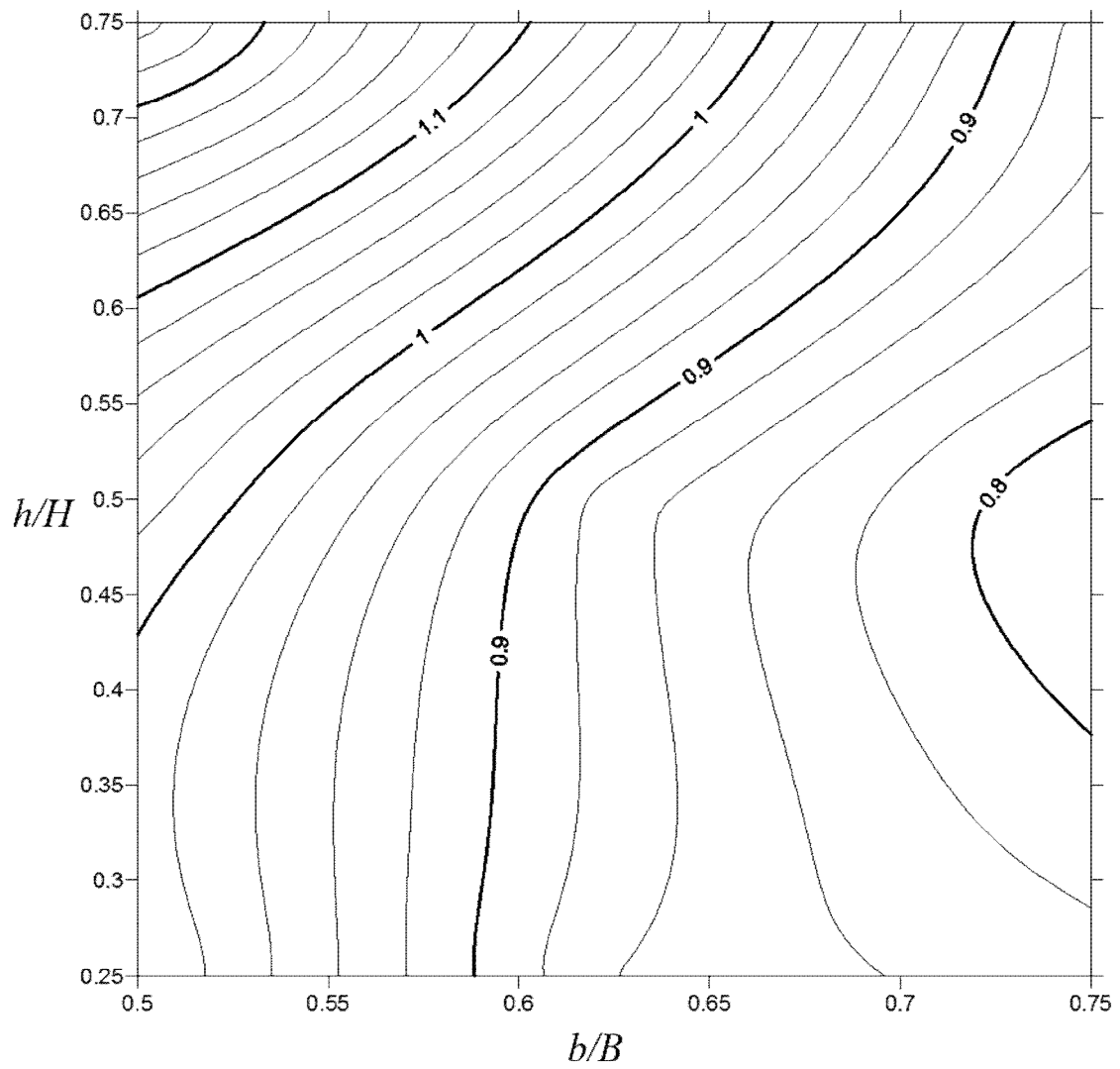


Figure 5.17 The design factors for trapezoidal compound channels with b/B and h/H (floodplain).

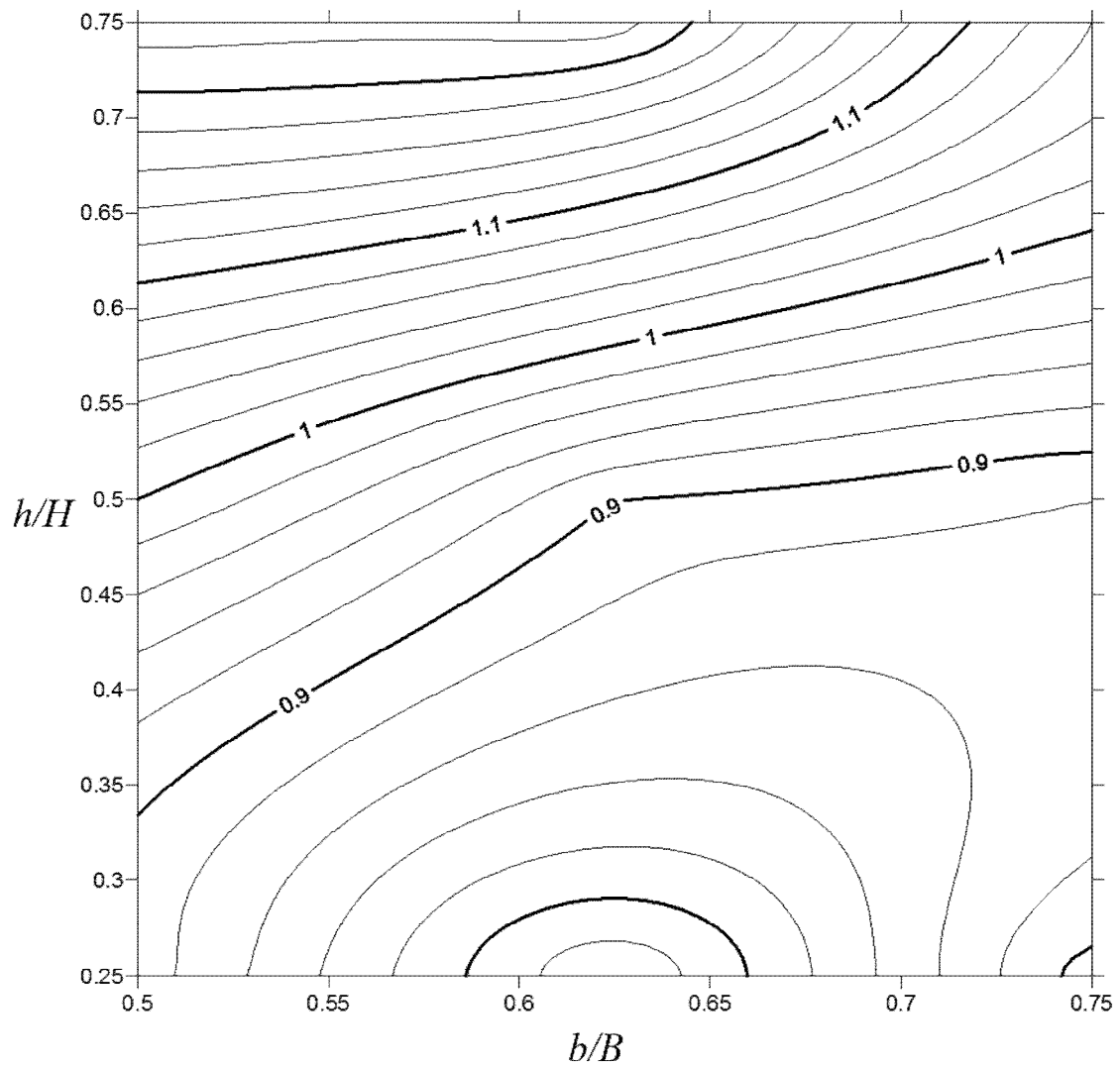


Figure 5.18 The design factors for trapezoidal compound channels with b/B and h/H (levee).

5.3 Design Friction Factors for Depth Averaged Velocity

5.3.1 Depth averaged velocity and friction factors

In this section, design friction factors for depth average velocity are presented based on the LES simulation results. In river or channel design, application of depth averaged two dimensional models increases and the results enhance the more accurate design considering local flow properties. However, in the compound open channel flows distribution of boundary shear stresses shows more complicated characteristics and fully

3d turbulence properties need to be considered as shown in Chapter 2 and Chapter 4.

The Shiono and Knight method is one of the most advanced method for evaluating the shear stress distribution in channels and rivers. However, implementation of the method is not easy for practical river design and the major constants are unclear.

In this study simple method is suggested using depth averaged velocity that can be obtained easily from 2D hydraulic numerical models. As provided equation 2.21, depth averaged velocity can be simply related to wall shear stress.

$$u_* = \sqrt{\frac{\tau_0}{\rho}} = \left(\frac{1}{8}f\right)^{1/2} U_d \quad (5.1)$$

If friction factor is known, wall shear stress can be calculated easily from depth averaged velocity. In this study, depth averaged velocity and the friction factors are evaluated from the LES results. Calculated depth averaged velocity and corresponding friction factors in the rectangular compound and trapezoidal compound channel cases are presented from Figure 5.19 to Figure 5.60.

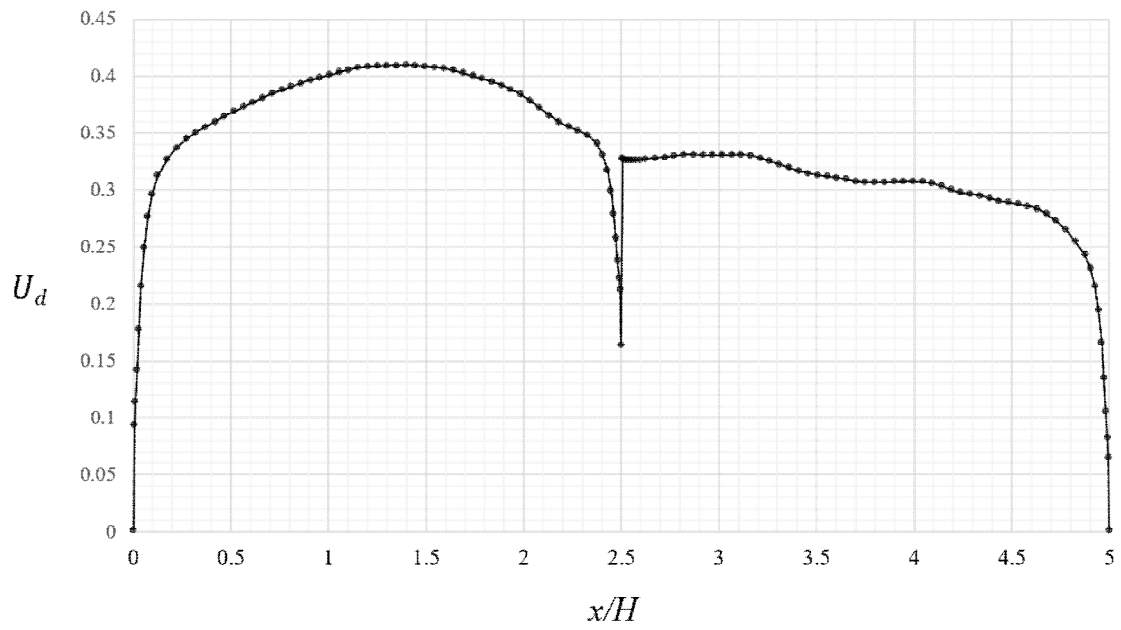


Figure 5.19 Depth averaged velocity in case CR01.

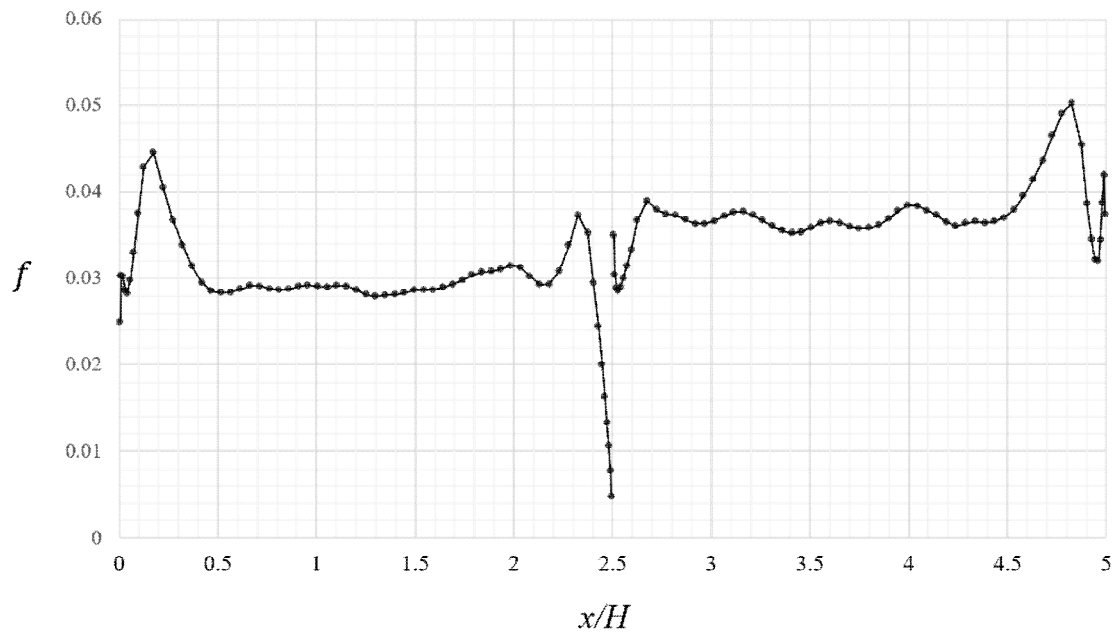


Figure 5.20 Friction factor from depth averaged velocity in case CR01.

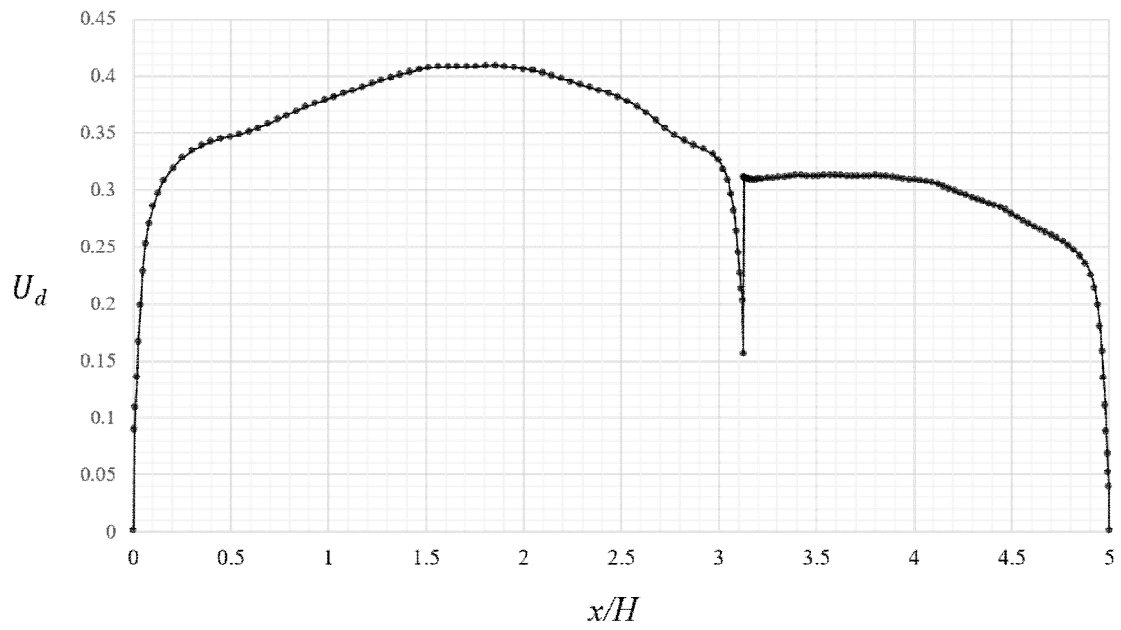


Figure 5.21 Depth averaged velocity in case CR02.

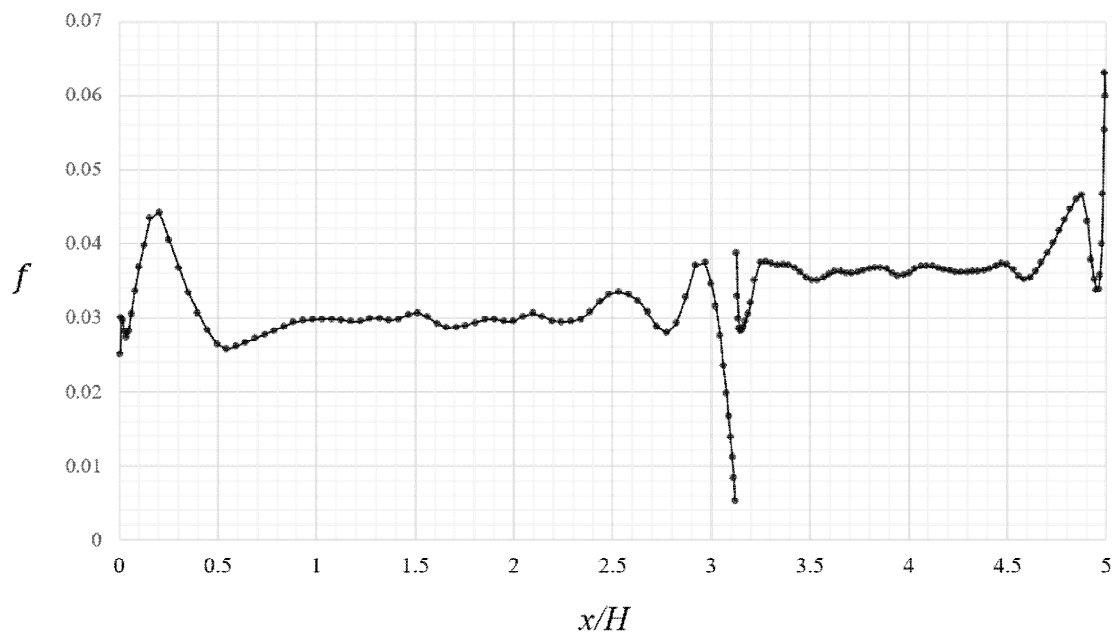


Figure 5.22 Friction factor from depth averaged velocity in case CR02.

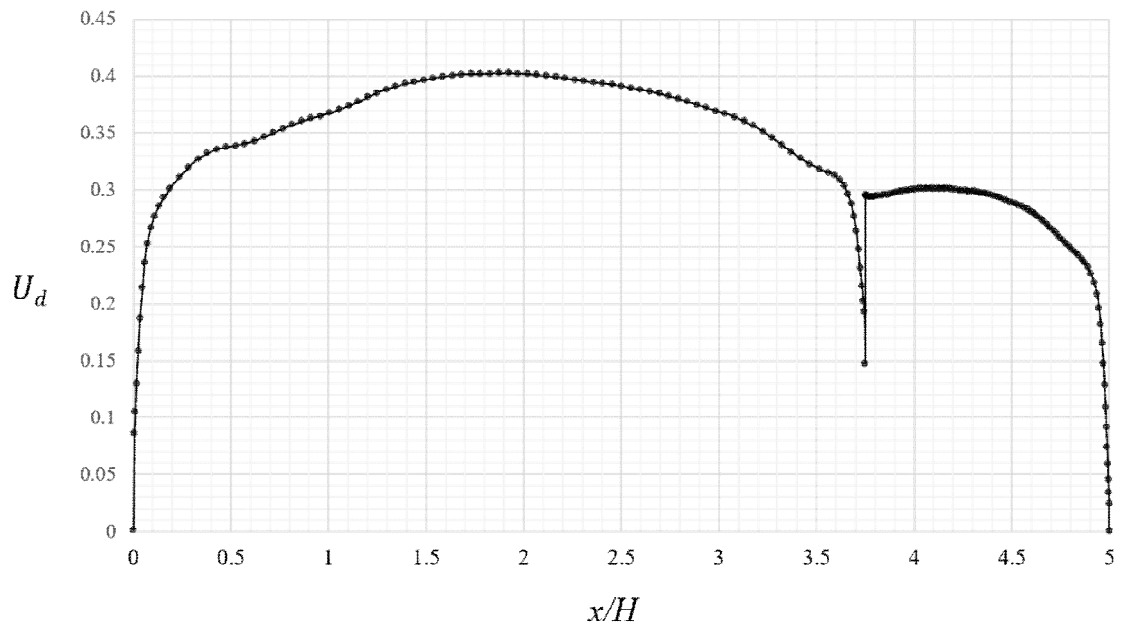


Figure 5.23 Depth averaged velocity in case CR03.

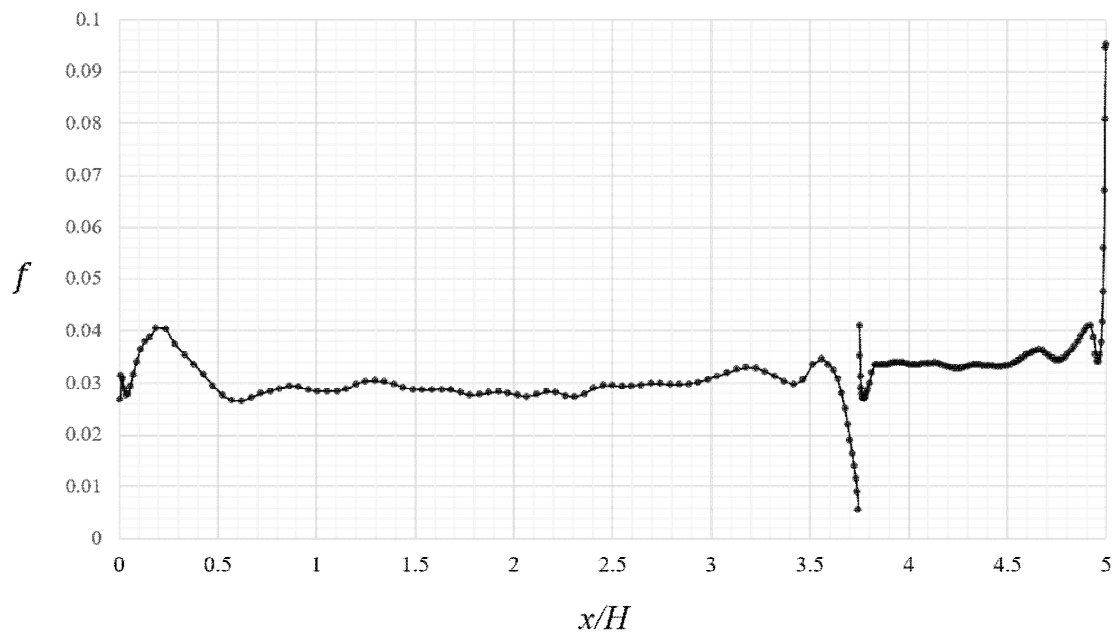


Figure 5.24 Friction factor from depth averaged velocity in case CR03.

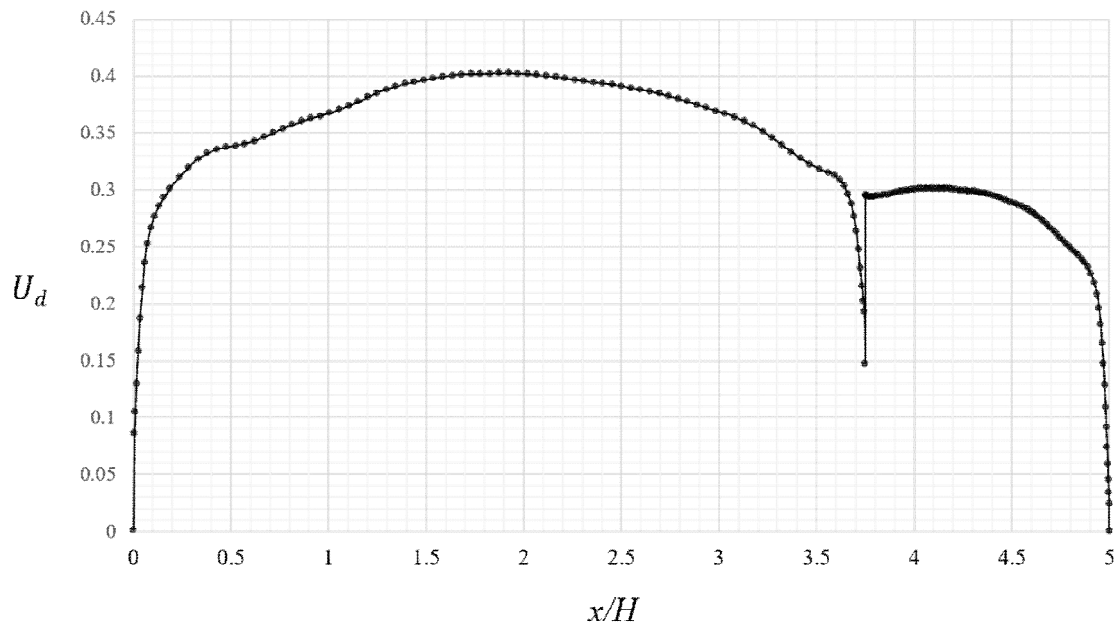


Figure 5.25 Depth averaged velocity in case CR04.

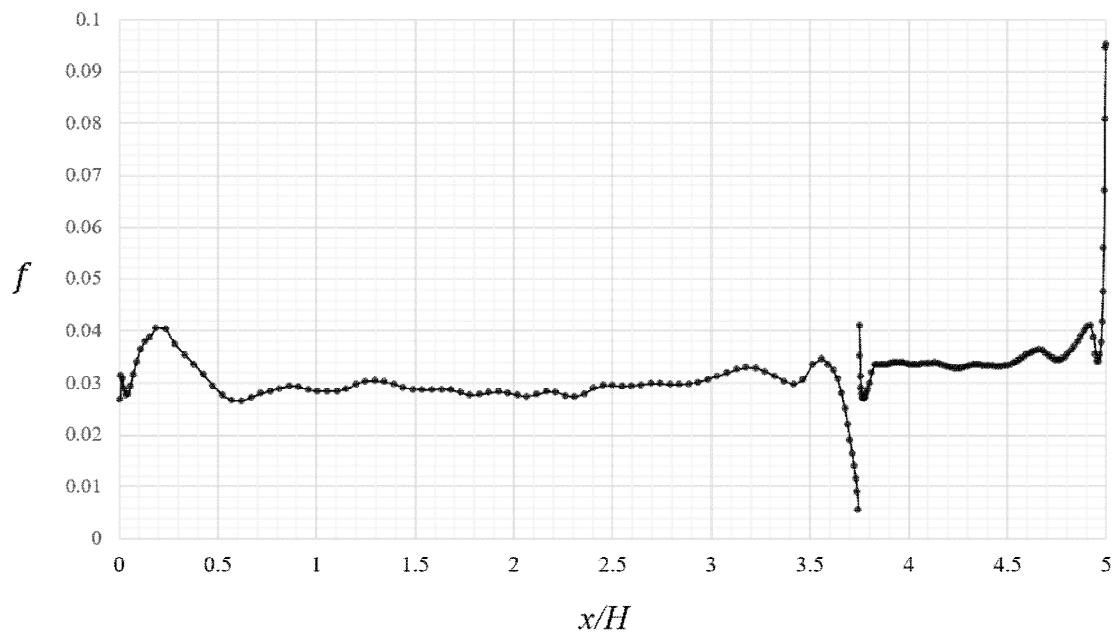


Figure 5.26 Friction factor from depth averaged velocity in case CR04.

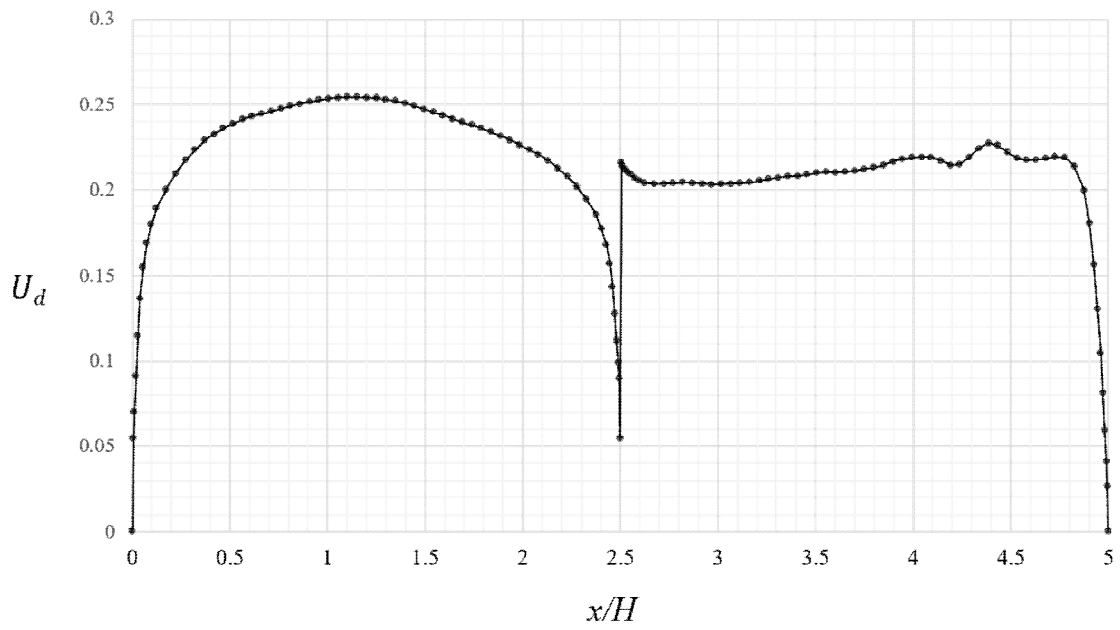


Figure 5.27 Depth averaged velocity in case CR11.

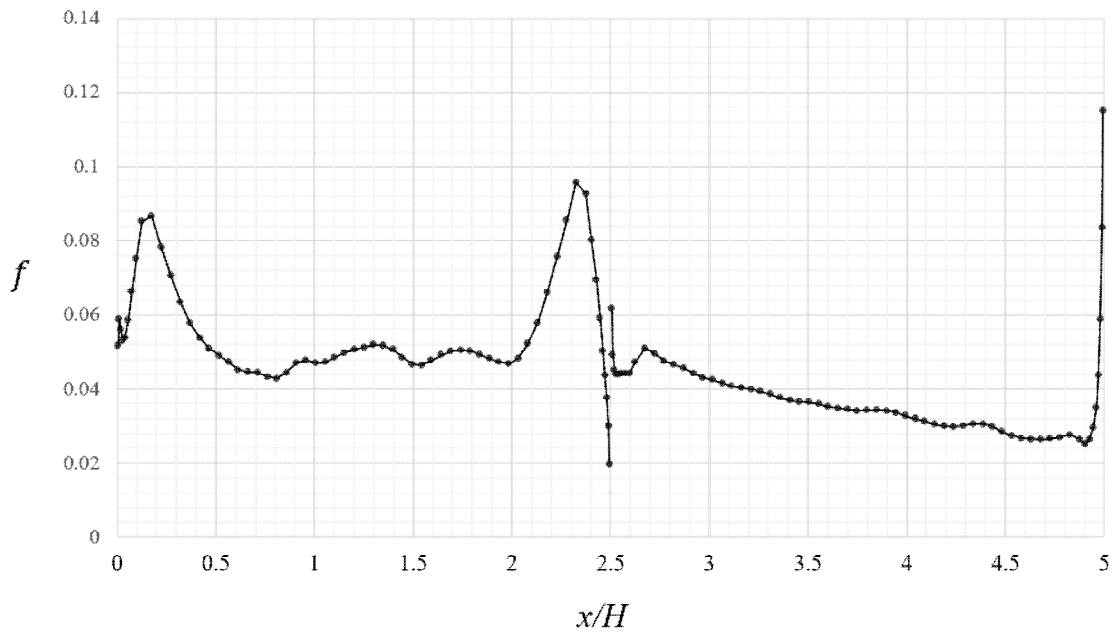


Figure 5.28 Friction factor from depth averaged velocity in case CR11.

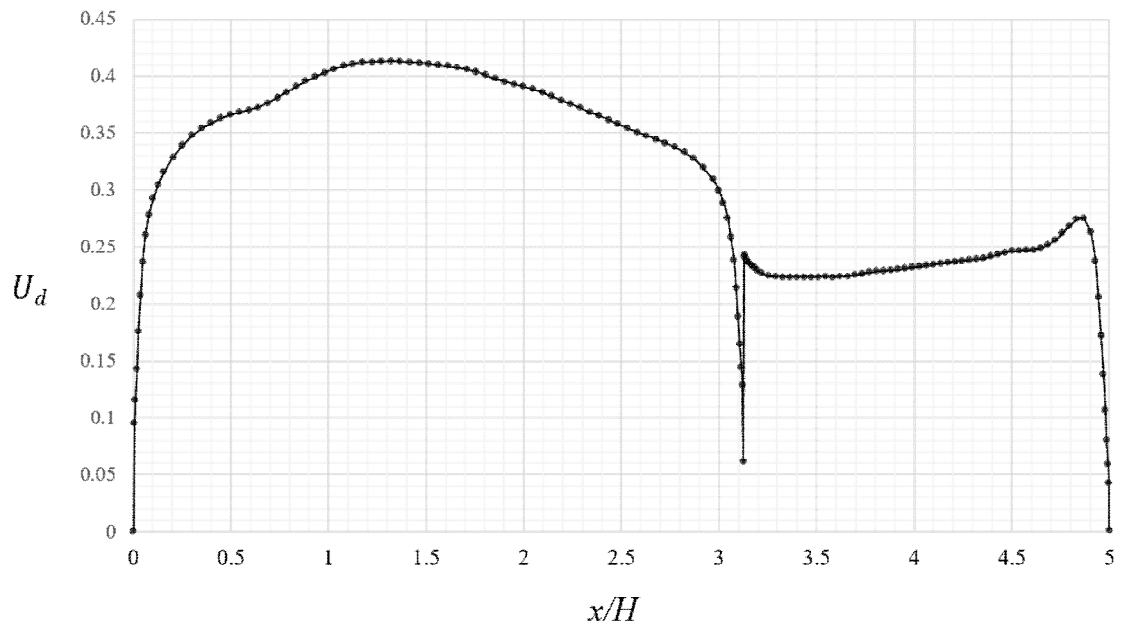


Figure 5.29 Depth averaged velocity in case CR12.

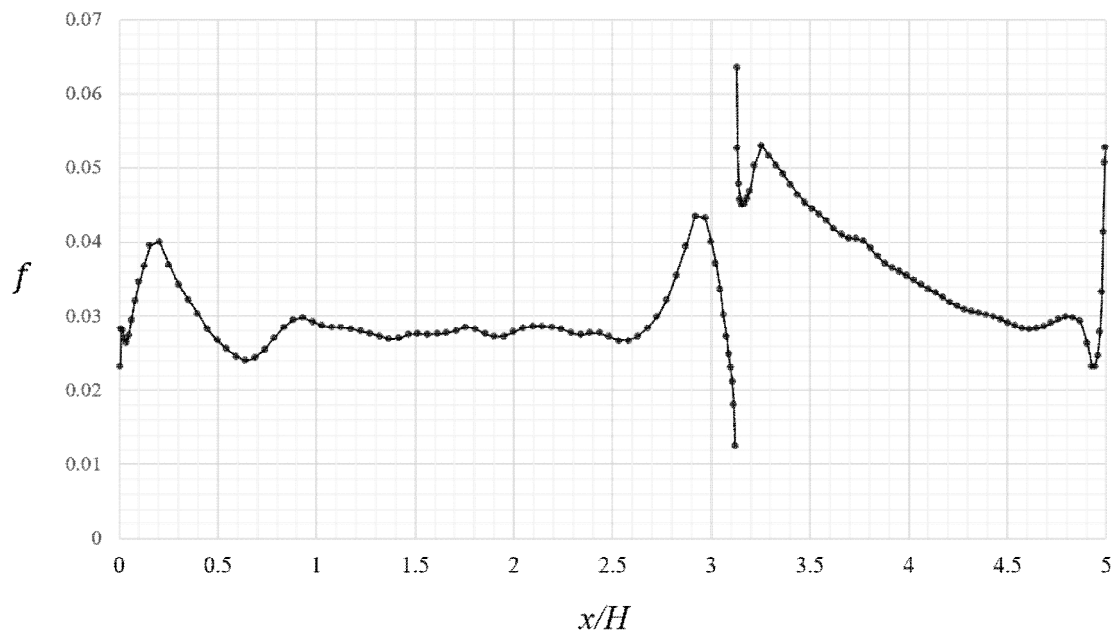


Figure 5.30 Friction factor from depth averaged velocity in case CR12.

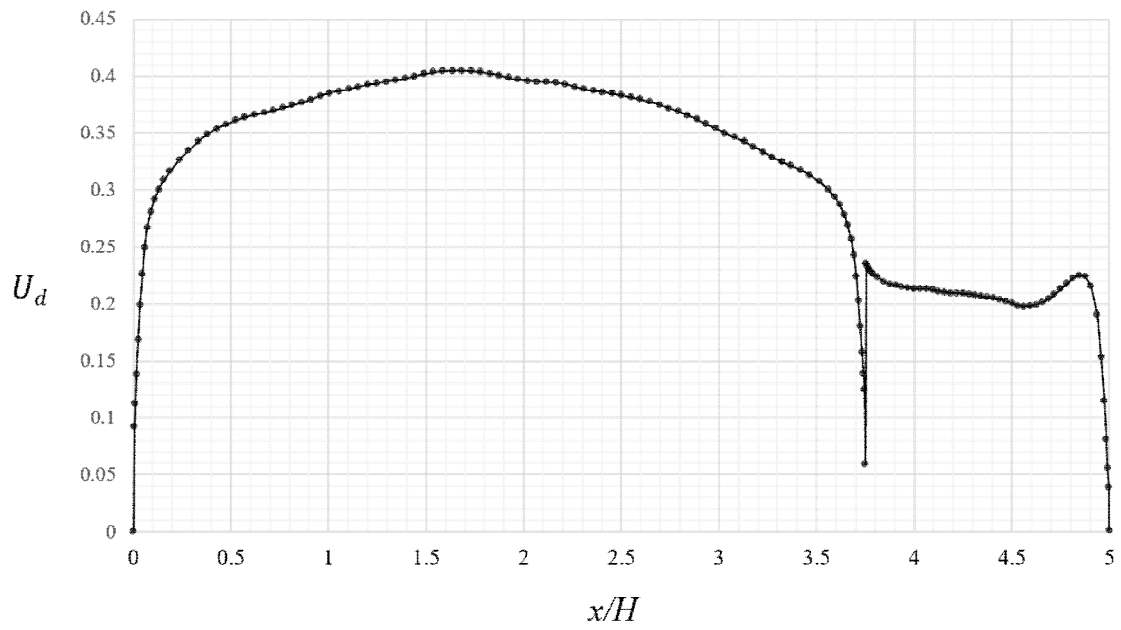


Figure 5.31 Depth averaged velocity in case CR13.

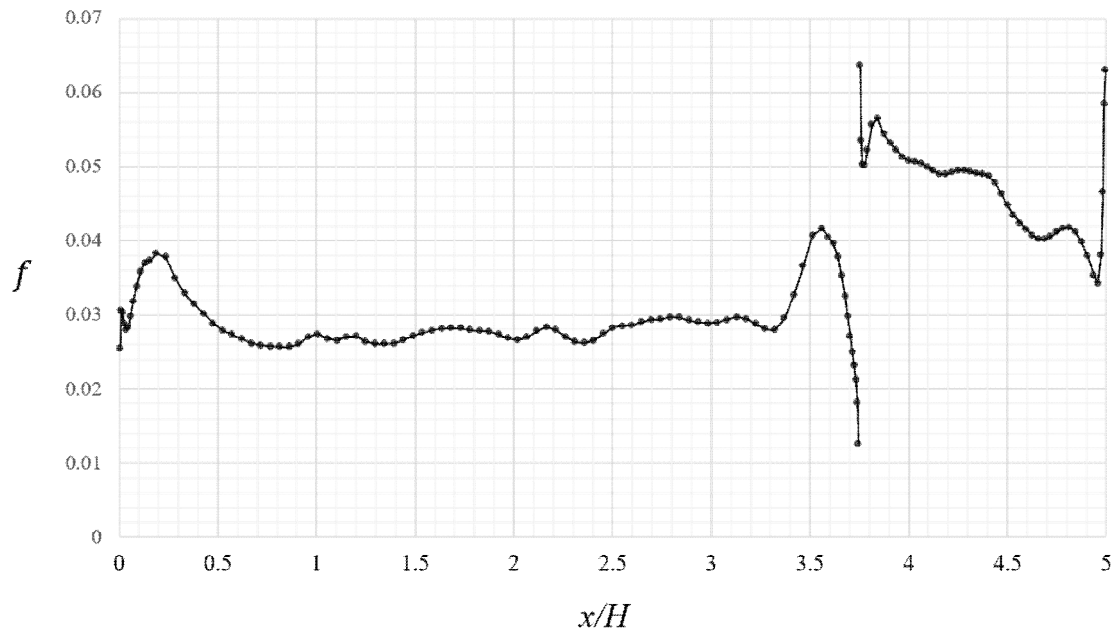


Figure 5.32 Friction factor from depth averaged velocity in case CR13.

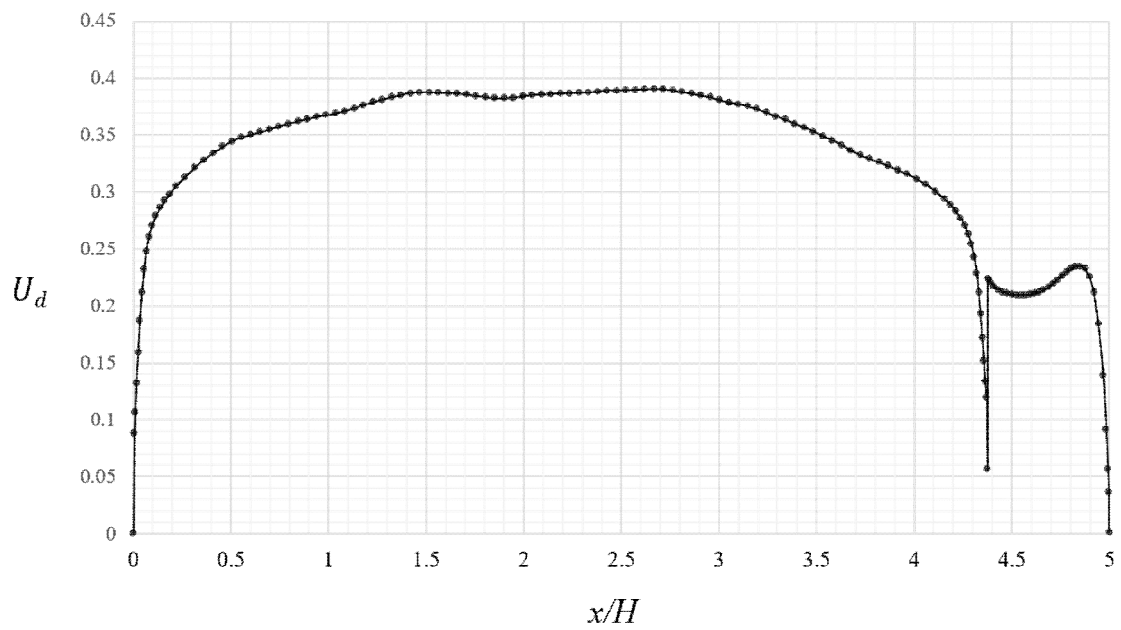


Figure 5.33 Depth averaged velocity in case CR14.

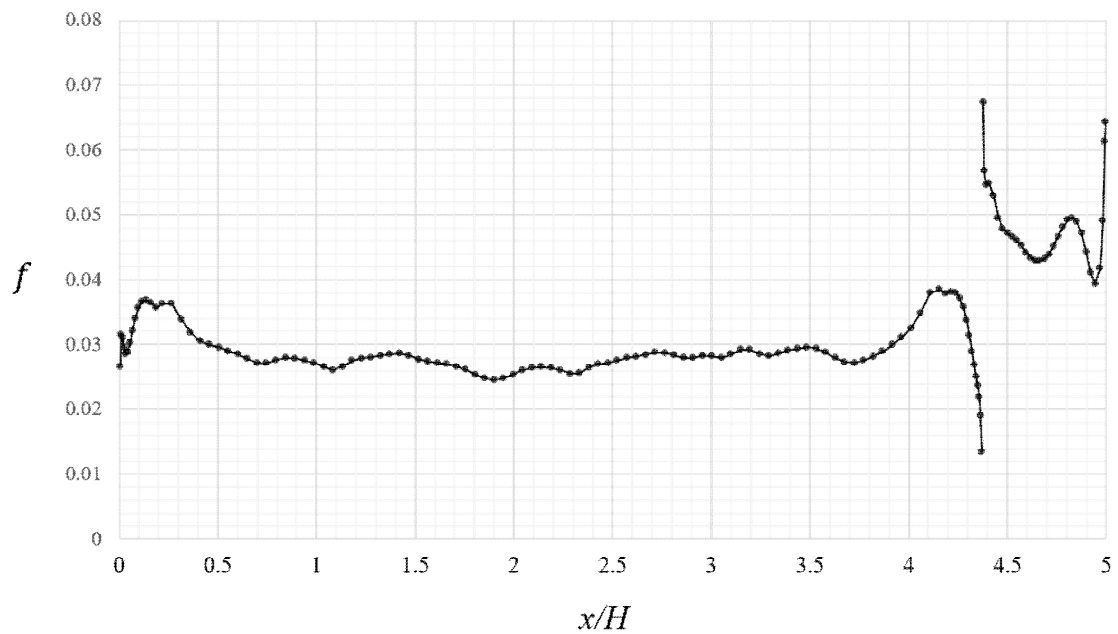


Figure 5.34 Friction factor from depth averaged velocity in case CR14.

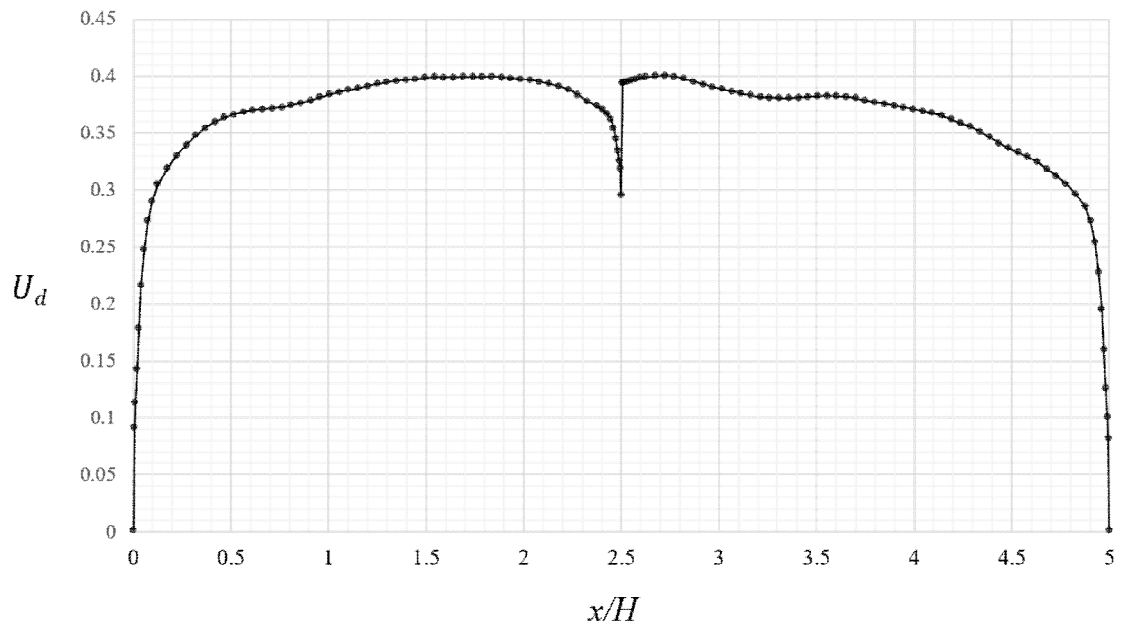


Figure 5.35 Depth averaged velocity in case CR21.

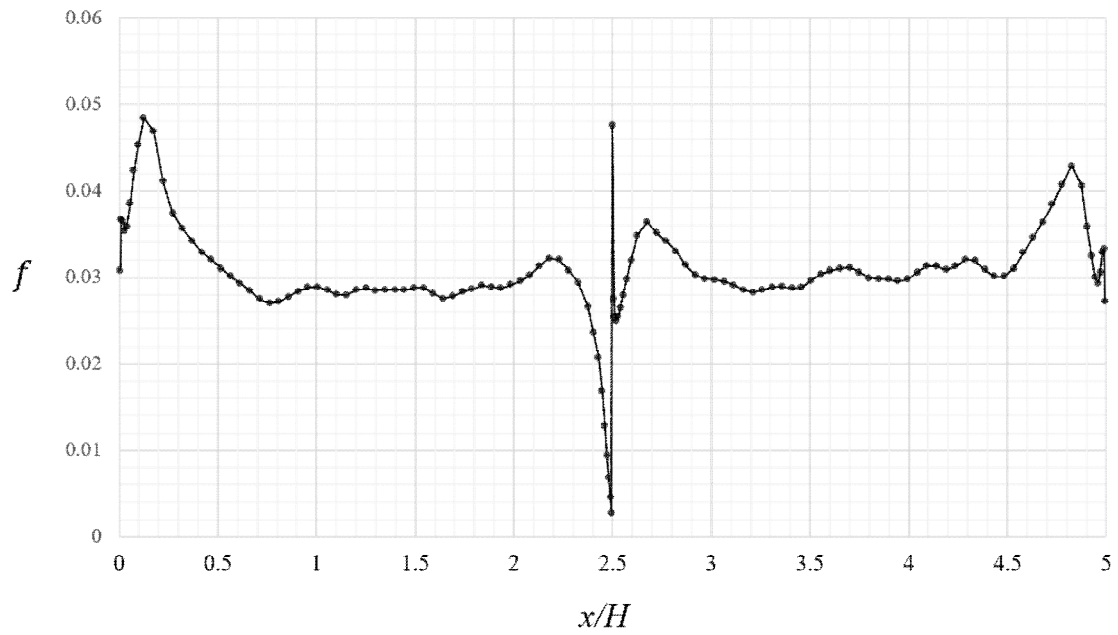


Figure 5.36 Friction factor from depth averaged velocity in case CR21.

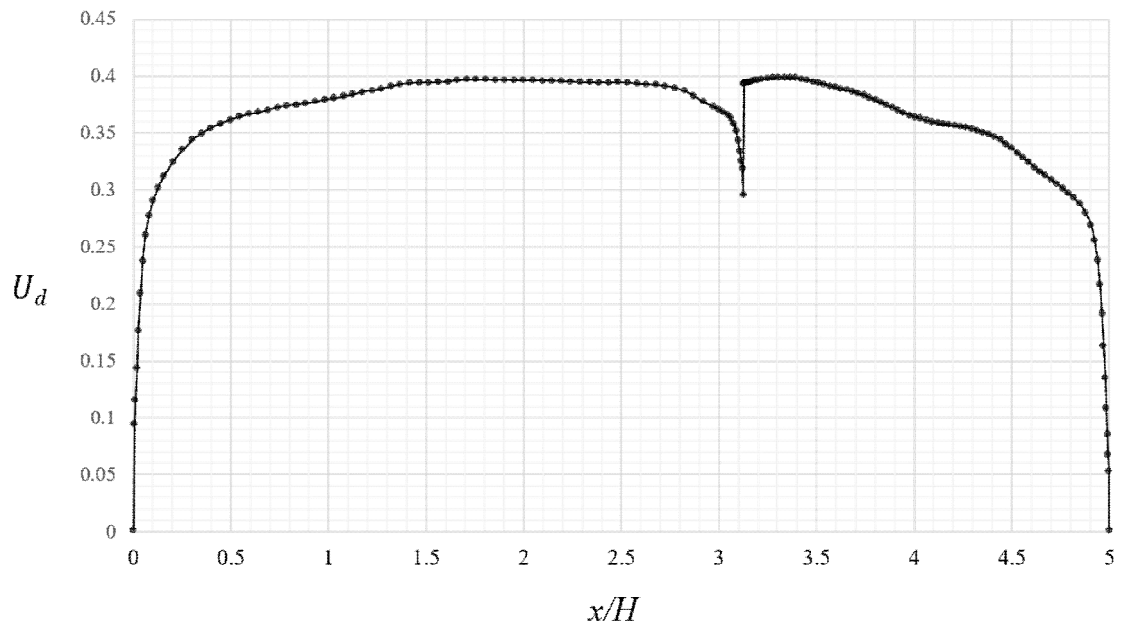


Figure 5.37 Depth averaged velocity in case CR22.

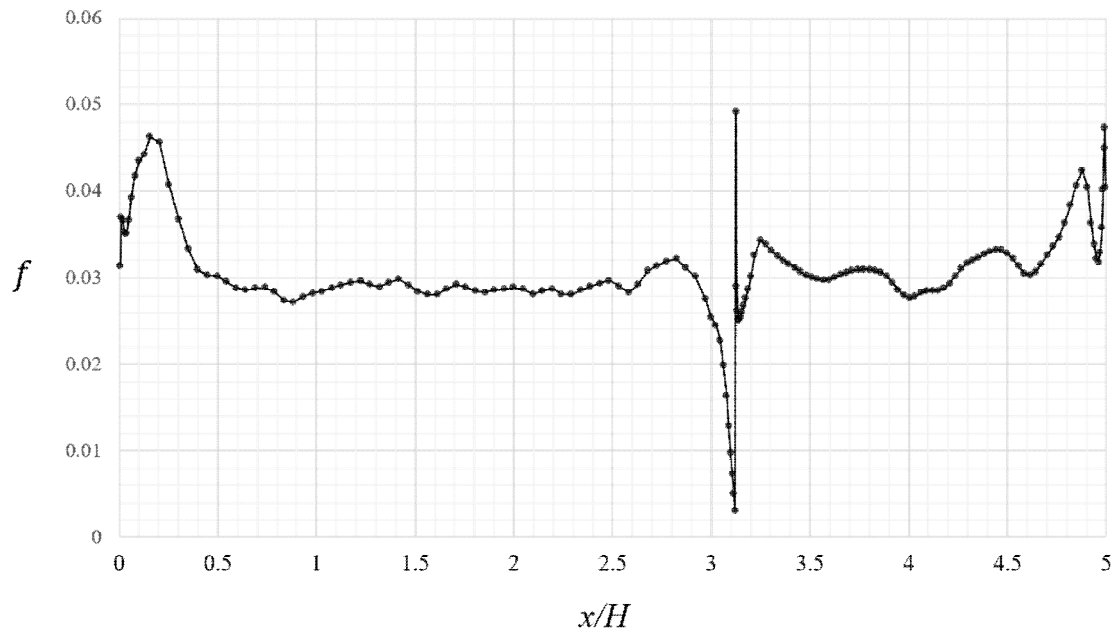


Figure 5.38 Friction factor from depth averaged velocity in case CR22.

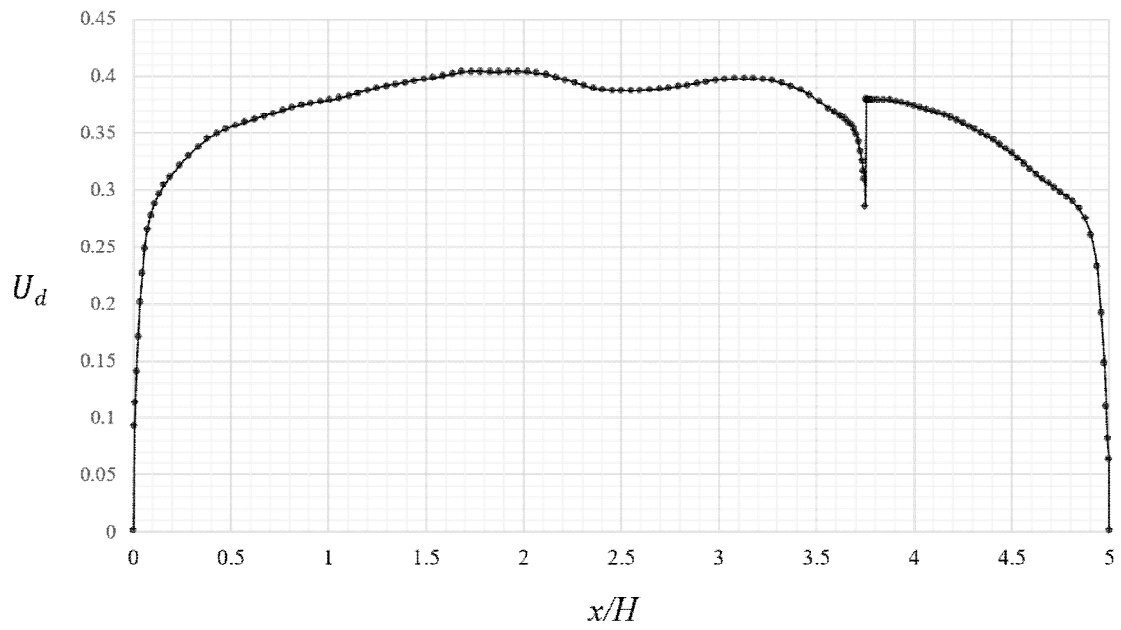


Figure 5.39 Depth averaged velocity in case CR23.

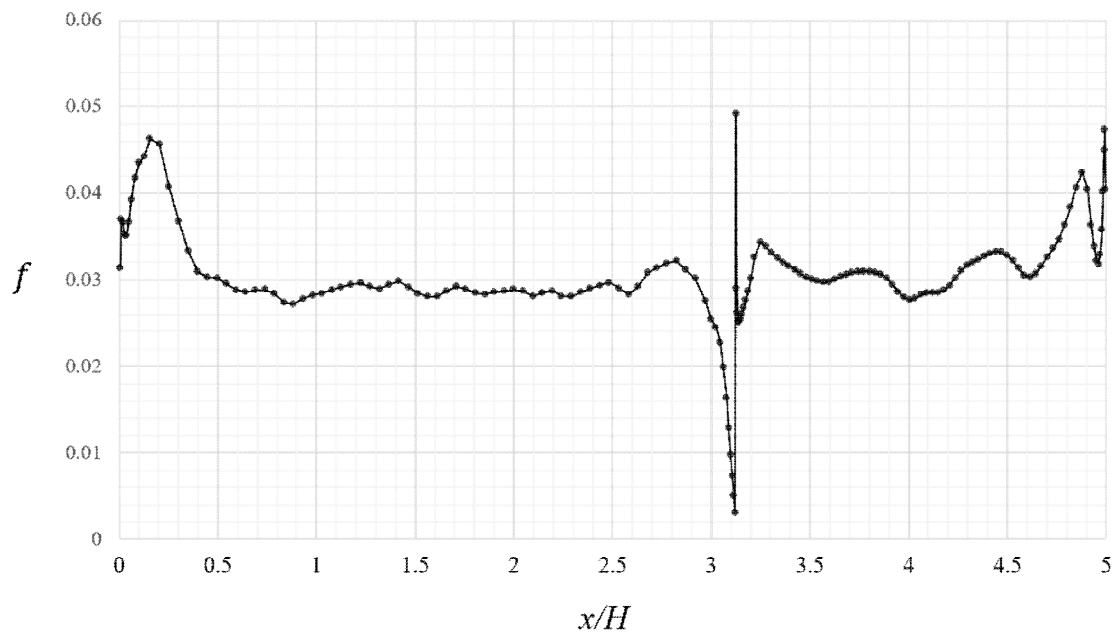


Figure 5.40 Friction factor from depth averaged velocity in case CR23.

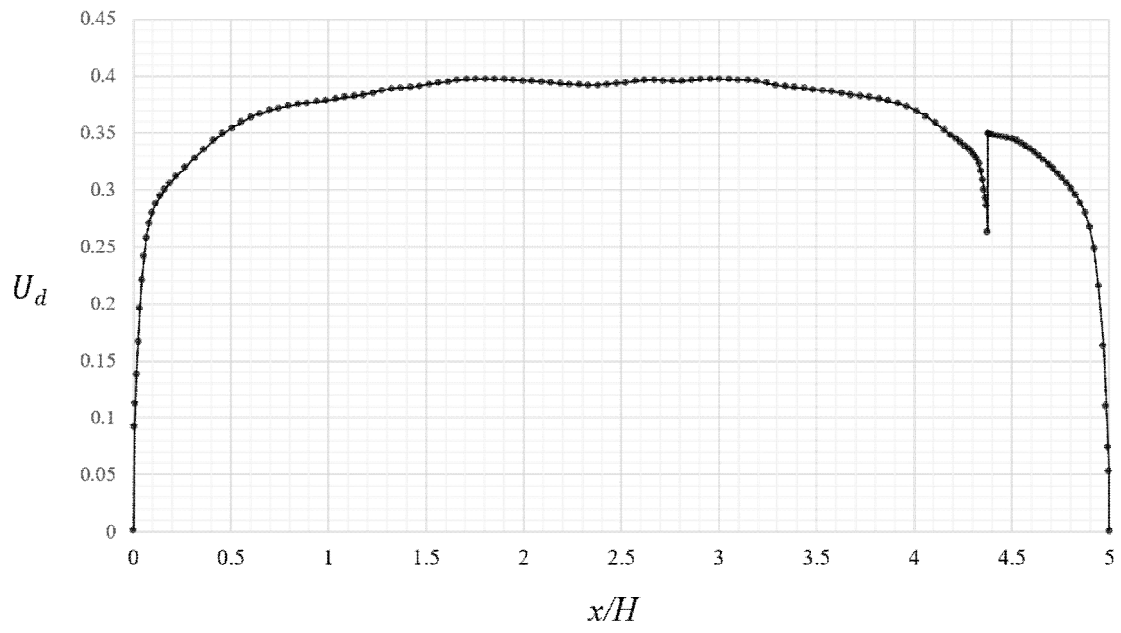


Figure 5.41 Depth averaged velocity in case CR24.

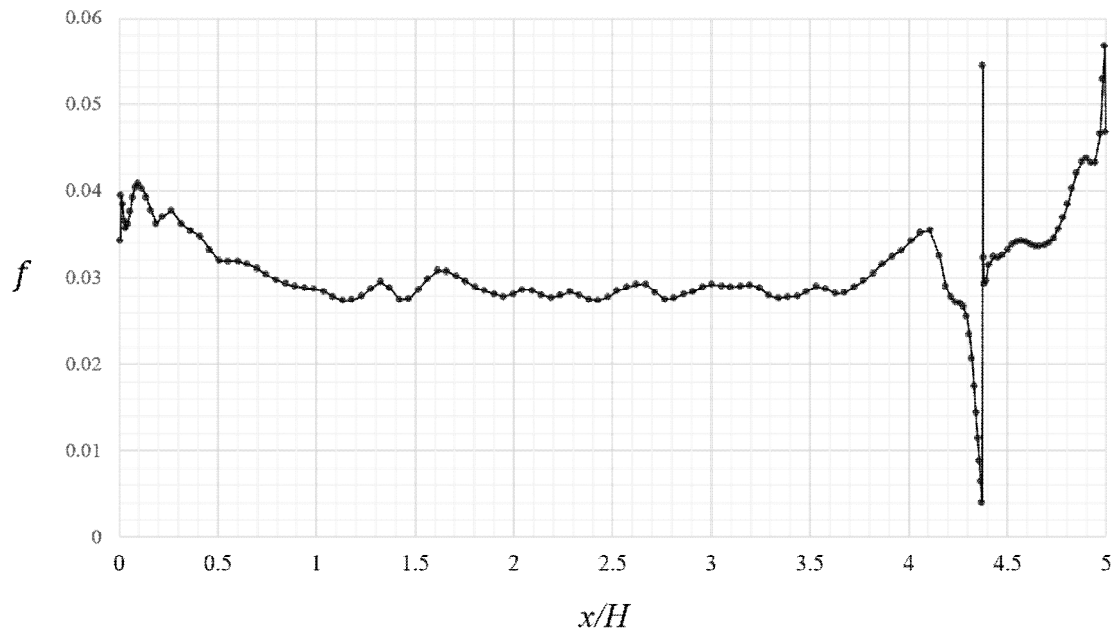


Figure 5.42 Friction factor from depth averaged velocity in case CR24.

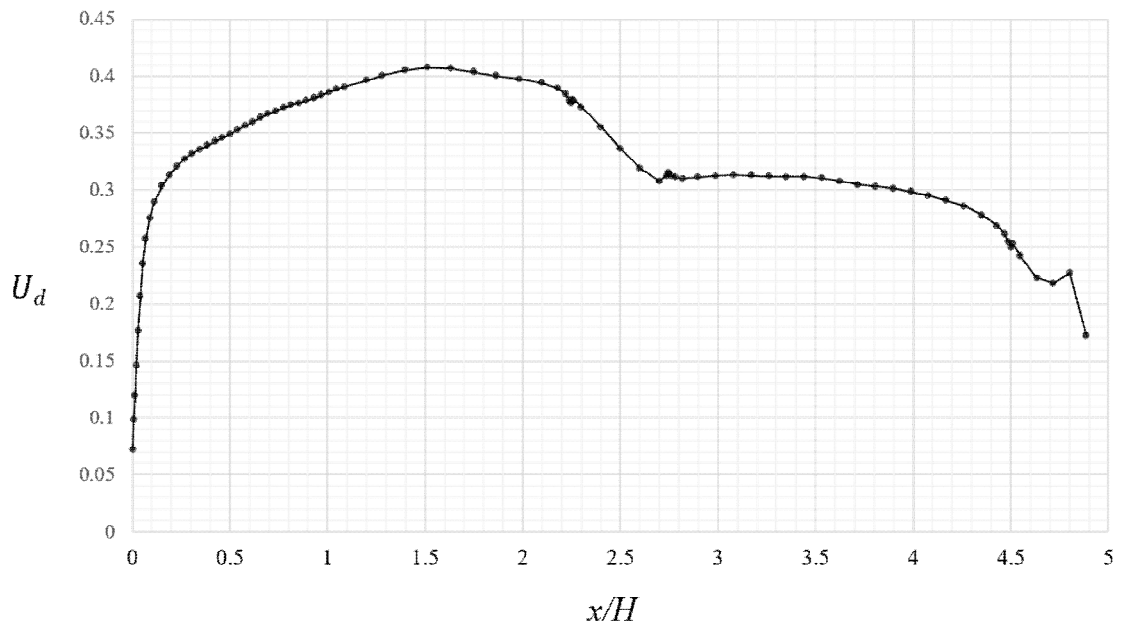


Figure 5.43 Depth averaged velocity in case CT01.

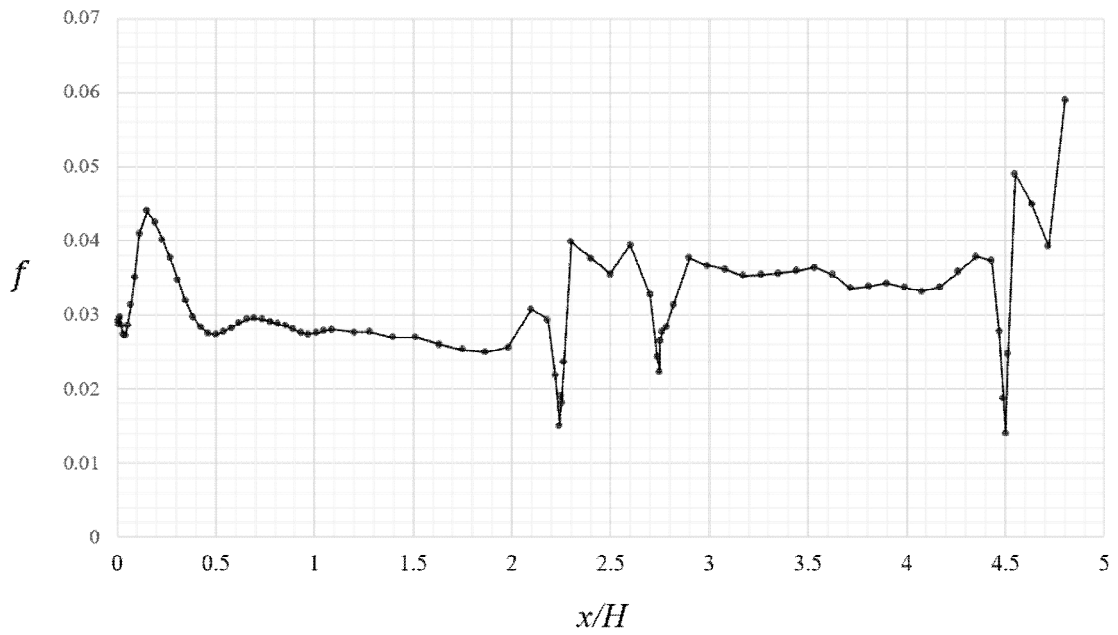


Figure 5.44 Friction factor from depth averaged velocity in case CT01.

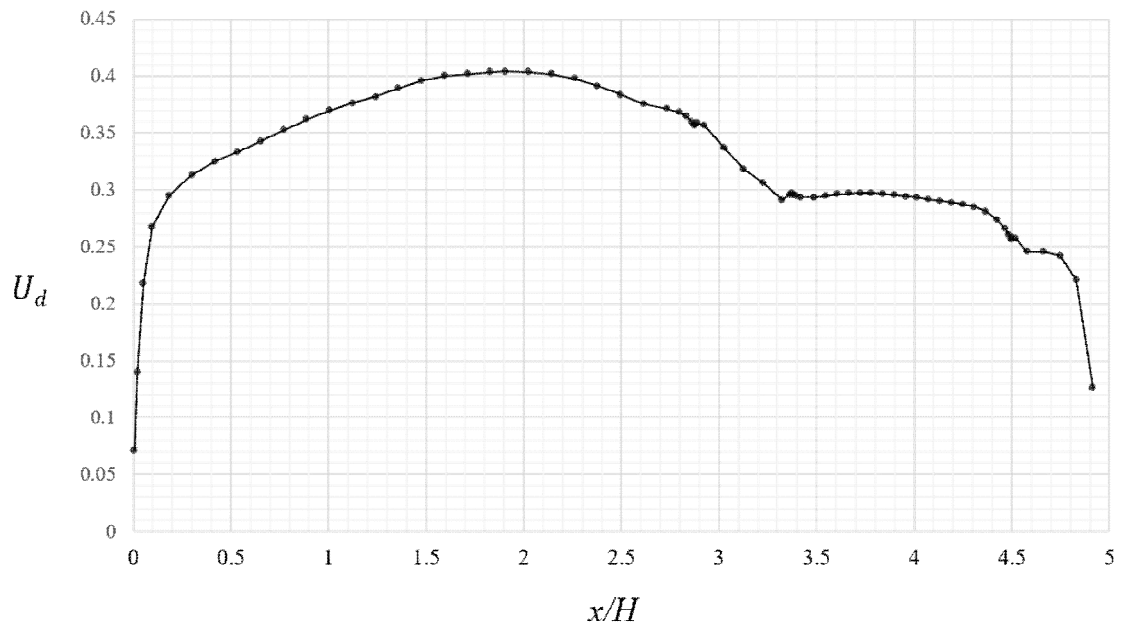


Figure 5.45 Depth averaged velocity in case CT02.

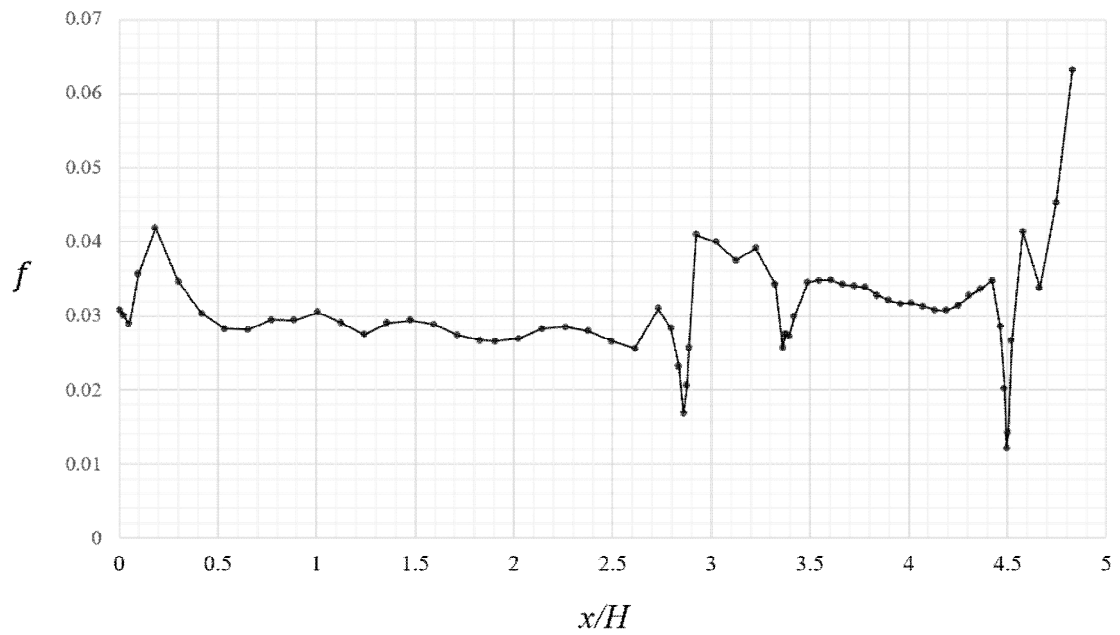


Figure 5.46 Friction factor from depth averaged velocity in case CT02.

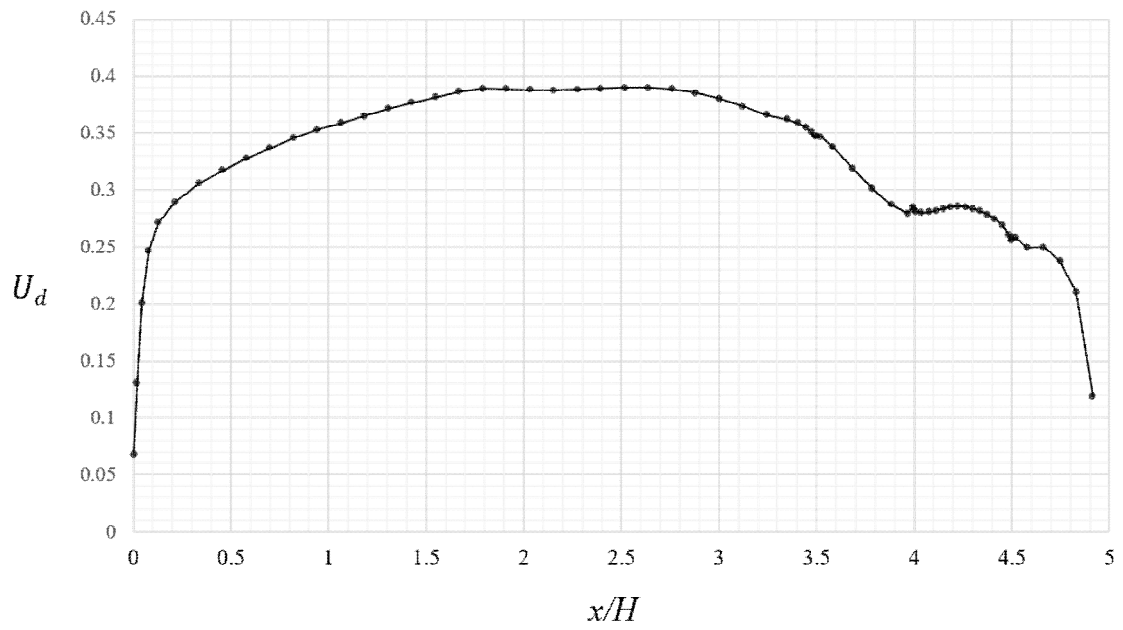


Figure 5.47 Depth averaged velocity in case CT03.

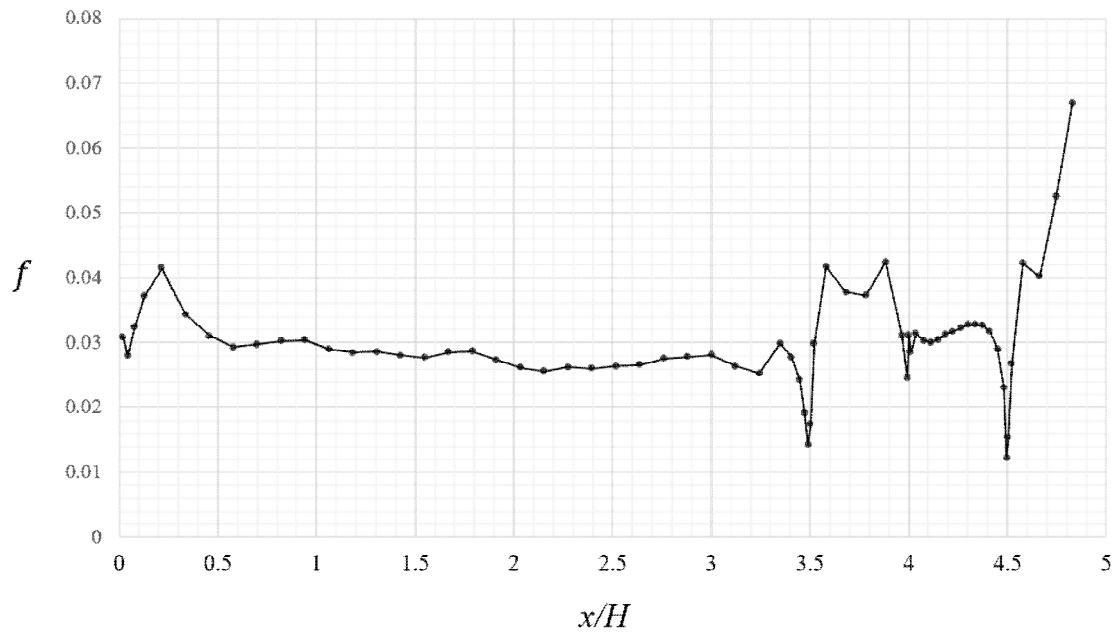


Figure 5.48 Friction factor from depth averaged velocity in case CT03.

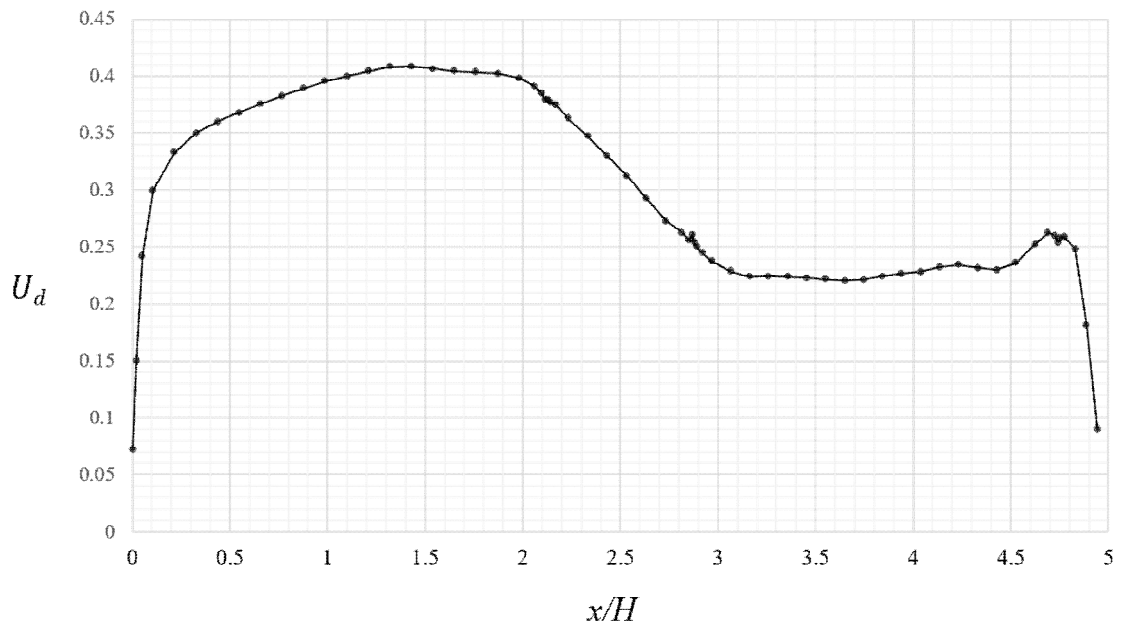


Figure 5.49 Depth averaged velocity in case CT11.

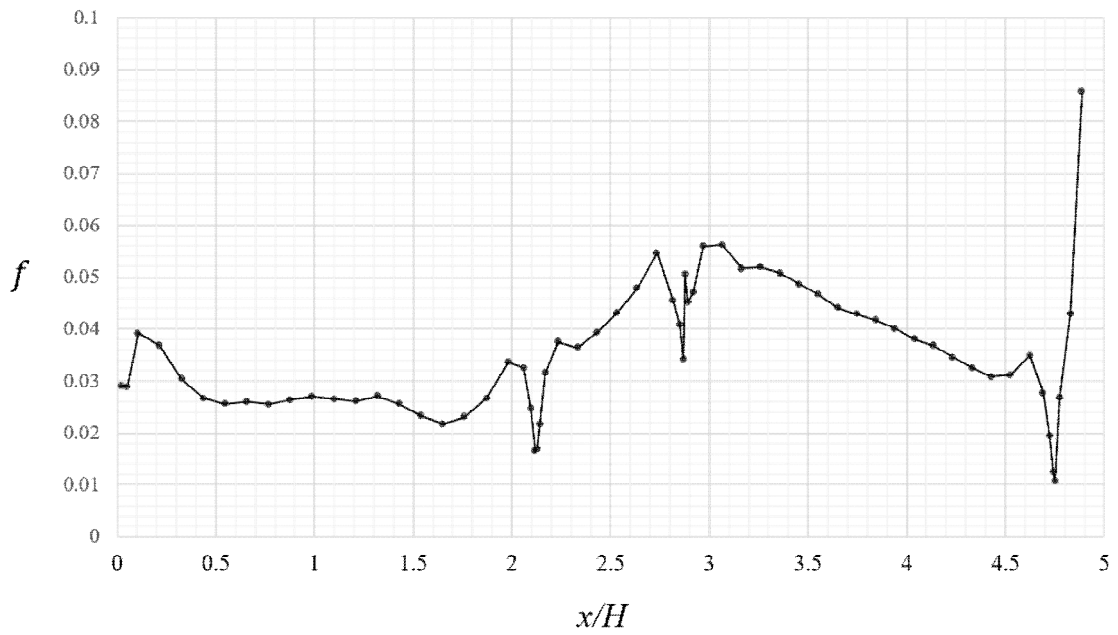


Figure 5.50 Friction factor from depth averaged velocity in case CT11.

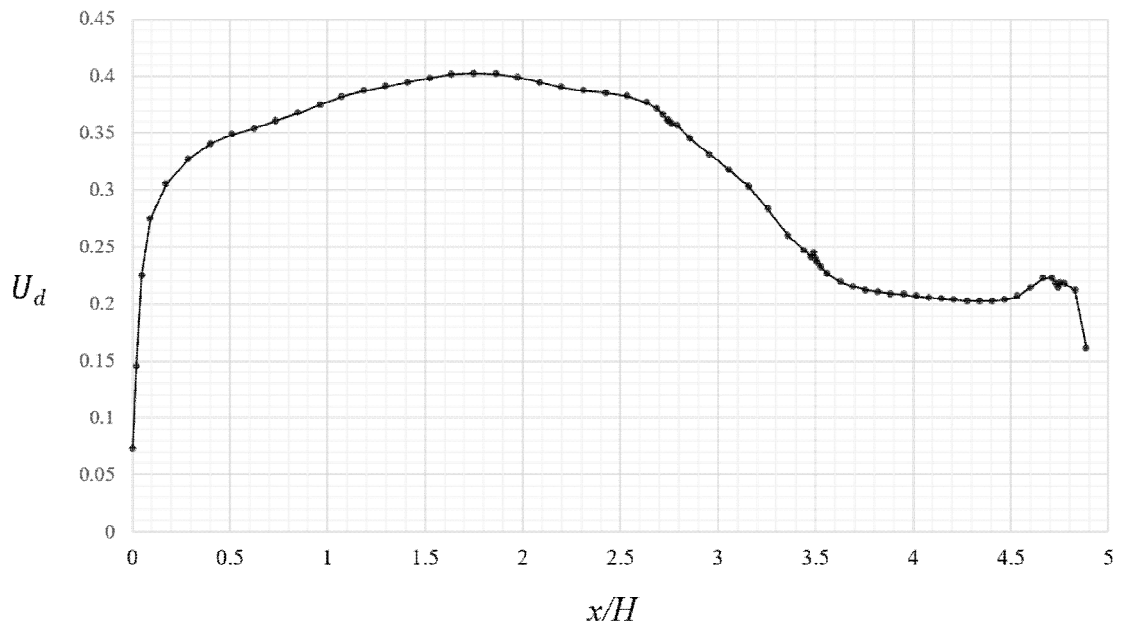


Figure 5.51 Depth averaged velocity in case CT12.

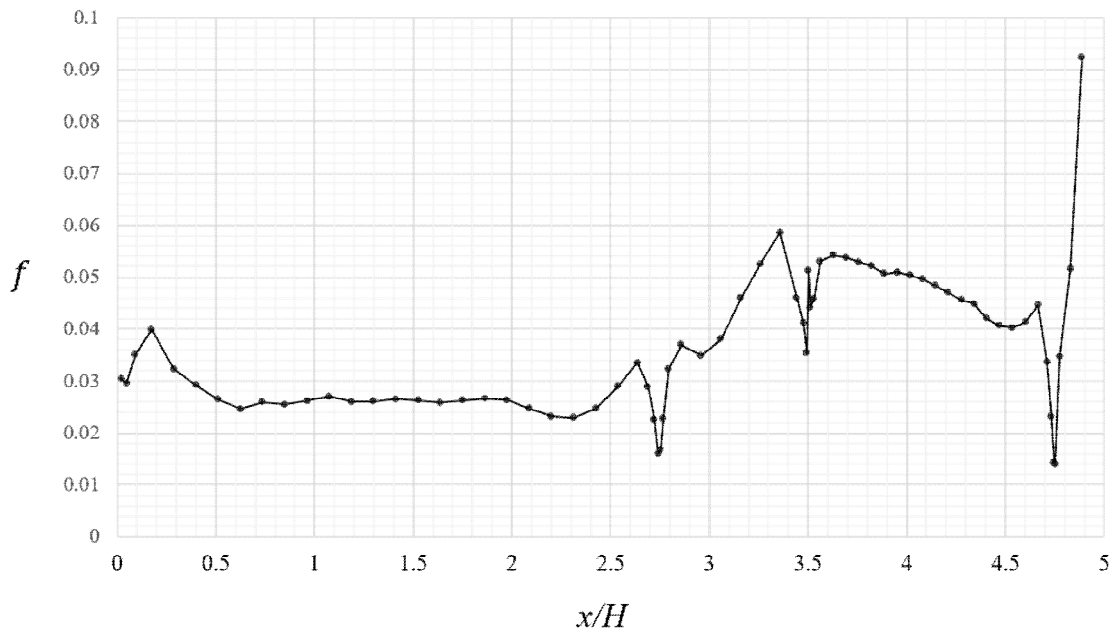


Figure 5.52 Friction factor from depth averaged velocity in case CT12.

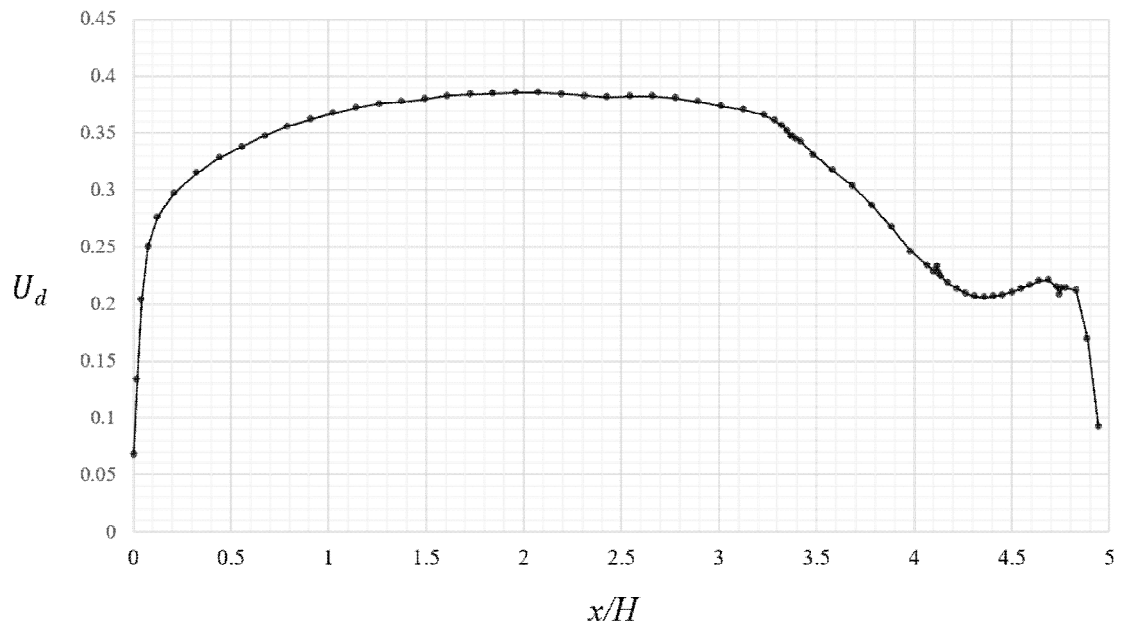


Figure 5.53 Depth averaged velocity in case CT13.

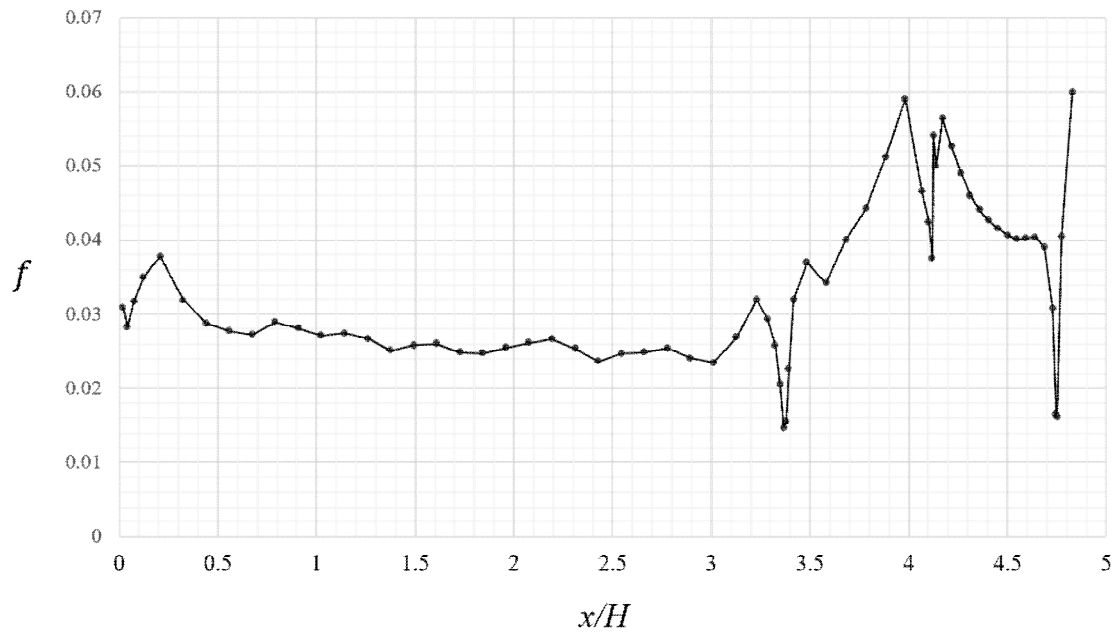


Figure 5.54 Friction factor from depth averaged velocity in case CT13.

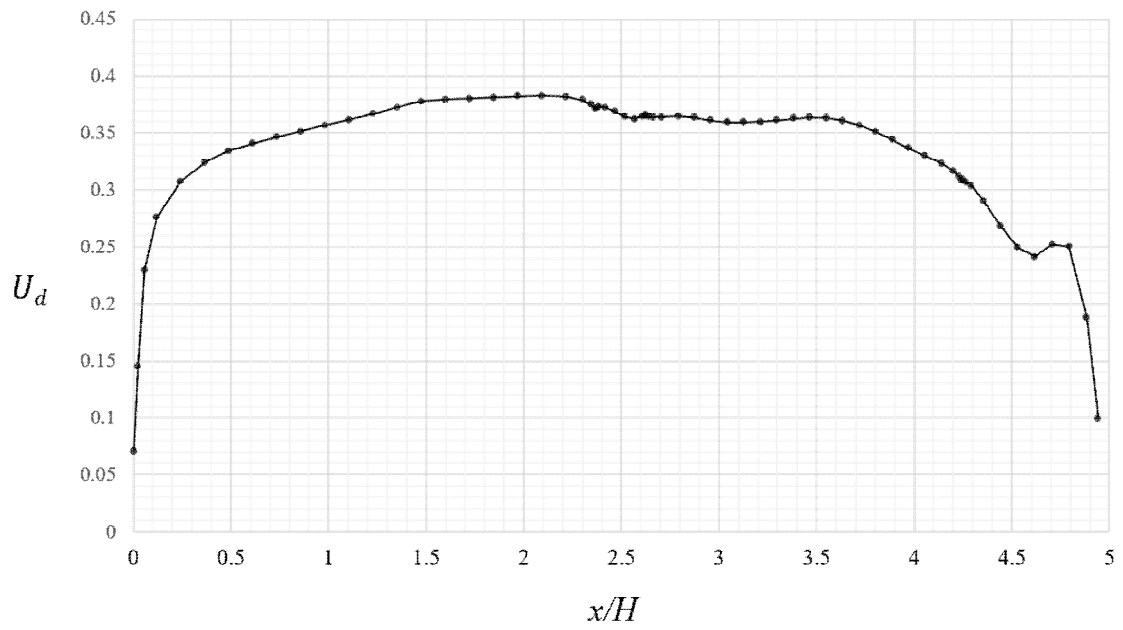


Figure 5.55 Depth averaged velocity in case CT21.

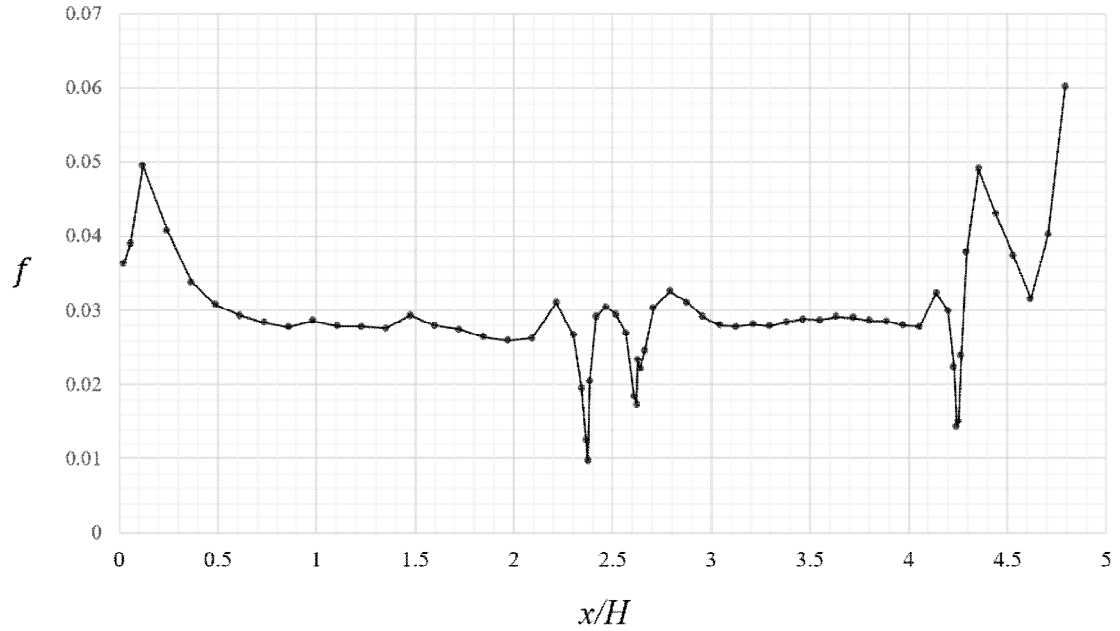


Figure 5.56 Friction factor from depth averaged velocity in case CT21.

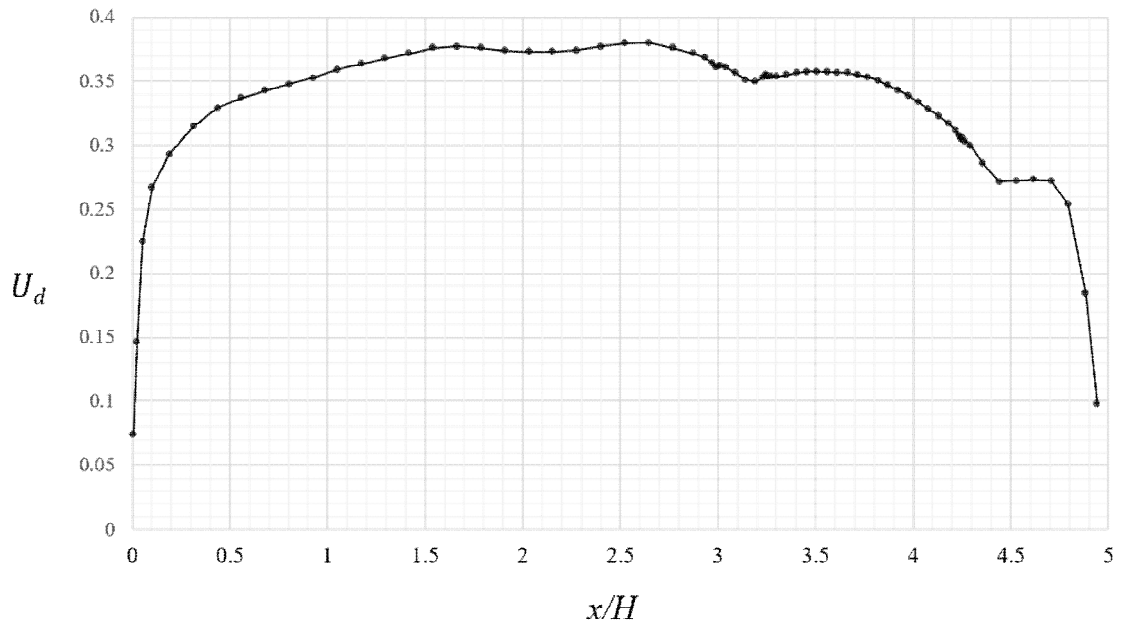


Figure 5.57 Depth averaged velocity in case CT22.

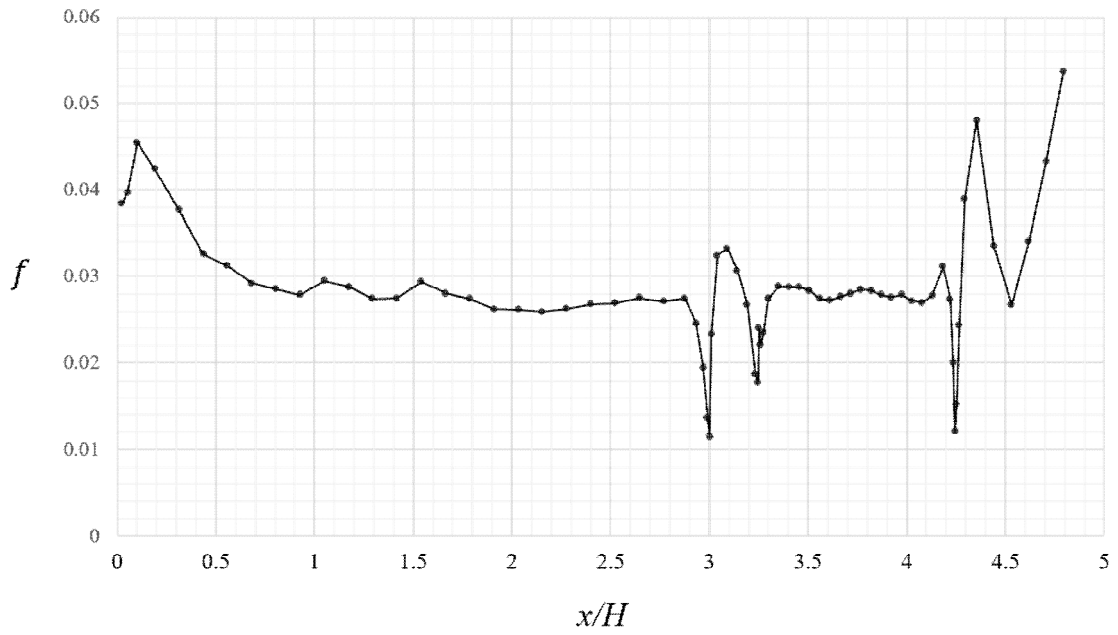


Figure 5.58 Friction factor from depth averaged velocity in case CT22.

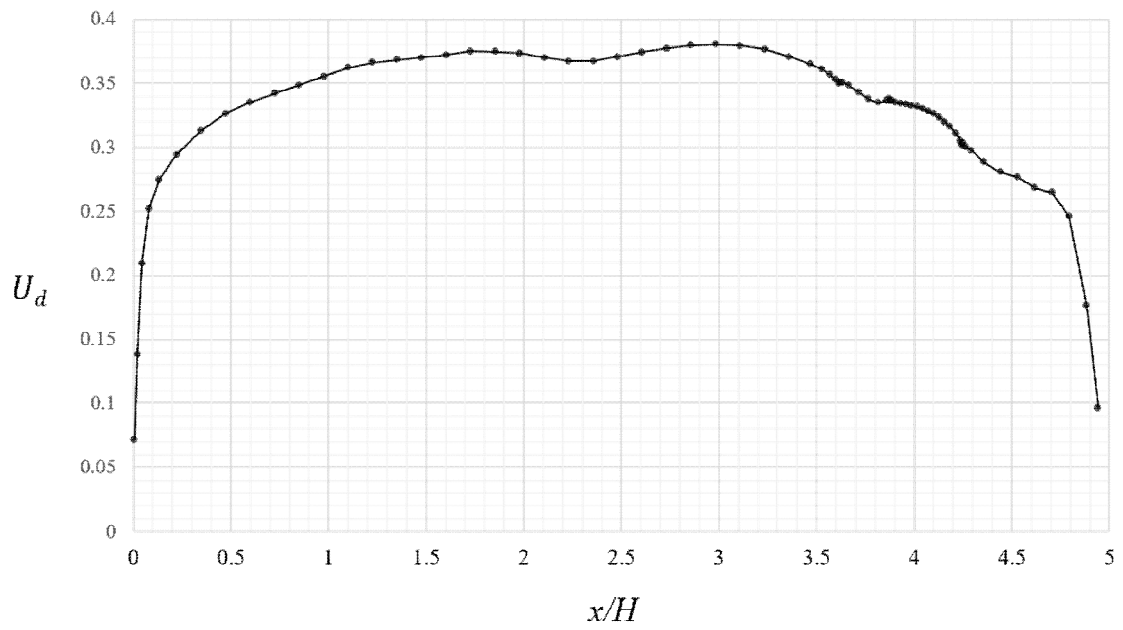


Figure 5.59 Depth averaged velocity in case CT23.

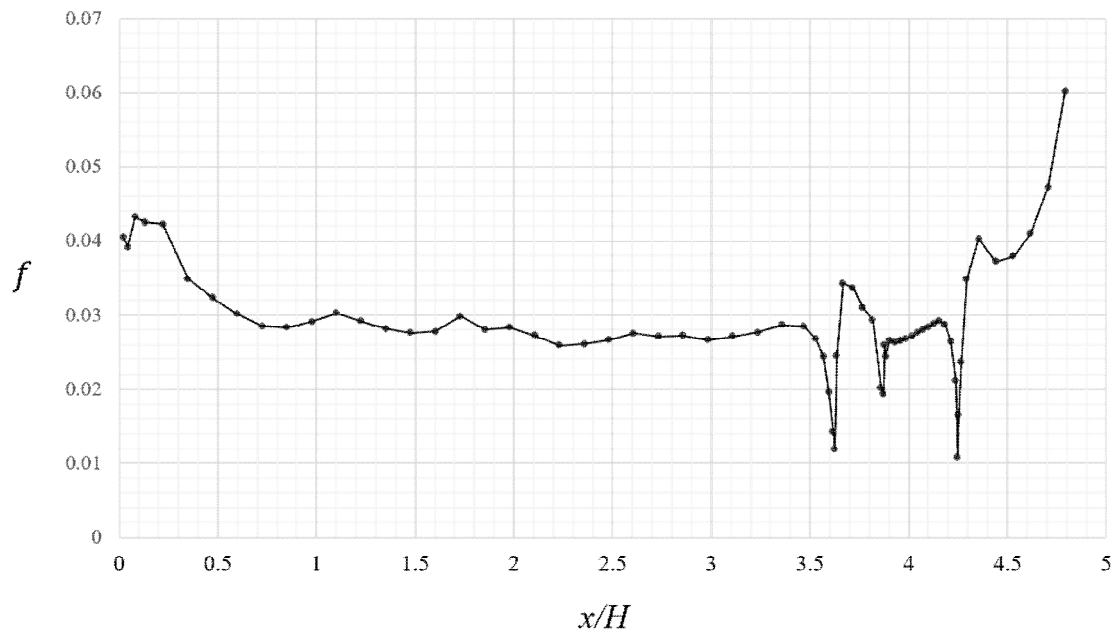


Figure 5.60 Friction factor from depth averaged velocity in case CT23.

5.3.2 Design friction factors

The design friction factors mean the friction factor in the channel part and the friction factors can be used to produce the design shear stress from depth averaged velocity as Equation 5.1.

The design friction factors for main channel, bank, floodplain, and levee in trapezoidal compound channels are provided as Table 5.3 to Table 5.6. These value are selected from the friction factor presented in subsection 5.3.1. From the plot of the normalized shear stress distribution, maximum shear stresses are chosen in the channel parts (main channel, bank, floodplain and levee) and then the friction factors in the corresponding location are selected as design friction factors. This procedure enables to select the conservative friction factors in view point of the safety.

The design friction factors show some consistency with depth and width ratio in the main channel and the floodplain, however, in the bank and the levee, the friction factors show high values in $h/H = 0.5$ due to the local vortex formations.

In the main channel, all factors range from 0.0266 to 0.0298 and the factors increase with depth and width ratio increase. Maximum factor in the main channel is seen in the narrow and deep floodplain. Minimum factor in the main channel is seen in the narrow and shallow floodplain.

In the floodplain, overall factors are lower than the factors in the main channels. The maximum value is seen in the narrow and deep floodplain and the value is 1.40. The factors in the floodplain increase with depth ratio increase and decrease with width ratio increase as expected. Minimum factor is seen in the wide and shallow floodplain and the value is 0.79.

The design factors with various combinations of width ratio and depth ratio can be easily selected from the Figure 5.5 and Figure 5.6.

Table 5.3 The design friction factors in trapezoidal compound channels (main channel).

b/B	h/H		
	0.25	0.5	0.75
0.500	0.0271	0.0295	0.0293
0.625	0.0266	0.0294	0.0293
0.750	0.0266	0.0287	0.0298

Table 5.4 The design friction factors in trapezoidal compound channels (bank).

b/B	h/H		
	0.25	0.5	0.75
0.500	0.0375	0.0398	0.0310
0.625	0.0370	0.0409	0.0332
0.750	0.0369	0.0417	0.0337

Table 5.5 The design friction factors in trapezoidal compound channels (floodplain).

b/B	h/H		
	0.25	0.5	0.75
0.500	0.0507	0.0378	0.0291
0.625	0.0537	0.0347	0.0283
0.750	0.0526	0.0326	0.0287

Table 5.6 The design friction factors in trapezoidal compound channels (levee).

b/B	h/H		
	0.25	0.5	0.75
0.500	0.0430	0.0589	0.0491
0.625	0.0516	0.0631	0.0481
0.750	0.0600	0.0668	0.0472

The values are selected from the LES simulation results of the chapter 4 and they are maximum normalized shear stresses of main channel and floodplain with different depth and width ratio. The design factors are also plotted with changes of depth and width ratio as Figure 5.1 to Figure 5.7. Overall design factors show some consistency with depth and width ratio, however, local reversal relations are also seen due to the local vortex formations.

In the main channel, all factors are over 1.1 and the factors decrease with depth and width ratio increase. Maximum factor in the main channel is seen in the narrow and shallow floodplain as expected and the value is 1.52. Minimum factor in the main channel is seen in the deep floodplain and the value is 1.12.

In the floodplain, overall factors are higher than the factors in the main channels and show much high range. The factors in the floodplain decrease with depth ratio increase. The maximum value is seen in the wide and deep floodplain. Minimum factor is seen in the wide and deep floodplain.

The design factors with various combinations of width ratio and depth ratio can be easily selected from the Figure 5.69 and Figure 5.72.

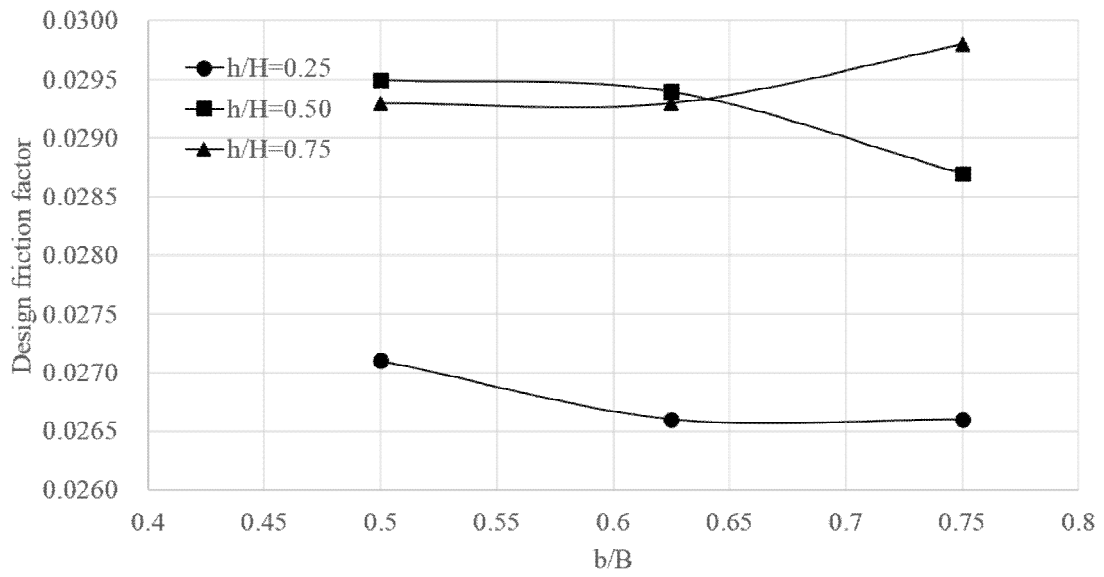


Figure 5.61 The design friction factors for trapezoidal compound channels with b/B (main channel).

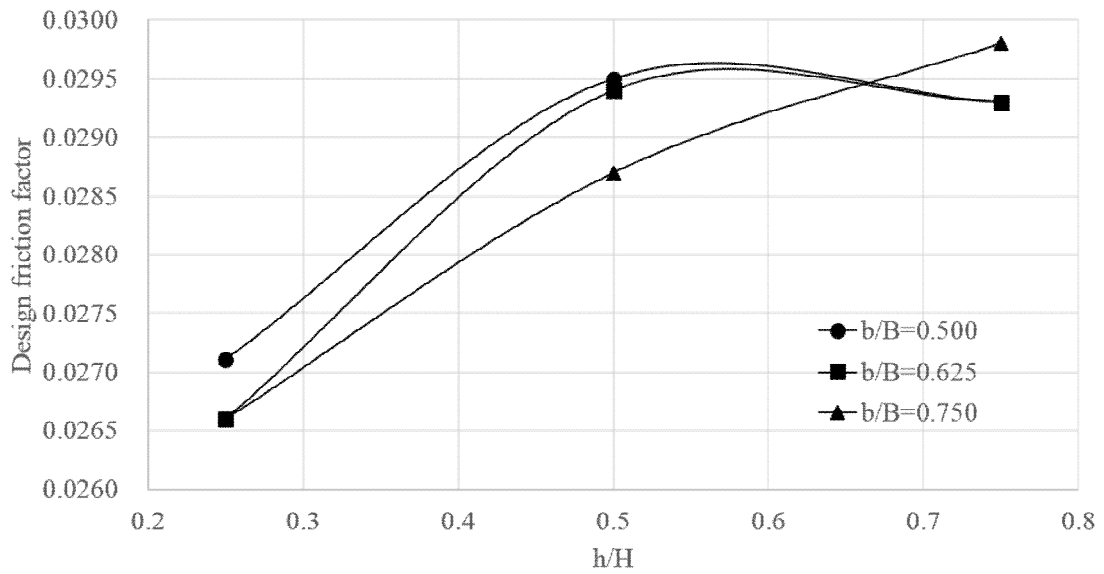


Figure 5.62 The design friction factors for trapezoidal compound channels with h/H (main channel).

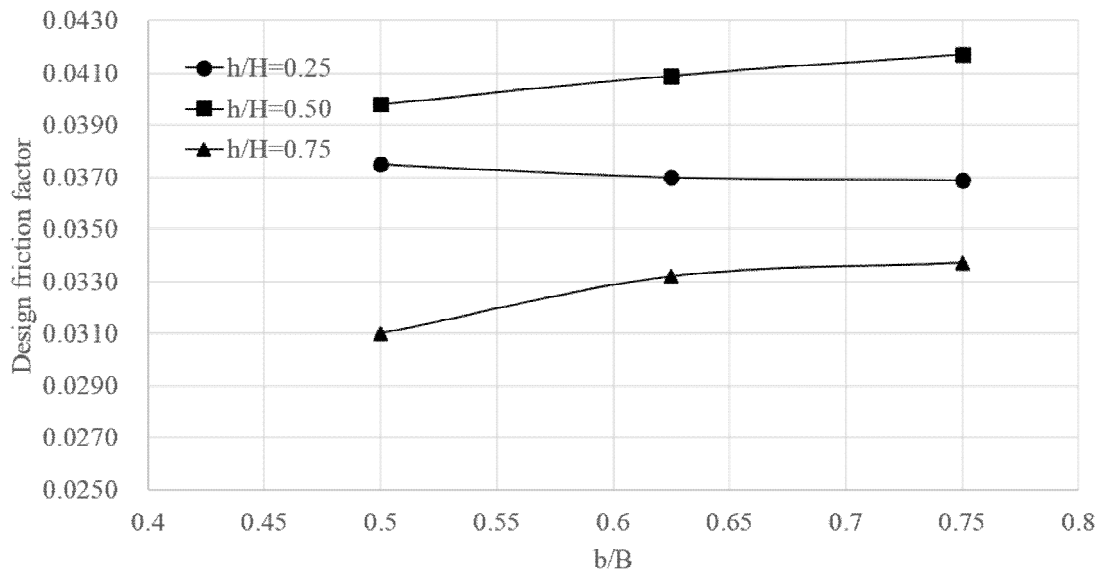


Figure 5.63 The design friction factors for trapezoidal compound channels with b/B (bank).

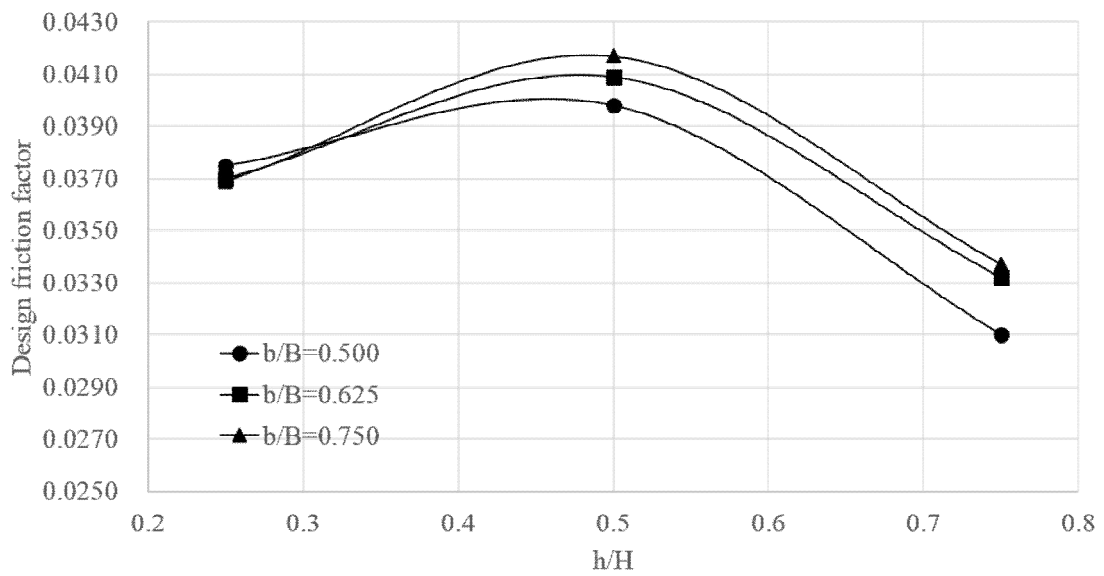


Figure 5.64 The design friction factors for trapezoidal compound channels with h/H (bank).

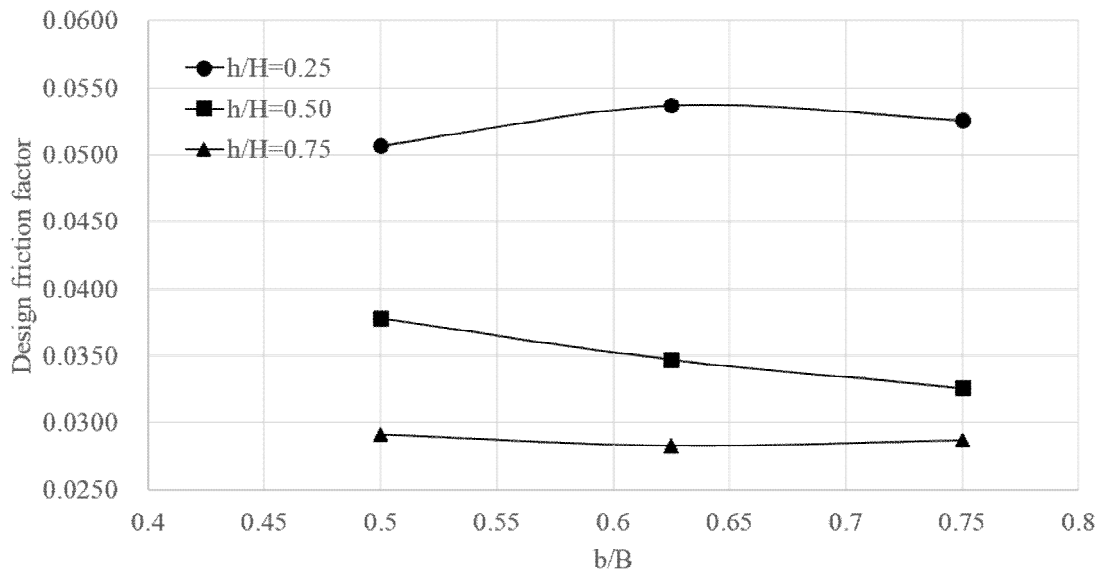


Figure 5.65 The design friction factors for trapezoidal compound channels with b/B (floodplain).

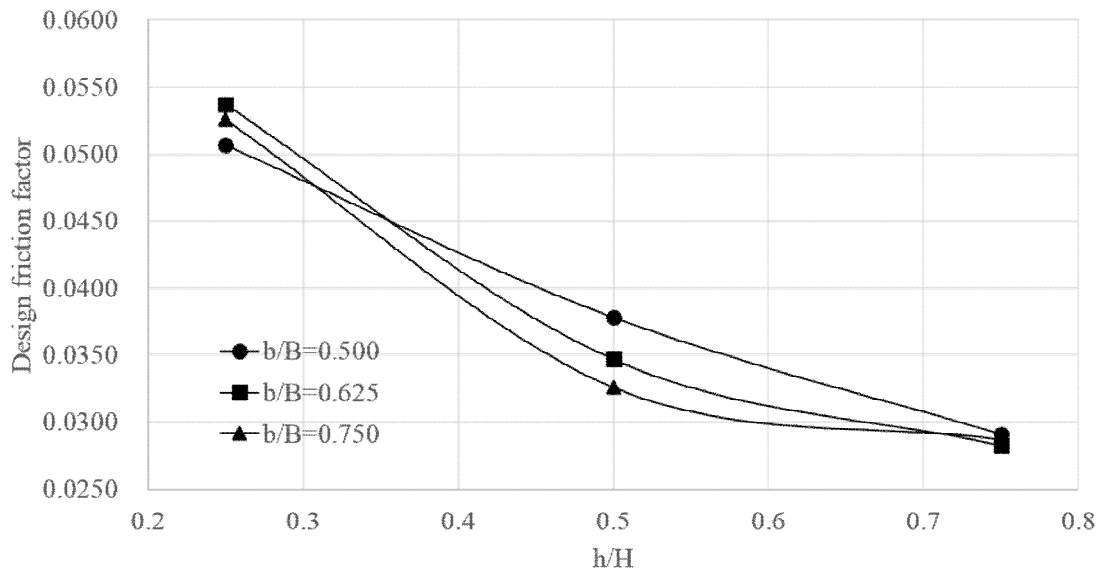


Figure 5.66 The design friction factors for trapezoidal compound channels with h/H (floodplain).

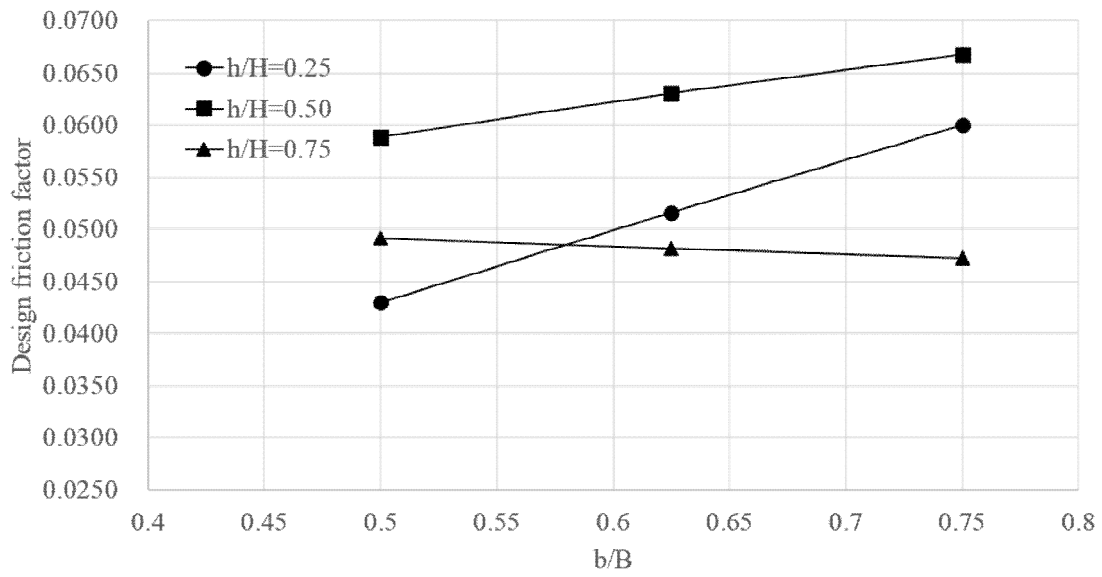


Figure 5.67 The design friction factors for trapezoidal compound channels with b/B (levee).

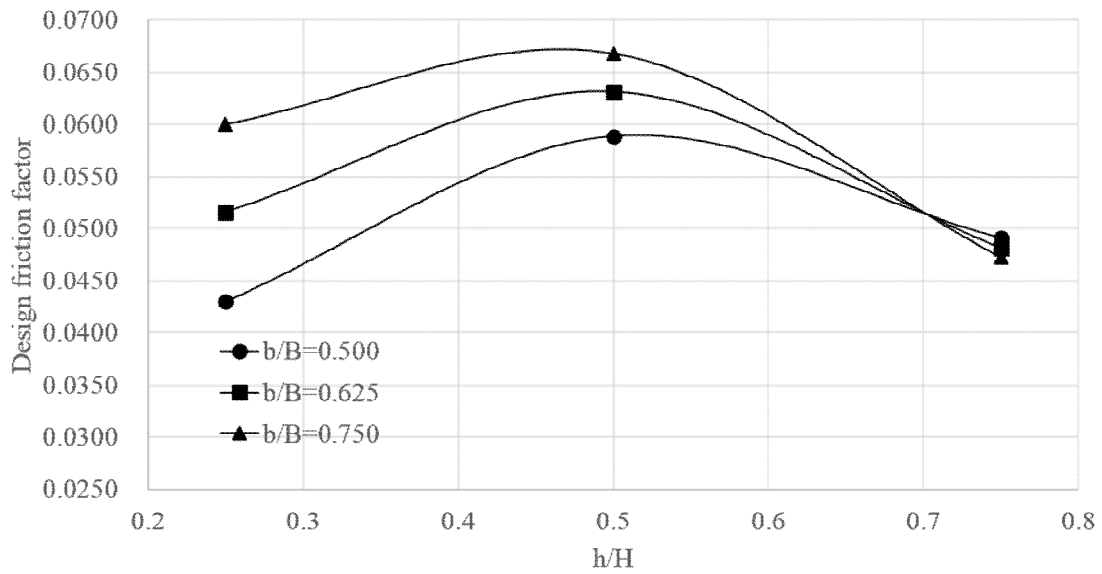


Figure 5.68 The design friction factors for trapezoidal compound channels with h/H (levee).

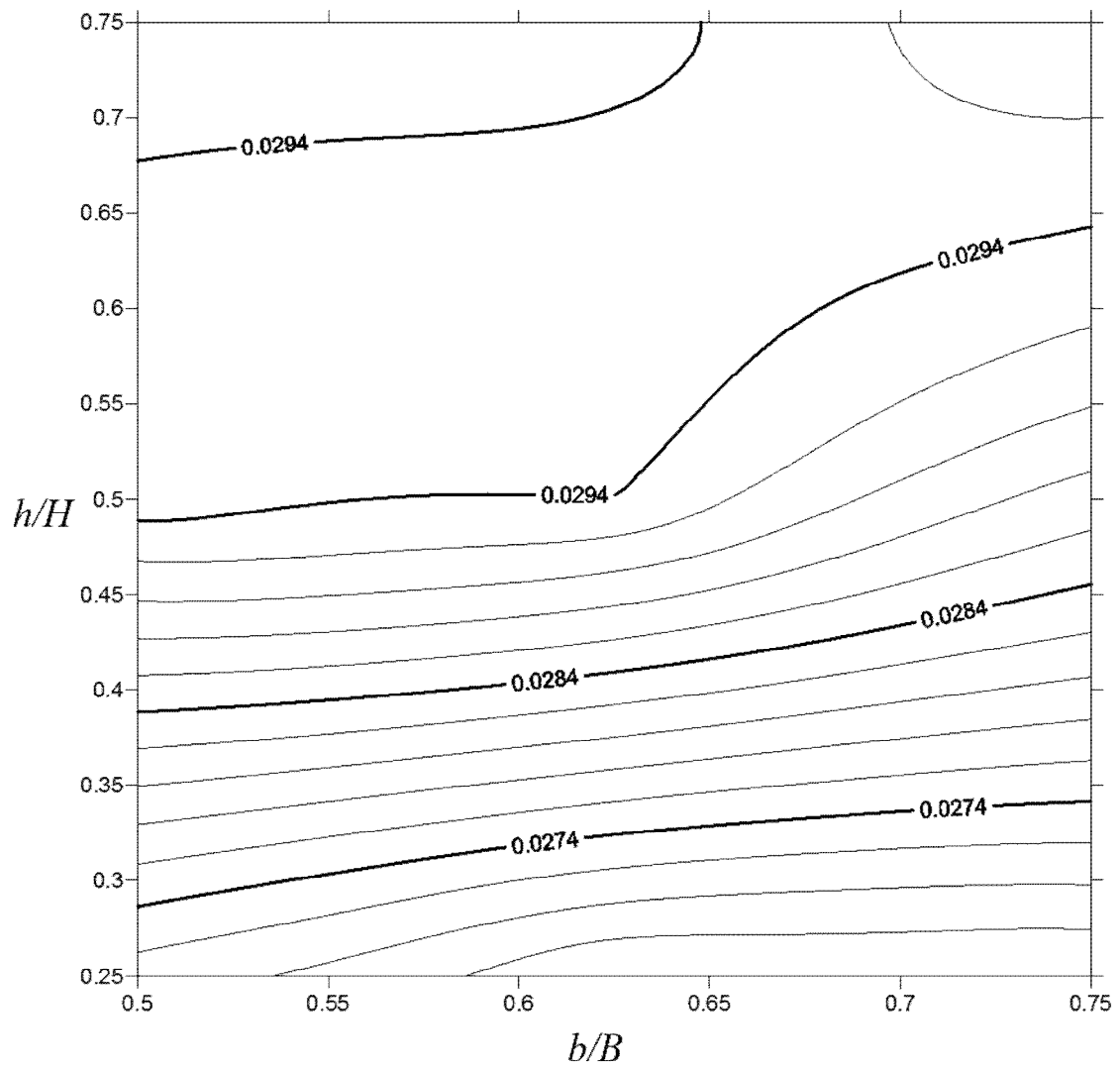


Figure 5.69 The design friction factors for trapezoidal compound channels with b/B and h/H (main channel).

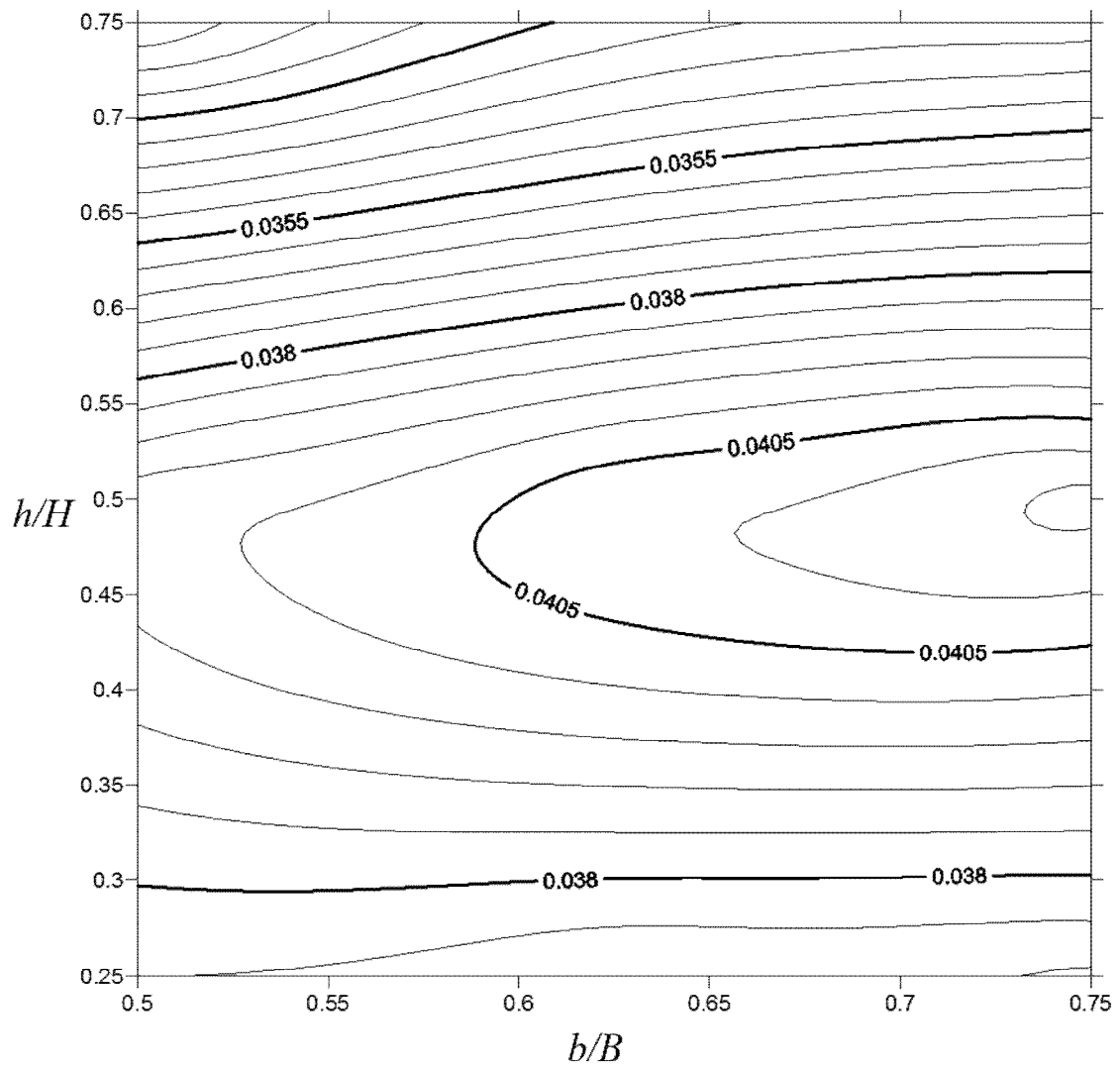


Figure 5.70 The design friction factors for trapezoidal compound channels with b/B and h/H (bank).

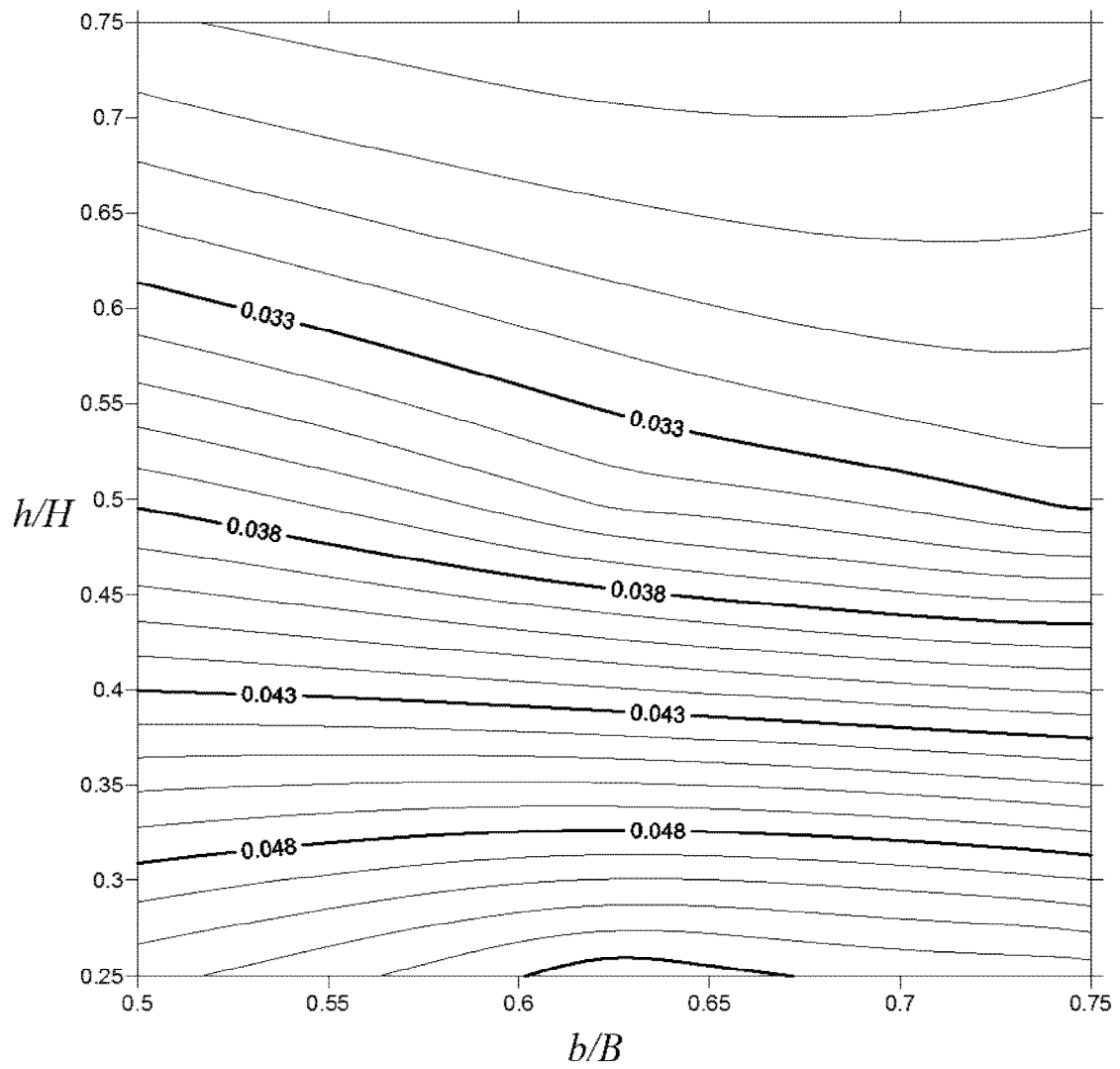


Figure 5.71 The design friction factors for trapezoidal compound channels with b/B and h/H (floodplain).

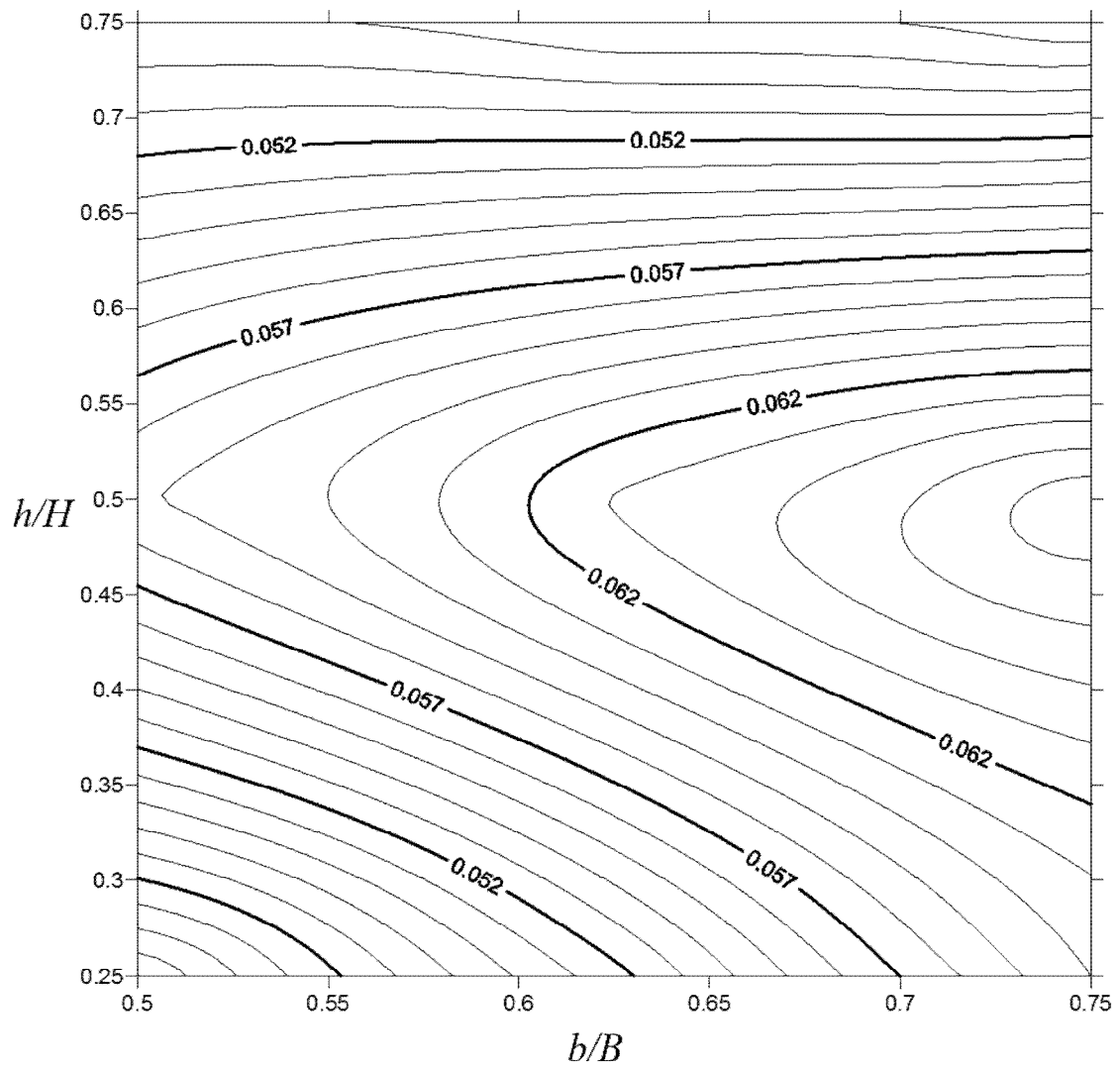


Figure 5.72 The design friction factors for trapezoidal compound channels with b/B and h/H (levee).

5.4 Application of the nomograph

5.4.1 Application of the design factor for design tractive forces

The design factor for design tractive force is multiplying factor to cross sectional averaged shear stress to produce the design shear stress. Average shear stress can be obtained easily from one dimension hydraulic analysis such as HEC-RAS.

If the section is given as Figure 5.73 and the calculated average shear stress is 0.5 N/m^2 , design tractive force can be determined by the nomograph of the design factor. From the section geometry and water elevation, b/B and h/H are 0.75 and 0.5 , respectively. From the nomograph of rectangular compound channels, the design factors in the main channel and floodplain are 1.28 and 0.85 , respectively (Figure 5.74 and Figure 5.75). Hence, resultant tractive forces in the main channel and floodplain are 0.64 N/m^2 and 0.425 N/m^2 .

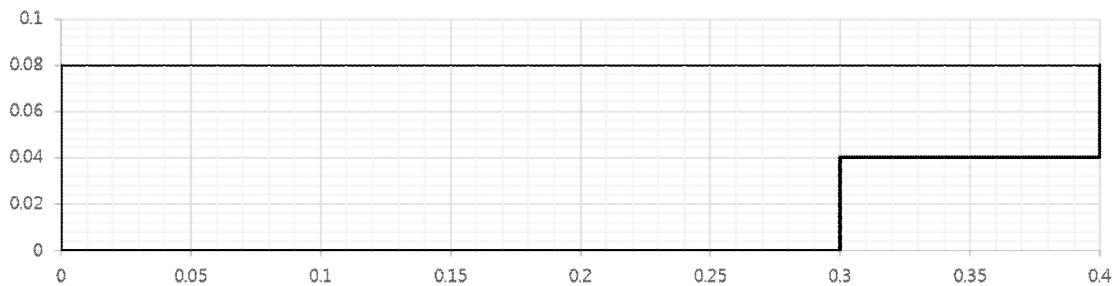


Figure 5.73 Test section 1 for a rectangular compound channel.

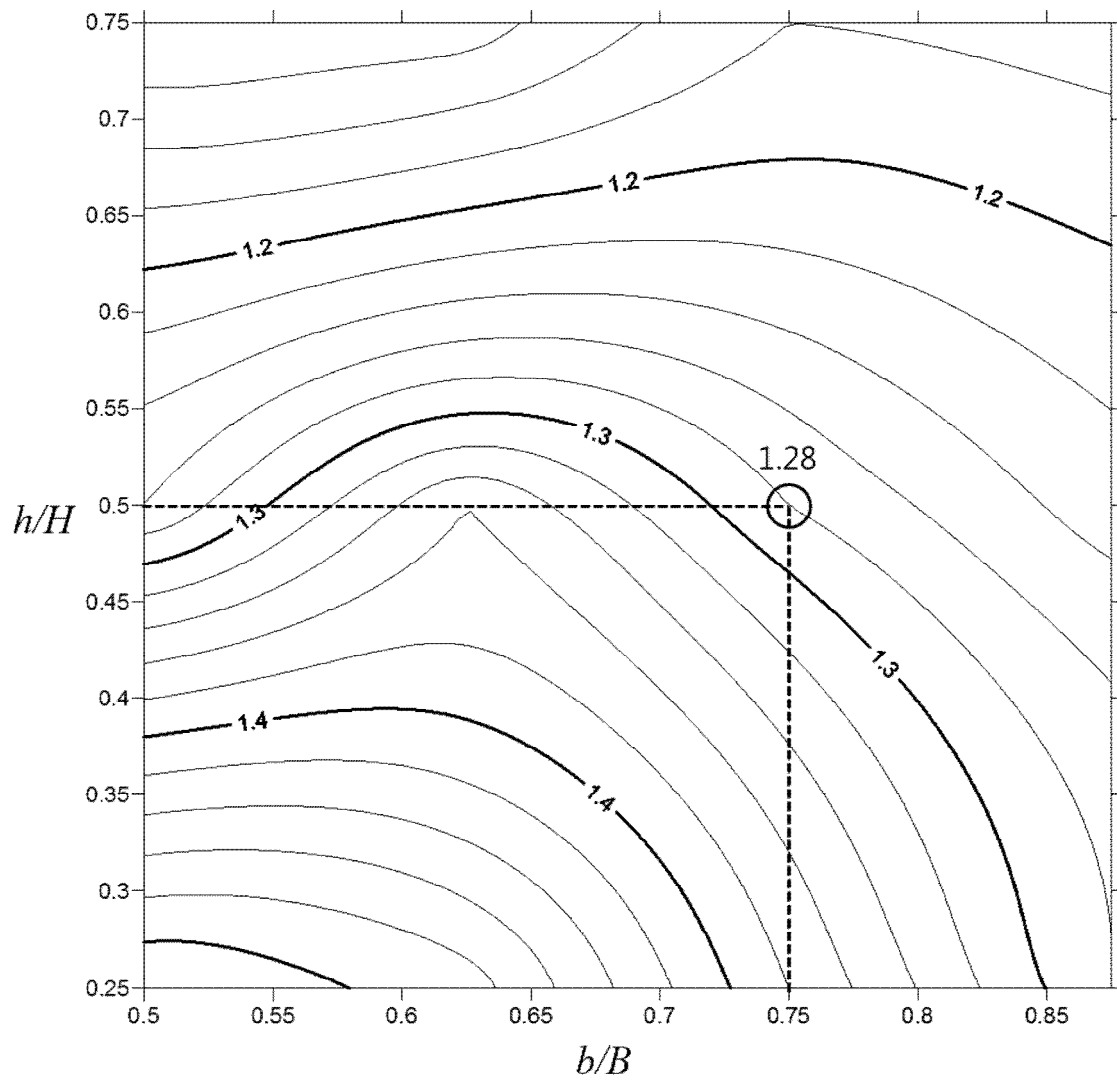


Figure 5.74 Design factor from the nomograph (main channel in rectangular open channels).

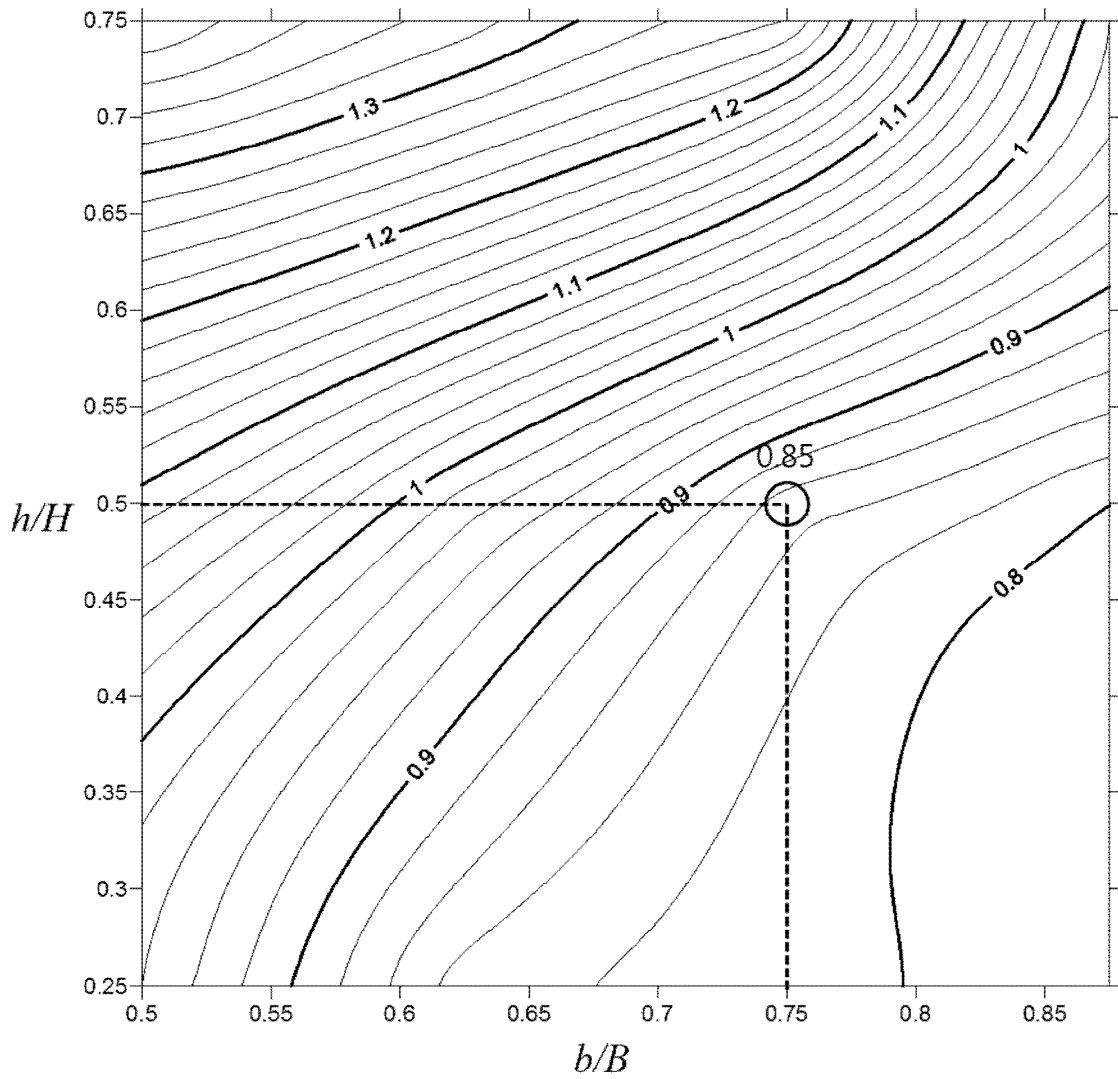


Figure 5.75 Design factor from the nomograph (floodplain in rectangular open channels).

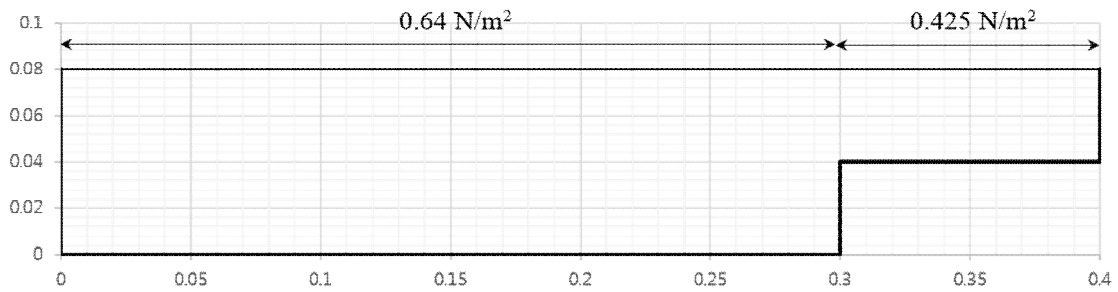


Figure 5.76 Resultant design tractive forces for test section 1.

In a trapezoidal compound channel, design tractive forces can be determined in similar procedure. If the section is given as Figure 5.76 and the calculated average shear stress is 0.5 N/m^2 , design tractive force can be determined by the nomograph of the trapezoidal design factor. From the section geometry and water elevation, b/B and h/H are 0.625 and 0.5 , respectively. From the nomograph of trapezoidal compound channels, the design factors in the main channel, bank, floodplain, and levee are 1.44 , 1.52 , 0.875 and 0.91 , respectively (from Figure 5.77 to Figure 5.80). Hence, resultant tractive forces in the main channel, bank, floodplain, and levee are 0.72 N/m^2 , 0.76 N/m^2 , 0.438 N/m^2 , and 0.455 N/m^2 , respectively.

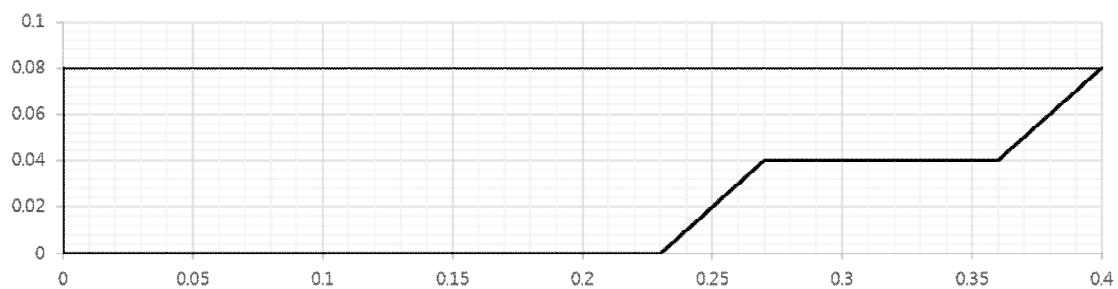


Figure 5.77 Test section 2 for a trapezoidal compound channel.

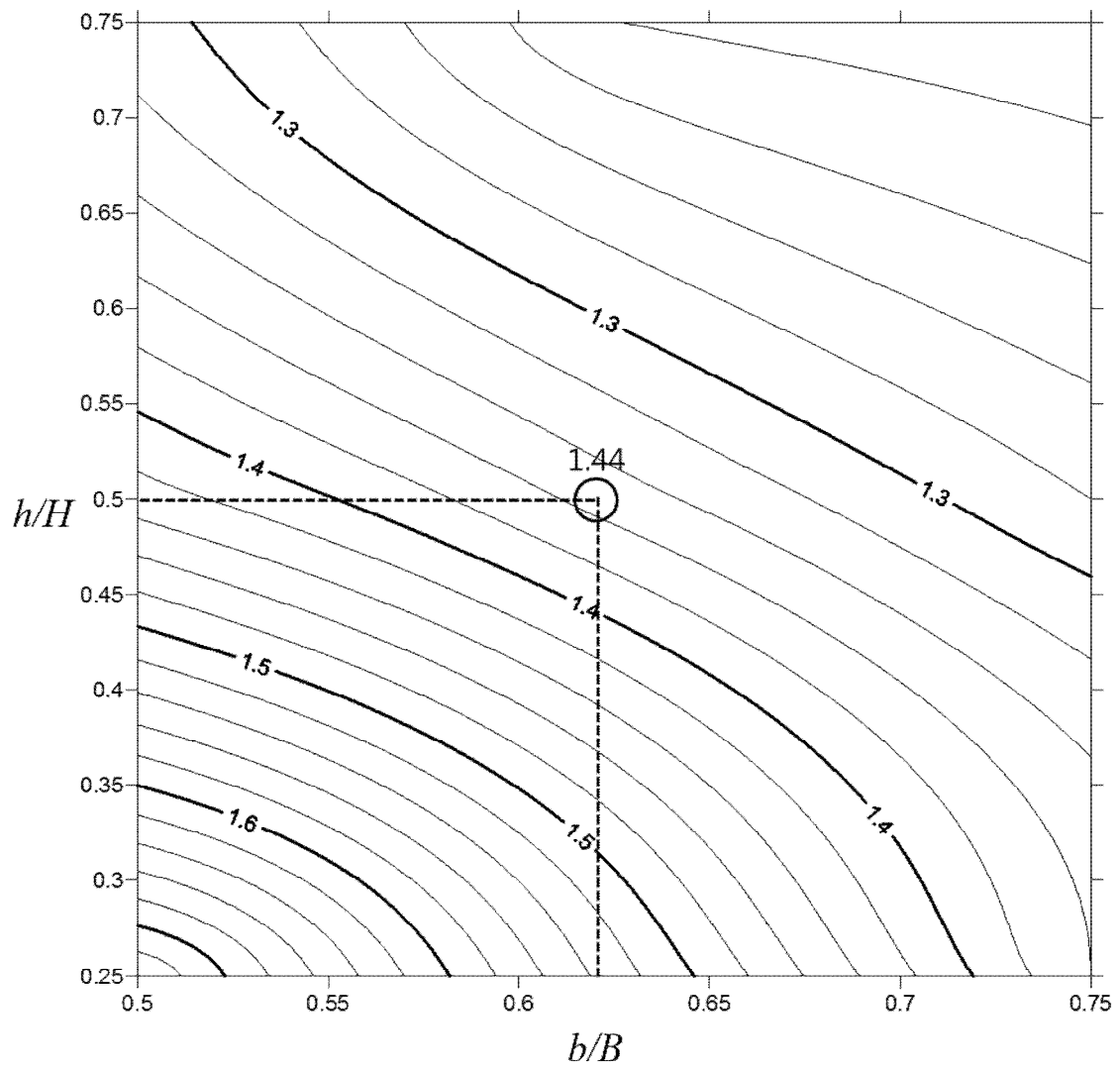


Figure 5.78 Design factor from the nomograph (main channel in trapezoidal open channels).

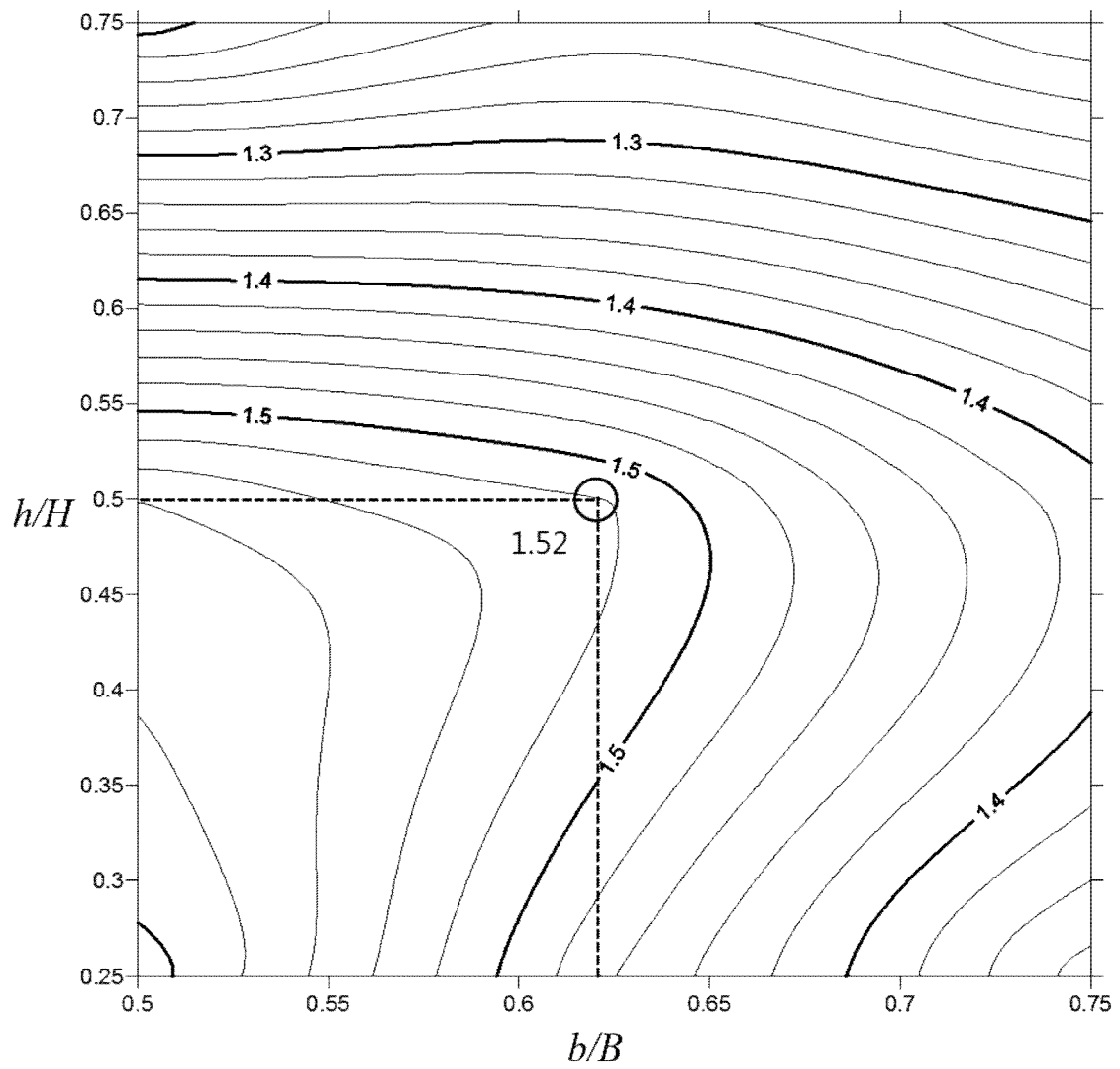


Figure 5.79 Design factor from the nomograph (bank in trapezoidal open channels).

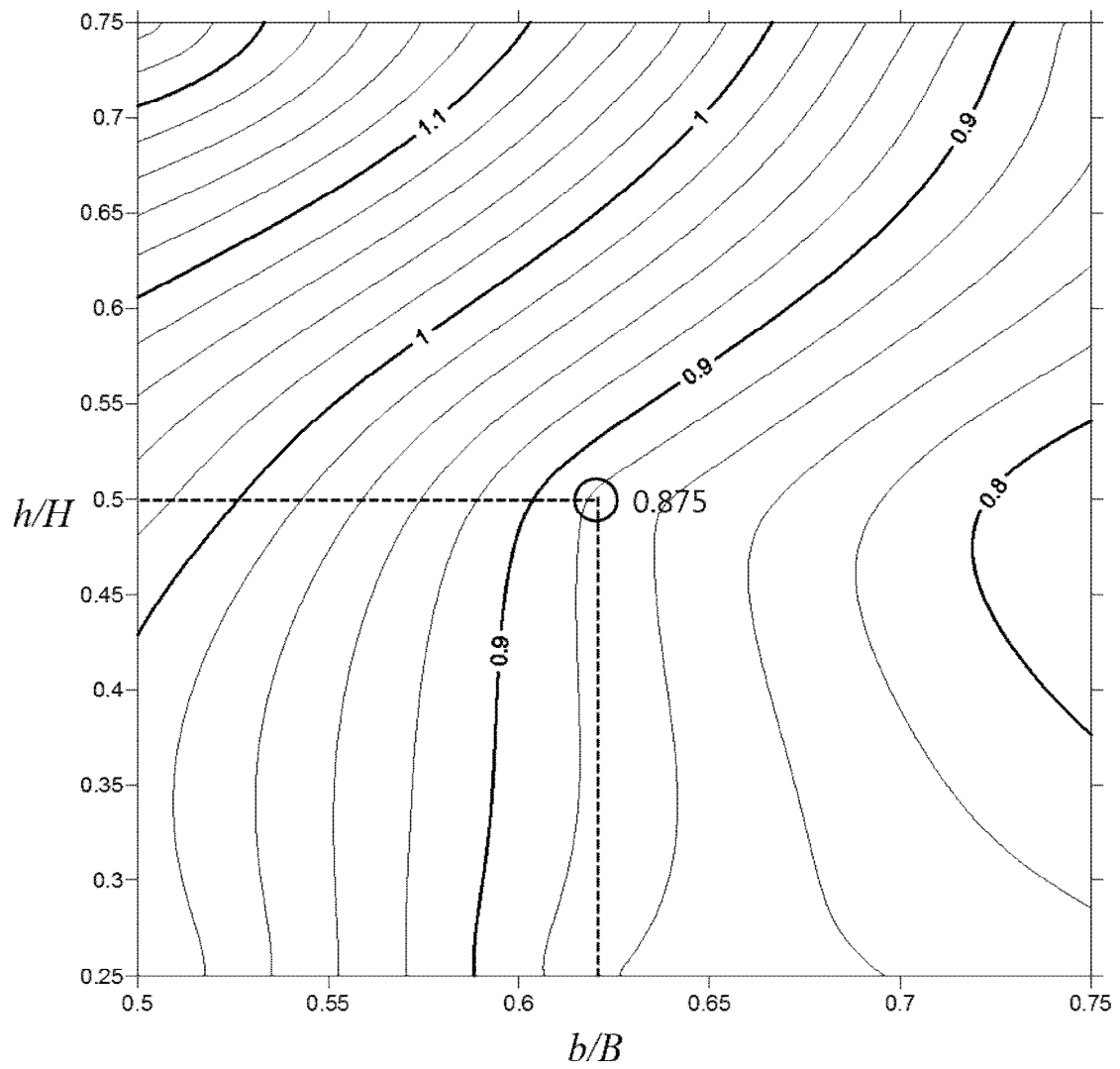


Figure 5.80 Design factor from the nomograph (floodplain in trapezoidal open channels).

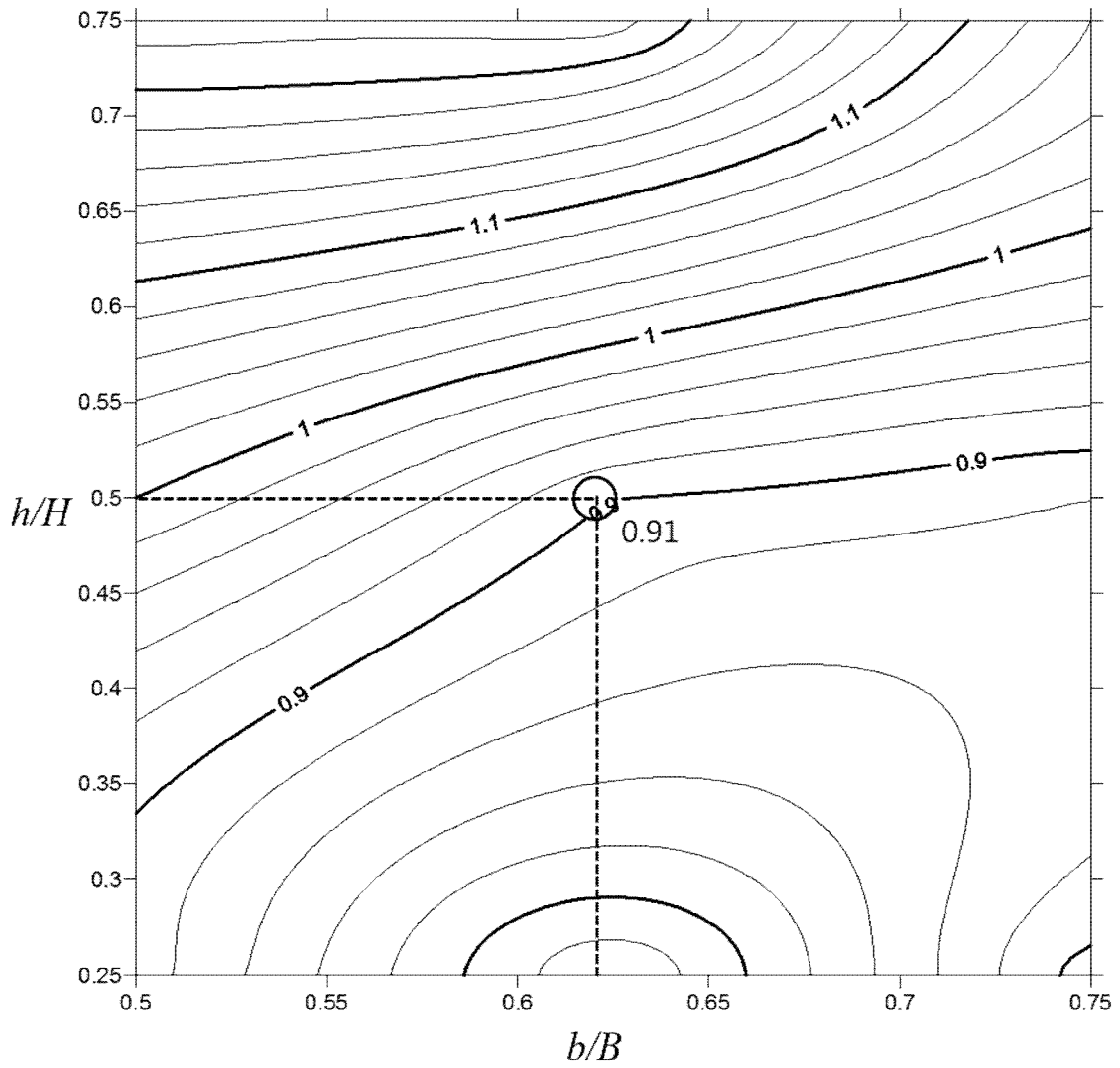


Figure 5.81 Design factor from the nomograph (levee in trapezoidal open channels).

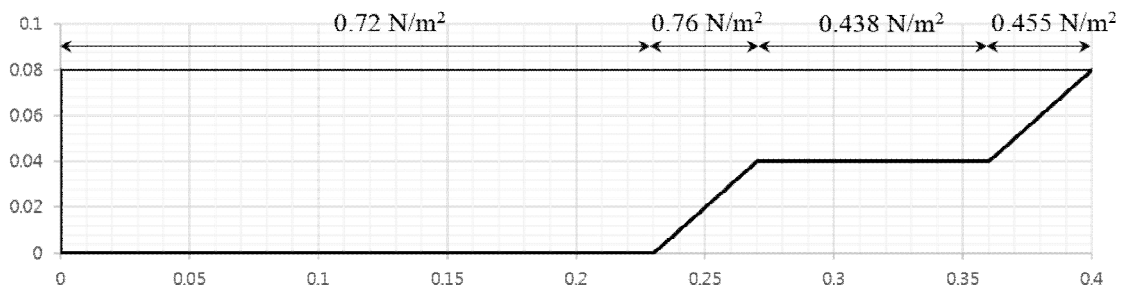


Figure 5.82 Resultant design tractive forces for test section 2.

5.4.2 Application of the design friction factor

The design friction factor can be applied to depth averaged velocity to produce the design tractive forces with corresponding width ratio and depth ratio. To apply design friction factor channel geometry and depth averaged velocity distribution are required. Depth averaged velocity distribution can be obtained easily from SKM or 2D hydraulic models. In this application, depth averaged velocity distribution is used from the LES simulation.

To verify the friction factor nomographs in trapezoidal compound channel measured shear stress distribution is required. However, experimental data for trapezoidal compound channel with corresponding depth and width ratio are not available. Although FCF experimental data can be a good choice for verification, the depth and width ratio are out of this study. Hence, numerical results are used to show the application of the nomograph.

In the case of CT02, b/B and h/H are 0.625 and 0.5, respectively and the distribution of the depth averaged velocity is shown in Figure 5.45. From the friction factor nomograph and geometric ratio, design friction factors are determined from Figure 5.83 to Figure 5.86. Determined friction factors of main channel, bank, floodplain, and levee are 0.0294, 0.0407, 0.035, and 0.061, respectively as shown in Figure 5.87.

Design tractive forces are calculated from the depth averaged velocity and the design friction factors by Equation 5.2.

$$\tau_0 = \frac{1}{8} f \rho U_d^2 \quad (5.2)$$

Calculated design tractive forces are seen in Figure 5.88, and the result is compared with LES results. The result agrees with high shear stress of LES results so these values can be used as design tractive forces.

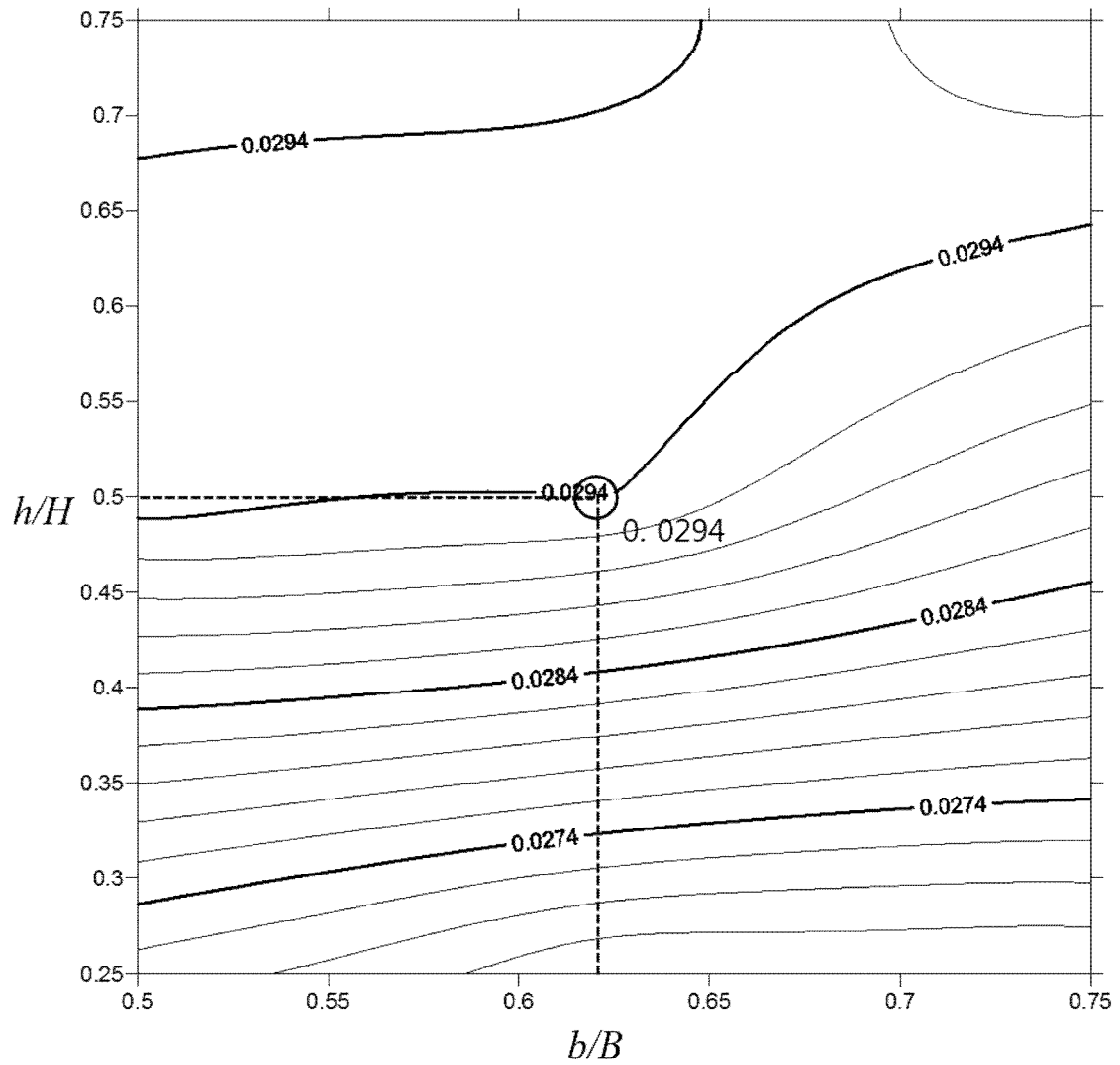


Figure 5.83 Design friction factor from the nomograph (main channel in trapezoidal open channels).

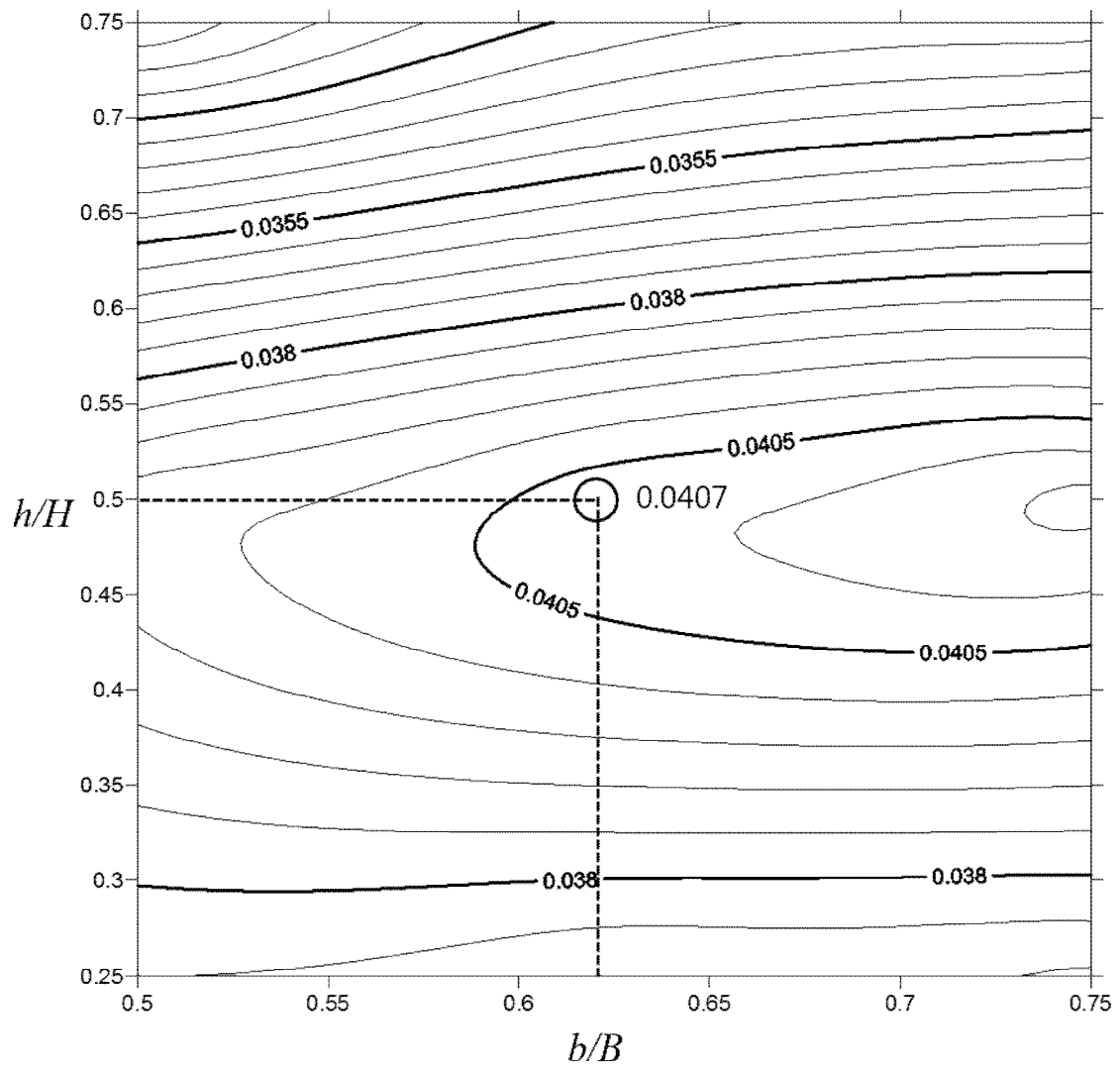


Figure 5.84 Design friction factor from the nomograph (bank in trapezoidal open channels).

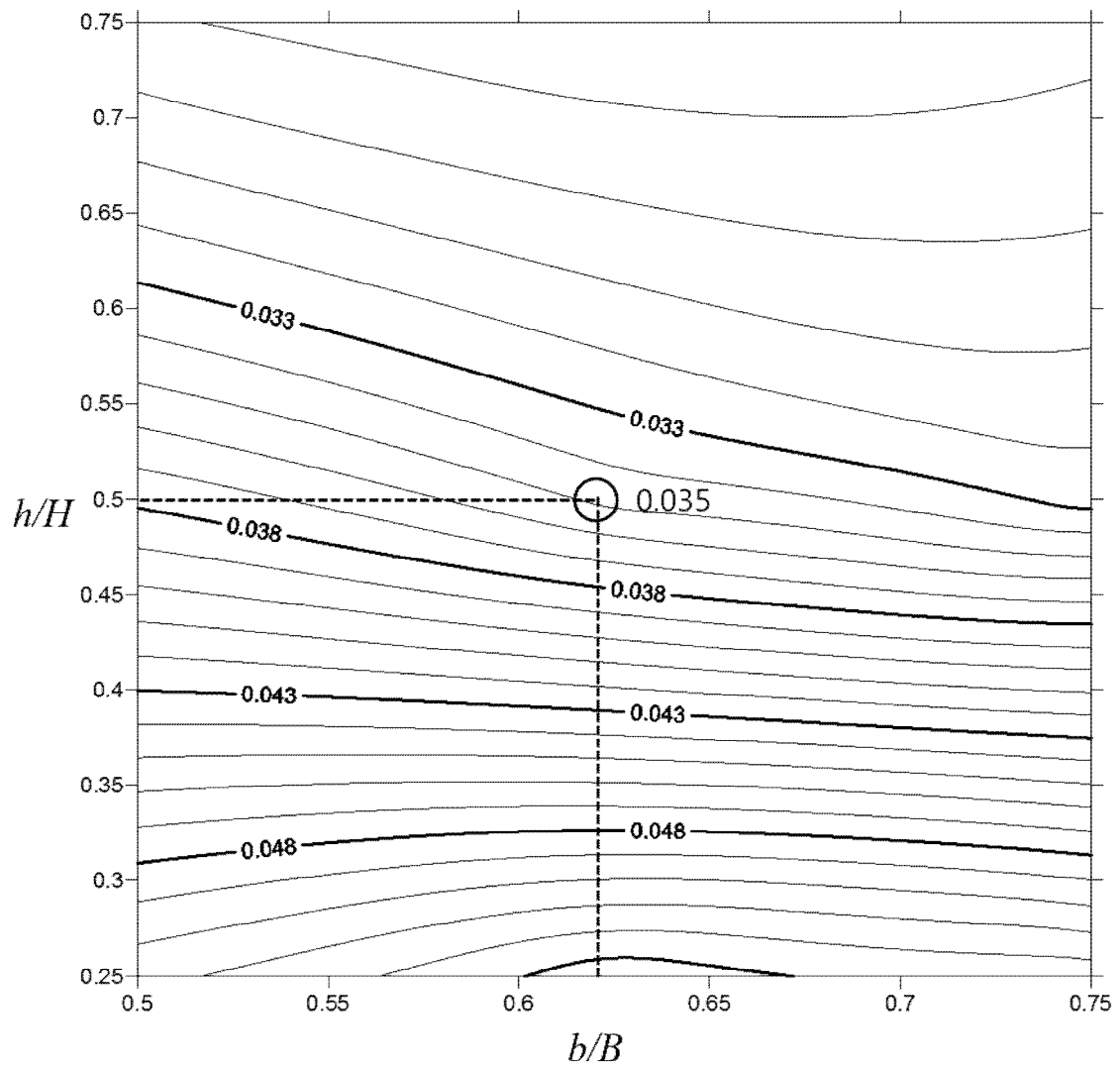


Figure 5.85 Design friction factor from the nomograph (floodplain in trapezoidal open channels).

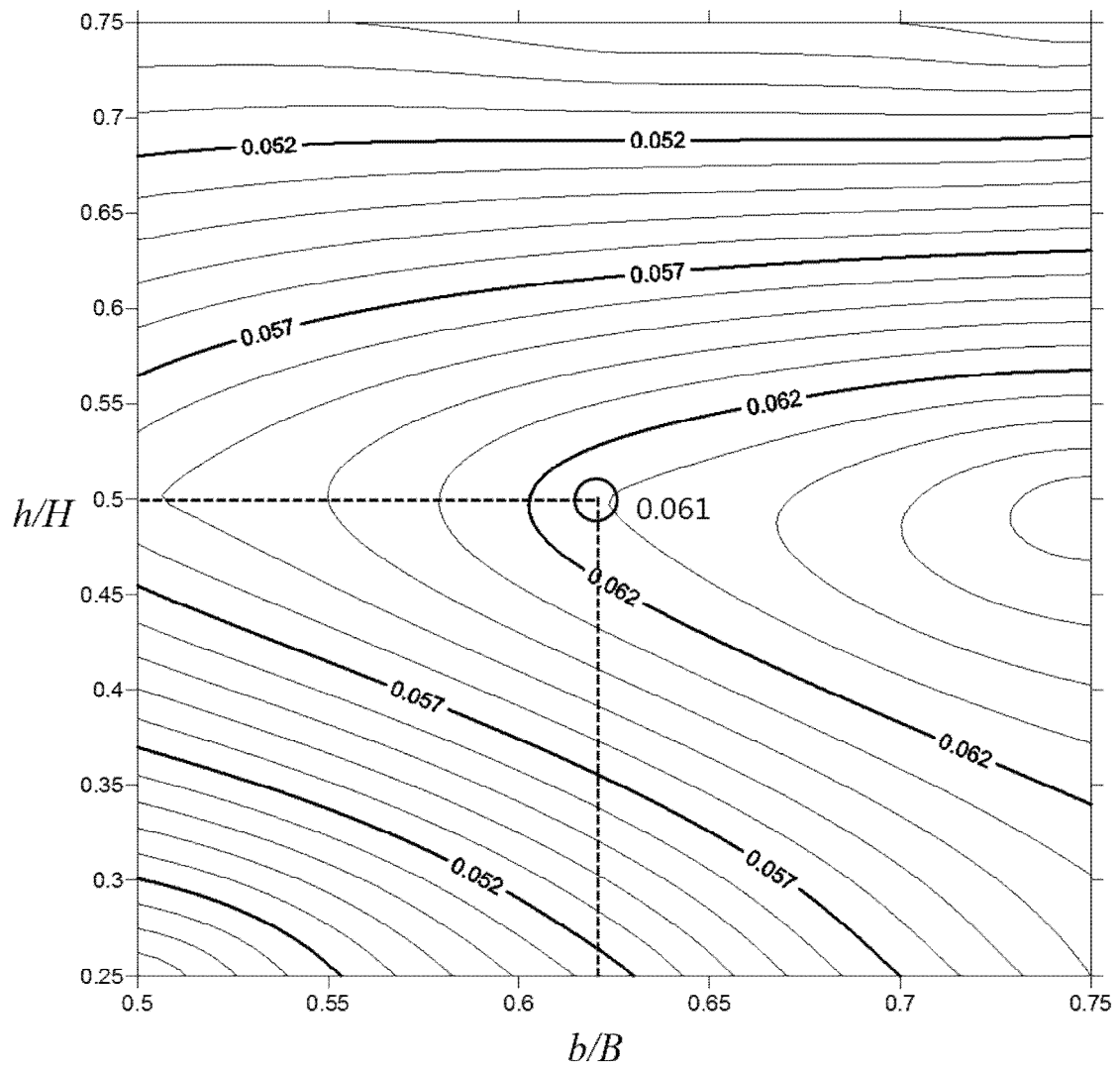


Figure 5.86 Design friction factor from the nomograph (Levee in trapezoidal open channels).

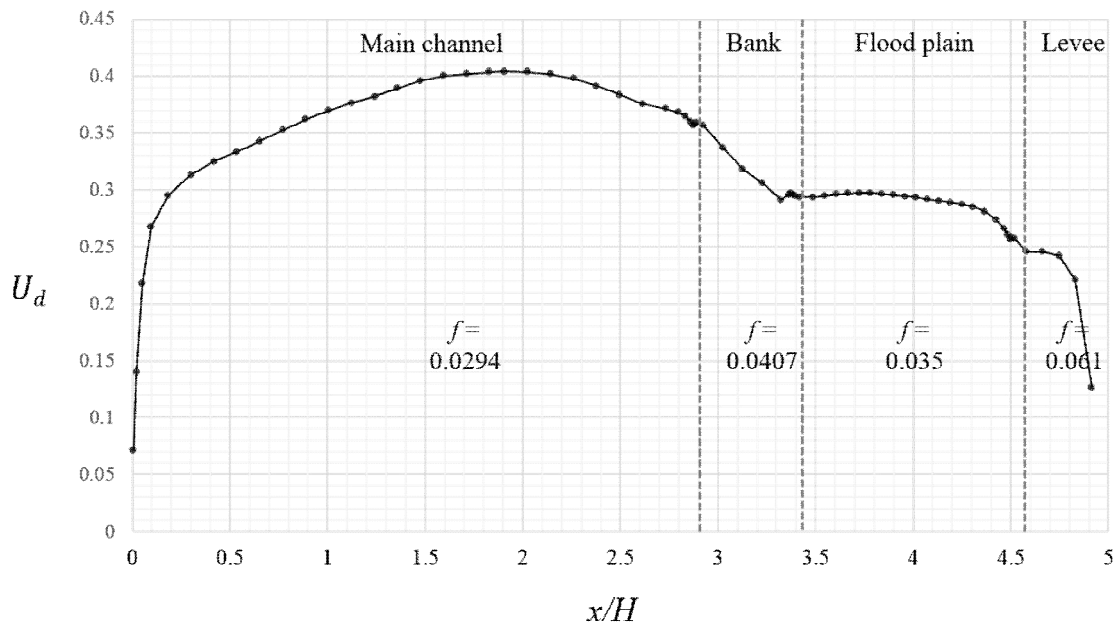


Figure 5.87 Determined friction factors from the nomograph.

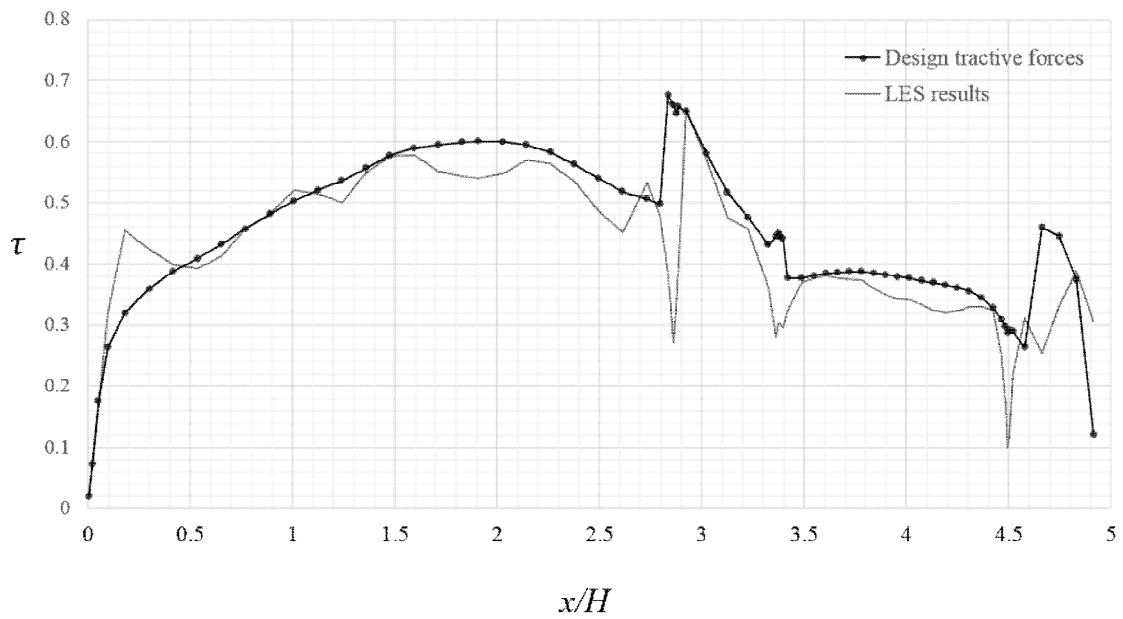


Figure 5.88 Calculated design tractive forces by nomograph and depth averaged velocity.

5.4.3 Applicability and limitation

As shown in above sections, design factors and design friction factors are proper to produce the design tractive force in the compound open channel. The nomographs are developed from the relation of bed shear stress distribution and geometric ratio, hence it is natural the calculated tractive forces from the nomographs show reasonable values.

The applicability of the nomograph depends on the exactness of the LES results and geometric ratio. The LES results are verified with rectangular compound channel, and the results shows good agreement with experimental results. In the trapezoidal compound channel, the LES results are not compared with experimental results. However, the results in the trapezoidal also can be reliable because same numerical schemes and similar mesh structures are applied.

Main limitations of the developed nomograph arise in the application for rough bed and geometric ratio out of this study. In this study bed roughness is assumed as smooth bed, and the developed nomograph should be applied to smooth bed.

Natural rivers show very wide range of the depth ratio and width ratio, however, in this study the depth ratio range from 0.25 to 0.75 and the width ratio range from 0.5 to 0.75. These geometric ratio is correspond to small stream or artificial channel. In FCF experiments depth ratio range from 0.05 to 0.5 and width ratio range from 0.15 to 0.40. With decrease of the depth ratio and the width ratio, the difference between the maximum shear stress and average shear stress decrease. Also the friction factor decreases with decrease of the depth ratio and the width ratio.

In this study narrow cases of the compound open channel are studied due to the limitation of computing resources. For wide application including large natural rivers, further study for lower depth ratio and width ratio is required.

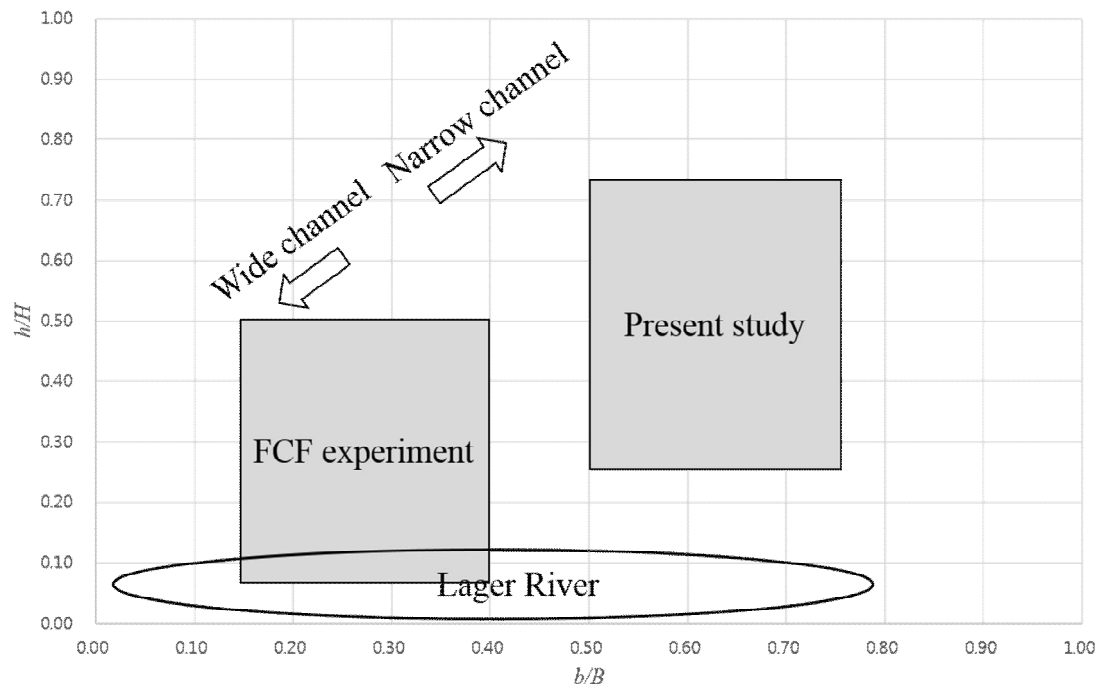


Figure 5.89 Comparison of geometric ratio.

CHAPTER 6

CONCLUSIONS

The main objective of this study is to suggest simple design factors of tractive force evaluation in compound open channel for various channel shapes to prevent the over-design and under-design in river design practice. To achieve the main objective 3D numerical simulations and laboratory experiments are performed to analyze the flow structures and wall shear stress distribution for various compound channel shapes.

In this study tractive forces in representative compound open channels are measured by experiments, and three dimensional CFD model is calibrated by the experimental results. In the LES non-uniform grid is applied to obtain the better results near the wall region, thus several inner vortex are detected and these vortex affect the wall shear stress distribution. Using the calibrated numerical model, characteristics of tractive force distribution with floodplain width and height are analyzed. Characteristics of tractive force distribution compared with average tractive forcings are investigated on bank, floodplain and levee.

In the experiment, shear stress in the rectangular compound channel is measured with calibrated Preston tube and compared with Tominaga and Nezu (1991). The results show good agreement in depth ratio 0.25 and 0.5, and relative large difference is detected in depth ratio 0.75. The case of depth ratio 0.75 underestimate shear stress of floodplain with 10%.

Shear stress distributions are widely simulated for various rectangular and trapezoidal compound open channels. From these simulation, two types of methods for design shear stress evaluation are suggested and these method can be applied easily to practical design work because of the simplicity of the methods.

Overall mean velocity distributions of rectangular and trapezoidal compound channel show similar patterns, however some differences are seen. In rectangular cases contour

lines are distorted slightly to the left side wall, on the other hand, in the trapezoidal cases contour lines are distorted slightly to the floodplain. This difference is due to resistance of the junction of the main channel and floodplain. More resistance due to the junction is produced in the rectangular cases than in the trapezoidal cases, hence the main channel velocity near the junction decreases in the rectangular cases.

Velocity bulge in the junction also decreases in the trapezoidal cases due to the decrease of the wall resistance. This decrease of the wall resistance in the trapezoidal cases is due to the decrease of the junction angle.

Velocity bulge in the sidewall of the floodplain is seen in the both of the rectangular and trapezoidal cases. This velocity bulge is more clear in the rectangular cases and this seem to be related to the formation of the inner vortex in the sidewall of the floodplain. Velocity dip in the main channel is more distinct in the shallow floodplain cases and it becomes unclear in the deep floodplain cases.

Local wall shear stresses are highly affected by inner vortex cell and local variance is observed in the junction and it is highly related to the floodplain depth. In the wide floodplain, local variance in shear decrease. In the levee, velocity bulge is observed by the formation of the inner vortex in high floodplain depth.

Design factors for averaged shear stress are suggested for depth ratio ranging from 0.25 to 0.75 and width ratio ranging from 0.5 to 0.75. In the rectangular compound channel, the design factors in the main channel range from 1.12 to 1.52, and the design factors in the floodplain range from 0.79 to 1.40. In the main channel, design factors increase with increase of depth ratio and width ratio, in the floodplain, design factors increase with increase of depth ratio and decrease of width ratio.

Design factors for the trapezoidal compound channel are also suggested. In the main channel design factors range from 1.21 to 1.74, in the bank the factors range from 1.20 to 1.61, in the floodplain the factors range from 0.78 to 1.25, and in the levee the factors range from 0.76 to 1.23.

Design friction factors for depth average velocity are suggested from the analysis of the LES results. In the main channel the friction factors range from 0.0266 to 0.298, in the bank the factors range from 0.332 to 0.417, in the floodplain the factors range from 0.283 to 0.537, and in the levee the factors range from 0.472 to 0.0600.

The nomograph developed in this study can be applied for the given geometric ratio and help to calculate the design tractive forces in the simple procedure.

REFERENCES

- Abril, J.B. and Knight, D.W. (2004). Stage-discharge prediction for rivers in flood applying a depth-averaged model. *Journal of Hydraulic Research*, IAHR, 42 (6), 616-629.
- Ackers, P. (1993a). Flow formulae for straight two-stage channels. *J. Hydraulic Research*, 31 (4), 509-531.
- Ackers, P. (1993b). Stage-discharge functions of two-stage channels: The impact of new research. *J. Institution of Water and Environmental Management*, 7 (1), 52-61.
- Alfredsson, P., Johansson, A., Haritonidis, J., and Eckelmann, H. (1987). The fluctuation wall-shear stress and the velocity field in the viscous sublayer. *Phys. Fluids*, 31, 1026-1033.
- Al-Hamid, A.A.I. (1991). Boundary shear stress and velocity distributions in differentially roughened trapezoidal open channels. PhD thesis, The University of Birmingham, Birmingham, UK.
- Azevedo, R., Rojas-Solórzano, L.R. and Leal, J.B. (2012). Experimental characterization of straight compound-channel turbulent field. In Proc. of 2nd European IAHR Congress, 27-29 June, Munich, Germany.
- Barr, D.I.H. (1979). Osborne Reynolds' turbulent flow resistance formulae. *Proceedings Institution of Civil Engineers*, Part 2, 67, 743-750.
- Bechert, D. (1995). On the calibration of preston tubes. *AIAA J.*, 34:205-206.
- Bilgil, A. (2005), Correlation and distribution of shear stress for turbulent flow in a smooth rectangular open channel. *Journal of Hydraulic Research*, IAHR, 43 (2), 165-173.
- Bousmar, D. and Zech, Y. (2004). Velocity distribution in non-prismatic compound channels. In Proc. Inst. Civil Eng. Water Manage., 157, 99-108.
- Bradbury, L. and Castro, I. (1971). A pulsed-wire technique for velocity measurements in highly turbulent flow. *J. Fluid Mech.*, 22, 679-687.
- Bradshaw, P. (1971). *An introduction to turbulence and its measurement*. Pergamon

- Press, Oxford.
- Bradshaw, P. (1987). Turbulent secondary flows. *Annual Review of Fluid Mechanics*, 19, 53-74.
- Bradshaw, P. and Gregory, N. (1959). The determination of local turbulent skin friction from observations in the viscous sub-layer,. Technical report, Reports and Memoranda 3202, ARC, London.
- Brogia, R., Pascarelli, A., and Piomelli U. (2003). Large-eddy simulation of ducts with a free surface. *Journal of Fluid Mechanics*, 484, 223-253.
- Brundrett, E. and Baines, W.D. (1964). The production and diffusion of vorticity in duct flow. *Journal of Fluid Mechanics*, Cambridge University Press, 19 (03), 375-394.
- Cater, J.E., and Williams, J.J.R. (2008). Large eddy simulation of a long asymmetric compound open channel. *Journal of Hydraulic Research*, 46(4), 445-453, DOI: [10.3826/jhr.2008.3134](https://doi.org/10.3826/jhr.2008.3134).
- Celik, I. and Rodi, W. (1984). Simulation of free-surface effects in turbulent channel flows. *PCH Physico Chemical Hydrodynamics*, 5(3/4), 217-227.
- CES, (2008) Conveyance Estimation System. <http://www.river-conveyance.net>.
- Chlebek, J. (2009). Modelling of simple prismatic channels with varying roughness using the SKM and a study of flows in smooth non-prismatic channels with skewed floodplains. PhD thesis, University of Birmingham, Birmingham, UK.
- Chlebek, J. and Knight, D.W. (2006). A new perspective on sidewall correction procedures, based on SKM modeling. In Ferreira, R. M. L., Alves, E. C. T. L., Leal, J. G. A. B. And Cardoso, A. H. (eds) *Proc. RiverFlow 2006*, Taylor & Francis, Lisbon, 1, 135-144.
- Chlebek, J. and Knight, D.W. (2006). A new perspective on sidewall correction procedures, based on SKM modeling. *Proceedings of the International Conference on Fluvial Hydraulics (River Flow 2006)*. [Eds. Ferreira, R.M.L., Alves, E.C.T.L., Leal, J.G.A.B. & Cardoso, A.H.], Lisbon, Portugal, 1, 135-144.
- Chow, V.T. (1959). *Open-channel hydraulics*. McGraw-Hill, New York.
- Christensen, B. and Fredsoe, J. (1998). Bed shear stress distribution in straight channels with arbitrary cross section. Lyngby, Denmark, Institute of Hydrodynamics and

- Hydraulic Engineering, Technical University of Denmark, 77.
- Cokljat, D. (1993). Turbulence models for non-circular ducts and channels. PhD thesis, Department of Civil Engineering, City University, London, England.
- Cokljat, D. and Younis, B.A. (1995). Second-order closure study of open-channel flows. *J. Hydraulic Eng. (ASCE)*, 121 (2), 94-107.
- Colebrook C.F. and White C.M. (1937). Experiments with fluid friction in roughened pipes, *Proceedings of the Royal Society*, A161, 367.
- Cunge, J.A., Holly, F.M. and Verway, A. (1980). *Practical aspects of computational river hydraulics*. The Pitman Press, Bath, UK.
- De Cacueray, N., Hargreaves, D.M. and Morvan, H.P. (2009). A computational study of shear stress in smooth rectangular channels. *Journal of Hydraulic Research, IAHR*, 47 (1), 50-57.
- Demuren, A.O. (1989). *Calculation of Turbulence-Driven Secondary Motion in Ducts with Arbitrary Cross Section*. NASA Technical Memorandum 102412, Institute for Computational Mechanics in Propulsion.
- Drazin, P.G. and Riley, N. (2006). *The Navier-Stokes equations: a classification of flows and exact solutions*. Cambridge University Press, Cambridge.
- Einstein, H.A. (1942). Formulas for transportation of bed load. *Transactions of the American Society of Civil Engineers*, 68 (8, Part 2), 561-577.
- Elder, J.W. (1959). The dispersion of marked fluid in turbulent shear flow. *Journal of Fluid Mechanics*, Cambridge University Press, 5 (4), 544-560.
- Engelund, F. (1964). Flow resistance and hydraulic radius. *Acta Polytechnica Scandinavica: Civil Engineering and Building*, 24, 532-543.
- Ervine, D.A., Babaeyan-Koopaei, K. and Sellin, H.J. (2000). Two-dimensional solution for straight and meandering overbank flows. *J. Hydraulic Eng.*, 126 (9), 653-669.
- Fernandes, J.N. (2013). Compound Channel Uniform and Non-Uniform Flows With and Without Vegetation in the Floodplain. PhD Thesis in Civil Engineering, Instituto Superior Técnico, Universidade de Lisboa.
- Fernholz, H. and Finley, P. (1981). A further compilation of compressible turbulent boundary layer data with a survey of turbulence data. Advisory Group Aerospace

- Research and Development, AGARDograph 263.
- Fernholz, H., Janke, G., Schober, M., Wagner, P., and Warnack, D. (1996). New developments and applications of skin-friction measuring techniques. *Meas. Sci. Technol.*, 7, 1396-1409.
- Filonovich, M.S., Azevedo, R., Rojas-Solórzano, L., and Leal, J.B. (2013). Credibility Analysis of Computational Fluid Dynamic Simulations for Compound Channel Flow. *Journal of Hydroinformatics*, 15(3), 926-938.
- Fischer, H.B. and Calif, M.P. (1967). Transverse mixing in a sand bed channel. U.S Geological Survey Professional Paper 575-D.
- Fischer-Antze, T., Stoesser, T., Bates, P. and Olsen, N.R.B. (2001). 3D numerical modeling of openchannel flow with submerged vegetation. *J. Hydraulic Research*, 39 (3), 303-310.
- Flintham, T.P. and Carling, P.A. (1988). Prediction of mean bed and wall boundary shear in uniform and compositely rough channels. *Proceedings of the International Conference on River Regime*, Oxon, UK, 267-286.
- Flow Database at the University of Birmingham (2009). <http://flowdata.bham.ac.uk>.
- Franke, M., Wallin, S., and Thiele, F. (2005). Assessment of explicit algebraic Reynolds-stress turbulence models in aerodynamic computations. *Aerospace Science and Technology*, 9(7), 573- 581.
- Frewer, M. (2009). More clarity on the concept of material frame-indifference in classical continuum mechanics. *Acta Mechanica*, 202, 213-246.
- Gatski, T.B. and Jongen, T. (2000). Nonlinear eddy viscosity and algebraic stress models for solving complex turbulent flows. *Progress in Aerospace Sciences*, 36, 655-682.
- Gatski, T.B. and Wallin, S. (2004). Extending the weak-equilibrium condition for algebraic Reynolds stress models to rotating and curved flows. *Journal of Fluid Mechanics*, 518, 147-155.
- Gatski, T.B., Speziale, C.G. (1993). On explicit algebraic stress models for complex turbulent flows. *Journal of Fluid Mechanics*, 254, 59-78.
- Gessner, F.B. (1973). The origin of secondary flow in turbulent flow along a corner.

- Journal of Fluid Mechanics*, 58 (1), 1-25.
- Gessner, F.B. and Jones, J.B. (1965). On some aspects of fully-developed turbulent flow in rectangular channels. *J. Fluid Mech.*, 23, 689-713.
- Ginder, R. and Bradbury, L. (1973). Preliminary investigation for skin friction measurements in highly turbulent flows,. Technical report, ARC Report.
- Girimaji, S.S. (1997). A galilean invariant explicit algebraic Reynolds stress model for turbulent curved flows. *Physics in Fluids*, 9, 1067-1077.
- Glover, R.E. (1964). Dispersion of dissolved or suspended materials in flowing streams. U.S. Geological Survey, Professional Paper 433-B.
- Goncharov, V.N. (1964). Dynamics of channel flow. Israel Program for Scientific Translations, Jerusalem.
- Grega, L.M., Wei, T., Leighton, R.I. and Nevens, J.C. (1995). Turbulent mixed boundary flow in a corner formed by a solid wall and a free surface. *J. Fluid Mech.*, 294, 17-46.
- Grundestam, O., Wallin, S., Johansson, A.V. (2006). Observations on the predictions of fully developed rotating pipe flow using differential and explicit algebraic Reynolds stress models. *European Journal of Mechanics - B/Fluids*, 25(1), 95-112.
- Guo, J. and Julien, P.Y. (2005). Shear stress in smooth rectangular open-channel flows. *Journal of Hydraulic Engineering*, 131 (1), 30-37.
- Hamba, F. (2006). Euclidian invariance and weak-1 equilibrium condition for the algebraic Reynolds stress model. *Journal of Fluid Mechanics*, 569, 399-408.
- Hanjalić, K. (1999). Second-Moment Turbulence Closures for CFD: Needs and Prospects. *International Journal of Computational Fluid Dynamics*, 12(1), 67-97.
- Haritonidis, J. (1989). The measurements of wall-shear stress. *Advances in Fluid Mechanics Measurements*, pages 229-261.
- Head, M. and Rechenberg, I. (1962). The preston tube as a means of measuring skin friction. *J. Fluid Mech.*, 14, 1-17.
- Head, M. and Vasanta Ram, V. (1971). Simplified presentation of the preston tube calibration. *Aeronautical Quarterly*, XXII:295-300.
- Heinz, M. (2002) Investigation of Bendway Weir Spacing. Master's Thesis, Colorado

- State University, Department of Civil and Environmental Engineering, Fort Collins, CO.
- Heinz, M. (2002). *Investigation of Bendway Weir Spacing*. Master's Thesis, Colorado State University, Department of Civil and Environmental Engineering, Fort Collins, Colorado.
- Hellsten, A, and Wallin, S. (2009). Explicit algebraic Reynolds stress and non-linear eddy-viscosity Models. *International Journal of Computational Fluid Dynamics*, 23(4), 349-361.
- Hellsten, A. (2004). *New two-equation turbulence model for aerodynamics applications*. PHD Thesis. Helsinki University of Technology, Espoo, Finland, ISBN 951-22-6933-3.
- Henderson, F.M. (1966). *Open channel flow*. Macmillan Publishing, New York.
- Hirt, F. and Thomann, H. (1986). Measurements of wall shear stress in turbulent boundary layers subject to strong pressure gradients. *J. Fluid Mech.*, 171:547-562.
- Hoagland, L.C. (1960). *Fully Developed Turbulence Flow in Straight Rectangular Ducts Secondary Flow - Its Cause and Effect on the Primary Flow*. Massachusetts Institute of Technology.
- Holley, E.R. and Abraham, G. (1973). Laboratory studies on transverse mixing in rivers. *Journal of Hydraulic Research*, IAHR, 11 (3), 219-253.
- Hsu, E.Y. (1955). The Measurement of Local Turbulent Skin Friction by Means of Surface Pitot Tubes." David W. Taylor Model Basin, Report No. 957, August.
- Hsu, T.Y., Grega, L.M., Leighton, R.I. and Wei, T. (2000). Turbulent kinetic energy transport in a corner formed by a solid wall and a free surface. *J. Fluid Mech.*, 410, 343-366.
- Ikeda, S. (1981). Self-formed straight channels in sandy beds. *Journal of the Hydraulics Division*, ASCE, 107 (HY4 Proc. Paper, 16195), 389-406.
- Ippen, A.T., Drinker, P.A., Jobin, W.R., and Noutsopoulos, G.K. (1960). The Distribution of Boundary Shear Stresses in Curved Trapezoidal Channels. Department of Civil and Sanitary Engineering, Massachusetts Institute of Technology, Technical Report No. 43, October.

- Jakirlić, S. and Hanjalić, K. (2002). A new approach to modelling near-wall turbulence energy and stress dissipation. *Journal of Fluid Mechanics*, 459, 139-166.
- Janke, G. (1987). Hot wire in wall proximity. In ed G Compte-Bellot and Mathieu, J., editors, *Advances in Turbulence*, pages 488-498.
- Janke, G. (1993). Über die Grundlagen und einige Anwendungen der Ölfilm-Interferometrie zur Messung von Wandreibungsfeldern in Luftströmungen. Master's thesis, Technische Universität Berlin.
- Kang, H. and Choi, S.-U. (2006a). Reynolds stress modelling of rectangular open-channel flow. *Int. Journal for Numerical Methods in Fluids*, 51, 1319-1334.
- Kang, H. and Choi, S.-U. (2006b). Turbulence modelling of compound open-channel flows with and without vegetation on the floodplain using the Reynolds stress model. *Advances in Water Resources*, 29, 1650-1664.
- Kara, S., Stoesser, T., and Sturm, T.W. (2012). Turbulence statistics in compound channels with deep and shallow overbank flows. *Journal of Hydraulic Research*, 50(5), 482-493, DOI: [10.1080/00221686.2012.724194](https://doi.org/10.1080/00221686.2012.724194).
- Kazemipour, A.K. and Apelt, C.J. (1980). Shape effects on resistance to flow in smooth rectangular channels. Research Report Series - University of Queensland, Department of Civil Engineering, CE9.
- Keller, R.J. and Rodi, W. (1989). Prediction of flow characteristics in main channel/flood plain flows. *J. Hydraulic Research*, 26 (4), 425-441.
- Kempf, G. (1929). Neue Ergebnisse der Widerstandsforschung. *Werft, Reederei, Hafen*, II:234-239.
- Khodashenas, S.R. and Paquier, A. (1999). A geometrical method for computing the distribution of boundary shear stress across irregular straight open channels. *Journal of Hydraulic Research*, 37 (3), 381-388.
- Kim, J., Moin, P. and Moser, R. (1987). Turbulence statistics in fully developed channel flow at low Reynolds number. *J. Fluid Mech.*, 177, 133-166.
- Knight, D.W. (1981). Boundary shear stress in smooth and rough channels. *Journal of the Hydraulics Division, ASCE*, 107 (7), 839-851.
- Knight, D.W. (1992). SERC Flood Channel Facility experimental data - Phase A, Vols.

- 1-15, School of Civil Engineering, The University of Birmingham: Birmingham.
- Knight, D.W. (2013). River hydraulics – a view from midstream. *J. Hydraulic Research*, 51 (1), 2-18.
- Knight, D.W. and Abril, B. (1996). Refined calibration of a depth-averaged model for turbulent flow in a compound channel. *Proceedings of the Institution of Civil Engineers, Water, Maritime and Energy Division*, 118 (3), 151-159.
- Knight, D.W. and Demetriou, J.D. (1983). Flood plain and main channel flow interaction, *Journal of Hydraulic Engineering*, 109(8), 1073-1092.
- Knight, D.W. and Patel, H.S. (1985). Boundary shear in smooth rectangular ducts. *Journal of Hydraulic Engineering*, ASCE, 111 (1), 29-47.
- Knight, D.W. and Sellin, R.H.J. (1987). The SERC Flood Channel Facility. *J. of the Institution of Water and Environmental Management*, 1 (2), 198-204.
- Knight, D.W. and Shiono, K. (1990). Turbulence measurements in a shear layer region of a compound channel. *Journal of Hydraulic Research*, IAHR, 28 (2), 175- 196.
- Knight, D.W. and Shiono, K. (1996). River channel and floodplain hydraulics. In Anderson, M.G., Walling, D.E. & Bates, P.D. (Eds.) *Floodplain Processes*. J.Wiley & Sons, 139-181.
- Knight, D.W., Demetriou, J.D. and Hamed, M.E. (1984a). Boundary shear in smooth rectangular channels. *Journal of Hydraulic Engineering*, ASCE, 110 (4), 405-422.
- Knight, D.W., Demetriou, J.D. and Hamed, M.E. (1984b). Stage discharge relationships for compound channels. Proceedings of the 1st International Conference on Hydraulic Design in Water Resources Engineering: Channels and Channel Control Structures. [Ed. Smith, K.V.H.], Southampton, 4.15-14.36.
- Knight, D.W., Omran, M., and Tang, X. (2007). Modeling depth-averaged velocity and boundary shear in trapezoidal channels with secondary flows. *Journal of Hydraulic Engineering*, 133(1), 39-47, DOI: [10.1061/ASCE0733-94292007133:139](https://doi.org/10.1061/ASCE0733-94292007133:139).
- Knight, D.W., Patel, H.S., Demetriou, J.D. and Hamed, M.E. (1983). Boundary shear stress distributions in open channel and closed conduit flows. *Proceedings of Euromech 156 - The Mechanics of Sediment Transport*. [Eds. Sumer, B.M. & Muller, A.], Istanbul, Turkey, 33-40.

- Knight, D.W., Wright, N.G. and Morvan, H.P. (2005). Guidelines for applying commercial CFD software to open channel flow. Report based on the research work conducted under EPSRC Grants GR/R43716/01 and GR/R43723/01.
- Knight, D.W., Yuen, K.W.H. and Al-Hamid, A.A.I. (1994). Boundary shear stress distributions in open channel flow. In Beven, K., Chatwin, P. & Millbank, J. (Eds.), *Physical Mechanisms of Mixing and Transport in the Environment*. John Wiley & Sons, 51-87.
- Kolmogorov, A.N. (1941). The local structure of turbulence in incompressible viscous fluid for very large Reynolds numbers. *Proceedings of the USSR Academy of Sciences* (in Russian), 30, 299-303.
- Konstantinov, N. and Dragnysh, G. (1960). The measurement of friction stress on a surface. English translation, DSIR RTS 1499.
- Krishnappan, B.G. and Lau, Y.L. (1986). Turbulence modelling of flood plain flows. *J. Hydraulic Eng.* (ASCE), 112(4), 251-266.
- KWRA (Korea Water Resources Association) (2007). *Standard Specification of River Construction*.
- Lambert, M.F. and Myers, W.R. (1998). Estimating the discharge capacity in straight compound channels, In Proc. of the Institution of Civil Engineers - Water, Maritime and Energy, 130, 84-94.
- Lambert, M.F. and Sellin, R.H.J. (1996). Discharge prediction in straight compound channels using the mixing length concept. *J. Hydraulic Research*, 34 (3), 381-394.
- Lau, Y.L. and Krishnappan, B.G. (1977). Transverse dispersion in rectangular channels. *Journal of the Hydraulics Division*, ASCE, 103 (10), 1173-1189.
- Lauder, B.E. and Ying, W.H. (1973). Prediction of flow and heat transfer in ducts of square cross section, In Proc. Inst. Mech. Engrs., 187, 455-461.
- Lauder, B.E., Reece, G.J., and Rodi, W. (1975). Progress in the development fo a reynolds-stress turbulence closure. *Journal of Fluid Mechanics*, 68(3), 537-566.
- Leighly, J. B. (1932). Toward a theory of the morphologic significance of turbulence in the flow of water in streams. *Geography*, University of California Publications, 6 (1), 1-22.

- Lin, B. and Shiono, K. (1995). Numerical modelling of solute transport on compound channel flows. *J. Hydraulic Research*, 33 (6), 773-788.
- Ludweig, H., and Tillman, W. (1950). *Investigations of the Wall-Shearing Stress in Turbulent Boundary Layers*. National Advisory Committee for Aeronautics, Technical Memorandum 1285, May.
- Lundgren, H. and Jonsson, I.G. (1964). Shear and velocity distribution in shallow channels. *Journal of the Hydraulics Division, ASCE*, 90 (1), 1-21.
- Massey, B.S. (1998). *Mechanics of fluids*. 6th edition, Chapman and Hall, London.
- McGahey, C. (2006). A practical approach to estimating the flow capacity of rivers. PhD thesis, The Open University, UK.
- McGahey, C., Knight, D.W. and Samuels, P.G. (2009). Advice, methods and tools for estimating channel roughness. *Proceedings of the Institution of Civil Engineers: Water Management*.
- McGahey, C., Samuels, P.G. and Knight, D.W. (2006). A practical approach to estimating the flow capacity of rivers-application and analysis. In Proc. Int. Conf. on Fluvial Hydraulics (River Flow 2006), Lisbon, Portugal, September, 1, 303-312. Taylor & Francis, London.
- McGahey, C., Samuels, P.G., Knight, D.W. and O'Hare, M.T. (2008). Estimating river flow capacity in practice. *Journal of Flood Risk Management*, Wiley InterScience, 1 (1), 23-33.
- Melling, A. and Whitelaw, J.H. (1976). Turbulent flow in a rectangular duct. *Journal of Fluid Mechanics*, Cambridge University Press, 78 289-315.
- Menter, F.R. (1994). Two-equation eddy-viscosity turbulence models for engineering applications. *AIAA Journal*, 32(8), 1598-1605.
- Menter, F.R. (2009). Review of the shear-stress transport turbulence model experience from an industrial perspective. *International Journal of Computational Fluid Dynamics*, 23(4), 305-316.
- Menter, F.R. (2011). Turbulence Modeling for Engineering Flows. Technical paper from ANSYS, Inc. 1-25.
- MOCT (Ministry of Construction and Transportation) (2008). *Planning Guideline for*

- Integrated Flood Management Plan in River Basin and River Master Plan.*
- MOCT (Ministry of Construction and Transportation) (2009). *River Design Criteria.*
- Moin, P. and Kim, J. (1981). *Numerical Investigation of Turbulent Channel Flow.*
NASA Technical Memorandum 81309, NASA.
- Moody, M.L. (1947). An approximate formula for pipe friction factors. *Transactions of ASME*, 69, 1005.
- Muller, A. and Studerus, X. (1979). Secondary flow in open channel. Congress of International Associations for Hydraulic Research, Italy, 189-222.
- Munson, Bruce R., et al. *Fundamentals of Fluid Mechanics*, 2nd Edition. New York: John Wiley and Sons, 1994.
- Myers, W.R.C. (1978). Momentum transfer in a compound channel. *J. Hydraulic Research*, 16 (2), 139-150.
- Naji, H., Mompean, G., and Yahyaoui, O. (2004). Evaluation of 1 explicit algebraic stress models using direct numerical simulations. *Journal of Turbulence*, 5(38), 1-25.
- Naot, D. and Rodi, W. (1982). Calculation of secondary currents in channel flow. *J. Hydraulic Div. (ASCE)*, 108 (8), 948-968.
- Naot, D., Nezu, I. and Nakagawa, H. (1993). Hydrodynamic behavior of compound rectangular open channels. *J. Hydraulic Eng. (ASCE)*, 122 (11), 625-633.
- Naot, D., Nezu, I. and Nakagawa, H. (1996). Hydrodynamic behavior of partly vegetated open channels. *J. Hydraulic Eng. (ASCE)*, 119 (3), 390-408.
- Nezu, I and Nakagawa, H. (1993). Turbulence in open-channel flows. In: IAHR Monograph Series. Rotterdam: Balkema.
- Nezu, I. (1994). Compound open-channel turbulence and its role in river environment. Keynote Address of 9th APD-IAHR Congress, Delft, The Netherlands, 1-24.
- Nezu, I. (1996). Experimental and numerical study on 3-D turbulent structures in compound open-channel flows. *Flow modelling and turbulence measurements*, C.J. Chen et al., eds., Balkema, Rotterdam, The Netherlands, 65-74.
- Nezu, I. (2005). Open-Channel Flow Turbulence and Its Research Prospect in the 21st Century. *J. Hydraulic Eng. (ASCE)*, 131 (4), 229-246.

- Nezu, I. and Nakagawa, H. (1984). Cellular secondary currents in straight conduit. *Journal of Hydraulic Engineering*, 110(2), 173-193.
- Nezu, I. and Nakagawa, H. (1993). Turbulence in open-channel flows. *IAHR-Monograph*, Balkema, Rotterdam, The Netherlands.
- Nezu, I. and Rodi, W. (1985). Experimental study on secondary currents in open channel flow. *Proceeding of 21st IAHR Congress*, Melbourne, Australia, 2, 115-119.
- Nezu, I. and Rodi, W. (1986). Open-channel flow measurements with a laser doppler anemometer. *Journal of Hydraulic Engineering*, 112(5), 335-355.
- Nezu, I., Onitsuka, K. and Iketani, K. (1999). Coherent horizontal vortices in compound open-channel flows. In *Hydraulic modelling* (ed. I. W. Seo V. P. Singh and J. H. Sonu). Water Resources Publications, Colorado, USA, 17-32
- Nikora, V. and Roy, A.G. (2012). Secondary flows in rivers: Theoretical framework, recent advances, and current challenges. *Gravel-bed Rivers: Processes, Tools, Environments*. M. Church, P.M. Biron, A.G. Roy, eds. John Wiley & Sons, USA, 3-22.
- Nikuradse, J. (1933). Translates to: Laws of Flow in Rough Pipes, Verein deutscher Ingenieure, Forschungsheft, 361, Berlin.
- Nokes, R.I. and Wood, I.R. (1988). Vertical and Lateral Turbulent Dispersion: Some Experimental Results. *Journal of Fluid Mechanics*, Cambridge University Press, 187 373-394.
- Odgaard, A.J. (1984). Shear-induced secondary currents in channel flows. *Journal of Hydraulic Engineering*, ASCE, 110 (7), 996-1004.
- Olivero, M., Aguirre-Pey, J. and Moncada, A. (1999). Shear stress distribution in rectangular channels. *Proceeding of XXVIII IAHR Congress*, Graz, Austria, papers on CD-ROM, 6.
- Omran, M.N. (2005). Modelling stage-discharge curves, velocity and boundary shear stress distributions in natural and artificial channels using a depth averaged model. PhD thesis, University of Birmingham, Birmingham, UK.
- Patel, V.C. (1965). Calibration of the Preston tube and limitations on its use in pressure

- gradients. *Journal of Fluid Mechanics*, 23, 185-208.
- Perkins, H.J. (1970). The formation of streamwise vorticity in turbulent flow. *Journal of Fluid Mechanics*, Cambridge University Press, 44 (04), 721-740.
- Pezzinga, G. (1994). Velocity distribution in compound channel flows by numerical modeling. *Journal of Hydraulic Engineering*, 120(10), 1176-1198.
- Piomelli U. (1999). Large-eddy simulation: achievements and challenges. *Progress in Aerospace Sciences*, 35, 335-362.
- Pizzuto, J.E. (1991). A numerical model for calculating the distributions of velocity and boundary shear stress across irregular straight open channels. *Water Resources Research*, 27 (9), 2457-2466.
- Pope, S.B. (2000), *Turbulent flows*. Cambridge University Press, Cambridge, United Kingdom. ISBN 0-521-59886-9.
- Prandtl, L. (1933). Neuere Ergebnisse der Turbulenzforschung, *Z. Ver. Deut. Ing.* 77, 105-114.
- Prandtl, L. (1952). *Essentials of Fluid Dynamics*, Hafner Publishing Co., New York.
- Prandtl, W. (1926). Auf der Suche nach dem Element Nr. 61. *Angewandte Chemie*, 39, 897-898, doi:10.1002/ange.19260393002.
- Preston, J. H. (1954) The Determination of Turbulent Skin Friction by Means of Pitot Tubes. *Journal of the Royal Aeronautical Society*, Vol. 58: 109-121.
- Qiu, J-F., Obi, S., and Gatski, T.B. (2008). On the weak-equilibrium condition for derivation of algebraic heat flux model. *International Journal of Heat and Fluid Flow*, 29, 1628-1637.
- Rameshwaran, P. and Naden, P. S. (2003). Three dimensional numerical simulation of compound channel flows. *J. Hydraulic Eng. (ASCE)*, 129 (8), 645-652.
- Reece, G.J. (1977). A generalized Reynolds stress model of turbulence. PhD thesis, Imperial College, University of London, London, England.
- Reynolds, A.J. (1974). *Turbulent flow in engineering*. John Wiley & Sons, Great Britain.
- Rezaei, B. (2006). Overbank flow in compound channels with prismatic and non prismatic floodplains. PhD thesis, University of Birmingham, Birmingham, UK.
- Rezaei, B., and Knight, D.W. (2009). Application of the Shiono and Knight method in

- compound channels with non-prismatic floodplains. *J. Hydraul. Eng.*, 47 (6), 716-726.
- Rhodes, D.G. and Knight, D.W. (1995). Lateral shear in wide compound duct. *Journal of Hydraulic Engineering*, ASCE, 121 (11), 829-832.
- Robertson, E., Choudhury, V., Bhushan, S., and Walters, D.K. (2015). Validation of OpenFOAM numerical methods and turbulence models for incompressible bluff body flows. *Computers and Fluids*, 123, 122-145, DOI: [10.1016/j.compfluid.2015.09.010](https://doi.org/10.1016/j.compfluid.2015.09.010).
- Rodi, W. (1976). A new algebraic relation for calculating the Reynolds stresses. *Zeitschrift fuer angewandte Mathematik und Mechanik*, 56, 219-221.
- Rodi, W. (1980). Turbulence models and their application in hydraulics: State of the art paper. IAHR, Delft.
- Rosemount. (2002) *Annubar Flowmeter Series Reference Manual*. Rosemount, 00809-0100-4809, August.
- Rouse and Hunter (1946). *Elementary Fluid Mechanics*. New York: Dover Publications.
- Rouse, H. (1936). Discharge characteristics of the free overfall. *Civil Engineering*, ASCE, 6 (4), 257-260.
- Rouse, H. (1943). Discussion on "Energy loss at the base of a free overfall" by W.L. Moore. *Transactions of ASCE*, ASCE, 108: 1383-1387.
- Rouse, H. (1946). *Elementary mechanics of fluids*. John Wiley and Sons, New York.
- Rouse, H. (1959). *Advanced mechanics of fluids*. Wiley & Sons, New York.
- Rouse, H. (1965). Critical analysis of open-channel resistance. *Journal of the Hydraulics*
- Saint-Venant, A. (1871). Theorie du mouvement non permanent des eaux, avec application aux crues des rivieres et a l'introduction de marees dans leurs lits. Comptes rendus des seances de l'Academie des Sciences.
- Sayre, W.W. and Chamberlain, A.R. (1964). Exploratory laboratory study of lateral turbulent diffusion at the surface of an alluvial channel. U.S. Geological Survey, Circular 484.
- Schlichting, H. (1979). *Boundary Layer Theory*. 7th edition, McGraw-Hill, London.
- Sellin, R.H.J. (1964). A laboratory investigation into the interaction between the flow in

- the channel of a river and that over its flood plain. *La Houille Blanche*, Paris, France, 7, 793-802.
- Shafi, H.S. and Antonia, R.A. (1995). Anisotropy of the Reynolds stresses in a turbulent boundary layer on a rough wall. *Experiments in Fluids*, 18(3), 213-215.
- Sharifi, S. (2009). Application of Evolutionary Computation to Open Channel Flow Modelling. PhD thesis, The University of Birmingham.
- Sharifi, S., Knight, D.W. and Sterling, M. (2008). Modelling flow using SKM and a multi-objective evolutionary algorithm. In: Altinakar, M.S., Kokpinar, M.A., Aydin, I., Cokgar, S. and Kirkgoz, S. (eds) In Proc. RiverFlow 2008, Cesme, Turkey, 3, 2149-2158.
- Sharifi, S., Knight, D.W. and Sterling, M. (2009) A novel application of a multi-objective evolutionary algorithm in open channel flow modelling. *J. of Hydroinformatics*, 11 (1), 31-50.
- Shi, J., Thomas, T.G., and Williams, J.J.R. (1999). Large eddy simulation of flow in a rectangular open channel. *Journal of Hydraulic Research*, 37(3), 345-361, DOI: [10.1080/00221686.1999.9628252](https://doi.org/10.1080/00221686.1999.9628252).
- Shiono, K. and Knight, D.W. (1988). Two-dimensional analytical solution for a compound channel. *Proceedings of the 3rd International Symposium on Refined Flow Modelling and Turbulence Measurements*, Tokyo, Japan, 503-510.
- Shiono, K. and Knight, D.W. (1990). Mathematical models of flow in two or multi stage straight channels. *Proceedings of the Conference on River Flood Hydraulics*. [Ed. White, W.R.], Wallingford, 229-238.
- Shiono, K. and Knight, D.W. (1991). Turbulent open-channel flows with variable depth across the channel. *Journal of Fluid Mechanics*, Cambridge University Press, 222, 617-646.
- Shiono, K., Scott, C.F. and Kearney, D. (2003). Predictions of solute transport in a compound channel using turbulence models. *J. Hydraulic Research*, 41 (3), 247-258.
- Shir, C.C. (1973). A preliminary study of atmospheric turbulent flow in idealized planetary boundary layer. *Journal Atmospheric Science*, 30, 1327-1339.

- Smagorinski J. (1963). General circulation experiments with the primitive equations. *Mon. Weather Rev.*, 91, 99.
- Sofialidis, D. and Prinos, P. (1998). Compound open-channel flow modelling with nonlinear low-Reynolds $k-\epsilon$ models. *J. Hydraulic Eng.*, 124 (3), 253-262.
- Spalart, P.R. and Shur, M. (1997). On the sensitization of turbulence models to rotation and curvature. *Aerospace Science and Technology*, 1(5), 297-302.
- Speziale, C.G. (1987). On nonlinear $k-l$ and $k-\omega$ models of turbulence. *J. Fluid Mech.*, 178, 459-475.
- Speziale, C.G. (1991). Analytical methods for the development of Reynolds stress closures in turbulence. *Annual Review of Fluid Mechanics*, 23, 107-157.
- Speziale, C.G. (1998). A review of material frame-indifference in mechanics. *Applied Mechanics Reviews*, 51(8), 489-504.
- Speziale, C.G. and Gatski, T.B. (1997). Analysis and modelling of Γ anisotropies in the dissipation rate of turbulence. *Journal Fluid Mechanics*, 344, 155-180.
- Speziale, C.G., Sarkar, S. and Gatski, T.B. (1991). Modelling the pressure-strain correlation of turbulence: an invariant dynamical systems approach. *J. Fluid Mech.*, 277, 245-272.
- Speziale, C.G., So, R.M.C., and Younis, B.A. (1992). *On the Prediction of Turbulent Secondary Flows*. ICASE Report No. 92-57, NASA Contractor Report 189722, NASA.
- Sterling, M., Beaman, F., Morvan, H. and Wright, N. (2008). Bed-Shear Stress Characteristics of a Simple, Prismatic, Rectangular Channel. *J. Eng. Mech.*, 134 (12), 1085-1094.
- Tanner, L. and Blows, L. (1986). A study on the motion of oil films on surfaces in air flow, with application to the measurement of skin friction. *J. Phys. E. Sci. Instrum.*, 9, 194-202.
- Taulbee, D.B. (1992). An improved algebraic Reynolds stress model and corresponding nonlinear stress model. *Physics of Fluids A*, 4(11), 2555-2560.
- TFFF (1963). Friction factor in open channels, Report of the ASCE Task Force. *Journal of Hydraulic Engineering*, ASCE, 89 (2), 97-143.

- Thomas, T.G. and Williams, J.J.R. (1995a). Large eddy simulation of turbulent flow in an asymmetric compound channel. *J. Hydraulic Research*, 33 (1), 27-41.
- Thomas, T.G. and Williams, J.J.R. (1995b). Large eddy simulation of a symmetric trapezoidal channel at a Reynolds number of 430,000. *J. Hydraulic Research*, 33 (6), 825-841.
- Thomson, R.L. and Mompean, G. (2010). An alternative assessment of weak-equilibrium conditions in turbulent closure modeling. *International Journal of Engineering Science*, 48(11), 1633-1640.
- Thornton, C.I., Cox, A.L., and Sclafani, P. (2008). *Preston Tube Calibration*. Colorado State University Engineering Research Center, Fort Collins, Colorado.
- Tominaga, A. and Ezaki, K. (1988). Hydraulic characteristics of compound channel flow. In Proc. 6th Cong. Asian and Pacific Regional Div., Int. Assoc. for Hydr. Res., Kyoto, Japan.
- Tominaga, A. and Nezu, I. (1991). Turbulent structure in compound open channel flows. *Journal of Hydraulic Engineering*, 117(1), 21-41.
- Tominaga, A., Ezaki, K., Nezu, I. and Nakagawa, H. (1989). Three-dimensional turbulent structure in straight open channel flows. *J. Hydraulic Research*, 27 (1), 149-173.
- Tominaga, A., Nezu, I., Ezaki, K. and Nakagawa, H. (1989). Three-dimensional turbulent structure in straight open channel flows. *Journal of Hydraulic Research*, 27 (1), 149-173.
- Tracy, H.J. and Lester, C.M. (1961). Resistance coefficients and velocity distribution, smooth rectangular channel. U.S. Geological Survey, Water-supply paper 1592-A, 1-18.
- Vagt, J. and Fernholz, H. (1973). Use of surface fences to measure wall shear stress in three-dimensional boundary layers. *Aeronautical Quarterly*, XXIV:87-91.
- Van Prooijen, B.C., Battjes, J.A. and Uijtewaal, W.S.J. (2005). Momentum exchange in straight uniform compound channel flow. *Journal of Hydraulic Engineering*, 131(3), 175-183.
- Versteeg, H.K. and Malalasekera, W. (2007). *An introduction to computational fluid*

- dynamics. The finite volume method.* 2nd Ed., Pearson Education Ltd., UK.
- Villiers, E.D. (2006). The Potential of Large Eddy Simulation for the Modeling of Wall Bounded Flows. PhD thesis, Imperial College of Science, Technology and Medicine.
- Wagner, P. (1991). The use of near-wall hot-wire probes for time-resolved skin-friction measurements. In ed A V Johansson and Alfredsson, P. H., editors, *Advances in Turbulence*, 3, 524-529.
- Wallin, S. and Johansson, A.V. (2000). An explicit algebraic Reynolds stress model for incompressible and compressible turbulent flows. *Journal of Fluid Mechanics*, 403, 89-132.
- Wallin, S. and Johansson, A.V. (2002). Modeling streamline curvature effects in explicit algebraic Reynolds stress turbulence models. *International Journal of Heat and Fluid Flow*, 23, 721-730.
- Webel, G. and Schatzmann, M. (1984). Transverse mixing in open channel flow. *Journal of Hydraulic Engineering*, ASCE, 110 (4), 423-435.
- Weis, J. and Hutter, K. (2003). On Euclidean invariance of algebraic Reynolds stress models in turbulence. *Journal of Fluid Mechanics*, 476, 63-68.
- Weisbach J. (1845). *Lehrbuch der ingenieur- und maschinen-mechanik*, Braunschweig.
- Winter, K. (1977). An outline of the techniques available for the measurement of skin friction in turbulent boundary layers. *Progr. Aerosp. Sci.*, 18:1-55.
- Wormleaton, P.R. (1996). Floodplain secondary circulation as a mechanism for flow and shear stress redistribution in straight compound channels. In Ashworth, Bennett, Best, and McLelland (Ed.) *Coherent flow structures in open channels*. Wiley, New York, 581-608.
- Wright, N.G. (2001). Conveyance implications for 2D and 3D modelling. Specialist Review for Scoping Study for Reducing Uncertainty in River Flood Conveyance, R & D Technical Report by HR Wallingford to DEFRA/Environment Agency.
- Wright, N.G., Crossley, A.J., Morvan, H.P. and Stoesser, T. (2004). Detailed validation of CFD for flows in straight channels, In Proc. River Flow 2004, Naples, Italy.
- Wu, W., Rodi, W. and Wenka, T. (2000). 3D numerical modelling of flow and

- sediment transport in open channels. *J. Hydraulic Eng.* (ASCE), 126 (1), 4-15.
- Xie, Z., Lin, B. and Falconer, R.A. (2013). Large-eddy simulation of the turbulent structure in compound open-channel flows. *Advances in Water Resources*, 53, 66-75.
- Yang, K., Nie, R., Liu, X. and Cao, S. (2013). Modeling Depth-Averaged Velocity and Boundary Shear Stress in Rectangular Compound Channels with Secondary Flows. *J. Hydraulic Eng.* (ASCE), 139 (1), 76-83.
- Yang, S.Q. and Lim, S.Y. (1997). Mechanism of energy transportation and turbulent flow in a 3D channel. *Journal of Hydraulic Engineering*, ASCE, 123 (8), 684-692.
- Yang, S.Q. and Lim, S.Y. (1997). Mechanism of energy transportation and turbulent flow in a 3D channel. *Journal of Hydraulic Engineering*, ASCE, 123 (8), 684-692.
- Yang, S.Q. and Lim, S.Y. (2005). Boundary shear stress distributions in trapezoidal channels. *Journal of Hydraulic Research*, IAHR, 43 (1), 98-102.
- Yen, B.C. (1991). Hydraulic resistance in open channels. In Yen, B.C. (Ed.) *Channel Flow: Centennial of Manning's Formula*. Water Resources Publications, Littleton, CO., 1-135.
- Yotsukura, N., Fischer, H.B. and Sayre, W.W. (1970). Measurement of mixing characteristics of the Missouri River between Sioux City, Iowa, and Plattsmouth, Nebraska. U.S. Geological Survey, Water Supply paper 1899-G.
- Yuen, K.W.H. (1989). A study of boundary shear stress flow resistance and momentum transfer in open channels with simple and compound trapezoidal cross-section, in Department of Civil Engineering, University of Birmingham: Birmingham.
- Zurfluh, U. (1984). Experimentelle bestimmung der wandschubspannung in turbulenten grenzschichten. Master's thesis, ETH Zurich.

국 문 요 지

복단면 하도의 소류력은 단면 형태에 따라 분포 특성이 다르게 나타난다. 국내 하천 설계에서는 주로 단면 평균 소류력 또는 2차원 모형에 의한 소류력 분포를 이용하여 설계 소류력을 산정하고 호안 등의 구조물의 외력으로 적용하고 있다. 그러나 복단면 하도의 횡단 소류력 분포는 단면형으로 인해 발생하는 이차류에 영향을 받으며 이는 3차원적 거동 특성을 나타낸다. 기존의 단면 평균 소류력 계산에 의한 설계 소류력은 하안부의 소류력을 과대 또는 과소하게 평가하여 하안 세굴 피해 또는 과대 설계의 문제가 발생한다. 본 연구에서는 복단면 하도의 형상에 따른 평균 소류력에 대한 국부 소류력의 관계를 연구하여 하도 설계 실무에서 활용할 수 있는 설계인자를 개발하였다. 대표적인 복단면 하도의 소류력을 실험을 통해서 측정하고, 이를 3차원 CFD 모형과 비교하여 검증하였다. 검증된 모형을 이용해서 고수부지의 폭과 높이를 대표 변수로 하도 형상에 따른 소류력의 분포를 분석하여 평균 소류력에 대한 하안, 고수부지, 제방 등의 소류력 분포 특성을 노모그래프로 제시하였다. 소류력 측정 실험에서는 프레스턴 튜브를 이용하여 측정하였으며, 3차원 CFD 모형은 OpenFoam 모형을 이용하였다. LES 모형을 적용하여 기존 실험결과 비교하여 검증하였으며 이를 기초로 다양한 하폭비와 수심비에 대한 복단면 하도 형상에 대한 수치모의를 수행하여 평균 소류력과 국부 소류력 간의 관계를 설계인자와 노모그래프로 제시하였다. 본 연구에서 도출된 복단면 하도의 흐름 구조와 설계인자는 복단면 하도의 적정 설계에 기여할 것으로 기대된다.

주요어 : 개수로 복단면, 설계 소류력, 바닥 전단력, OpenFoam, Large eddy simulation, 노모그래프